Analysis of novel therapeutic options for Adenoid cystic carcinoma of the salivary glands

Alexandra Rose

December 2020

Institute of Cancer Research

University of London

This thesis is submitted for the degree of Doctor of Philosophy

Declaration

This thesis was completed under the supervision of Dr Amanda Swain and Prof. Kevin Harrington. The work described here was completed at the Institute of Cancer Research, Chester Beatty Laboratories, 247 Fulham Road, London, SW3 6JB.

I, Alexandra Rose, confirm that the work presented in this thesis is my own, and where others have contributed, they have been acknowledged. Where information has been derived from other sources, it is indicated in the text.

Signed: 

Date: 10/12/2020

COVID-19: Statement of impact

During my final year, the COVID-19 pandemic interrupted my studies. For a period of 10 weeks I was unable to perform experiments, and subsequently was awarded a 10-week extension by the Institute of Cancer Research (ICR). In order to follow the government safety guidelines, when the Institute reopened following the national lockdown the number of people allowed into specific work spaces was limited. Therefore, as my access on site was limited, my productivity within the lab was impacted.

When the lockdown was introduced, I lost on-going experiments and cultures that were challenging to re-establish when the ICR reopened. For example, long-term cultured organoids were lost when the Institute closed. These were PDX-derived organoid cultures that had been passaged over two months in a hypoxic chamber and were on-going. However, on return to the labs, the hypoxic chamber was in high demand and so I could not re-establish these lines, therefore could not investigate the effect of hypoxia on ACC growth further. In addition, I was unable to confirm MYB-expression under different culture conditions in multiple PDX lines as desired due to limited sample availability following lockdown, and the slow-growing nature of the samples meant assays were two weeks long further limiting my progress.

In summary, due to the nature of my project and the requirement of long-term PDX-derived *in vitro* cultures, the COVID-19 pandemic impacted my progress in the fifth results chapter investigating 2D and 3D PDX-derived model establishment.

Signed: 

Alexandra Rose

Signed: 

Dr Amanda Swain

Abstract

Adenoid cystic carcinoma (ACC) of the salivary glands is characterised by slow growth, frequent metastasis and low survival rates. ACC is resistant to conventional chemotherapy and currently, no systemic agent has proven effective. MYB activation is a hallmark of ACC, with the most common genetic aberration being the *MYB-NFIB* translocation, occurring in 50-60% of cases. Research has been hindered by the lack of validated pre-clinical ACC models, hence there is an urgent need to develop relevant models to test novel therapeutic options. Therefore, I aimed to establish patient-derived xenograft (PDX)-derived pre-clinical *in vitro* models, and to identify potential drug targets and therapies based on the properties of eight sequenced metastatic ACC patient tumour samples.

The success rate of ACC PDX establishment was 54.5%; three of which possessed the *MYB-NFIB* translocation, one the *MYBL1-NFIB* translocation, and the other two expressed high MYB via alternative mechanisms. Using ACC PDX-derived primary cells I successfully established and developed culture conditions for 2D growth and 3D ACC organoid models that maintain high MYB expression and histologically recapitulate the PDX tumours derived from. I optimised 2D and 3D drug sensitivity assays to assess potential therapies for ACC, targeting genes and pathways identified using the patient tumour sequencing data. A promising drug combination of a CDK2, 5, 9 inhibitor and bromodomain inhibitor was highly synergistic in the PDX-derived models. A short-term *in vivo* drug assay in one PDX line identified engrailed-1 (EN1), MYC and SOX9 as potential candidate biomarkers for therapeutic activity of the drug combination, and Ki-67 staining identified that the combination treatment significantly reduced the proportion of actively proliferating cells. On-going long-term *in vivo* assays will determine whether this promising combination inhibits ACC growth.

Here I discuss the optimisation and establishment of relevant PDX-derived ACC 2D and 3D organoid models representing MYB-NFIB, MYBL1-NFIB and MYB driven ACC subsets. I also demonstrate the application of these models by identifying a promising novel drug combination for ACC that could potentially inform clinical trials.

Acknowledgments

The work presented in this thesis was made possible by funding from Oracle Cancer Trust and Get ahead Charitable Trust.

I would like to express my sincerest gratitude to my supervisor Dr Amanda Swain for the opportunity to work in her lab, and her enthusiasm, support, and guidance throughout my project. My thanks go to Prof. Kevin Harrington for his guidance and insight into this research area which has been invaluable. I also want to acknowledge the TPU, bioinformaticians and BSU for all their assistance in my project. A big thank you also goes to the Swain lab group – past and present members – for their helpful discussions, in particular Jeff for always being willing to help and Mercy for her PCR skills. I would like to say a special thank you to Eleanor for all her support over the past four years and encouragement during tea breaks when needed.

I thank all my friends (far too many to name but you know who you are) for all their support, encouragement and glasses of wine throughout the challenging times, many shared virtually over the past nine months. I am also eternally grateful for the love and support of my family, particularly over this past year.

Table of contents

List of figures

Chapter 5

Chapter 6

List of tables

Abbreviations

ACC	Adenoid cystic carcinoma
ACCRF	ACC Research Foundation
ALL	Acute lymphoblastic leukaemia
AML	Acute myeloid leukaemia
APL	Acute promyelocytic leukaemia
ATCC	American Type Culture Collection
ATP	Adenosine triphosphate
ATRA	All-trans retinoic acid
BBE	Bovine brain extract
BET	Bromodomain and extra-terminal domain
BRD	Bromodomain
C. bovis	Corynebacterium bovis
CAF	Cancer-associated fibroblast
CCh	Carbamoyl choline
CD1	Crl:CD1-Foxn1nu
ChIP-seq	Chromatin immunoprecipitation sequencing
CI	Combination index
CK5	Cytokeratin 5
CK8	Cytokeratin 8
CML	Chronic myeloid leukaemia
CRC	Colorectal cancer
CSC	Cancer stem cell
CTG	CellTiter Glo®
DAB	3,3'-diaminobenzidine
DBD	DNA binding domain
DEAB	4-diethylamino-benzaldehyde
DEG	Differentially expressed gene
EMT	Epithelial-mesenchymal transition
EN1	Engrailed homeobox 1
ER	Oestrogen receptor
Fa	Fraction affected
FDA	Food and Drug Administration
FFPE	Formalin-fixed paraffin embedded
FNAC	Fine needle aspiration cytology
GRCH37	Genome Reference Consortium Human genome build 37
GSEA	Gene set enrichment analysis
H&E	Haematoxylin and eosin
HDAC	Histone deacetylase
HPV	Human papillomavirus

ICR	Institute of Cancer Research
I.D.	Identification number
IHC	Immunohistochemistry
KEGG	Kyoto Encyclopaedia of Genes and Genomes
NRD	Negative regulation domain
NRG	Neuregulin
NSG	NOD.Cg-Prkdc^{SCID} Il2rg^{tm1Wjl}/SzJ
P-TEFb	Positive transcription elongation factor
p-yH2AX	Phospho-Histone H2A.X (Ser139)
PBS	Phosphate-buffered saline
PDAC	Pancreatic ductal adenocarcinoma
PDO	Patient-derived organoid
PDX	Patient-derived xenograft
PF	post fertilisation
PFA	Paraformaldehyde
PHE	Public Health England
PNSI	Perineural space invasion
q rt-PCR	Quantitative real-time PCR
RAR	Retinoic acid receptor
RECIST	Response Evaluation Criteria in Solid Tumours
RNAseq	RNA sequencing
RNPII	RNA polymerase II
RT-PCR	Reverse-transcription polymerase chain reaction
SE	Standard error
SEER	Surveillance, Epidemiology and End Results
SF	Survival fraction
SG	Salivary glands
SMA	Smooth muscle actin
TAD	transcriptional activation domain
TERT	Telomerase reverse transcriptase
Tet	T-cell epitope
TK	Tyrosine kinase
TPU	Tumour profiling Unit
UTR	Untranslated region
VAF	Variant allele frequency
WES	Whole exome sequencing
WHO	World Health Organisation

1. Introduction

1.1. Normal salivary gland overview

1.1.1. Major and minor salivary glands

The human salivary glands (SGs) are exocrine secretory glands, classified as either major or minor glands. There are three pairs of major SGs; parotid, submandibular and sublingual, shown in Figure 1-1A. These are encased by a fibrous capsule and produce saliva that is delivered to the oral cavity via the excretory ducts. There are 800-1000 minor SGs with short excretory ducts, concentrated in the tongue and in the walls of the oral cavity although absent in the gingiva and anterior hard palate (Figure 1-1B) (Varga, 2015). Minor SGs are also present in the nasal cavity, paranasal sinuses, pharynx and larynx. The minor glands are named according to their location; buccal, labial, lingual, palatine and glossopalatine.

The parotid gland is the largest of the three major SGs. It is located next to the facial nerve and the external carotid artery, between the masseter and the sternocleidomastoid muscle, one of the largest most superficial cervical muscles (Marieb & Hoehn, 2010). The submandibular gland is the second largest major SG, located below the mandible, parallel to the hypoglossal nerve. The sublingual gland is the smallest of the major SGs, and is located beneath the submucosa in the floor of the mouth, alongside the submandibular nerve.

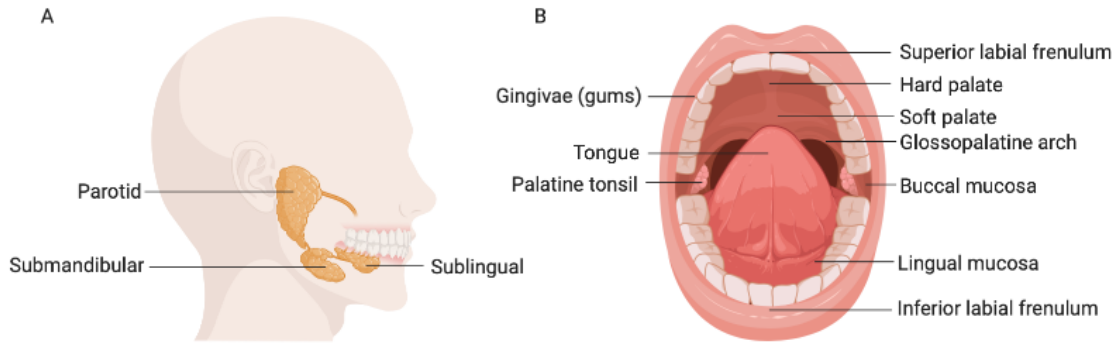

Figure 1-1 Sites of major and minor salivary glands

A) Diagram of the three paired major salivary glands; the parotid, submandibular and sublingual glands. B) Anatomy of the oral cavity, indicating areas of the minor salivary glands. Diagrams created using BioRender.com.

1.1.2. Salivary gland structure and function

The SGs are composed of three major cell types; acinar, ductal and myoepithelial cells. All cell types are required to complete the main function of the SGs; to produce and deliver saliva to the oral cavity. Saliva is important for many different reasons such as supporting mastication and swallowing, digestion via enzyme secretion such as amylase, protective roles due to antimicrobial components such as autolysin and lactoferrin, and the facilitation of proper speech (Carpenter, 2013; Marieb & Hoehn, 2010). The minor SGs in the sinonasal tract do not contain amylase as their main roles are for lubrication and protection. The major SGs produce between 92-95% of total saliva, with the parotid glands alone responsible for at least 50% of the total volume (Varga, 2015).

Unlike the parotid and submandibular glands that have one main secretory duct into the oral cavity, the sublingual gland has 10-12 smaller shorter ducts that secrete directly into the floor of the mouth (Marieb & Hoehn, 2010). Despite this, all SGs have the same fundamental branched ductal structure beginning with luminal secretory units known as acini, that produce the saliva. Acini and intercalated ducts are surrounded by myoepithelial cells that, upon stimulation by nerves, contract aiding saliva secretion from the acinar units into and along the ductal system, releasing the saliva into the oral cavity (Figure 1-2) (de Paula et al., 2017).

There are three main types of acini; serous, mucinous and seromucous (Marieb & Hoehn, 2010). Serous acini secrete a watery fluid rich in enzymes such as amylase, and are spherical in morphology. Mucinous acini produce a glycoprotein-rich secretion, which becomes hydrolysed to form mucus, and generally have a tubular morphology. Seromucous acini produce both types of secretions but normally one type predominates. The parotid glands contain predominantly serous acini, the submandibular glands contain both types of acini but a higher proportion of serous, whereas the sublingual glands contain both types but produces predominantly mucous secretions. The minor salivary glands are predominantly formed by mucinous acini (de Paula et al., 2017).

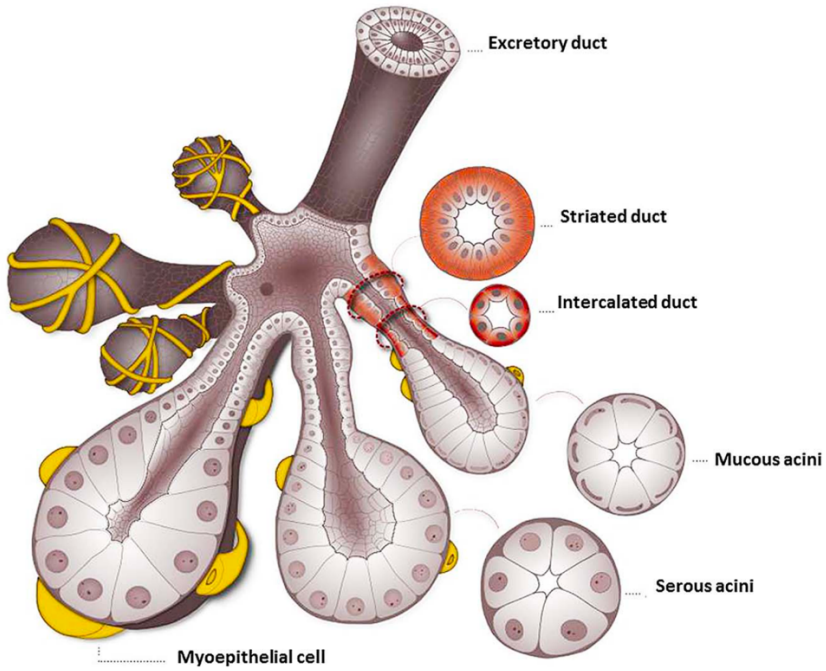

Figure 1-2 Salivary gland structure

A diagram to show the basic structure and cell types within the salivary glands. Acini secrete into the intercalated ducts, which lead into the striated ducts. The striated ducts drain into the excretory ducts and into the oral cavity. This diagram is taken from (de Paula et al., 2017).

1.1.3. Salivary gland development

Initial SG development begins with the thickening of the oral ectoderm due to interactions between the epithelium and adjacent mesenchyme, a stage known as the prebud stage, occurring around 6-8 weeks post fertilisation (pf) (Knosp et al., 2012; V.

N. Patel & Hoffman, 2014). The thickening protrudes into the mesenchyme and invaginates forming a bud on a stalk. The bud then undergoes branching morphogenesis, a process involving cell proliferation, clefting, differentiation, migration and apoptosis. All of these processes are highly regulated and induced by specific signalling pathways initiated by interactions between the epithelial, mesenchymal, endothelial and neuronal cell network. Terminal buds become acini at 14 weeks pf. By 16 weeks pf, the basal lamina surrounds the epithelium and myoepithelial cells have differentiated. Intercalated and striated ducts form in the following weeks, and by 28 weeks pf the SGs are fully developed.

SGs are innervated by neural crest progenitor cells that have migrated to the oral epithelium and differentiated into mesenchyme, and in the submandibular gland formed the parasympathetic submandibular ganglion that surrounds the stalk that differentiates into the major secretory duct (Knosp et al., 2012; V. N. Patel et al., 2006; V. N. Patel & Hoffman, 2014). There is some controversy within the literature about whether the developmental origin of the major gland epithelium is ectodermal or endodermal in origin. Genetic-lineage tracing using Wnt1-cre recombinase identified that the mesenchyme and nerves are of neural crest origin (V. N. Patel & Hoffman, 2014). A lineage experiment using Sox17-2A-iCre/R26 reporter mice, marking endodermal cells, identified that the major SGs are not endodermal, suggesting that they are ectodermal. However, a study should be completed to positively determine that the epithelium is ectodermal in origin (Rothova et al., 2012).

1.2. Neoplasms of the salivary glands

SG cancers are rare, accounting for less than 1% of all malignant neoplasms, with an incidence of 1.4 cases per 100,000 per year according to the Information Network on Rare Cancers, collating data from 94 European population-based cancer registries (www.rarecarenet.eu). However, the incidence of SG cancers is rising. A report published by Public Health England (PHE) studying the epidemiology of major SG cancers between 1990 and 2013 in England, identified that over the last decade the number of

new cases has increased by 2.5% annually (Girdler et al., 2016). A study using the Surveillance, Epidemiology and End Results (SEER) database for cancer statistics in the United States, identified an annual increase of 0.99%, with an annual increase in parotid SG cases of 1.13% (Del Signore & Megwalu, 2017). A 15-year population-based study in Demark identified that of all SG sites, the parotid gland was the most common primary site accounting for 52.5% of cases (Bjørndal et al., 2011). In England between 2009-2013, 77% of major SG cancer cases occurred in the parotid SG, 14% in the submandibular, and 2% in the sublingual glands, the remaining cases occurred in overlapping major glands or were unspecified (Girdler et al., 2016). The minor SGs account for 14-26.3% of all SG tumours, principally occurring in the palate (37-54%) (Bjørndal et al., 2011; Eveson & Cawson, 1985; Spiro et al., 1973).

According to the 2005 World Health Organisation (WHO) classification, there are 24 different histologic subtypes of SG cancer (Thompson, 2006). PHE reported that between 2004-2013, 78.3% of major SG cases diagnosed accounted for the 4 most common histologically SG cancer types; mucoepidermoid carcinoma (20.5%), adenocarcinoma (19.8%), acinic cell carcinoma (19.6%), and adenoid cystic carcinoma (18.4%). The proportion of these top four cancer subtypes of major SG origin varies between different studies, however for minor SG tumours, the most common malignant cancer subtype is adenoid cystic carcinoma, reportedly accounting for 40% of cases (Bjørndal et al., 2011; Eveson & Cawson, 1985; Spiro et al., 1973).

SG tumours are diagnosed by MRI and fine needle aspiration cytology (FNAC). The most common false negative cases (malignant but identified as benign) were adenoid cystic carcinoma, acinic cell carcinoma and basal cell adenocarcinoma (Daneshbod et al., 2009; B. J. Lu et al., 2005). This would prolong diagnosis and could suggest why many SG cancer cases are diagnosed in later disease stages. Moreover, specific SG tumour diagnosis is extremely difficult due to similar morphologic features, particularly between adenoid cystic carcinoma, basal cell adenoma and pleomorphic adenoma (B. J. Lu et al., 2005; Nagel et al., 1999).

Standard treatment for all SG tumours is surgery, with 90% of 5,880 major SG cancer cases in England having surgery as first-line treatment. Post-operative adjuvant

radiotherapy is common, administered in 40% of all cases, although this treatment rate increases with disease advancement (Girdler et al., 2016). Chemotherapy is not the normal first-line treatment option for SG cancers, being prescribed in only 2% of all cases, however, chemotherapy is used palliatively for metastatic or unresectable SG cancers. Molecular genetic studies have identified that each SG cancer subtype has unique tumour-specific genetic characteristics, therefore treatment advancements are focused on distinguishing these differences and identifying therapeutic targets to treat SG cancers based on cancer subtype rather than general standard non-specific treatments.

Of all SG cancer subtypes, adenoid cystic carcinoma has the largest area of clinical unmet need due to its unpredictable disease course, biological properties and apparent resistance to conventional chemotherapeutics. Therefore, herein, I will discuss in detail adenoid cystic carcinoma of the SGs.

1.3. Adenoid cystic carcinoma of the salivary glands

1.3.1. Overview

Adenoid Cystic Carcinoma (ACC) is a rare cancer, with an incidence of 4.5 per 1 x 10^6 according to a 30-year Nova Scotia population-based study, and is therefore referred to as an "orphan" disease (Boneparte et al., 2008). ACC can arise in exocrine glands such as the trachea, breast, skin and vulva. However, 58% of ACC occurs in the oral cavity, mainly the SGs (Ellington et al., 2012). 32-52% of ACC cases occur in the minor glands in the palate, the rest occurring in the major SGs (Bjørndal et al., 2011; Spiro et al., 1973). In Denmark, ACC was the most common SG cancer subtype, accounting for 25.2% of cases between 1990-2005 (Bjørndal et al., 2011).

Most patients are diagnosed in the fourth to sixth decades of life, however there is a wide range in the age of patients at diagnosis with SEER database analysis reporting patients from 3 to 99 years, with an average age of 55 (Lloyd et al., 2011). There is a higher occurrence in Caucasians (82%) (Ellington et al., 2012). There is also a slight

gender specific trend in ACC of all tissue origins with a higher occurrence in females (62%) compared to males (38%), although it is suggested this could be due to female organ incidence, the PHE report focusing on major SG primary sites reports a similar trend with 40% of cases in males and 60% females (Ellington et al., 2012; Girdler et al., 2016). The disease is not hereditary, being regarded as sporadic, and there is also little evidence to show an association between lifestyle factors such as alcohol or tobacco use. There is no evidence that the human papillomavirus (HPV) plays a causal role in ACC development, however this conclusion is based on a limited study of 13 cases (Haeggblom et al., 2018). Due to the rarity of the cancer, lack of patients within one geographical area, and no known stages of pre-malignancy, risk factor studies are challenging to conduct.

ACC is an indolent but ultimately relentless cancer having a low survival rate. Whilst the short-term prognosis is good, recurrence and metastasis are common leading to poor long-term survival. The average 5-, 10-, and 15-year disease-free survival rates from a 15-year Danish population-study are reported as 72%, 60% and 55% respectively. These rates mirror the 5-, 10-, and 15-year overall survival rates of 80%, 58% and 46% respectively (Bjørndal et al., 2015). However, the site of primary tumour, histological growth pattern, and neural invasion are all factors that impact prognosis, and will be further discussed.

1.3.2. Clinical behaviour and biological properties

ACC is a slow growing tumour, having periods of dormancy followed by spurts of growth, nevertheless the course of ACC is unpredictable and relentless. In most cases ACC arises as a painless, small, slow growing lump in the oral cavity. The development of pain indicates neural involvement via perineural space invasion (PNSI), a known characteristic of ACC (M. Amit et al., 2015). The slow and indolent clinical course means diagnosis is often late, when the tumour is in more advanced stages, and systemic intervention may be required to prevent recurrence and distant metastasis following surgical resection.

Treatment is challenging due to three biological properties of ACC; PNSI associated with incurable relapse at the skull base, local recurrence, and the emergence of distant metastases via haematogenous dissemination after long periods of dormancy. Invasion of the lymph nodes is relatively uncommon in ACC, only occurring in 11% of cases (Matsuba et al., 1986).

Neural invasion in ACC has classically been reported as invasion of the perineurium, occurring in 52-78% of cases including early stage tumours, resulting in a poor prognosis with 5-year survival reports of 38.5% compared to 73.4% in patients without neural involvement (M. Amit et al., 2015; M. Huang et al., 1997; Ko et al., 2007; Vrielinck et al., 1988). However, a recent study of 239 ACC patient samples with positive neural invasion distinguished between three types of invasion previously recognised in squamous cell carcinoma and pancreatic cancer; perineurial invasion with viable tumour cells in the perineurial space, intraneural invasion where tumour cells invade and/or destruct the axon containing the nerve bundles, and perineural inflammation defined as invasion into the perineurial space with the observation of lymphocytic infiltration (M. Amit et al., 2015; De Matos et al., 2012; Mitsunaga et al., 2007). This study identified that the only type of neural invasion with a significant impact on disease-free and overall survival was intraneural invasion.

Local recurrence is a common occurrence despite primary surgical removal, with 10-year local recurrence-free survival rates of 40.8% (Iseli et al., 2009). Positive surgical margin status did not significantly correlate with local recurrence. Cases originating from the major SGs have lower rates of local and regional recurrence compared to minor SG primary sites, although there is no significant difference in disease-specific survival (N. Li et al., 2012). Local recurrence occurred in 25% of cases of parotid gland origin compared to 40.9% of cases arising from the minor glands. This may be due to the propensity of minor SG ACC to migrate along fascicle planes and smaller nerves, hindering complete surgical excision (Khafif et al., 2005).

Distant metastasis occurs in 35-56% of cases predominantly to the lungs (72.2-89.7% of metastatic cases) followed by liver and bone (M. Huang et al., 1997; Ko et al., 2007; van der Wal et al., 2002). Moreover, one third of cases have distant metastasis despite local

control, implying that cancer cells had spread undetected prior to primary site treatment (Matsuba et al., 1986). Cases with lung metastasis have a median survival time of 2.2 years from diagnosis, whereas cases with liver and brain metastasis have a lower median survival of only 1.4 years (Bjørndal et al., 2015). Therefore, it is highly recommended that patients have regular X-ray or CT scans on the lungs, and possibly CT and MRI scans for metastasis in other areas, for earlier detection and therefore possible treatment.

1.3.3. Histology

A diagnosis is made by FNAC and biopsies for histological analysis. FNAC is not the most accurate method for diagnosis, with a study reporting 77% of ACC samples correctly typed by cytology (Nagel et al., 1999). Therefore, the "gold standard" for diagnosis is histopathological analysis (van Weert et al., 2015). ACC is typically bi-phenotypic; composed of large ductal cells surrounded by myoepithelial cells. ACC has three histologic growth patterns; cribriform (most common), tubular, and solid, although tumours are usually heterogeneous (Figure 1-3) (van Weert et al., 2015). Tumours with solid areas have a higher proportion of luminal cells and are more aggressive, having 10-year recurrence-free survival of 38%, almost half of that for cribriform and tubular growth (Bjørndal et al., 2015). Furthermore, cases with solid areas have significantly lower 10-year disease-specific survival compared to the other two growth patterns; 52% and 78% respectively. Samples with solid growth have also been reported to develop distant metastasis sooner and in a study of 81 ACC cases, all but 1 case with lymph node invasion had predominantly solid growth (Matsuba et al., 1986; van Weert et al., 2015).

As the majority of tumours are heterogenous, the two most common grading systems use the percentage of solid growth within the tumour to determine poor prognosis (described by Perzin et al./Szanto et al. as >30% and Spiro et al as >50%) (Perzin et al., 1978; Spiro et al., 1974; Szanto et al., 1984). Szanto et al suggest three grades; grade I has tubular and cribriform areas, grade II has mixed growth with >30% solid areas, and grade III has almost all solid growth. Based on the Perzin/Szanto grading system, 5-year disease-specific survival is 90% for grade I, 75% for grade II and 36% for grade III, therefore histologic grade is a clear indicator of prognosis (van Weert et al., 2015).

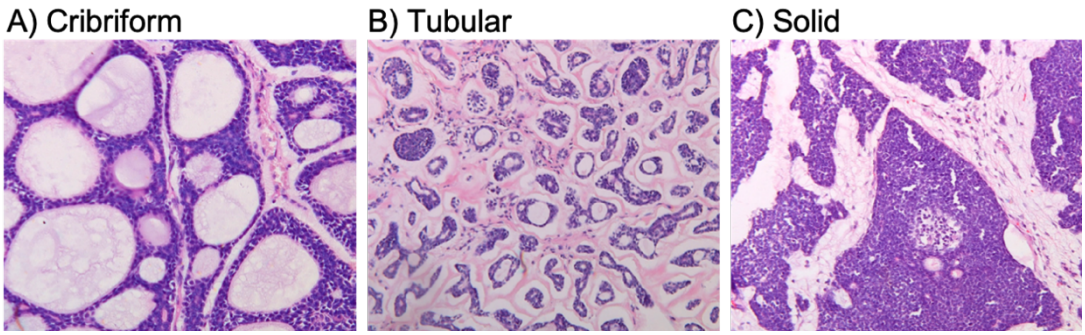

Figure 1-3 ACC histologic growth patterns

A) Cribriform is the most common growth pattern of ACC. Basal myoepithelial cells surround pseudocysts, hence the alternative name "swiss cheese pattern". B) With tubular growth, nests of tumour cells are surrounded by eosinophilic stroma. C) Solid growth shows no tubular or cystic formation. These representative images of each growth pattern are adapted from (van Weert et al., 2015).

1.3.4. Current therapeutic options

Initial treatment is surgical resection of the primary site, often followed by adjuvant radiotherapy. Following surgical removal, the tumour is checked by a pathologist to confirm margin status, and if margins are positive with residual tumour cells around the surgical area radiotherapy is given. In some cases, depending on the site of the primary tumour, surgical resection may not be advised therefore patients receive only radiotherapy. PHE collated treatment information for 1260 ACC cases, and reported that 54.1% of cases had surgery and radiotherapy, 32.4% had surgery alone, and that 9.8% of cases only received radiotherapy (Girdler et al., 2016). The remainder 3.7% had various combinations of chemotherapy, radiotherapy and surgery. The preservation of major nerves and tissue function is attempted however, this is dependent on margin status and primary site. Following surgical resection, patients can experience a number of complaints such as chronic pain and permanent changes to appearance. Furthermore, radiotherapy can result in a dry mouth, difficulty swallowing, loss of taste and tooth decay.

As discussed, local recurrence and distant metastasis is a common characteristic of ACC, and in those cases systemic intervention is required. However, due to a complicated clinical course, other than surgical excision and post-operative radiotherapy for

locoregional control, therapy for advanced ACC is not standardised. Chemotherapy is generally given when patients have rapidly progressive disease and is used for palliative care as the toxicity of cytotoxic agents outweighs the side effects of ACC at the indolent/dormant stage (Laurie et al., 2011). Agents commonly administered as mono-therapy for advanced ACC are cisplatin, epirubicin, gemcitabine and paclitaxel. In a review by Laurie et al, chemotherapy phase II trial regimens were systematically assessed (Laurie et al., 2011). From all single-agent trials in 141 patients, objective responses were only reported for 18 patients, 7 of which were treated with cisplatin (n=10) (Schramm et al., 1981). No objective responses were reported for the 14 patients that received paclitaxel or the 21 patients who received gemcitabine (Gilbert et al., 2006; van Herpen et al., 2008). However, two independent trials investigating cisplatin treatment reported a total of 2 out of 23 partial or complete responses, therefore the effect of cisplatin on advanced ACC remains unclear (Dick de Haan et al., 1992; Licitra et al., 1991). Disease stabilisation rather than partial or objective responses were more common in chemotherapy trials, in 64 of 111 patients recorded, however length of stabilisation is not generally documented. Combination cytotoxic treatments were also assessed. The most promising combinations investigated were cisplatin, doxorubicin and cyclophosphamide, and the combination of epirubicin, cisplatin and 5-fluorouracil. However, for the latter combination the results were not superior to previous phase II studies of either cisplatin and 5-fluorouracil in combination or epirubicin alone, and it was concluded by Laurie et al that combination therapies had no advantage over single-agent chemotherapeutics (Laurie et al., 2011; P. J. Ross et al., 2009). Iseli et al retrospectively reviewed 183 cases treated over 40 years and reported that survival in patients with distant metastasis did not significantly improve with chemotherapy, however eating and aesthetic scores were improved therefore chemotherapy could improve the quality life of these patients (Iseli et al., 2009).

There are two reports investigating chemotherapy as a radiosensitiser, termed chemoradiotherapy, to be given post operatively to prevent local and regional recurrence (Pederson et al., 2011; Schoenfeld et al., 2012). However, median follow-up is reported as 2.3 and 3.5 years whereas metastasis can be detected over 10 years later,

therefore longer monitoring of these patients must continue ideally up to 5 years, to determine whether chemoradiotherapy is a promising treatment to prevent recurrence.

To date, systemic agents have not proven effective against both loco-regional or systemic disease. Furthermore, since 1985, none of the phase II clinical trials (over 22) for ACC patients have progressed to phase III. Therefore, research is now focussed on identifying targeted therapies for ACC.

1.4. Molecular landscape

1.4.1. Low and uncommon mutational burden

Due to the failure of conventional systemic therapies, research is now focused on identifying molecular drivers of ACC that can be targeted by specific inhibitors. Three studies analysing a total of 109 tumour samples with matched normal DNA reported a low somatic mutation rate; with Ho et al (2013) identifying a mean of 22 somatic mutations per sample, correlating to a non-silent mutation rate of 0.31 mutations per megabase (A. S. Ho et al., 2013; Rettig et al., 2016; Stephens et al., 2013). The mutation profile of ACC is highly diverse, with mutations associated with epigenetic modifications (chromatin regulation), DNA damage pathways (ATM/ATR activation), growth factor signalling (FGF, IGF and PI3K), differentiation pathways (Wnt and Notch) and axonal guidance factors (Table 1-1).

Table 1-1 Published ACC mutation profiles by associated pathway

	Paper			
Pathway	**Ho et al. (2013) (n=60)**	**Rettig et al. (2016) (n=25)**	**Stephens et al. (2013) (n=24)**	**Average (± SD) (%)**
MYB	34 (57%)	11 (44%)	19 (79%)	**60% (±17.7%)**
Notch	8 (13%)	9 (36%)	3 (12.5%)	**20.5% (±13.4%)**
FGF/IGF/PI3K	18 (30%)	15 (60%)	4 (17%)	**35.7% (±20.1%)**
Chromatin remodelling	21 (35%)	11 (44%)	16 (67%)	**48.7% (±16.5%)**
DNA damage	16 (26%)		2 (8%)	**17% (±12.7%)**
Axonal guidance		14 (56%)		**56%**

1.4.2. MYB and MYBL1 oncogenic drivers of ACC

The most frequent genetic alteration in ACC is activation of the proto-oncogene *MYB* (c-MYB) reported in approximately 65-80% of cases (Brayer et al., 2016; Brill et al., 2011; Persson et al., 2009). MYB protein is a DNA-binding transcription factor implicated in the regulation of both differentiation and proliferation. It has a highly conserved N-terminal DNA binding domain (DBD), central transcriptional activation domains (TAD), and conserved specificity and negative regulation C-terminal domains (NRD) (Figure 1-4A) (O. L. George & Ness, 2014). High *MYB* transcript expression has been documented in a number of cancers such as leukaemia, pancreatic tumours and colon tumours (Hugo et al., 2006; O'Rourke & Ness, 2008; Wallrapp et al., 1997). However, evidence suggests that C-terminal NRD truncation is required to induce MYB oncogenic effects. In leukaemia, enhanced alternative RNA splicing results in truncated oncogenic c-MYB variants (O'Rourke & Ness, 2008). Due to the presence of at least six alternative exons and a number of splice donor and acceptor sites in the standard exons, the *MYB* gene can be transcribed to more than 60 different mRNA variants that encode over 20 MYB protein variants. Furthermore, all alternative RNA splicing occurs at the C-terminal NRD. There is also evidence that c-terminal truncations increase *MYB* transcript stability (O. L. George & Ness, 2014).

The most common mechanism of *MYB* activation is the *MYB-NFIB* t(6;9) (6q22-23; 9p23-24) translocation, in 50-67% of cases (Drier et al., 2016; A. S. Ho et al., 2013; Stephens et al., 2013). The minimal common region of *MYB* deletion via the fusion is exon 15, including the 3' untranslated region (UTR). The 3'UTR contains several highly conserved microRNA docking sites (miR-15a/16 and miR-150) which have been shown to negatively regulate *MYB* expression (Persson et al., 2009). Reported *MYB* breakpoints have ranged from exon 8-15 whereas *NFIB* breakpoints have a range of exon 9-12, with the most common resulting transcript identified from 11 ACC samples being *MYB* exon14-*NFIB* exon9 in 64% (Figure 1-4B) (Mitani et al., 2010; Persson et al., 2009). Overall, the vast majority of translocations result in a C-terminal *MYB* deletion and fusion to the *NFIB* C-terminal. *NFIB* has flanking super-enhancer elements. The translocation juxtaposes these super-enhancers to the *MYB* locus. The super-enhancers contain MYB binding sites, creating a positive feedback loop, so *MYB* is constitutively activated (Figure 1-4C) (Drier et al., 2016). *MYB* translocation partners other than *NFIB* have been detected at much lower frequencies, such as *TGFBR3* and *RAD51B*, that also have flanking super-enhancers (Andersson et al., 2017; Cornett et al., 2019; Drier et al., 2016). Alternative mechanisms of *MYB* activation, accounting for 10% of ACC cases, include gene amplifications and alternative RNA splicing of MYB transcripts, similar to mechanisms detected in leukaemia (Brayer et al., 2016; Frerich et al., 2018; Kim et al., 2018).

ACC whole genome and whole-transcriptome analyses identified a novel gene fusion between the MYB related protein, *MYBL1* (A-MYB) and *NFIB* t(8;9), in 35% of ACC (Brayer et al., 2016; Mitani et al., 2016). MYBL1 is structurally similar to MYB with almost identical DNA binding domains. MYB and MYBL1 expression in ACC appears to be mutually exclusive, implying they are independent drivers of ACC having identical functions (Mitani et al., 2016). This is supported by the fact that gene expression profiles are similar between MYB-NFIB and MYBL1-NFIB expressing tumours (Brayer et al., 2016; Mitani et al., 2016). Detected *MYBL1* breakpoints range between exons 8-15, with a study of 13 MYBL1-NFIB fusion positive ACC cases identifying 8 samples with a breakpoint at exon 8 (Mitani et al., 2010). Other *MYBL1* translocation partners have also been detected, such as *ACTN1*, *RAD51B* and *YTHDF3*, however all fusion proteins result

in a MYBL1 c-terminal truncation (Brayer et al., 2016; Kim et al., 2018; Mitani et al., 2016).

Although MYB and MYBL1 are widely accepted as oncogenic drivers of ACC due to the high frequency of activating mutations and increased expression, there has been a lack of functional studies proving this. Therefore, the development of accurate relevant preclinical models would enable confirmatory studies to prove whether MYB/MYBL1 activation is sufficient to transform normal epithelial cells, and whether MYB knockdown inhibits tumour growth. There has been one study conducting a MYB-NFIB knockdown in one PDX-derived 2D *in vitro* culture, however instead of studying the role of MYB in ACC oncogenesis, the paper compared the molecular effects observed to the effect of a potential drug therapy, therefore further studies are required (Andersson et al., 2017).

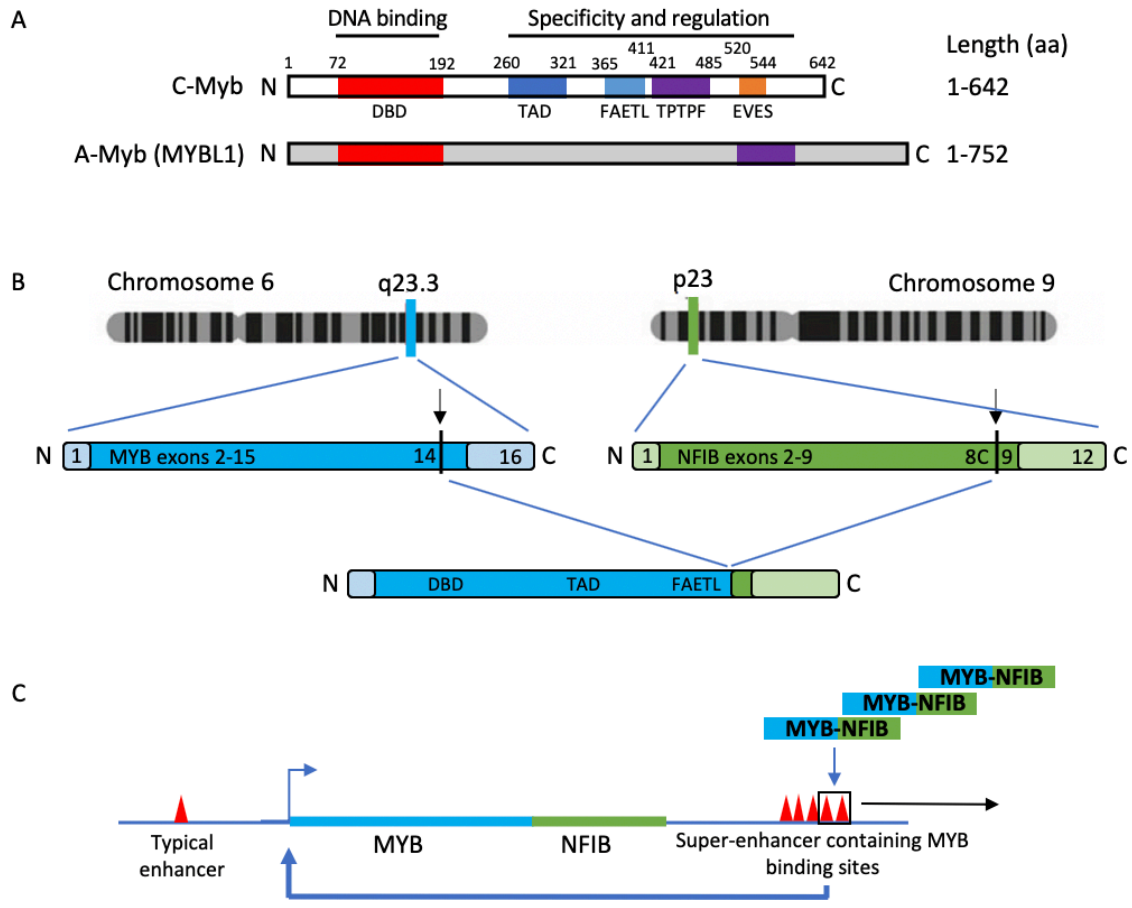

Figure 1-4 MYB/MYBL1-NFIB translocations

A) Schematic to show c-MYB and MYBL1 proteins, depicted N-terminal to C-terminal. Conserved domains are coloured: DNA binding domain (DBD) in red, transcriptional activation domain (TAD) in

dark blue, the transformation domain (FAETL) in light blue, and negative regulatory domains (TPTPF and EVES) in purple and orange respectively. The numbers above the C-MYB plot indicate the amino acid (aa) residues as well as the protein full length in aa in the column on the left. MYBL1 has a DBD and TPTPF as indicated. The normal forms of c-MYB and A-MYB have been adapted from (O. L. George & Ness, 2014). B) Schematic depicting the *MYB* and *NFIB* genes, and resulting translocation at the most common breakpoint; *MYB* exon14 and *NFIB* exon9. Coding exons are shown in bolder shades of green and blue, and breakpoints are indicated by arrows. DBD, DNA binding domain; NRD, negative regulatory domain; TAD, transactivation domain. Schematic has been adapted from (Persson et al., 2009). C) Diagram to show the constitutive *MYB* activation via the *MYB-NFIB* translocation. *NFIB* flanking super-enhancers have MYB binding sites, promoting a positive feedback loop.

1.4.3. Other potential oncogenic drivers of ACC

The largest ACC study to date comparing genetic alterations in 177 primary tumours to 868 recurrent or metastatic tumours, also reported a low mutational burden of 0.34 mutations per megabase (A. S. Ho et al., 2019). Due to the large sample size of recurrent/metastatic cases, four distinct ACC subgroups were identified; *MYB* translocation^{+} and *NOTCH1*$^{+}$, *MYB* translocation^{+} and other mutation, *MYB*^{WT} and NOTCH1^{+}, and lastly MYB^{WT} and telomerase reverse transcriptase (*TERT*) promoter mutation^{+}. The remaining cases were referred to as “triple-negative” (*MYB*^{WT}, *NOTCH*^{WT}, and *TERT*^{WT}), where potential driver mutations have not been identified for this subgroup.

NOTCH1 activating mutations have been identified previously in ACC in 14% of cases, being the most frequently altered gene, however Ho et al reported that these mutations are more prevalent in recurrent/metastatic tumours (26.3% compared to 8.5% in primary) (Ferrarotto et al., 2016; A. S. Ho et al., 2019; Rettig et al., 2016). Therefore, Ho et al confirm other reports that *NOTCH1* is a potential driver of ACC, or more specifically a driver of aggressive, metastatic ACC. Ferrarotto et al previously identified a distinct subgroup of particularly aggressive ACC cases with *NOTCH1* activating mutations that significantly corresponded with solid histology, advanced stage at diagnosis, increased rate of liver and bone metastasis and both shorter relapse-free survival and overall survival (Ferrarotto et al., 2017). Significantly lower overall survival in NOTCH1 positive

patients was also reported by Ho et al. Notch signalling is known to have a key role in cell fate determination as well as proliferation, angiogenesis, epithelial-mesenchymal transition (EMT) and evading cell death in cancer (Aster et al., 2017).

Other genetic alterations significantly enriched in recurrent/metastatic tumours were involved in chromatin-remodelling, DNA damage repair and tumour suppression. Ho et al identified a potential cooperativity between *NOTCH1* and chromatin remodelling genes. *NOTCH1* mutations co-occurred at a significant rate in samples also with mutations in the genes *KDM6A*, *ARID1A* and *CREBBP*, and it was found that patients harbouring a *KDM6A* mutation also had significantly lower survival (A. S. Ho et al., 2019). This suggests that epigenetic mechanisms may biologically synergise with increased Notch pathway activity promoting ACC progression and that both Notch signalling molecules and chromatin remodelling proteins could be potential therapeutic targets.

In addition, *TERT* promoter mutations were present in 13.1% of recurrent/metastatic cases and were mutually exclusive with both *MYB/MYBL1* fusions and *NOTCH1* mutations. This highlights an alternative mechanism of ACC tumorigenesis, independent of the *MYB/MYBL1* translocation. *TERT* promoter mutations have been widely reported in a number of cancers, such as 59% of bladder and 43% of central nervous system cancers, and function to avoid replicative senescence (Vinagre et al., 2013). However, *TERT* promoter mutations have not been reported in other ACC sequencing papers, only in a single case study of metastatic ACC (Rafael et al., 2016). Therefore, this suggests that *TERT* promoter mutations may only be drivers of recurrent or metastatic disease, not primary, and could be a potential therapeutic target for these advanced cases.

1.4.4. Cancer stem cell genetic signature

Cancer stem cells (CSCs) account for a small fraction of the tumour cell population, and are responsible for tumour initiation and aggressive disease having the capacity to self-renew, and differentiate into multiple cell lineages. It is these cells that are hypothesised to cause relapse, metastasis and radio/chemo-resistance. CSCs were first isolated from ACC patient-derived xenograft (PDX) models by Panaccione et al (Panaccoine et al., 2016). This $CD133^{+}$ cell population had high expression of NOTCH1, SOX10 and FABP7,

which all indicate the aberrant activation of a transcriptional programme promoting neural stem cells (Yarbrough et al., 2016). SOX10 is highly expressed in other cancers that originate from the neural crest such as melanoma, neuroblastoma and glioblastoma (Ivanov, Panaccione, Nonaka, et al., 2013). The neural crest contains arguably the most plastic cells in human development, excluding embryonic stem cells, giving rise to diverse tissue types of both ectodermal and endodermal designation. As discussed, during development the SGs are innervated by neural crest progenitor cells that form the mesenchyme, parasympathetic submandibular ganglion and are suggested to form myoepithelial cells (V. N. Patel & Hoffman, 2014). It has been identified that the dedifferentiation of a melanocyte to the neural crest stem state defines the origin of melanoma, and this has been suggested for ACC with the dedifferentiation of neural crest-derived myoepithelial cells (Kaufman et al., 2016). Neural crest progenitor cells express a specific gene signature that coordinates neural crest maintenance, migration and development; SOX10, NOTCH1, MYB, WNTs, and FGFRs (Betancur et al., 2010; Simões-Costa & Bronner, 2015). This signature has also been reported in ACC samples, further supporting neural crest-like stemness (Drier et al., 2016; A. S. Ho et al., 2013; Mitani et al., 2016; J. S. Ross et al., 2014; Stephens et al., 2013). Further characterisation of the identified $CD133^{+}$ CSC population in ACC is required, as targeting CSC survival could increase tumour sensitivity to current therapies, and prevent recurrence.

1.5. Targeted therapy

Given the ineffectiveness of systemic chemotherapy and radiotherapy in ACC, research is now focussed on identifying targeted therapies. Targeted therapy is a type of cancer treatment designed to specifically target molecules promoting the growth, survival and dissemination of cancer cells, whilst sparing normal cells. Often, the molecules targeted drive cancer progression as a result of oncogenic mutations or epigenetic modifications that are absent or expressed at lower levels in normal healthy cells. Alternatively, cancers can be driven by mutations in a tumour suppressor gene leading to its loss of function. There are a number of types of targeted therapy such as ligand or receptor-

targeted inhibitors, hormonal therapies, immunotherapies, angiogenesis inhibitors and apoptosis agonists.

As previously described, there is large variability in the ACC genetic landscape, with few common mutations, therefore it is not a case of “one therapy fits all” and patient responses will differ depending on their tumour genomic and molecular profile. For a number of cancer types there are specific lines of treatment for distinct subtypes targeting particular characteristics, such as hormonal therapy to lower oestrogen levels or inhibit the oestrogen receptor (ER) in ER+ breast cancer. Although Ho et al identified four distinct ACC subgroups in recurrent and metastatic cases, there are some differences in the mutational profiles of these tumours compared to primary cases, for example TERT promoter mutations have not been reported in primary tumours (A. S. Ho et al., 2019). This could mean that treatment designed according to these subgroups is mainly stratified towards advanced stage ACC and potentially not applicable to unresectable primary cases, for which currently only radiotherapy and chemotherapy are therapeutic options. Therefore, patient tumours should be screened to detect targets from the four subgroups to determine whether they could benefit from a specific therapy.

As ACC is a rare cancer, often only a few ACC cases are tested in basket trials, where different cancer types are grouped together that possess the same mutation or biomarker. However, as ACC is an orphan disease, promising drugs in clinical trials can be granted accelerated progression by the Food and Drug Administration (FDA) for patients based on a surrogate endpoint due to the lack of treatment options available for patients, this known as “orphan drug designation”. To date there are 50 registered completed, on-going, or recruiting targeted clinical trials for ACC on ClinicalTrials.gov (Table 1-2).

1.5.1. MYB

High expression of MYB is a hallmark of ACC, occurring in up to 70% of cases. However, as it is a transcription factor it is difficult to directly inhibit. It has been reported that the retinoic acid receptor (RAR) and MYB are mutual antagonists, having opposing effects

during proliferation, differentiation and haematopoiesis (Zemanová & Smarda, 1998). In addition, RAR has previously been identified to suppress *MYB* expression at the transcriptional level, and inhibit growth in neuroblastoma and acute promyelocytic leukaemia (APL) by promoting terminal differentiation (Degos & Wang, 2001; Smarda et al., 1995; Thiele et al., 1988). Recently, Mandelbaum et al showed that treatment of ACC PDX models *in vivo* with RA agonists significantly inhibited tumour growth (Mandelbaum et al., 2018). Furthermore, chromatin immunoprecipitation sequencing (ChIP-seq) analysis in ACC PDX tumours harbouring the *MYB-NFIB* translocation identified that all-trans-retinoic acid (ATRA) inhibits MYB binding at the translocated super-enhancers by increasing RAR expression and its binding at the *MYB* promoter and translocated enhancers. RAR binding at these *MYB* regulatory elements is repressive, and results in reduced expression of *MYB* and MYB downstream targets. Based on this evidence, there are currently two registered clinical trials for ATRA recruiting ACC patients, NCT03999684 (USA) and NCT04433169 (China). ATRA is approved for the treatment of APL.

There is currently an on-going first-in-human phase 1 clinical trial for a MYB targeted vaccine, TetMYB, being investigated as a single agent and in combination with an anti-PD-1 antibody to treat ACC and colorectal cancer (CRC) for which aberrant MYB expression is frequent (NCT03287427) (Pham et al., 2019). TetMYB is a DNA vaccine carrying a fusion construct consisting of human *MYB* cDNA and the universal tetanus toxin T-cell epitope (Tet) cDNA. The vaccine induces a cytotoxic T lymphocyte-mediated immune response against high MYB-expressing cells, and the anti-PD-1 treatment aims to prevent T-cell exhaustion. In preclinical *in vivo* CRC mouse models, when the mice were re-challenged with CRC an immune response was instantly activated killing the cancer cells, proving that the vaccine can induce a sustained population of memory T-cells which could potentially prevent tumour recurrence (Cross et al., 2015). There is no published preclinical data for ACC, however, the vaccine is constructed using the full coding region of *MYB* so MYB-NFIB positive ACC tumours with *MYB* breakpoints in earlier exons should have also been assessed prior to clinical studies.

1.5.2. Notch

Activating mutations in the NOTCH signalling pathway occur in approximately 25% of ACC samples representing a cohort of particularly aggressive disease, therefore NOTCH inhibitors have been widely investigated. These mutations include activating NOTCH1 mutations or loss-of-function mutations in the Notch transcriptional repressor SPEN (Drier et al., 2016). Furthermore, NOTCH expression is a marker of ACC CSCs and *in vitro* NOTCH inhibition selectively inhibited $CD133^+$ CSC proliferation and induced cell death (Panaccoine et al., 2016). NOTCH is the only targetable marker of these CSCs, therefore notch inhibition could also sensitise the CSCs to chemo- or radiotherapy. A phase 1a trial of the NOTCH inhibitor LY3039478 (NCT01695005) was promising, being well-tolerated and having clinical activity in heavily pre-treated patients (Massard et al., 2018). However, the phase 1b trial confirming the recommended phase 2 dose reported no confirmed responses out of 22 enrolled ACC patients (Even et al., 2020). Despite this, NOTCH remains a promising target for ACC patients and there are currently two actively recruiting clinical trials for patients with NOTCH pathway alterations, one in Europe (NCT03422679) and one in the USA (NCT03691207). The US clinical trial is a phase 2 trial investigating the drug AL101 (Ferrarotto et al., 2020). In May 2019, the FDA granted AL101 orphan drug designation for the treatment of ACC as preliminary results from the phase 2 study were very promising with 15.3% of patients having a partial response and 53.8% achieving stable disease (Ferrarotto et al., 2020; Rehovot et al., 2019). This trial is ongoing and is actively recruiting patients with recurrent or metastatic ACC harbouring activating *NOTCH* mutations. The predicted completion date is July 2021.

1.5.3. Tyrosine kinases

Receptor Tyrosine kinases (TKs) are a family of enzymes that regulate a range of critical cellular processes such as proliferation, differentiation, survival and migration. Upon ligand binding and activation via phosphorylation, TKs activate an intracellular signalling cascade resulting in the transcription of target genes. TK inhibitors have been widely investigated as potential ACC therapies. Sequencing studies have identified a number of targetable mutations in primary samples, and it was reported that 40.3% of recurrent and metastatic ACC samples harbour activating mutations in genes targetable by TK

inhibitors (A. S. Ho et al., 2019). Of all NCT registered targeted on-going and completed clinical trials for ACC, 62% are investigating TK inhibitors.

c-KIT is a TK particularly important in haematopoiesis. It is highly expressed in other cancers such as acute lymphoblastic and chronic myeloid leukaemia (AML and CML) and the c-KIT inhibitor, Imatinib-mesylate, is approved for treatment of these indications. However, although 80-94% of ACC samples are positive for c-KIT expression, a phase 2 imatinib study of 10 patients found the only response to be stable disease in 2 patients for 11-14 months (NCT00045669) (Jeng et al., 2000; S. K. Lee et al., 2012; Pfeffer et al., 2005). This could be because none of these studies detected c-*KIT* amplifications or activating mutations in the samples (Jeng et al., 2000). In a recent sequencing study, *KIT* amplification was detected in 3.8% of samples (Hou et al., 2020). In addition, a single study analysing only eight ACC samples reported a potential gain-of-function mutation in exon 11 in seven of the samples, suggesting KIT could be involved in the pathogenesis of ACC (Vila et al., 2009). However, Lee et al concluded that c-KIT positivity was not correlated with ACC recurrence or prognosis (S. K. Lee et al., 2012).

VEGF is critical for angiogenesis, and a study of 80 surgically resected ACC and 20 normal SG samples showed that high VEGF expression is significantly correlated with clinical stage, tumour size, vascular invasion, recurrence and metastasis ($P < 0.05$, Cox's proportional hazards model), making VEGFR an ideal therapeutic target for ACC (J. Zhang et al., 2005). Axitinib was tested in 33 patients and reported 3 (9.1%) partial responses and 25 (75.8%) patients with stable disease (NCT01558661) (A. L. Ho et al., 2016). Furthermore, a recent report identified that axitinib significantly prolonged stable disease compared to an observation group (NCT02859012) (Keam et al., 2020). Lenvatinib has been tested in two clinical trials (NCT02860936 and NCT2780310) and reported very similar results with 11.5% and 15.6% of patients having partial responses respectively and 76.9% and 75% of patients with stable disease (Locati et al., 2020; Tchekmedyian et al., 2018). A phase 2 study of apatinib had very striking results compared to other VEGFR inhibitor trials with a reported response rate of 47.1% and stable disease in a further 51% of patients (G. Zhu et al., 2018). This suggests that targeting VEGFR could be relatively effective in ACC.

EGFR is highly expressed in approximately 50-60% of cases, however activating mutations have only been reported for 1.4% of cases (S. K. Lee et al., 2012; Saida et al., 2018). Therefore, it is not surprising that EGFR inhibitors have not shown much promise in clinical trials. A phase 2 gefitinib trial (NCT00509002) of 18 ACC patients reported only 1 stable disease outcome (Jakob et al., 2015). However, a phase 2 lapatinib trial (NCT00095563) of 19 patients reported 15 (79%) with stable disease of which 4 were stable for over 6 months (Agulnik et al., 2007). Neither trial reported partial responses. Moreover, in a study detecting EGFR pathway mutations, *RAS* family mutations were present in 14.3% and were significantly associated with lower overall survival (P = 0.024) (Saida et al., 2018). Mutations in *KRAS*, located downstream of EGFR, are known to confer resistance to EGFR targeted therapies in other cancers, therefore *RAS* genes may be better therapeutic targets in ACC opposed to EGFR (Boeckx et al., 2013). Unfortunately, in the completed EGFR inhibitor clinical trials, *RAS* mutation status was not examined. There are currently trials on-going of EGFR inhibitors in combination with chemotherapeutic agents or immune checkpoint inhibitors that may be more effective.

The FGF signalling pathway is highly upregulated in ACC, with 4-12% of ACC samples harbouring FGFR activating or enhancing mutations. Amplifications of *FGFR1* and *2* have been detected in patient samples, furthermore FGFR2 is known to be a downstream effector of MYB, and the FGFR1 ligand, FGF2, is also upregulated by MYB (Andersson et al., 2017; J. S. Ross et al., 2014; Stephens et al., 2013). Whilst no single FGFR inhibiting agents have been tested in the clinic, multi-targeting TK inhibitors have been trialled that inhibit FGFR but with little response.

High copy number gain, amplification and general over-expression of *c-MET* has been reported to promote tumour growth, invasiveness and metastasis in a number of cancers such as breast, colorectal and lung (Christensen et al., 2005). Immunohistochemical (IHC) analysis of 200 archived ACC patient samples identified strong c-MET expression in 53.2% of cases, however expression did not correlate with clinicopathologic parameters or patient overall survival (Bell et al., 2015). Although, despite this, it could still be a potential drug target and deserves further investigation.

There are currently no single c-MET targeted clinical trials on-going, although it is targeted by some multi-TK inhibitors in the clinic.

Neurotrophic TKs (NTRKs) play important roles in neurogenesis, embryonic pluripotent stem cell survival, and migration (Castellanos et al., 2002; E. J. Huang & Reichardt, 2001; Pyle et al., 2006). TrkC (*NTRK3*) is highly expressed in ACC, with expression levels up to 100 fold higher in 17 out of 18 ACC samples when compared to normal tissue controls, although all samples had wild-type *NTRK3* lacking activating mutations (Ivanov, Panaccione, Brown, et al., 2013). The TrkC ligand NT-3 was also expressed in ACC, suggesting an autocrine signalling loop. Directional migration abilities observed in co-culture assays of Schwann cells and the ACC cell line SACC-83 were inhibited when treated with the TrkC inhibitor, AZD7451, suggesting a mechanism of neural attraction and invasion (H. Li et al., 2019). It is important to note that the SACC-83 cell line is not acknowledged as a validated cell line (see 1.6.1). Furthermore, *in vivo* assays demonstrated that AZD7451 reduced tumour growth in two ACC PDX models (Ivanov, Panaccione, Brown, et al., 2013). This demonstrates that NTRK inhibitors could be promising therapeutic targets for ACC treatment. There is an ongoing basket clinical trial currently recruiting ACC patients targeting TrkA (NCT03556228), however TrkC inhibitors are yet to be tested.

It has also been reported that targeting certain TK pathways inhibits MYB/MYB-NFIB oncogenic effects in ACC and promotes cell differentiation (Andersson et al., 2017). Andersson et al identified in ACC PDX-derived *in vitro* cultures that IGF1R specifically regulates *MYB/MYB-NFIB* expression regardless of the *MYB* activation mechanism, in an AKT-dependent manner. *MYB-NFIB* knockdown downregulated over 50% of the same genes as IGF1R inhibition, indicating that the oncogenic transcriptional program induced by MYB-NFIB can be reversed by inhibition of IGF1R. Despite these findings, single treatment of the IGF1R inhibitor linsitinib did not inhibit tumour growth in two ACC PDX lines. Only the combined treatment of linsitinib, gefitinib (EGFR inhibitor) and crizotinib (MET inhibitor) significantly inhibited tumour growth in both PDX models, although did not induce apoptosis. Furthermore, the triple TK inhibitor combination *in vitro* reduced proliferation synergistically, suggesting crosstalk between EGFR and MET. This triple

targeted combination could be an effective therapy in the clinic, despite not inducing apoptosis in PDX studies, as currently there are no available targeted treatments for ACC patients. However, multi-targeted combination therapies may induce excess toxicity, so perhaps identifying a single drug that targets both IGF1R and MET may be more effective and tolerable for patients.

1.5.4. Epigenetic modification

Epigenetic processes and modifications induce changes in gene expression without altering the DNA sequence. It has been reported that 35% of ACC tumours possess mutations linked to epigenetic modifications such as histone acetyltransferase and methyltransferase activity, the SWI/SNF chromatin regulator complex and chromatin remodelling (A. S. Ho et al., 2013). Histone acetyltransferase and deacetylase are key regulators of gene transcription by altering histone structure. A phase 2 clinical trial testing the histone deacetylase (HDAC) inhibitor, vorinostat, in 30 ACC patients reported partial responses in 2 patients, with response durations of 53 and 7.2 months, and progression in 1 patient (NCT01175980) (Goncalves et al., 2017). However, both responses were detected late into therapy, after 8 and 10 cycles. Both responders had mutations in methyltransferases (*KMT2A* and *KTM2E*), bromodomain (BRD) proteins (*BRD1* and *BRD3*), and members of the SWI/SNF chromatin regulator family (*SMARCA2*). Alternatively, the patient who had disease progression possessed an activating *NOTCH1* mutation, suggesting a high-grade ACC with NOTCH signalling dependency. However, as only a small number of samples were sequenced it cannot be claimed that the presence of these mutations are the reasons for vorinostat response or resistance. There is currently an on-going combination phase 2 trial investigating the HDAC inhibitor chidamide with chemotherapy (NCT03639168).

As explained, the *MYB-NFIB* translocation brings *NFIB*-flanking super-enhancers into close proximity to the *MYB* locus, and MYB protein binds to these super-enhancers creating a positive feedback loop sustaining MYB expression. Drier et al identified that these super-enhancers have high occupancy of the transcriptional co-activator extra terminal (BET) bromodomain (BRD) protein BRD4 (Drier et al., 2016). BRD4 is a global regulator of gene transcription and plays an important role in transcription initiation and

elongation by recruiting the positive transcription elongation factor (P-TEFb) to acetylated chromatin, which in turn activates RNA polymerase II (Yang et al., 2005). BRD4 is a druggable epigenetic target, and BET inhibitors have been reported to suppress MYB function in AML and suppress the activity of super-enhancers with high BRD4 occupancy (Roe et al., 2015). Therefore, Drier et al treated ACC PDX models *in vivo* with the BRD inhibitor JQ1. However, although grade II ACC tumour growth was reduced compared to the vehicle treated mice, along with a decrease in *MYB* and MYB target gene expression, grade III ACC tumours did not respond to BET inhibition. Drier et al reported that MYB coordinates distinct regulatory programmes in differing cell lineages by binding to different enhancers; cooperating with TP63 in myoepithelial cells and NOTCH in luminal epithelial cells. High grade ACC has the highest proportion of solid growth and has a higher proportion of luminal cells compared to lower grades. Therefore, these results suggest that that low-grade ACC is sensitive to BRD inhibition and that high-grade tumours with a higher proportion of solid growth may be more sensitive to Notch inhibitor intervention.

1.5.5. Immunotherapy

Immunotherapy is a type of targeted therapy that promotes the patients immune system to attack cancer cells by promoting the recognition of cancer cells, and enhancing immune responses to aid cancer cell elimination. There has been one report investigating the immunologic profile of ACC tumours studying 28 primary and metastatic ACC samples, focussing on infiltrating immune cells and the immune checkpoint blockade PD-1 pathway (Sridharan et al., 2016). Of the 28 primary and metastatic samples, PD-L1 and PD-1 expressing infiltrating immune cells were detected in 45% of samples, and PD-L2 expression in 65.4% of tumour samples. PD-L2, like PD-L1, also binds to the PD-1 receptor and decreases T-cell proliferation and cytokine production, promoting immune tolerance and evasion. Therefore, this study suggests that a high proportion of ACC cases could be responsive to PD-L1 targeted therapy. However, a more recent study compared the immune microenvironment of 20 primary and metastatic ACC patient samples to 10 other cancer types, including urothelial carcinoma and breast cancer that are currently treated with immune checkpoint therapies in the clinic (Linxweiler et al., 2020). RNAseq identified universally low

expression of T cell checkpoints in the ACC samples suggesting that checkpoint inhibitors, such as anti-PD-1 monotherapy, would not be effective. Linxweiler et al suggest that ACC has an immune “cold” microenvironment due to T cell exclusion and comparably higher levels of immunosuppressive myeloid-derived suppressor cells and M2-polarised tumour-associated macrophage populations. This indicates that a potential immunotherapeutic approach for ACC would be to make the tumours more immune “hot” by using vaccines or immune agonists.

There are currently six ongoing PD-1 targeting clinical trials; two of which are in combination with VEGFR inhibitors, one in combination with the anti-MYB vaccine TetMYB and one in combination with another immune checkpoint pathway inhibitor targeting CTLA4, Ipilimumab. The only published results for ACC treatment with a PD-1 inhibitor are from a phase 1 study treating 26 patients with SG carcinoma, only two of which were ACC patients. For this trial, 3 partial responses were reported however none were ACC (Cohen et al., 2018). Therefore, anti-PD-1 therapy in combination with other targeted therapies may be more effective for ACC than anti-immune checkpoint agents alone.

Table 1-2 Completed and on-going targeted therapy clinical trials for ACC

Target(s)	Drug(s)	NCT no.	Phase	Status	No. of patients	Partial response	Stable disease
Abl, Scr TKs	Dasatinib	NCT00859937	2	C	40	1 (2.5%)	20 (50%)
Akt	MK2206	NCT01604772	2	C	16	0	13 (81.25%)
c-KIT, PDGFR, VEGFR3, FGFR	Dovitinib	NCT01524692	2	C	34	2 (5.9%)	22 (64.7%)
c-KIT, PDGFR, Abl	Imatinib	NCT00045669	2	C	10	0	2 (20%)
c-KIT, PDGFR, Abl + chemo	Imatinib + Cyclophosphamide	NCT01046487	1	C (-R)			
c-KIT, PDGFRß, FLT3, VEGFR2	Sunitinib	NCT00886132	2	C	13	0	11 (84.6%)
EGFR	Gefitinib	NCT00509002 NCT00068497	2 2	C C (-R)	18	0	1 (5.55%)
EGFR2	Rivoceranib	NCT04119453	2	R			
EGFR + EGFR	Erlotinib + cetuximab	NCT00397384	1	C (-R)			
EGFR + EGFR +/- VEGFR	Erlotinib + cetuximab +/- Bevacizumab	NCT00101348	1/2	C (-R)			
EGFR + HER2	Lapatinib	NCT00095563	2	C	19	0	15 (79%)
HDAC	Vorinostat	NCT01175980	2	C	30	2 (6.66%)	27 (90%)
HDACi + chemo	Chidamide + cisplatin	NCT03639168	2	R			
HER2	Trastuzumab	NCT00004163	2	C (-R)			

HER2	Trastuzumab + IL-12	NCT00004074	1	C (-R)			
HER2 + chemo	Thalidomide + Docetaxel	NCT00049296	1	C (-R)			
HER2 + FTase	Trastuzumab + Tipifarnib	NCT00005842	1	C (-R)			
HPV16 E6 and E7	Vaccine therapy	NCT00019110	1	C (-R)			
HSP90	Alvespimycin hydrochloride	NCT00089362	1	C (-R)			
mTOR	Everolimus	NCT01152840	2	C	34	0	27 (79.4%)
mTOR + EGFR	Everolimus + cetuximab	NCT01627194	1	C (-R)			
mTOR + TNFa, VEGF, FGF	Everolimus + Lenalidomide	NCT01218555	1	C	36	5 (13.8%)	24 (66.7%)
MYB + PD-1	TetMYB + BGB-A317	NCT03287427	1	R			
NOTCH	AL101	NCT03691207	2	R			
NOTCH	CB-103	NCT03422679	1/2	R			
Oncolytic virus + PD-1	Talimogene laherparepvec (TVEC) + Nivolumab	NCT02978625	2	R			
PD-1 + CTLA-4	Nivolumab + Ipilimumab	NCT02834013 NCT03146650	2 2	R A			
PD-1	Pembrolizumab	NCT02054806	1b	A			
PD-1	Pembrolizumab +/- radiation	NCT03087019	2	A	10/arm		7 P (70%) 5 P+RT (50%)
PRMT5	PRT543	NCT03886831	1	R			
PRMT5	GSK3326595	NCT02783300	1	R			

Protease	Nelfinavir	NCT01065844	2	C	11	0	7 (63.6%)
Proteasome (20S) + chemo	Bortezomib + doxorubicin	NCT00077428	2	C	21	0	15 (71%)
RAR	Tretinoin (All-trans retinoic acid)	NCT03999684 NCT04433169	2 2	A R			
TrkA	VMD-928	NCT03556228	1	R			
Vascular targeting peptide + TNFa	NGR-TNF	NCT00098943	1	C (-R)			
VEGFR	Apatinib	NCT02775370 NCT04119453	2 2	C R	59	28 (47.1%)	30 (51%)
VEGFR	Axitinib	NCT02859012 NCT01558661	2 2	A C	30 33	1 (3.33%) 3 (9.1%)	29 (96.6%) 25(75.8%)
VEGFR	Lenvatinib	NCT02780310 NCT02860936	2 2	C C	32 26	5 (15.6) 2 (11.5%)	24 (75%) 20 (76.9%)
VEGFR2, c-MET	Cabozantinib	NCT03729297	2	C	17	Closed due to toxicity	
VEGFR, RET, Raf-1, c-KIT	Regorafenib	NCT02098538	2	A	38	0	17 (44.7%)
VEGFR2 + chemo	Semaxanib + paclitaxel	NCT00005647	1	C (-R)			
VEGFR + PD-1	Axitinib + Avelumab	NCT03990571	2	R			
VEGFR + PD-1	Lenvatinib + Pembrolizumab	NCT04209660	2	R			

A = active, C = completed, C (-R) = completed results not published, R = recruiting

1.6. ACC pre-clinical models

Molecular and therapeutic studies of ACC have been complicated by the differences in diagnosis and characterisation, the rarity of tumours and the lack of bona fide ACC cell lines (Nagel et al., 1999; Zhao et al., 2011). Genetic profiling of six commercially available cell lines identified cross contamination with HeLa and T24 bladder cancer cells, and two lines were identified to be of rodent not human origin (Phuchareon et al., 2009). To-date, there are no validated SG ACC cell lines available from the American Type Culture Collection (ATCC), and there is a need for the establishment of novel ACC preclinical models to accurately predict therapeutic responses. More generally, in research a large number of compounds fail phase 2-3 studies resulting in a discrepancy between pre-clinical results and patient outcomes. This is partly due to poor pre-clinical models failing to represent tumour and patient heterogeneity. Patient-derived xenografts (PDXs) and patient-derived organoids (PDOs) are proving to be translational models bridging the gap between preclinical and patient studies. A comparison between 2D, 3D and PDX preclinical models is summarised in Table 1-3.

1.6.1. ACC cell lines

As mentioned, to-date there are no validated ACC cell lines commercially available. One proposed cell line is SACC-83, that has been used in a number of *in vitro* ACC studies (H. Li et al., 2019; Sha et al., 2019; Shan et al., 2016; Xu et al., 2019). This line was derived from the adenoepithelial cells of a female patients sublingual gland (L. Wang et al., 2013). A limitation of this cell line is that SACC-83 does not express high levels of MYB, and studies using this line to model ACC often overexpress MYB via lentiviral transduction so MYB regulation does not mirror mechanisms observed in the clinic (Xu et al., 2019). SACC-83 is not acknowledged as a validated cell line.

A very recent, promising ACC-derived cell line has been established by Warner et al, UM-HACC-2A (Warner et al., 2019). This line took eight years to successfully establish and validate, however is yet to be made commercially available. Culture conditions included

fibronectin-coated plates and the addition of 1% bovine brain extract (BBE), described to provide “critical” neural factors for ACC growth and survival. Although, as BBE is an unspecified mixture of cytokines and growth factors, further studies could aid the specific identification and characterisation of ACC growth requirements and dependencies. Furthermore, MYB expression was significantly reduced until passage 20, and the reason for this is unknown. The length of time to establish this single ACC cell line highlights the need for alternative ACC pre-clinical models and the lack of MYB expression in early passages draws attention to the difficulty in accurately modelling ACC patient tumours.

1.6.2. Patient-derived xenografts

PDXs are preclinical *in vivo* models where fragments of patient tumours are engrafted into immunocompromised mice. Engrafted tumours grow recapitulating the primary patient tumour by maintaining molecular characteristics, tumour histology and heterogeneity, including maintenance of CSC populations. As only a small volume of patient tumour is originally implanted, it may not represent the heterogeneity of the whole tumour, therefore often PDX lines are generated from biopsies from multiple regions of the patient tumour.

A key study by Toolan et al proved that it was possible to grow human tumour cells in x-irradiated mice and rats, and subsequent trials demonstrated that suppressing the immune system increased tumour proliferation and implant success rate (Phillips & Gazet, 1970; Toolan, 1953). This prompted the generation of modified immune-deficient mice such as the NOD/SCID/IL2Rcnull (NSG) mouse, enabling the establishment of PDX models (Shultz et al., 2005).

PDX lines have now been established for a large range of cancer types, including breast, colorectal, lung and ovarian (Figure 1-5) (Bruna et al., 2016; Cutz et al., 2006; E. George et al., 2017; Guenot et al., 2006). There are currently a number of PDX initiatives such as the EurOPDX collection, which is an extensive collection of over 1,500 subcutaneous and orthotopic models from more than 30 different pathologies, collated from 16 European academic institutions (Byrne et al., 2017). These large biobanks improve the

diversity of tumours modelled for each cancer type at the epidemiological and molecular levels. As PDX models increase the amount of tissue available from one patient, they are particularly useful models for rare cancer types, such as ACC. The University of Virginia, in collaboration with the ACC Research Foundation (ACCRF) have developed over 20 ACC PDX models, with 12 available to external research groups for in-house *in vivo* drug-sensitivity studies at South Texas Accelerated Research Therapeutics (XenoSTART). Full sequencing data are available for 10 models (Moskaluk et al., 2011).

PDXs are used for pre-clinical drug testing, with reportedly similar drug responses as those observed in the clinic. Moreover, PDXs have also been utilised to predict therapy biomarkers and mechanisms of drug resistance and acquired resistance, and to develop regimes to prevent or overcome this. For example, Bertotti et al found concordance between the responses to EGFR inhibitor cetuximab in *EGFR*-amplified CRC PDXs and patients in the clinic (Bertotti et al., 2011). They also identified that *HER2* amplification was a biomarker for cetuximab resistance and that the combination of cetuximab with HER2 inhibition resulted in long-lasting tumour suppression in PDXs. This is clear evidence that this combined therapy could be very promising in cetuximab-resistant patients. Furthermore, Gao et al conducted high-throughput screening using PDXs established from the Novartis Institutes for BioMedical Research PDX encyclopaedia (NIBR PDXE) to determine population responses to 62 treatments across 6 different cancer types (H. Gao et al., 2015). This large-scale screen used the “one animal per model per treatment” approach (1 x 1 x 1), that enables modelling of inter-patient response heterogeneity. From this study, novel therapies dismissed in cell line *in vitro* screens were reported as sensitive, and responses were similar to those observed in patients according to available clinical data. In addition, mechanisms of acquired resistance were identified and matched with existing mechanisms reported in the clinic. Altogether, there is strong evidence indicating that PDX models are a potential tool to improve predictions of patient responses in the clinic. However, as PDX maintenance costs are high, an alternative drug screening method has been developed using short term PDX-derived 2D cultures. In these studies, PDX tumours are dissociated to single cells and grown in a 2D high-throughput format and treated with drug candidates *in vitro*. Based on cell viability results, only the most sensitive therapies *ex vivo* are

confirmed in PDX studies *in vivo*. This method was utilised by Bruna et al, and they reported that 82.5% of PDX-derived 2D drug responses were recapitulated when repeated in PDXs *in vivo* (Bruna et al., 2016).

An important consideration for assessing outcomes from PDX drug sensitivity studies conducted at a range of institutions is that there should be standardized methods and defined quantitative assessment to ensure reproducibility and enhance extrapolation to clinical settings. Recently, clinical Response Evaluation Criteria in Solid Tumours (RECIST) has been adapted to suit PDX application, defining "best response" and "best average response" and outlining tumour volume cut offs (H. Gao et al., 2015; Therasse et al., 2000). These allow categorizing responses as either progressive disease, stable disease, partial response or complete response and improve predictability of patient outcomes from PDX studies.

PDXs are mostly subcutaneous implants, however, orthotopic transplantation at the physiological site of tumour origin can lead to local invasion and metastasis similar to the disease progression observed in patients (Dai et al., 2015; Hoffman, 2015). Furthermore, the stroma may be different at the orthotopic site compared to the subcutaneous site, more accurately modelling the primary tumour by mimicking the native tumour microenvironment. However, these models are more technically challenging in terms of micro-surgical engraftment and, depending on the engraftment site, monitoring tumour progression. Therefore, the majority of studies use subcutaneous engraftment. The issue of whether subcutaneous or orthotopic implantation affects drug responses has not been determined. It is probable that therapies targeting tumour microenvironment components or inhibiting metastatic spread would be more accurately recapitulated in orthotopic PDXs, whereas therapies targeting oncogenes and genetic driver mutations would be less dependent on anatomical engraftment site.

Although there is evidence that PDXs overcome the issues of maintaining the phenotypic and genomic characteristics of patient tumours, accurately predicting drug responses and predicting mechanisms of drug resistance, some limitations must still be addressed:

Firstly, early passage PDX models maintain tumour-stromal interactions, vasculature immune cells and fibroblasts, however with increasing passages the human stroma is replaced by murine stromal components. This raises the question as to whether PDXs are appropriate models for some therapies targeting microenvironmental processes and although most murine cytokines or growth factors are able to cross-react with human receptors expressed by the tumour, it is not always the case such as for HGF ligand and MET receptor (Brodeur et al., 2009; Mestas & Hughes, 2004). In addition, as the mice used are immune-deficient to prevent tumour rejection, they cannot currently be used to assess immunotherapies. This is beginning to be addressed by the development of humanised mice (human haemato-lymphoid chimeric mice and human immune system (HIS) models). These are immunocompromised mice in which selected immune components have been introduced (usually haematopoietic stem cells, peripheral blood mononuclear cells or tumour infiltrating lymphocytes), generating mice with a human immune system with different degrees of immune activity (Byrne et al., 2017). These models are relatively novel and have already been used to study immune checkpoint inhibitors and oncolytic viruses (Tsoneva et al., 2017; Zheng et al., 2018). However, the development of humanised mice with immune cells and tumour sample from the same patient would enable more accurate modelling of personalised treatment and disease progression whilst avoiding immune reactions caused by human leukocyte antigen mismatch (Kooreman et al., 2017).

Secondly, it has been reported that tumour growth rate increases with PDX passage and that there is a significant correlation between PDX passage and high-grade tumour features, as identified in three head and neck squamous cell carcinoma PDXs and one ACC PDX (A. T. Pearson et al., 2016). This suggests that clonal selection occurs over increasing passage, selecting for the most proliferative cell types. Other studies do not report this observation, with a study of breast cancer explants preserving the morphological and molecular characteristics of the primary tumours throughout serial passaging (Bruna et al., 2016). However, it is generally advised that translational research should be conducted on PDXs at lower passages to reduce the risk of variation from the original patient tumour, although this may be impractical due to tissue availability and time taken for tumour growth.

Finally, another drawback of PDX models is that continuous passaging and line expansion is time consuming with high maintenance costs. This makes large scale studies difficult for individual institutions, hence the development of large PDX initiatives promoting collaboration in this research area. However due to expense, PDXs are mainly used to confirm sensitivities identified from drug screening in alternative pre-clinical models, such as 2D cultures or 3D patient-derived organoids (PDOs).

1.6.3. 3D organoids

Alternative patient-specific *in vitro* pre-clinical models increasingly used to predict drug responses are primary cell 3D organoids. Over the last decade major strides have been made in *in vitro* 3D organoid establishment and culture. Organoids are defined as isolated embryonic or adult stem cells able to differentiate, proliferate and self-organise into 3D structures resembling the tissue of origin. Initial research into 3D culture was to generate organoids from normal tissues. All organ and tissue types have specific growth requirements and dependencies which are required in culture to recapitulate the tissue of origin. The first adult stem cell-derived organoids reported were established from $Lgr5^+$ mouse intestinal stem cells and grown in culture conditions mimicking the intestinal niche; plated in a basement membrane and culture medium optimised with specific growth factors required for proliferation and differentiation to form structures resembling the intestinal epithelium (Sato et al., 2009). Since this key publication, organoids have been established for a number of normal tissues including colon, liver, prostate and fallopian tube (Chua et al., 2014; Huch et al., 2015; Karthaus et al., 2014; Kessler et al., 2015; Sato et al., 2011). Two studies to date have demonstrated the use of murine normal SG organoids to restore function *in vivo*, and these studies have defined specific medium requirements to culture functional SG organoids (Maimets et al., 2016; Nanduri et al., 2014).

Tumour-organoids have also been established for a number of human cancers, derived from patient tumour samples. These are isolated patient-derived cancer cells grown in a 3D matrix with the capacity to proliferate and differentiate into “mini-tumours”. These cancers include breast, lung, ovarian, and prostate and are summarised in Figure 1-5

(Drost et al., 2016; D. Gao et al., 2014; Hoffmann et al., 2020; Kopper et al., 2019; Sachs et al., 2018, 2019). However, whilst normal murine SG organoids have been developed, the culture of SG tumour-derived organoids are a novel area of investigation. To date, all tumour organoids established are derived from epithelial tumours, so cannot yet be used to model cancers such as leukaemia or lymphoma for which PDX models have been established (Chapuy et al., 2016).

Organoid lines are thoroughly tested to confirm that they accurately recapitulate the patient tumour from which they are derived. For example, Sachs et al established a library of 95 primary and metastatic breast cancer organoid lines, achieving a success rate of 61.3%, and for each compared tumour histopathology, grade and hormone receptor status. Furthermore, copy number variations and mutational signatures were consistent between tumour samples and matching derived organoid lines and this was maintained following long term expansion (Sachs et al., 2018). However, Fujii et al established 54 CRC PDOs and reported that microsatellite unstable CRC organoid genetic and cellular heterogeneity are modified with continual passage, therefore genetic stability should be investigated routinely following passages to ensure reliability of research (Fujii et al., 2016). In addition, clonal expansion from single cells could maintain tumour heterogeneity representation. Studies such as these have led to the generation of living organoid biobanks. These are repositories of a large number of organoid lines representing a diverse range of cancer types and reflecting the diversity of subtypes observed in the clinic. Each organoid line is well characterised and has been expanded long-term and cryopreserved ensuring accessibility, sample viability and proliferative capacity, as well as being cost effective. These biobanks are particularly useful for rare cancer types for which stable cell line generation is challenging.

Organoids have been utilised to investigate a range of factors. Fujii et al identified the optimum niche factor requirements for CRC PDO growth, for organoids harbouring differing mutations (Fujii et al., 2016). They reported that CRC organoids carrying mutations in *APC*, *CTNNB1* and *TCF7L2* could grow in the absence of Wnt activators, and that samples harbouring mutations in both *KRAS* and the PI3K pathway were EGF

independent. These findings demonstrate how organoids can be used to study the interaction between tumour mutational profiles and the tumour microenvironment.

PDOs can be applied to drug screens and used to validate drug sensitivities identified from patient-specific genomic sequencing. The Rubin lab (Cornell) have established organoids for 38.6% of patient samples of 17 different tumour origins, and successfully designed a high-throughput organoid drug screening method (Pauli et al., 2017). Comparison of drug sensitivities between 2D and 3D showed high concordance with a Spearman's rank correlation coefficient of 0.77, validating organoid cultures as a pre-clinical drug-screening model. Moreover, a phase I/II clinical trial evaluated the clinical value of PDOs to predict clinical outcomes in patients in response to anti-cancer therapy for CRC or gastroesophageal cancer (Vlachogiannis et al., 2018). Biopsies were collected from 71 patients and they reported that the derived organoids displayed 100% sensitivity, 93% specificity, 88% positive predictive value and 100% negative predictive value when compared to patient clinical responses to targeted and chemotherapeutic agents (Fishers exact test, $P < 0.0001$). This provides promising evidence that organoids are clinically relevant drug sensitivity models.

Other applications also include studying mechanisms of metastasis, invasion and tumour dormancy (reviewed in Fan et al., 2019). Organoids can also be genetically altered using gene editing technologies to study the effects of oncogenic mutations. Two studies used CRISPR/Cas9 technology to modify the most commonly mutated genes in CRC into normal human intestinal organoids (Drost et al., 2015; Matano et al., 2015). Drost et al concluded that combined loss of APC and P53 induces extensive aneuploidy and chromosome instability. CRISPR/Cas9 technology was also used to demonstrate the multiple key driver mutations in pancreatic ductal adenocarcinoma (PDAC) that induce niche independence during tumorigenesis (Seino et al., 2018). These studies are examples of how organoid gene editing methods can be used to study genetic mechanisms of cancer initiation and progression.

A limitation of organoid models is that they cannot mimic tumour vasculature, stroma, or incorporate an immune component. However, in order to address these issues, co-culture organoids are a growing area of research. Co-culture systems have been

developed to investigate immunotherapy responses and to generate tumour-reactive T-cells. Dijkstra et al co-cultured autologous CRC or lung cancer organoids and peripheral blood lymphocytes isolated from matching patient blood samples (Dijkstra et al., 2018). Tumour-reactive T-cells with patient-specific immunogenic mutations were expanded when grown in the co-culture organoid system and had the ability to recognise and kill the autologous tumour organoids, proving organoids can be used to support T-cell-based therapies. Furthermore, developments are being made using co-culture models to investigate tumour-stroma interactions. Öhlund et al isolated murine pancreatic stellate cells which differentiate into cancer-associated fibroblasts (CAFs) (Öhlund et al., 2017). They found that co-culture of these CAFs with murine PDAC organoids mimicked desmoplastic stroma, and that CAFs differentiate into two distinct subgroups. In addition, Seino et al found that PDAC tumours were dependent on Wnt signalling for proliferation when co-cultured with CAFs, identifying that CAFs provide a Wnt niche for PDAC tumour growth (Seino et al., 2018). These studies highlight the importance of CAFs in the tumour microenvironment promoting tumorigenesis. However, further development is needed to model tumour vasculature interactions and potentially to model multiple microenvironmental factors together to more accurately recapitulate the patient tumour native microenvironment.

Overall, organoids are a growing area of translational research. There are 68 projects registered on ClinicalTrials.gov (as of 5th December 2020) covering a range of study aims; including organoid line establishment, patient response correlations, drug screening including T-cell immunotherapies and cancer progression investigations. They are a useful tool particularly for rare cancer subtypes and, like PDXs, are beginning to bridge the gap between pre-clinical and clinical studies, particularly with co-clinical trials.

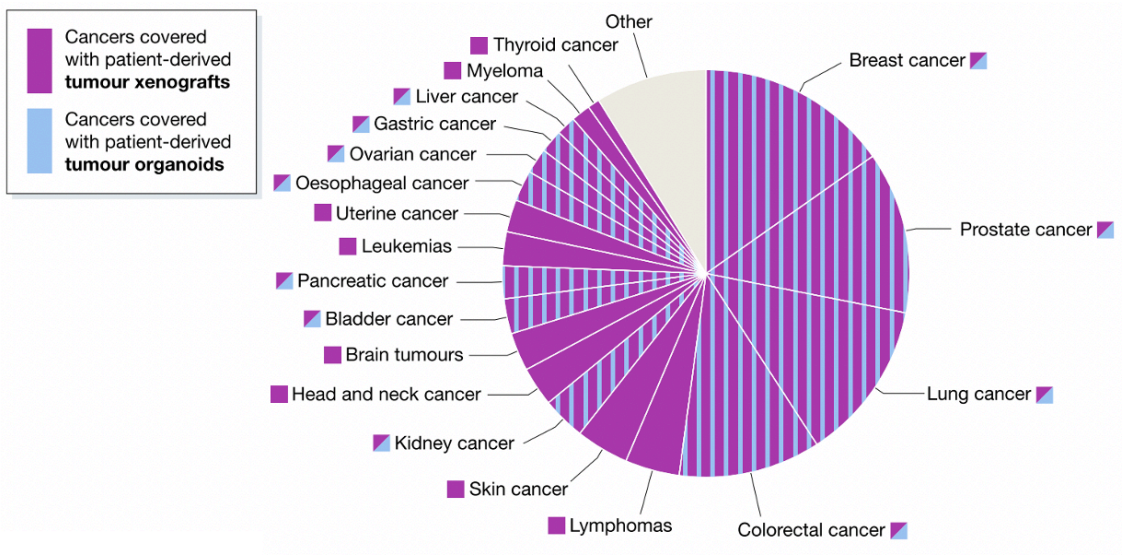

Figure 1-5 Pie chart depicting the different cancer types for which patient-derived tumour xenografts and organoids have been established.

Taken from (Bleijs et al., 2019).

Table 1-3 Comparison between 2D, 3D and PDX pre-clinical models

Feature	**Cell lines**	**Organoids**	**PDX models**
Generation efficiency	-	30-80%	17-72%
Tumour tissue source	Surgical biopsies or PDX tissue	Surgical biopsies or PDX tissue	Surgical biopsies
Retention of heterogeneity	No	Yes	Yes
Generation time	1 week	2-12 weeks	4-12 months
Passage efficiency	High	High	Low
Genetic manipulation	Yes	Yes	No
Immune components	No	In development	In development
High-throughput drug screening	Yes	Yes	No
Cost	Low	Middle	High

1.7. Aims of research

It is clear from reviewing the literature that there is a need for novel targeted therapeutic strategies for ACC. However, pre-clinical research would be greatly propelled by the generation of improved *in vitro* ACC models, which could be applied to both drug sensitivity assays and utilised to identify drivers of and niche requirements for ACC growth.

Therefore, the aims of this studentship were to:

a) Identify potential therapeutic targets from the genomic and transcriptomic analyses of ACC patient tumours
b) Optimise and establish relevant PDX-derived preclinical models in both 2D and 3D conditions
c) Use these models to identify novel therapeutic options for ACC, to confirm these *in vivo* and identify potential therapeutic biomarkers to demonstrate therapeutic efficacy.

2. Materials and methods

2.1. Patient samples

2.1.1. Sample collection

Fresh tumour tissue from radiologically-guided percutaneous needle biopsies were obtained from 12 patients at The Royal Marsden acquired under ethical approval. Matched peripheral blood samples were also acquired from all patients. All stored samples are recorded under the Human Tissue Act.

2.1.2. Patient sample RNA sequencing and whole exome sequencing

Sequencing was conducted by the Tumour Profiling Unit (TPU). Briefly, DNA and RNA were extracted from frozen sections of primary tumours using the AllPrep^{TM} DNA/RNA Micro kit (Qiagen). DNA exome sequencing followed the SureSelectXT Target Enrichment Kit (Agilent). Total RNA was ribosomal RNA depleted using the Ribo-Zero rRNA Removal Kit (Illumina), prior to library preparation using the NEB Next Ultra Directional RNA Library Prep Kit for Illumina (New England Biolabs). Both DNA and RNA were sequenced using the HiSeq 2500 system (Illumina). Each sample required a sequencing depth of 50 x 10^6 reads and 2 x 100 cycles. DNA extracted from matched peripheral blood samples were also sequenced to identify germline mutations.

RNAseq data was mapped to Genome Reference Consortium Human Build 37 (GRCh37). Differential gene expression of the ACC samples was normalised in two different ways. Firstly, all ACC samples were normalised to published raw sequencing data from 5 normal salivary gland samples (Bell et al., 2016). Secondly, each ACC sample was normalised to the sample SG0043, acinic cell carcinoma of the salivary glands. This sample was chosen as there was a previous project within the Swain laboratory to establish PDX lines from multiple SG cancer subtypes, however SG0043 was the only successful line that was not of ACC origin. Acinic cell carcinoma is thought to be driven by the transcription factor *NR4A3*, that is activated via a translocation to the SCPP gene

cluster resulting in SCPP super-enhancer hijacking (Haller et al., 2019). Importantly, aberrant MYB expression is not a hallmark of acinic cell carcinoma. Enrichr was used for Kyoto Encyclopedia of Genes and Genomes (KEGG) pathway analysis of differentially expressed genes (DEGs) (E. Y. Chen et al., 2013; Kuleshov et al., 2016).

2.2. Patient-derived xenograft line establishment

2.2.1. PDX line establishment

Primary patient tumour samples were implanted subcutaneously onto both flanks of female 6-8-week-old CD1 nude (Crl:CD1-Foxn1nu) mice. Tumour fragments were passaged to new mice when they reached 1000 mm^3, calculated as ($width^2$ x length)/2. At each passage one snap-frozen, one formalin- or 4% paraformaldehyde (PFA)-fixed and one viable frozen sample in DMSO was taken for reference. Additionally, samples were also stored to produce single cells for downstream experiments.

Re-establishment of all lines was required in 2018, three years after initial implantation due to Corynebacterium bovis (C. bovis) infection. SG0028, 36 and 37 lines were re-established via single cell injections. Briefly, 1 x 10^6 PDX-dissociated single cells (without mouse depletion) were mixed with 50% Matrigel® Basement Membrane Matrix (Corning®) in 100 µL volumes and injected into each flank of 6-8-week-old NSG mice (NOD.Cg-$Prkdc^{SCID}$ $Il2rg^{tm1Wjl}$/SzJ).

2.2.2. Orthotopic PDX model engraftment

Single SG0032 tumour fragments, approximately 5 mm^3, were implanted into the submandibular gland of 6-8-week-old CD1 nude mice. Tumour growth was monitored and when reaching a volume of 1000 mm^3, SG0032 was passaged once. On tumour harvest the submandibular gland, lungs, and liver were dissected and fixed in 10% formalin for histological analysis.

2.2.3. PDX line validation

For samples with either the *MYB-NFIB* or *MYBL1-NFIB* translocations, the presence of the translocated transcripts in different passage numbers were confirmed via reverse-transcription polymerase chain reaction (RT-PCR) with primers designed for the breakpoint in each sample (see 2.8.1-2.8.3). All custom DNA oligos used in this project were ordered from Sigma.

PDX lines were also validated by confirming selected somatic mutations with a high variant allele frequency (VAF), or germline mutations where the mutation was at a higher VAF than the matching normal sample, chosen from the whole exome sequencing (WES) data of the patient samples. DNA was extracted using the DNeasy Blood and Tissue kit (Qiagen). Primer design and PCR completion was conducted by Mercy Fleming in the Swain laboratory. Each 25 µL reaction was prepared using 1 µL template DNA, 1.25 µL of each 10 µM Forward and Reverse primer (Table 2-1) and 0.25 µL Q5 Hot Start High-fidelity DNA polymerase (NEB) as per the manufacturers protocol. The MJ Research PTC-200 Thermal Cycler (Marshall Scientific) was used. The amplification program comprised of a denaturation step at 98°C for 30 seconds followed by 35 amplification cycles of a denaturation step at 98°C for 10 seconds, an annealing step at the optimal temperature specific for the primer pair (Table 2-1) for 30 seconds, followed by an elongation step at 72°C for 30 seconds, and a final elongation step at 72°C for 5 minutes.

PCR products were purified using QIAquick® PCR Purification Kit (Qiagen) and 5 µL of each purified DNA product, with 5 µL of the corresponding forward primer (10 mM) was sent to Genewiz for Sanger sequencing. The resulting AB1 files were downloaded and viewed using 4Peaks software (Nucleobytes B.V.). The location of the variant was found in each sequence and the sample from the tumour compared to a tumour lacking the mutation as a control sequence to confirm the presence of the variant in the tumour.

Table 2-1 PDX line mutation confirmation primer pairs

Sample	Gene	Forward primer	Reverse primer	Annealing temp. (°C)
SG0027	ELF4	TTCAGCTCCATTCCTCTCGTG	GGAAAGAGGCCTGCAAAGTG	66
SG0027	FANCD2	AGCACCACCTACATGTGTCTC	TGACACTTGTTCTGGGAGGTT	65
SG0028	BRD1	AAACGCTGACCTACGCTCAA	CCTCGTCGATCAGAGACTGC	66
SG0028	RTTN	TACTTGACGAGGGGTTTGCG	GCATTGCCTGCCTTACCTTTT	65
SG0032	CREBBP	ACCCCAAGGGAGAAGTGTTG	TCAGTTGTGACAAAAGCCACC	65
SG0032	KIT	CACATAGCTTTGCATCCTGCC	TAGAGCACTCTGGAGAGAGAACA	65
SG0036	FGA	CTTGTCGAGGGTCATGCAGT	GAGTTCCAGCTTCCAGCACT	66
SG0036	HIP1	AGGGGCTCCTAATGACCAGA	CTGGACTGAGGCTAAGAGCTG	66
SG0037	BCL11B	TTCTGCGGCAAGACCTTCAA	CCCACGTTCTCCATGACCTT	66
SG0037	WDR45	CTGATCTGGGACGATGCCC	GTGTATCTGAGCCCTCTCACC	66
SG0069	ABL1	GAGTGGAGGTCAGTCACGC	GCGACTCAGAGGAGTGCTTG	67
SG0069	TMPRSS2	GTGGTGTCAGTCCCTCCAAG	CCCTAGGAAGCAGGTGCAAT	66

2.3. PDX tumour and tissue dissociation

Samples were mechanically minced using a scalpel to approximately 1 mm^3. They were dissociated in dissociation medium (Table 2-2) for 2 hrs at 37°C on a rotor at 100 rpm. Samples were then washed with Phosphate-buffered saline (PBS) with 5 µM Y-27632 dihydrochloride (Tocris), and red blood cells were lysed (red blood cell lysis solution, Sigma). The cells were then trypsinised using 0.05% Trypsin/EDTA for 8 minutes in a water bath at 37°C and then treated with DNAse solution (10 units/mL, Roche) with Y-medium (Table 2-3) at a ratio of 1:1 to prevent cell clumping for 5 minutes. Cell pellets were re-suspended in Y-medium, filtered through a 70 µM strainer and counted using a haemocytometer.

2.4. PDX-derived single cell 2D culture

Following tumour dissociation, 2-3 x 10^6 single cells were depleted to remove mouse stroma using a mouse depletion kit (Miltenyi Biotec, product 130-104-694) via a MidiMACS™ separator, as in culture mouse fibroblasts can outgrow human primary cells. The depleted cells were counted and plated at 1 x 10^6 cells per T25 culture flask in

6 mL Y-medium. Cells were grown as adherent cultures and when 80% confluent were dissociated using 0.25% Trypsin for 10 minutes at 37°C. They were then counted and re-seeded at 1 x 10^6 cells per T25. Optimisation of growth conditions is discussed in chapters 4 and 5.

Table 2-2 Dissociation medium components

Reagent	Concentration	Supplier
Dulbecco's Modified Eagle Medium: Nutrient Mixture F-12 (DMEM/F12)		Invitrogen
Heat-inactivated Foetal Bovine Serum (FBS)	5%	Invitrogen
Penicillin/Streptomycin	1x	ThermoFisher Scientific
Insulin-Transferrin-Selenium	1x	ThermoFisher Scientific
Human recombinant EGF	10 ng/mL	Sigma
Hydrocortisone	10 µg/mL	Sigma
Collagenase	0.5 mg/mL	Sigma
Hyaluronidase	0.1 mg/mL	Sigma
DNase1	10 units/mL	Roche
Y-27632 dihydrochloride	10 µM	Tocris

Table 2-3 Y-medium components

Reagent	Concentration	Supplier
Dulbecco's Modified Eagle Medium: Nutrient Mixture F-12 (DMEM/F12)		Invitrogen
Heat-inactivated Foetal Bovine Serum (FBS)	10%	Invitrogen
Penicillin/Streptomycin	1x	ThermoFisher Scientific
L-glutamine	1x	ThermoFisher Scientific
Insulin	5 µg/mL	ThermoFisher Scientific
Hydrocortisone	0.4 µg/mL	Sigma
Human recombinant EGF	10 µg/mL	Sigma
Gentamicin	1 µg/mL	Invitrogen
Amphotericin	0.5 µg/mL	ThermoFisher Scientific
Cholera toxin	8.4 ng/mL	Sigma
Y-27632 dihydrochloride	5 µM	Tocris

2.5. Organoid establishment and culture

2.5.1. PDX-derived organoids

Matrigel Basement Membrane Matrix (growth factor-reduced, phenol red-free, protein concentration ≥8.9, Corning) was mixed on ice with freshly dissociated PDX-derived single cells in Y-medium at a ratio of 3:1, 10,000 cells per well. 50 µL of the Matrigel/cell mix was plated into the centre of each well of a pre-warmed 24-well suspension plate (Starstedt). The plate was placed in an incubator to set (37°C, 5% CO^2) and after one minute the plate was turned upside down to avoid cells settling at the bottom, and left for 40 minutes. 0.5 mL organoid medium was added per well and replaced every 3-4 days. Organoid medium was adapted from published murine SG protocols and optimised for the culture of ACC PDX-derived organoids (Table 2-4) (Maimets et al., 2016; Nanduri et al., 2014).

2.5.2. Embryonic and adult mouse salivary gland organoids

Embryonic mice at stage E16.5 were culled, and salivary glands micro-dissected. Adult salivary glands were harvested from 15-20-week-old C57BL/6J mice. The salivary glands were dissociated to single cells following the same protocol as PDX dissociation, without mouse depletion. To plate the murine organoids, 2000 cells were plated per well in the same 3:1 Matrigel/Y-media mix as PDX organoids. Mouse salivary gland organoid medium is outlined in Table 2-4.

2.5.3. Organoid imaging

For high-quality organoid morphology analysis, images were taken at 10x and 20x magnification on the EVOS XL Cell Imaging System (ThermoFisher Scientific).

To compare organoid number and size in different culture conditions, organoids were imaged and analysed via the ImageXpress Micro Confocal High-Content Imaging System at 20x magnification using the MetaXpress® High-Content Image Acquisition and Analysis Software. Each well of the 24-well plate was imaged as a grid of 4 by 4 squares, with each square producing a compressed image of 26 z-stack projections. Analysis was

set to measure organoids greater than 50 µm in diameter. The output for organoid count and area were expressed as the average for each square, to take into account organoids counted over two squares from image overlay in the grid compressed images.

Table 2-4 Organoid media components

Reagent	Concentration		Supplier
	PDX	Mouse	
B27 serum supplement	1x		ThermoFisher Scientific
N2 serum supplement		1x	ThermoFisher Scientific
Glutamax	1x	1x	ThermoFisher Scientific
HEPES	1x	1x	ThermoFisher Scientific
Penicillin/Streptomycin	1x	1x	ThermoFisher Scientific
Insulin	10 µg/mL	10 µg/mL	ThermoFisher Scientific
Primocin	100 µg/mL		Invivogen
A83-01	500 nM		Bio-Techne
Y-27632 dihydrochloride	10 µM	10 µM	Tocris
Recombinant human FGF2	20 ng/mL	20 ng/mL	PeproTech
SB202190	1 µM		Sigma
Dexamethasone	2 µM	2 µM	Sigma
Human recombinant EGF	20 ng/mL	20 ng/mL	PeproTech
Wnt3a		50 ng/mL	PeproTech
R-spondin		500 ng/mL	PeproTech

2.6. *In vitro* drug sensitivity assays

2.6.1. 2D assays

PDX-derived single cells were plated at a density of 2000 cells/well, and cell line controls at 1000 cells/well in 100 µL, in 96-well plates (Cellstar®). Cell line controls were obtained in-house (Table 2-5). After 24 hr incubation to allow cells to adhere, cells were drugged. Cell line controls were treated for 5 days, whereas PDX-derived single cells were re-drugged on day 5 and viability determined on day 10. Cell viability was determined via CellTiter Glo® (CTG) (Promega, Southampton, UK). This reagent indicates viability as a

measure of metabolically active cells by Adenosine triphosphate (ATP) levels. Medium was removed from the wells and CTG added (diluted 1:4 in PBS). The plate was kept in the dark at room temperature for 10 minutes on a shaker before reading using the Victor 5X luminescent plate reader (Perkin Elmer, Seer Green, UK). Luminescence readings were normalised to average of the DMSO control and expressed as the survival fraction (SF). Results were plotted as the mean SF +/- standard error (SE) in GraphPad Prism8.

Table 2-5 Control cell line culture conditions

Cell Line	Culture medium
A375	Dulbecco's Modified Eagle Medium, 10% FBS, 1x Pen/Strep, 1x Glutamax
Capan-1	Iscove's Modified Dulbecco's Medium, 10% FBS, 1x Pen/Strep, 1x Glutamax
HCT-116	McCoy's 5A Medium, 10% FBS, 1x Pen/Strep, 1x Glutamax
LNCaP	RPMI-1640 Medium, 10% FBS, 1x Pen/Strep, 1x Glutamax
MDA MB 231	Leibovitz's L-15 Medium, 10% FBS, 1x Pen/Strep, 1x Glutamax
PC3	RPMI-1640 Medium, 10% FBS, 1x Pen/Strep, 1x Glutamax
Snu-16	RPMI-1640 Medium, 10% FBS, 1x Pen/Strep, 1x Glutamax
TOV21G	RPMI-1640 Medium, 10% FBS, 1x Pen/Strep, 1x Glutamax, 1x HEPES

2.6.2. 3D assays

PDX-derived single cells grown in 2D were plated in 96 well plates at a density of 1000 cells in a Matrigel-media mix (3:1) in 25 µL. The Matrigel was left to set as with normal organoid set up. Three days after plating, the organoids were imaged and drugged. Serial drug dilutions were made up in organoid medium. On day four of drugging, organoids were re-drugged and cell viability measured on day seven of the assay. Cell viability was measured using CTG 3D (Promega). Media was gently removed and 50 µL CTG was added to the plates diluted 1 in 4 with PBS. The plate was placed in the dark on a shaker for 1 hour before being analysed using the Victor 5X luminescent plate reader (PerkinElmer). Results were analysed in the same way as the 2D drug sensitivity assays.

2.6.3. Drug synergy assays

Drug combination synergism was determined following the Chou-Talalay constant ratio method. In brief, PDX-derived single cells were plated in a 384-well plate at 1000 cells per well, in 35 µL. The following day each single agent was drugged in multiples of the IC_{50} concentration, at a constant ratio. Drugs were plated at 4x the desired dose in 17.5 µL. The single agents were drugged in a grid format (Figure 2-1). Cells were re-drugged on day 5 of the assay and cell viability was measured on day 10 via CTG.

Drug synergy was determined using the programme CompuSyn (Version 1) (Ting Chao Chou & Martin, 2005). Fractions affected (1-SF) for single agents, and the combination in constant ratios were analysed by the programme to determine the combination index (CI) values for each dose point. CI results were plotted against the fraction affected (Fa) and expressed using a line of best fit +/- SE.

		Drug A					
		0	0.25 x IC_{50}	0.5 x IC_{50}	IC_{50}	2 x IC_{50}	4 x IC_{50}
Drug B	0						
	0.25 x IC_{50}						
	0.5 x IC_{50}						
	IC_{50}						
	2 x IC_{50}						
	4 x IC_{50}						

Figure 2-1 Chou-Talalay combination assay plate layout.

Plate layout for constant ratio Chou-Talalay synergy analysis. Each drug is plated in constant ratios of the IC_{50} doses either vertically or horizontally. The single agent growth curves (the ascending concentration of one agent with the DMSO control of the other) were compared to the constant ratio addition of both drugs (the doses highlighted in green). The fraction affected (Fa) was plotted against the combination index (CI) calculated using CompuSyn (Version 1) (Chou & Martin, 2005).

2.7. Fixed sample processing

2.7.1. Processing of fixed PDX and tissue samples

Samples were fixed overnight in 10% formalin (at room temperature) or 4% PFA (at 4°C). Fixed samples were washed twice with PBS for 30 minutes. Samples were then dehydrated in graded ethanols, cleared of ethanol using histoclear, and embedded in paraffin wax heated to 60°C.

2.7.2. Organoid embedding

Each well was washed with PBS then fixed in 4% PFA for 20 minutes at room temperature. The Matrigel was broken up using a pipette and transferred to a 15 mL falcon tube. The organoids were washed once in PBS and twice in 0.2% TWEEN20. Prior to embedding, the organoids were washed twice in PBS and re-suspended in 50 µL Richard-Allan Scientific™ HistoGel™ (ThermoFisher Scientific) heated to 65°C and set on ice for 10-15 minutes. The set organoid-containing HistoGel discs were then loaded into embedding cassettes, and processed as the fixed PDX samples.

2.8. RNA analysis

2.8.1. RNA extraction

RNA was extracted following the RNeasy® mini kit (Qiagen). Firstly, samples were homogenised in RLT buffer with 40 mM Dithiothreitol (DTT). Cells grown in 2D were scraped and vortexed at room temperature for 30 seconds. To extract RNA from organoids, the Matrigel was disrupted by the RLT buffer and then shaken at room temperature for 30 minutes and vortexed to ensure the breakdown of Matrigel and lysis of the organoids. Snap frozen PDX samples were disrupted using the TissueRuptor II (Qiagen) for 30 seconds in RLT buffer. The kit protocol was followed according to the RNeasy® handbook and the resulting RNA was eluted in 30 µL.

2.8.2. cDNA synthesis

RNA concentration was determined using the Nanodrop Spectrophotometer (ThermoFisher Scientific). 500 ng of template RNA was used for cDNA synthesis following the SuperScript™ IV First-Strand cDNA Synthesis System User Guide (MAN0012442 Rev. B.0, Invitrogen). Briefly, total template RNA was primed with oligo $d(T)_{20}$. SuperScript™ IV Reverse Transcriptase was then added to synthesise the complementary DNA sequence at 55 °C. Ribonuclease inhibitor was added to the reaction mix to inhibit ribonuclease interference if contamination was present.

2.8.3. Reverse-transcription PCR

A standard 10 µL PCR reaction using 1 µL cDNA, Taq DNA polymerase (New England Biolabs) as per manufacturers protocol and primers from Table 2-6 was used. The amplification program comprised of a denaturation step at 95°C for 30 seconds followed by 29 amplification cycles of a denaturation step at 95°C for 15 seconds, an annealing step at the optimal temperature specific for the primer pair (Table 2-6) for 30 seconds, followed by an elongation step at 68°C for 30 seconds, and a final elongation step at 68°C for 5 minutes. All custom DNA oligos were ordered from Sigma. Amplicon PCR products were then separated by electrophoresis on a 2% agarose gel stained with ethidium bromide, and visualised under UV light.

Table 2-6 MYB/MYBL1/NFIB translocation primer pairs

Sample	MYB/MYBL1 (5'-3')	NFIB (5'-3')	Annealing temp. (°C)
SG0032	TACCCAACTGTTCACGCAGA	TTCAGAGGCACTGTGAGTGG	53
SG0036	CTCCAGTCATGTTCCATACCC	GAACCAAGCTAGCCCAGGTA	52
SG0037	CCCCAGCTATCAAAGGTCA	GAACCAAGCTAGCCCAGGTA	52
SG0069	AGCCACTTGCTTTCTTGGAA	GAACCAAGCTAGCCCAGGTA	52

2.8.4. Quantitative real-time PCR

Gene expression was analysed using 2x PowerUp SYBR green master mix (ThermoFisher Scientific). Following manufacturers instructions, cDNA was diluted 1 in 10, primers were designed to have a melting temperature of 60°C and were added to the cDNA/SYBR green mix at 500 nM (Table 2-7). The Applied Biosystems QuantStudio 6 Flex Real-Time PCR system (ThermoFisher Scientific) was used in standard cycling mode. The amplification program comprised of a denaturation step at 95°C for 2 minutes followed by 40 amplification cycles of a denaturation step at 95°C for 15 seconds, an annealing and elongation step at 60°C for 1 minute which was the annealing temperature for all qPCR primers. qPCR data was analysed using the comparative CT method ($\Delta\Delta$CT), with samples normalised to the relative housekeeping gene GAPDH values, and then to the untreated samples.

Table 2-7 Quantitative PCR primers

Target	Sequence
BCL2	Fwd: GAGTACCTGAACCGGCACCT Rev: GAAATCAAACAGCGGCCGCAT
BCL2L11	Fwd: GCTGTCTCGATCCTCCAGTG Rev: CCAATACGCCGCAACTCTTG
BIRC3	Fwd: GACACATGCAGCCCGCTTTA Rev: CCACCATCACAGCAAAAGCA
CDK6	Fwd: GGAGTGCCCACTGAAACCAT Rev: CGATGCACTACTCGGTGTGA
CDKN2A	Fwd: CAGCCGCTTCCTAGAAGACC Rev: CACGGGTCGGGTGAGAGT
EN1	Fwd: GCAACCCGGCTATCCTACTT Rev: GATGTAGCGGTTTGCCTGGA
FOS	Fwd: GCGTTGTGAAGACCATGACAG Rev: TATCAGTCAGCTCCCTCCTCC
GAPDH	Fwd: CTATAAATTGAGCCCGCAGCC Rev: GCGCCCAATACGACCAAATC
KI67	Fwd: GCAGCAAAACAGCCATCTGA Rev: TAGGTGTTCCTGGGCGTTTT
MYB	Fwd: TGTGGCAGATGCACCGAATA Rev: CACAAAGGCTGAACAGTGCC
MYB-NFIB SG0032	Fwd: TACCTAAAAACAGGTCCCTGGC Rev: CTACTCATGCCCTTGGGTGA
MYC	Fwd: GTCCTCGGATTCTCTGCTCT Rev: CTTGTTCCTCCTCAGAGTCGC
NOTCH1	Fwd: CGCACAAGGTGTCTTCCAGA Rev: CAGGATCAGTGGCGTCGTG
NTRK3	Fwd: AGGGAACAGCAATGGGAACG Rev: GACTGCGCCAGTTCTCTATGT
PRAME	Fwd: CTGGATCAGTTGCTCAGGCA Rev: ATGCATCACATCCCCTTCCG
SOX9	Fwd: AGACAGCCCCCTATCGACTT Rev: TCGTTGACATCGAAGGTCTCG
SOX10	Fwd: GCTGCTGAACGAAAGTGACA Rev: GTCTTTCTTGTGCTGCATACGG

2.9. Immunohistochemistry (IHC)

2.9.1. Sectioning

Formalin-fixed paraffin embedded (FFPE) PDX and mouse tissue, and organoids were sectioned to 4 µm thick on a microtome (Leica), and softened in a water bath heated to 40°C for 1 minute, to adhere when transferred to Polysine™ microscope slides (VWR). Slides were left to air-dry overnight before staining or storage.

2.9.2. Staining

In brief, following dewaxing, washing, and rehydration of the slides through histoclear and graded ethanols, sodium citrate buffer (10 mM sodium citrate, 0.05% Tween20, pH6) was used for antigen retrieval. Slides were subsequently treated with 3% hydrogen peroxide to block endogenous peroxidase. Slides were then blocked for 1 hour at room temperature in 10% sheep serum. Primary antibodies (Table 2-8) were applied to the slides in 1% sheep serum and left to incubate overnight at 4°C. Following washes in 0.2% PBTween20, the secondary conjugate antibodies were applied (ABC kit, Vector labs) following manufacturers instructions. Finally, the stain was visualised using 3,3'-diaminobenzidine (DAB) chromogen (Dako) and counterstained with Harris haematoxylin. Slides were dehydrated and mounted with cover glass using DPX mountant.

For all antibodies used, positive and negative tissue controls were simultaneously stained. These were adrenal or prostate tissue sections that had been previously tested within the laboratory. For the MYB antibody, SG0069 PDX tumour sections were used as the negative control. To control for endogenous tissue background signal, no primary antibody (secondary antibody only) controls were used.

2.9.3. Analysis

Slides were scanned using the NanoZoomer S210 (Hamamatsu). When quantification was required, 40x images from three different areas of each slide were taken. Positive cells were counted and expressed as a percentage of total cells for each image. The

percentage of positive cells from all three images were averaged for the mean positive count for each condition. Statistical analysis was conducted using a nested 1way ANOVA followed by Tukey's multiple comparisons test, comparing treated groups to the vehicle treated samples.

Table 2-8 Antibodies

Antibody	Supplier	Product no.	Use	Dilution	Host
Actin	Bethyl Laboratories	A300-485A	WB	1:2000	Rabbit
Aquaporin 5 (AQP5)	Alomone Labs	AQP-005	IHC	1:400	Rabbit
Caspase-3	Abcam	AB2303	IHC WB	1:100 1:1000	Rabbit
CK5	Covance	PRB-160p	IHC	1:200	Rabbit
CK8	Covance	MMS-162p	IHC	1:2000	Mouse
Engrailed-1 (EN1)	Abcam	AB70993	IHC	1:50	Rabbit
p-Histone H2A.X (Ser139)	Upstate	05-636	WB	1:1000	Mouse
MYB	Abcam	AB45150	IHC WB	1:200 1:1000	Rabbit
$P21^{WAF1/CIP1}$	Dako	M7202	WB	1:500	Mouse
TP63	SantaCruz	SC-8431	IHC	1:200	Mouse
RB	Abcam	AB181616	WB	1:1000	Rabbit
pRB S780	NEB	8180S	WB	1:1000	Rabbit
pRB Thr821	ThermoFisher Scientific	44-582G	WB	1:1000	Rabbit
RBP1 (RNA polymerase II)	New England Biolabs	2629S	WB	1:1000	Mouse
pRNPII S2	Abcam	AB5095	WB	1:1000	Rabbit
Smooth muscle actin (SMA)	Sigma	A2547	IHC	1:4000	Mouse

2.10. Protein analysis

2.10.1. Protein extraction

Protein was extracted using the lysis RIPA buffer (50 mM Tris-HCl, pH 8.0, with 150 mM sodium chloride, 1.0% Igepal CA-630 (NP-40), 0.5% sodium deoxycholate, and 0.1% sodium dodecyl sulfate, Sigma) and 100x protease and phosphatase inhibitor cocktail (New England Biolabs). Cells grown in 2D were scraped and lysis collected. To extract protein from organoids, the Matrigel was dissolved in Cell Recovery Solution (Corning)

for 15 minutes. The organoids were then centrifuged at 1500 rpm for 5 minutes, the Cell Recovery solution removed and the pellet resuspended in lysis buffer. Snap frozen PDX samples were disrupted using the TissueRuptor II (Qiagen) for 30 seconds in buffer. All samples were then shaken on ice for 30 minutes and then centrifuged at 10,000 rpm for 10 minutes at 4°C. The supernatant was then aliquoted and protein concentration determined via the Pierce BCA protein assay kit (ThermoFisher Scientific).

2.10.2. Western blot

To prepare the protein lysate, water was added to 15-30 µg of protein to the same total volumes. NuPage reducing agent was diluted 1 in 10 in NuPage sample buffer (ThermoFisher Scientific). This was added to each sample at a 1 in 4 dilution, and samples were heated for 10 minutes at 70°C. Samples were then briefly centrifuged and then were loaded on a 4-12% Bis-Tris Novel gel (ThermoFisher Scientific), placed in the electrophoresis tank in 1x MOPS buffer (ThermoFisher Scientific). Gels were run slowly, at 100V for 2 hours. Once finished, the protein bands were then transferred onto a nitrocellulose membrane at 100V for 90 minutes in transfer buffer (25 mM Tris, 200 mM methanol, 192 mM glycine, pH 8.3). Following protein transfer, the membranes were then blocked for one hour in 5% milk/TBST, and incubated in primary antibody in 2.5% milk/TBST overnight at 4°C (Table 2-8). The membranes were washed 3 times for 10 minutes in TBST and then incubated in the relevant secondary antibody diluted in 2.5% milk/TBST. Membranes were washed again and then visualised using Amersham™ ECL™ Prime western blotting detection reagent (GE Healthcare) and exposed using the Odyssey® FM Imaging system (Li-Cor).

For MYB staining via Western blot, the lysate from the cell line MOLT-4 (ALL) was used as a positive control to confirm expected band size as it is known to express high levels of c-MYB (data not shown).

2.10.3. Analysis

Western blots were analysed using ImageJ (1.52K). Band intensity of the protein of interest was normalised to that of the housekeeping loading control, actin. The normalised intensity for each condition was then normalised to that of the untreated

sample to give the fold change in protein expression due to conditions. Statistical analysis was conducted using a nested 1way ANOVA followed by Tukey's multiple comparisons test, comparing treated groups to the vehicle treated samples.

2.11. *In vivo* drug studies

2.11.1. Short term pilot combination study

SG0032 tumour fragments were implanted on the right flank of female 6-8-week-old CD1 nude mice. When tumours reached 200 mm^3, mice were allocated into the four treatment groups (n=3); vehicle, 55 mg/kg CYC065 (H_2O), 50 mg/kg JQ1 (10% DMSO, 10% hydroxypropyl-β-cyclodextrin), and the combination of both drugs. CYC065 was administered via oral gavage and JQ1 via intraperitoneal injection. Mice were treated for 5 days, and on the final day of treatment tumours were harvested 3 hours post treatment. Half the tumour was snap frozen for RNA and protein extraction, and half was fixed in 10% formalin for histological analysis.

2.11.2. Long term combination study

SG0032 tumour fragments were implanted on the right flank of female 6-8-week-old CD1 nude mice. When tumours reached 200 mm^3, mice were allocated into the four treatment groups (n=3); vehicle, 25 mg/kg CYC065 (H_2O), 20 mg/kg JQ1 (10% DMSO, 10% hydroxypropyl-β-cyclodextrin), and combination. Mice were treated for 5 days on, 2 days off for a total for 35 days. On the final day of treatment tumours were harvested 3 hours post treatment; half the tumour was snap frozen for RNA and protein extraction, and half was fixed in 10% formalin. PDX growth was expressed as percentage increase from the first day of drugging, and expressed as mean +/- SEM.

3. Patient samples and PDX establishment

3.1. Introduction

ACC is a rare cancer, with a reported incidence of 4.5 cases per 1 x 10^6, making therapeutic research challenging due to the lack of patient sample availability (Boneparte et al., 2008). PDXs are useful pre-clinical models for rare cancers such as ACC. Through serial passaging they provide larger quantities of tumour tissue for pre-clinical investigations that maintain tumour heterogeneity and key molecular features present in the original patient tumour. The Swain laboratory at the ICR received 11 ACC patient tumours from metastatic sites from The Royal Marsden Hospital, Chelsea, for PDX engraftment prior to the start of my studentship. The primary patient tumours were analysed using whole exome sequencing (WES) and RNA sequencing (RNAseq) to identify common mutations or differentially expressed genes (DEGs) that could be therapeutically targeted. In this chapter I will discuss these molecular features and the steps taken to confirm the derived PDX lines.

3.2. ACC patient samples

Anonymised patient information was supplied by The Royal Marsden Hospital on receipt of the biopsies to generate PDX models. Full patient information was received with histology reports for 10 of the 11 samples (Table 3-1). The histology report for sample SG0069 was not delivered.

All tumours were from metastatic sites, and of those with site information the majority of samples were from the lung, whereas SG0069 was from the nasal cavity. Where age at diagnosis was documented most patients were diagnosed between 40-60 years, although patient SG0036 was diagnosed particularly young at 23, mirroring the range of age reported in the literature. Lympho-vascular invasion was reported for three of 11 samples, whereas perineural invasion was documented for five, although these details

were not always reported therefore confirmed lack of invasion is documented in Table 3-1 as "N". Histology reports identified that all ACC samples had some degree of cribriform growth. SG0028 also had areas of tubular growth, whereas SG0026, 27, 35, 38 and 69 are potentially higher-grade ACC with solid areas. Although, as all samples are from metastatic sites, all cases are classified as advanced ACC.

Table 3-1 Patient sample information

Sample	Age at diagnosis	Sex	Site	Lympho-vascular invasion	Perineural invasion	Histology	PDX
SG0026				Y	Y	Solid, cribriform	
SG0027	48	F	Lung	-	Y	Solid, cribriform	Y
SG0028	42	M	Lung	-	-	Tubular, cribriform	Y
SG0031		M	Lung	-	-	Tubular, cribriform	
SG0032	58	F	Lung	-	-	Cribriform	Y
SG0035	45	F		Y	Y	Solid (40%), tubular, cribriform	
SG0036	23	M	Lung	Y	-	Cribriform	Y
SG0037	31	M	Lung	N	-	Cribriform	Y
SG0038		M		Y	-	Solid (15%), tubular, cribriform	
SG0066		F		N	Y	Solid, cribriform	
SG0069		F	Nasal cavity	-	Y	Appears solid	Y

3.2.1. Genomic analyses

All patient tumours were delivered with matched patient blood samples as “normal” patient tissue, and eight patient samples were analysed via WES and RNAseq. The ACC tumour reads were aligned to the reference genome GRCh37 and normalised to the matching blood sample to identify disease associated variants. Table 3-2 summarises key mutations identified from the WES. The most common aberrations are copy number variations. SG0036, 37 and 69 had a heterozygous deletion at 12q12-12q14.1, whereas SG0035 had a homozygous deletion at this region. This region corresponds to genes including *ARID2*, *SMARCD1* and *CDK4*. SG0032 had a heterozygous deletion at only 12q14.1, corresponding to *CDK4*. SG0069 had a homozygous deletion at 7p12-17p13.3 corresponding to the genes *MAP2K4*, *TP53* and *NCOR1*. SG0031 and 32 had an amplification at 4q12 corresponding to PDGFRA. SG0069 also possessed a *FGFR2* amplification which could potentially be therapeutically targeted.

Despite SG0036 having the highest somatic mutation rate of 3.1 per megabase of exonic region, no mutations were significant having low VAF tumour values compared to tumour purity for each patient sample. SG0027 had the most somatic mutations at a high VAF, including a potentially actionable mutation in *STAG2* with a VAF of 0.98 (tumour purity of 92%). SG0032 had a somatic mutation at a high VAF of 0.67 (tumour purity of 88%); a nonsynonymous mutation in *CREBBP*. Overall, there are few common targetable mutations between the ACC patient samples. WES data for all samples are attached in appendix 1 (Chapter 9.1).

The most common aberration is the *MYB-NFIB* genetic translocation, present in five of the eight ACC patient samples, with sample SG0069 possessing a translocation between *MYBL1* and *NFIB*. These translocations will be discussed in more detail later in this chapter (see 3.2.4).

Table 3-2 Summary of ACC sample WES results

		SG0027	SG0028	SG0031	SG0032	SG0035	SG0036	SG0037	SG0069
	MYB (fusion+)			+	+	+	+	+	L1
	Somatic mutation rate*	1.29	0.51	0.55	0.49	0.67	3.1	0.47	0.92
	6q24 loss								
	12q12-14 loss								
MAPK/PI3K-Akt/Ras signalling	DAXX								
	FGFR2								
	KDR								
	KIT								
	MAGI1								
	MAP2K4								
	PDGFRA								
	PIM1								
DNA repair	FANCE								
	TP53								
Cell cycle	CCND3								
	CDK4								
	STAG2								
Transcription	BIRC3								
	CREBBP								
	ELF4								
	NCOR1								
	TFEB								
	WDR45								
Chromosome associated proteins	ARID2								
	BCOR								
	BRD1								
	CEP135								
	HMGA1								
	SMARCD1								
Cytoskeletal signalling	COL2A1								
	FLNB								
	KTN1								

* (/Mb exonic region)

Nonsynonymous
Frame shift
Stop gained
High level amplification
Homozygous deletion
Heterozygous deletion

Variants were called using the GATK best practice pipeline (V2) from Broad Institute using standard settings. All somatic mutations were annotated using the snpEff (http://snpeff.sourceforge.net/) which provides information on genes affected by mutations and the likely consequences for the encoded gene products, such as synonymous, non-synonymous, stop gained. Somatic mutations found in Cosmic and Cancer Gene Census (CGC) were highlighted. ASCAT software was used to

determine tumour purity, allele-specific ploidy and to identify copy number aberrations. CNV were identified using a genome wide approach.

3.2.2. Transcriptomic analyses normalised to normal salivary glands

RNAseq was conducted for all ACC patient samples and reads were mapped to the GRCh37. As I did not have access to normal human salivary gland tissue, I normalised the ACC samples to the raw reads of five published normal SG samples sequenced by Bell et al (Bell et al., 2016). Both Bell and the TPU at the ICR used the HiSeq 2500 system (Illumina) therefore the published normal SG data was somewhat comparable.

Up- and downregulated DEGs are depicted in a volcano plot (Figure 3-1A). There are 1063 significantly upregulated DEGs and 1121 significantly downregulated DEGs (Log2 fold change < -2 or > 2, $P < 0.01$). It is highlighted that *MYB* is significantly upregulated compared to the published normal salivary glands by 5.97 Log2 fold (Padj = 1.23E-24). KEGG pathway analysis of both up- and downregulated DEGs identified associated pathways that are significantly different ($P < 0.05$) (Figure 3-1B and C). Pathways upregulated in the ACC samples compared to normal SG included a number of cancer associated pathways, transcriptional misregulation, Wnt signalling and DNA replication. Interestingly, genes associated with the pathways viral carcinogenesis and HPV infection are also significantly upregulated. The pathway most significantly downregulated in ACC compared to normal SG was salivary secretion ($P < 0.00001$). Other pathways downregulated include retinol metabolism, serotonergic synapse and choline metabolism in cancer. The full list of KEGG pathways and associated genes differentially expressed in ACC when normalised to the published normal SG samples is provided in appendix 2 (Chapter 9.2).

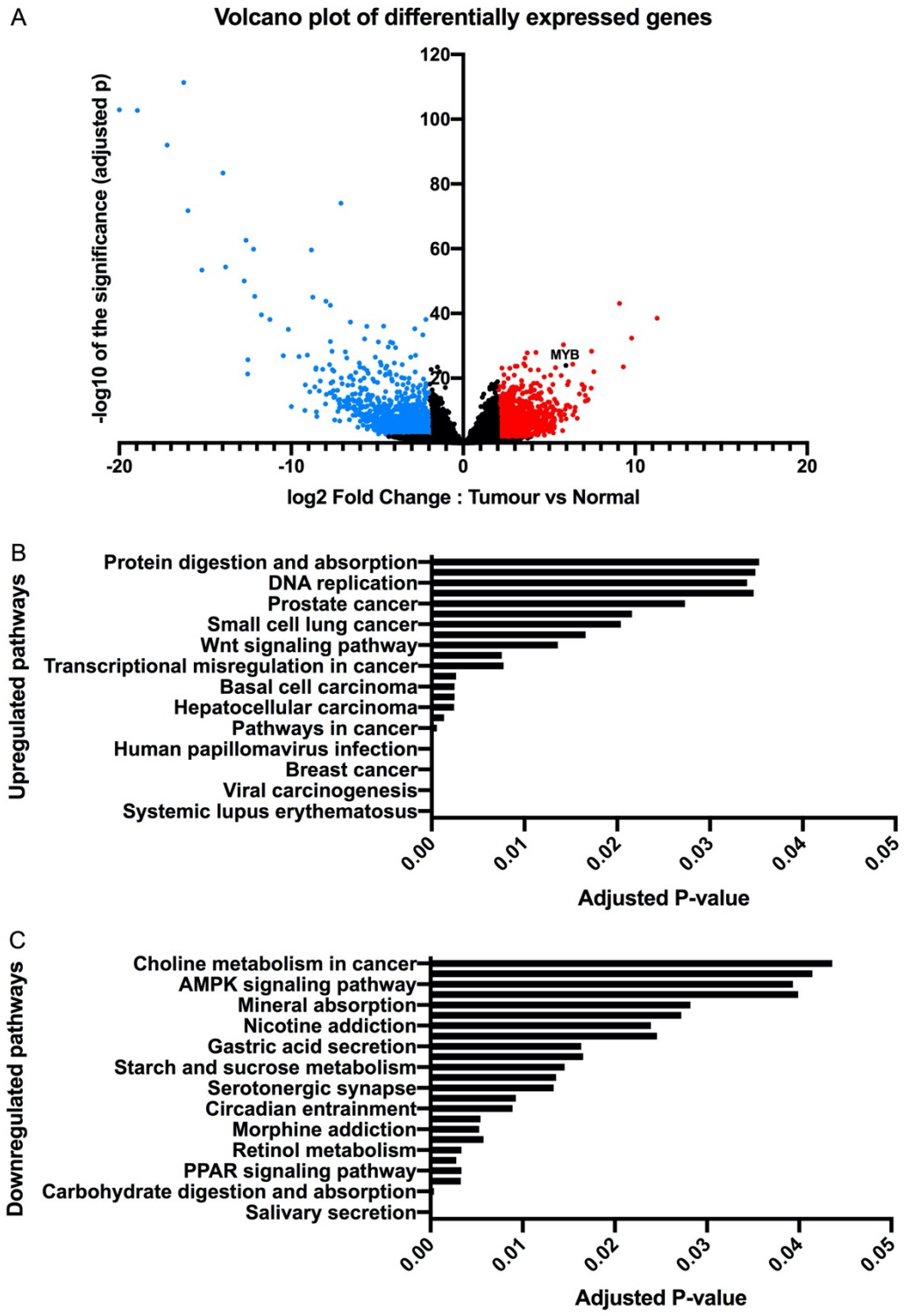

Figure 3-1 RNAseq summary of ACC patient samples normalised to normal salivary gland

A) Volcano plot of all up- and down- differentially expressed genes (DEGS) in ACC patient samples compared to the published normal salivary gland samples. Significantly up- and downregulated DEGS are highlighted in red and blue respectively (Log2 fold change < -2 or > 2, P < 0.01). Significantly upregulated (B) and downregulated (C) KEGG pathways according to significant DEGs, P < 0.05.

3.2.3. Transcriptomic analyses normalised to a non-ACC tumour

In addition to normalising the ACC RNAseq data to the published normal SG data, each ACC sample was individually normalised to a non-ACC SG tumour sample, SG0043, also received from The Royal Marsden. This sample was acinic cell carcinoma. It is important to note that high MYB expression is not a hallmark of this cancer subtype (S. Zhu et al., 2015). This was conducted to identify ACC-specific differences compared to another salivary gland cancer subtype. Key upregulated DEGs compared to SG0043 are listed in Table 3-3 and grouped in terms of associated pathway. SG0027 and 28 did not have *MYB* translocations but had high *MYB* expression via an alternative mechanism, having Log2 fold change values of 3.1 when normalised to SG0043, higher than samples SG0031-37 that possessed the translocation. SG0069 had upregulated *MYBL1* which corresponds to possessing the *MYBL1-NFIB* translocation. *FGFR2* expression was 5.293 Log2 fold higher in SG0069 than SG0043, due to the amplification detected by WES.

Genes associated with epigenetic and transcriptional regulation, DNA damage, cell cycle and neural factors were highly expressed in the ACC samples compared to SG0043. In addition, there were particularly a high number of upregulated genes associated with Wnt signalling, which was also a significantly upregulated pathway when normalised to the normal SGs. The full list of KEGG pathways and associated genes upregulated in ACC when normalised to SG0043 is provided in appendix 3 (Chapter 9.3).

Table 3-3 Heat map of key differentially expressed genes in the ACC patient samples normalised to SG0043

Pathway	Gene	SG0027	SG0028	SG0031	SG0032	SG0035	SG0036	SG0037	SG0069
MYB/MYC	MYB	3.129	3.172	2.196	2.756	2.711	2.431	2.433	-0.243
	MYBL1	-1.418	-1.491	-0.938	-0.596	-0.339	-1.115	-1.293	2.718
	MYCL1	3.326	2.258	2.154	1.575	2.748	1.914	1.923	2.090
	MYCN	2.212	1.189	3.463	2.076	1.831	2.155	3.068	1.114
Epigenetic/ transcriptional regulation	EN1	4.710	3.994	4.241	3.867	4.938	4.460	4.528	3.920
	ARID5B	2.816	2.847	2.271	2.729	2.385	2.154	1.883	1.948
	HIST1H4D	4.077	4.993	3.898	2.972	4.317	3.248	1.961	3.828
	HIST1H4F	4.631	5.378	3.416	2.666	2.709	3.633	2.179	3.860
	RUNX1	3.027	3.028	3.618	3.550	3.00	3.925	3.961	2.497
	TP63	5.247	4.261	4.758	5.484	3.657	4.530	4.245	2.533
DNA damage	KANK4	5.546	3.214	4.075	2.961	3.900	3.166	5.651	2.284
EGF/FGF/IGF/PI3K signalling	EGFR	2.786	3.173	2.491	2.866	1.609	2.621	2.690	0.890
	FGF2	5.058	4.264	2.563	4.225	2.898	3.764	2.570	0.677
	FGFR2	2.099	1.386	1.927	1.451	2.305	1.501	1.378	5.293
	IGF2	6.237	5.799	1.290	3.299	4.635	5.480	5.851	1.853
	MET	2.833	3.484	2.935	3.983	2.299	2.783	2.565	0.998
	PIK3CD	2.741	0.392	2.339	2.281	1.748	1.484	2.590	3.158
Wnt signalling	DKK1	3.869	5.520	1.232	1.642	3.731	2.351	1.121	3.511
	FZD1	3.546	3.234	1.850	2.351	2.297	2.626	2.344	1.461
	LEF1	3.117	2.680	3.058	2.648	2.728	2.824	2.536	2.743
	MMP7	3.274	4.988	4.388	0.900	3.360	6.044	4.896	3.796
	WNT3A	4.233	3.090	3.790	3.547	1.929	3.037	3.171	-0.090
	WNT5B	4.793	4.522	4.608	3.271	2.164	4.511	4.346	2.130
	WNT6	3.809	2.736	3.016	1.978	2.793	2.787	3.231	1.249
Axonal guidance/ neural signalling	EPHA4	3.654	3.201	3.195	2.791	2.739	3.074	2.867	1.578
	EPHA7	3.066	3.015	2.378	2.557	3.504	1.461	1.653	2.122
	NTRK2	6.098	3.742	2.549	2.302	2.567	1.246	2.757	3.146
	NTRK3	4.172	4.657	4.348	4.669	4.184	5.352	5.656	1.648
	SEMA3A	3.029	3.520	4.758	5.657	4.058	4.434	4.632	1.566
	SLITRK6	2.928	4.768	4.257	6.769	3.624	3.637	3.035	3.456
	VIT	3.526	3.786	5.298	5.697	4.714	4.808	4.345	2.086
Cell cycle	CDK6	2.322	2.991	2.818	2.453	2.910	2.245	2.198	2.632
	GADD45B	2.642	2.810	2.220	1.962	3.310	2.832	2.720	2.706
	SFN	4.280	1.775	3.164	0.582	0.507	3.833	2.821	-0.319
Cytoskeletal signalling	ICAM5	3.324	2.965	0.722	2.484	0.420	0.056	3.038	0.996
	KRT5	5.072	5.200	5.329	4.303	3.206	5.570	5.065	2.395
	KRT17	4.741	5.355	4.598	4.023	4.412	5.065	4.739	2.851
	PDPM	5.207	3.266	3.965	4.303	3.016	4.438	3.708	0.564

3.2.4. MYB

As discussed in Chapter 1.4.2, overexpression of the oncogenes *MYB* and *MYBL1* are the most frequent genetic alterations associated with ACC. The most common mechanism of *MYB* activation is the *MYB-NFIB* t(6;9) (6q22-23; 9p23-24) translocation. RNAseq identified that five of the ACC samples had *MYB-NFIB* translocations, and that SG0069 had a *MYBL1-NFIB* translocation (Table 3-2). The site of the *MYB* breakpoint differed between each sample, whereas the *NFIB* breakpoint was at the same site in four of the samples (Figure 3-2A). WES detected that SG0035 had two *MYB* breakpoints that fused at the same *NFIB* breakpoint. The translocation in all samples resulted in a deletion at the MYB/MYBL1 C-terminal NRD as depicted by the schematics of the fusion proteins for each sample (Figure 3-2B). All samples except SG0032 expressed the c-terminal of NFIB, this is because the *NFIB* breakpoint in SG0032 was in the 3'UTR so no protein was transcribed.

SG0027 and 28 had high MYB expression via an alternative method of activation. This was identified by RNAseq, having high MYB expression compared to SG0043 and a high number of raw reads. When all samples were analysed to form a sample-by-sample cluster plot, the samples most similar had the same methods of *MYB/MYBL1* activation indicating similar transcriptional programmes are activated (Figure 3-3). SG0027 and 28 clustered together, and SG0031-37 closely clustered. The SG0069 expression profile was more closely related to those of SG0027 and 28 than SG0031-37.

A

Sample	MYB/MYBL1 breakpoint	NFIB breakpoint (Chr 9)	MYB/MYBL1-NFIB fusion transcripts
SG0031	Chr6:135517140	14102509	MYB exon 9-NFIB exon 11
SG0032	Chr6:135524462	14084728	MYB exon 15 (NFIB translocation site in 3'UTR)
SG0035	Chr6:135520188 Chr6:135521553	14088325 14088325	MYB exon 10-NFIB exon 10 MYB exon 12-NFIB exon 10
SG0036	Chr6:135515598	14102509	MYB exon 8- NFIB exon 11
SG0037	Chr6:135521553	14102509	MYB exon 12-NFIB exon 11
SG0069	Chr8:67478919	14102509	MYBL1 exon 14-NFIB exon 11

B

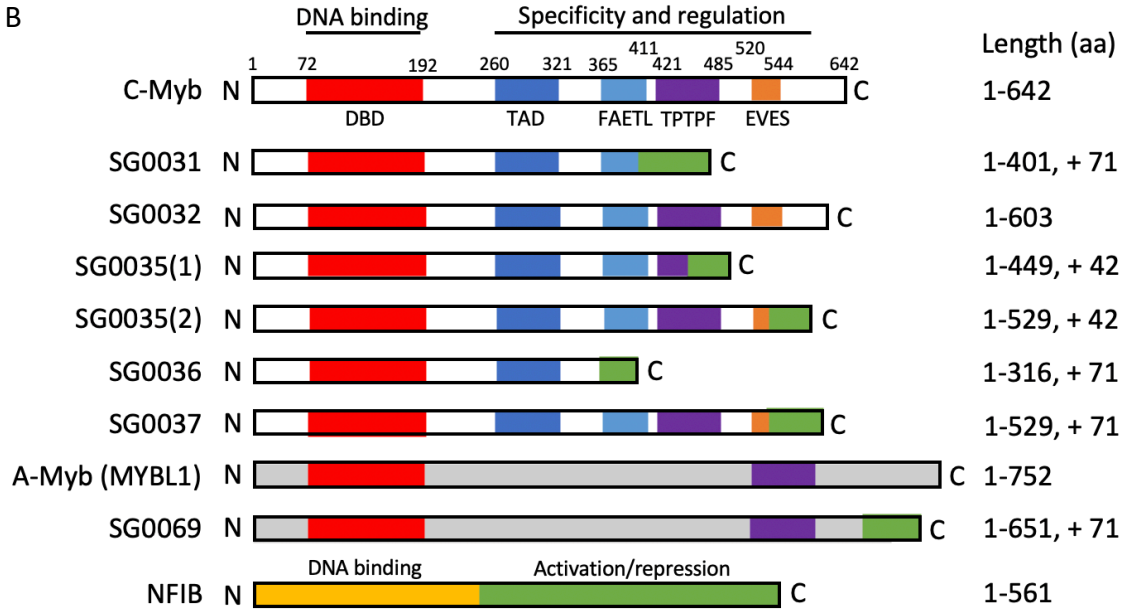

Figure 3-2 ACC patient sample MYB/MYBL1-NFIB translocations

A) A table to show the exact breakpoints in *MYB/MYBL1* and *NFIB* for each sample identified by WES, and the resulting fusion transcript, mapped to GRCh37. B) Diagrams to show the normal forms of MYB, MYBL1, and NFIB protein, and the fusion proteins for each sample, depicted N-terminal to C-terminal. Conserved domains are coloured: DNA binding domain (DBD) in red, transcriptional activation domain (TAD) in dark blue, the transformation domain (FAETL) in light blue, and negative regulatory domains (TPTPF and EVES) in purple and orange respectively. The numbers above the C-MYB plot indicate the amino acid (aa) residues as well as the protein full length in aa in the column on the right. MYBL1 has a DBD and TPTPF as indicated, and NFIB has an N-terminal DBD and a C-terminal TAD. The normal forms of C-MYB and A-MYB have been adapted from (O. L. George & Ness, 2014). The fusion proteins for each ACC sample are depicted with the total length of MYB/MYBL1

indicated in the right-hand column, plus the additional length of NFIB. This has been adapted from (Brayer et al., 2016) to present the ACC patient samples collected in this study.

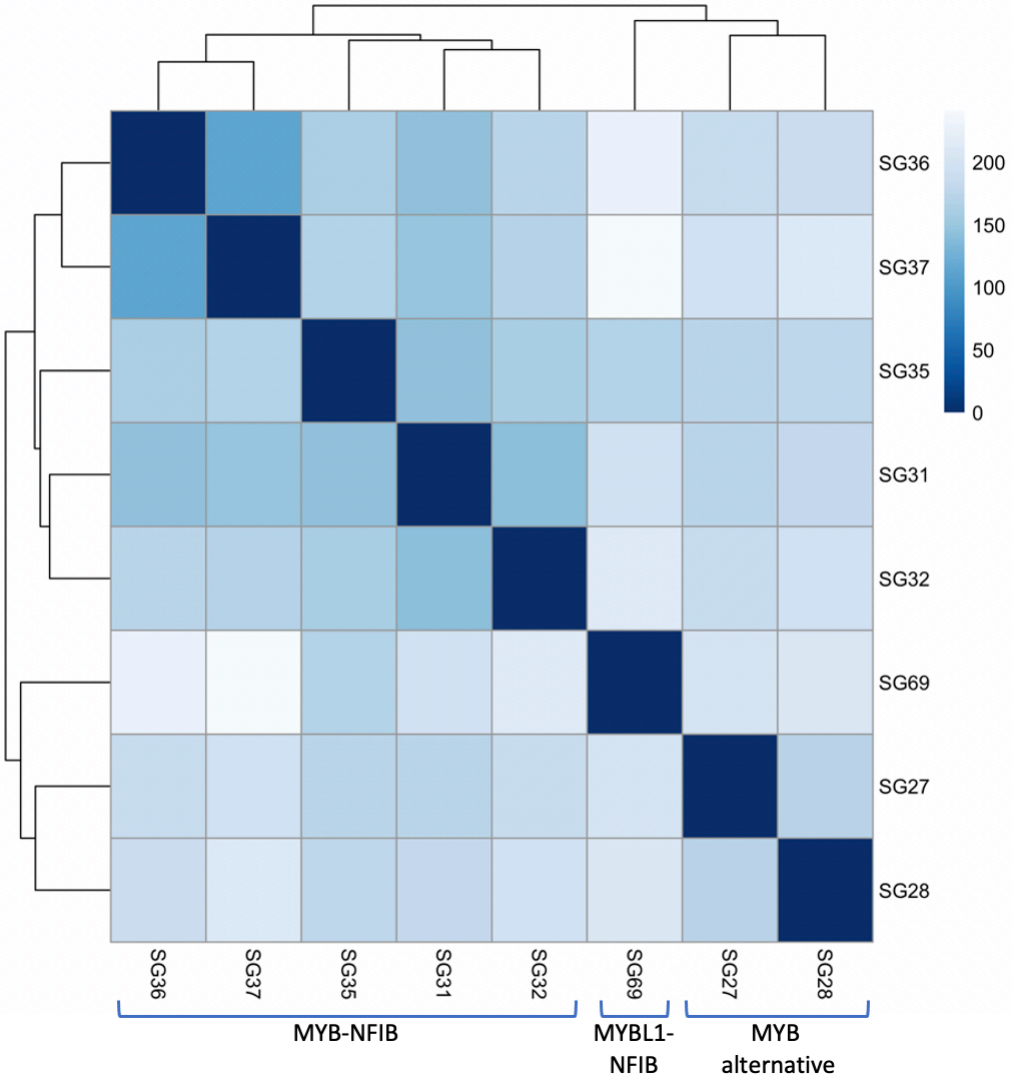

Figure 3-3 ACC patient sample cluster plot

A cluster plot to show the distances in similarity between each patient ACC sample based on RNAseq data. Distances were calculated by the euclidean method. The lower the distance (darker shade of blue), the more similar the samples. The samples with the same mechanism of MYB activation have the most similar transcriptional profiles.

3.3. PDX establishment

Initially, the patient samples were engrafted subcutaneously as tumour fragments to generate PDXs and of the 11 samples implanted, 6 successfully formed PDX lines (Table 3-1). These lines were SG0027, 28, 32, 36, 37 and 69. The time from engraftment to passage, when the tumours reached 1000 mm^3, ranged from 5 to 12 months with SG0032 being the fastest growing tumour and SG0069 the slowest (Figure 3-4). Growth rate remained consistent for each line at each subsequent passage, with a variance of +/- one month.

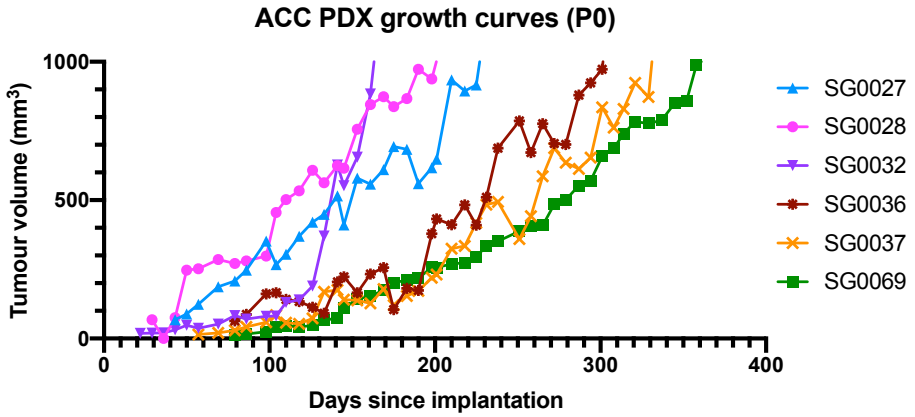

Figure 3-4 ACC PDX Passage 0 growth curves

Growth curves of successful ACC PDX lines at Passage 0, from day of ACC patient sample implantation in CD1 (Crl:CD1-Foxn1nu) nude mice. Curves represent data for the volume of one tumour on one flank of one mouse, but are representative of the growth of other tumours derived from the same patient sample in other mice. Tumours were passaged when they exceeded 1000 mm^3. Measurements were taken twice a week, and volume calculated as (width2 x length)/2.

3.3.1. Histological confirmation of PDX lines

Histological analysis of each PDX sample was performed via haematoxylin and eosin (H&E) staining and IHC analyses of cell types present. Samples were found to match the reported histological growth pattern of the corresponding patient tumour sample. Small areas of solid growth were observed in SG0027, although the majority of the tumour had cribriform growth (Figure 3-5). SG0028 had a mix of tubular and cribriform growth whereas SG0032, 36 and 37 all had a clear cribriform growth pattern. Although a

histological report for SG0069 was missing, the PDX appeared to have completely solid growth.

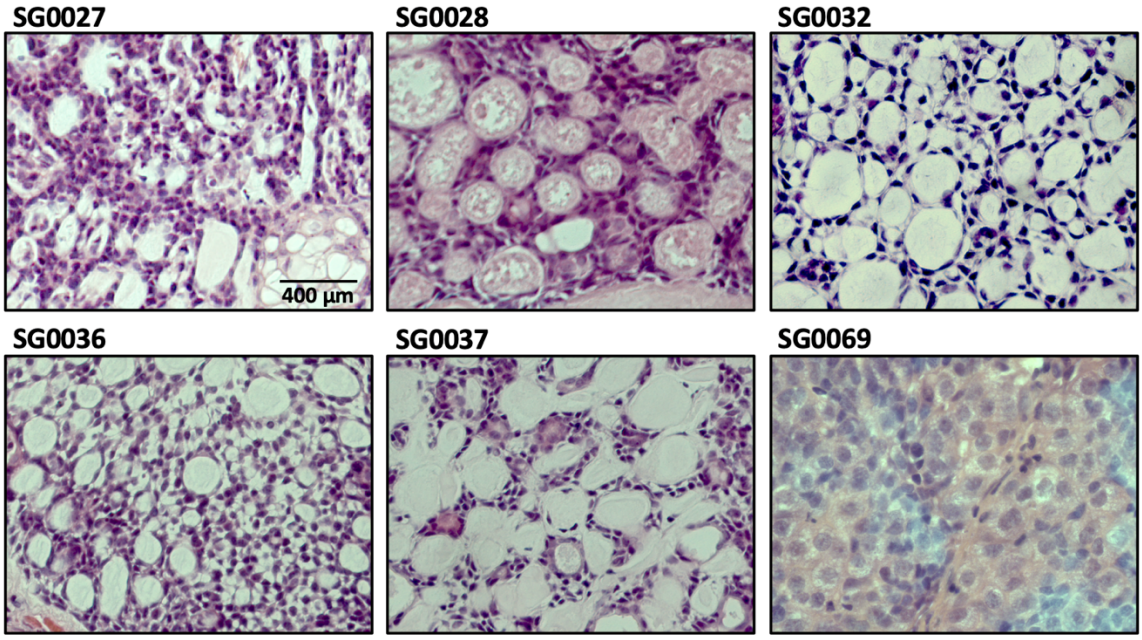

Figure 3-5 Histological analysis of ACC PDX lines

H&E staining of 4 µm thick sections of each ACC formalin-fixed paraffin-embedded (FFPE) samples. Passage numbers are as follows: SG0027 P3, SG0028 P4, SG0032 P3, SG0036 P2, SG0037 P1, SG0069 P2. H&E staining was performed on tumours from all passages for each line and images shown are representative. Slides were imaged at 20x magnification. Scale bar = 400 µm.

To identify the cell types present in each PDX, I conducted IHC for the luminal marker cytokeratin 8 (CK8), basal markers cytokeratin 5 (CK5) and TP63, and the myoepithelial marker α-smooth muscle actin (SMA) (Figure 3-6). TP63 can also stain positively in myoepithelial cells. Both CK5 and 8 are expressed in the cytoplasm, TP63 is nuclear, whereas SMA is usually cytoplasmic however can occasionally be expressed in the nuclear membrane (S. Zhu et al., 2015). CK5 expression correlates with the RNAseq data normalised to SG0043, being highly expressed in almost all cells in SG0036 and lowest in SG0027 and 69 (Table 3-3). In addition, TP63 expression also correlates with the RNAseq data, being the most strongly expressed in SG0027 and 37, and the least in SG0069. SG0028 has strong positive staining for CK8 and TP63. SG0028, 32, 36, and 37 has positive TP63 and SMA myoepithelial cells surrounding the pseudocysts, a feature associated with the cribriform growth pattern. SG0069 having low expression of the

basal markers CK5 and TP63, correlates with its solid growth pattern which is reported to have fewer basal cells and a higher proportion of luminal cells, as seen by stronger cytoplasmic CK8 staining. Strong SMA staining in SG0069 indicates the presence of myoepithelial cells, however the staining appears to be nuclear which is different to all other samples.

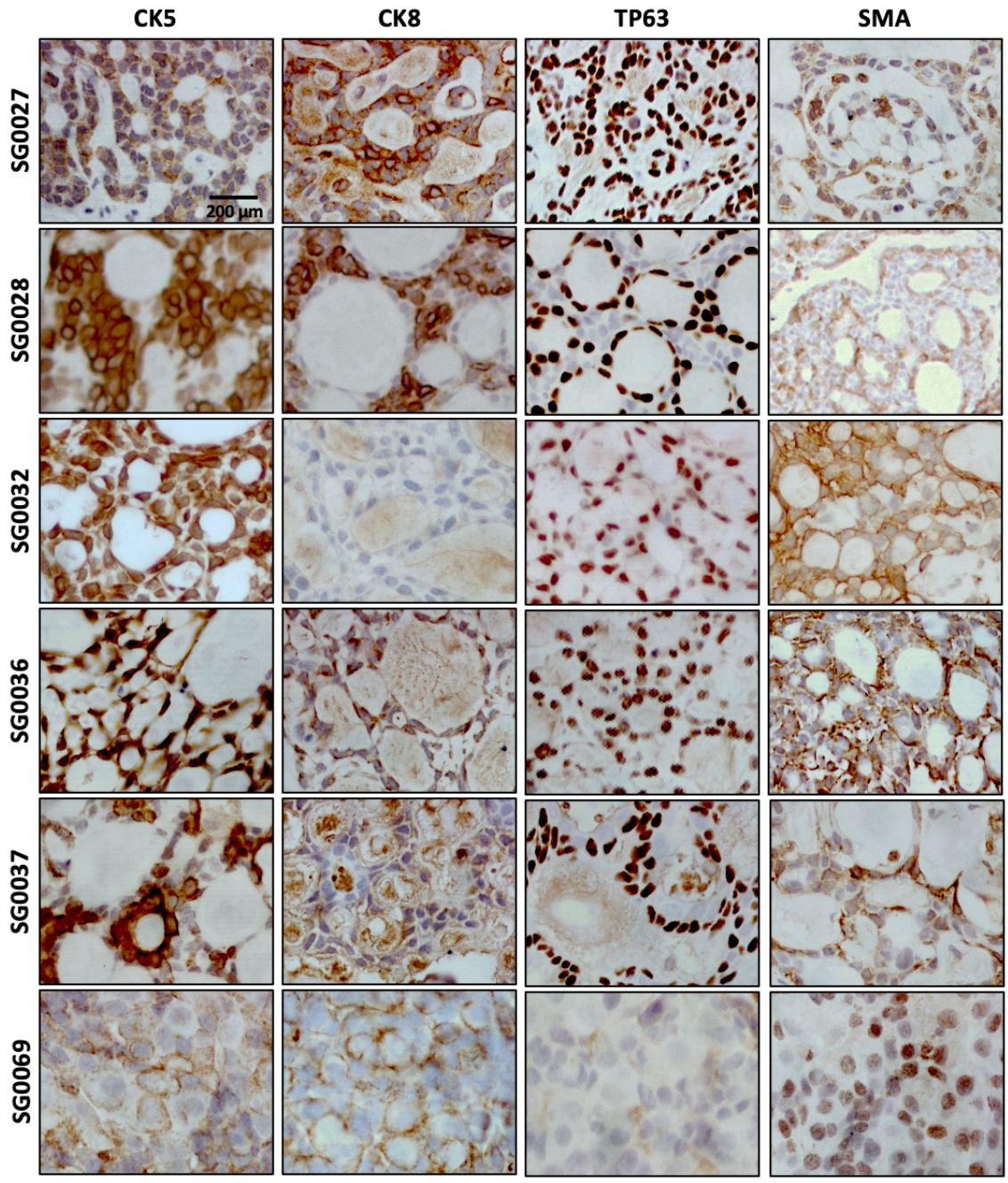

Figure 3-6 Cell type analysis of ACC PDX lines

IHC staining of 4 µm thick sections of each ACC PDX FFPE sample. Cytokeratin 8 (CK8) is a marker for luminal cells, cytokeratin 5 (CK5) and TP63 are basal cell markers, and α-smooth muscle actin (SMA)

is a myoepithelial cell marker. Antibody signal was amplified via DAB and counterstained using Harris haematoxylin. All slides for each antibody were stained in parallel to allow comparison of staining intensity. Tumours from three different passages (chosen at random between P1-P5) were stained for each marker and images are representative for each line as IHC phenotype was maintained through serial passaging of the tumours. Slides were imaged at 40x magnification. Scale bar = 200 µm.

IHC staining identified that PDX MYB expression correlates with the levels identified in the patient tumours via RNAseq (Figure 3-7). It is highly expressed in samples SG0032, 36, and 37 that possess the *MYB-NFIB* translocation, and also high in samples SG0027 and 28 that have high MYB via an alternative mechanism. In agreement with the RNAseq analysis, MYB expression is lowest in SG0069 that harbours the *MYBL1-NFIB* translocation.

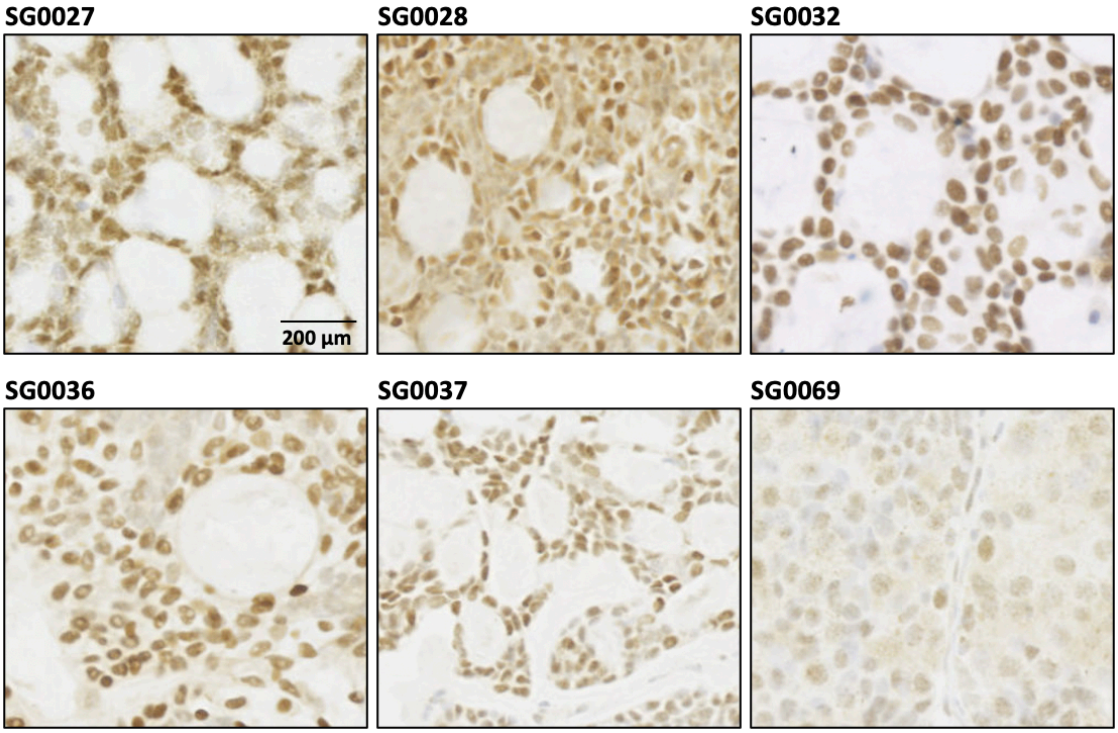

Figure 3-7 MYB staining of PDX sections

IHC staining for MYB on 4 µm thick sections of each ACC FFPE sample. Antibody signal was amplified via DAB and counterstained using Harris haematoxylin. MYB staining was performed on tumours from three passages for each line and images are representative. Slides were imaged at 40x magnification. Scale bar = 200 µm.

3.3.2. Molecular confirmation of PDX lines

MYB/MYBL1-NFIB translocations

As well as histological confirmation based on growth pattern, I also confirmed PDX lines via RT-PCR. Firstly, I confirmed that all samples were of human origin and not spontaneous mouse tumours using primers for human β-actin (Figure 3-8C). For samples with *MYB/MYBL1-NFIB* translocations, I confirmed the lines were derived from the correct patient tumour by designing primers for the *MYB-NFIB* or *MYBL1-NFIB* breakpoints. Each patient sample with a translocation had breakpoints at differing sites (Figure 3-2A). All SG0069 samples at different passages (P) were the correct sample, having clear bands visible (Figure 3-8B). The double band is a SG0069 specific product as it is not visible in the other samples.

The initial SG0032 and 37 samples tested were also correct. However, SG0036 P3 and P6 were not positive for the translocation which was faintly seen in P1, therefore, they were not the same sample (Figure 3-8A). I then ran the PCR using the same passage samples with both the SG0036 fusion primers and SG0032 (Figure 3-9A). This identified that there has been a cross-over of SG0032 and 36 between passage 1 and 3 as both SG0036 P3 and P6 samples were positive for the SG0032 translocation. By testing more samples at different passages, I was able to identify at which passage the cross-over occurred (Figure 3-9B-F). SG0032 P4 (mouse identification number (i.d) 5616)) had been crossed with SG0036 P2 (mouse i.d. 5617) whilst being housed at St George's, University of London. This simple RT-PCR identification method enabled me to continue the passage of these lines and to relabel drug-sensitivity assays conducted previously with these samples.

Patient sample mutations

PDX lines were also validated by confirming selected somatic mutations with a high VAF, or germline mutations where the mutation was at a higher VAF than the matching normal sample, chosen from the WES data of the patient samples. This was particularly essential for SG0027 and SG0028 line confirmation as they do not possess and *MYB/MYBL1-NFIB* translocation. Two mutations were chosen for each line, and confirmed in PDX passage 2 (Figure 3-10). In the PCR product sequencing analysis,

mutations occurring at a tumour VAF of over 0.9 had a single base peak at the mutation site (such as the SG0028 somatic mutation in BRD1), whereas mutations occurring at a tumour VAF of around 0.5 indicates a heterozygous mutation so double peaks representing both alleles were detected at the mutation site (such as the SG0036 somatic mutations in FGA and HIP1).

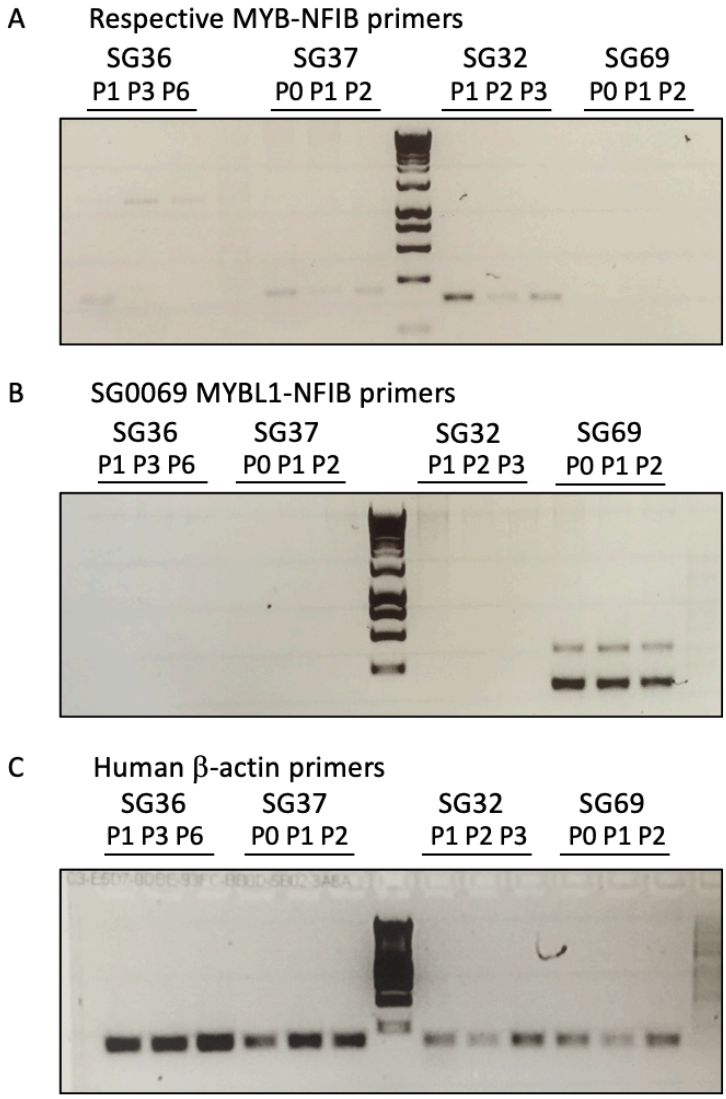

Figure 3-8 PDX line confirmation by MYB/MYBL1-NFIB translocation detection

Ethidium bromide-stained 2% agarose gel images of RT-PCR products. A) SG0036, 37 and 32 samples at different passages amplified with the respective *MYB-NFIB* breakpoint primers. SG0069 was used a negative control, amplified using the SG0032 *MYB-NFIB* breakpoint primers. SG0036 is lacking the fusion PCR product for P3 and P6. The correct bands are observed for SG0037 and SG0032 samples. B) All samples were amplified using the primers designed for the SG0069 *MYBL1-NFIB* breakpoint. C)

All samples were amplified using human ß-actin primers, a mouse adrenal negative control is included in the right-hand lane.

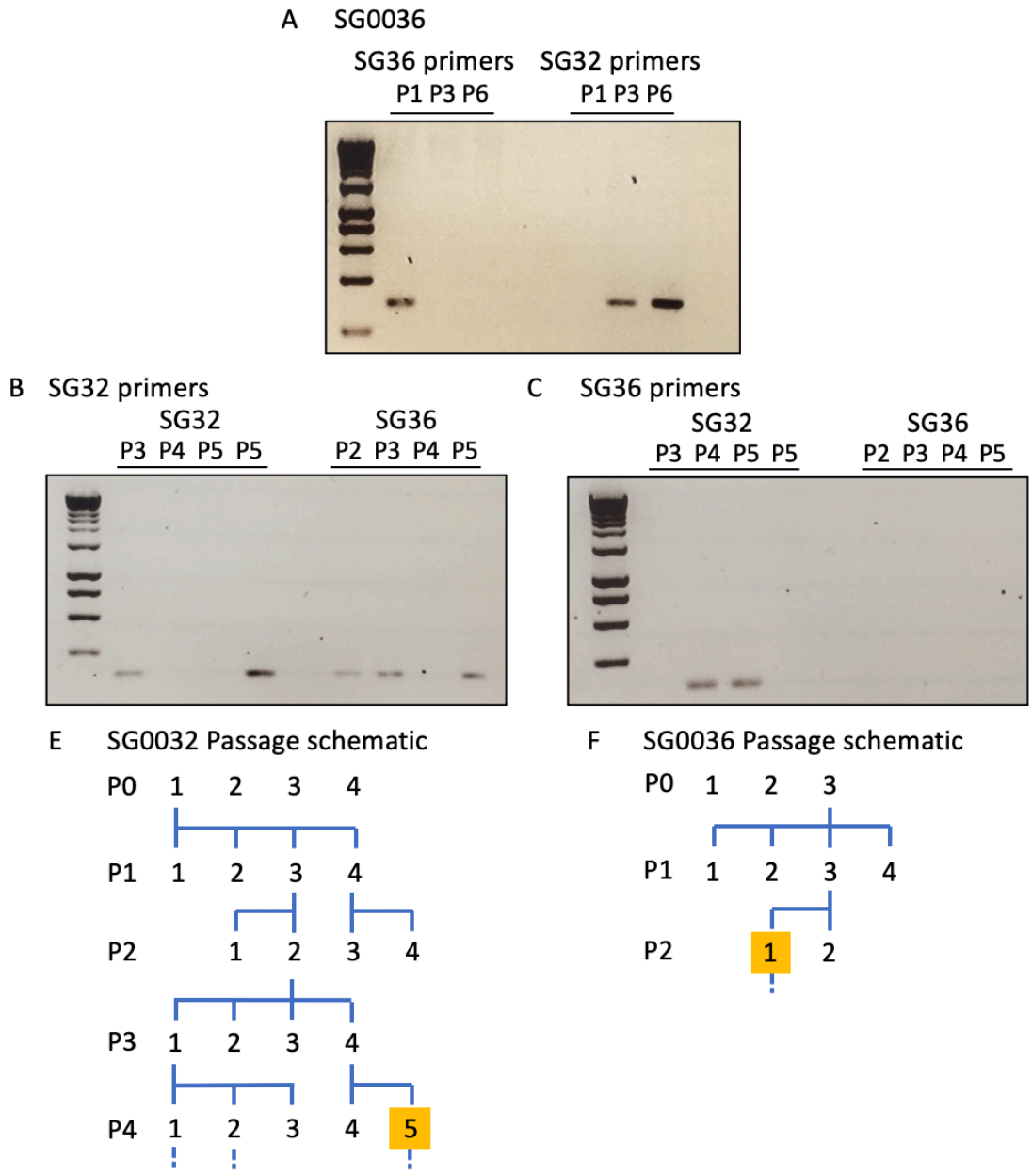

Figure 3-9 SG0032 and 36 PDX origin investigation

Ethidium bromide-stained gel images of RT-PCR products. A) SG0036 samples were amplified using both SG0032 and SG0036 *MYB-NFIB* breakpoint primers. PCR products are seen with SG0032 primers for P3 and P6 indicating there is a cross over in sample between P1 and P3 of SG0036. SG0032 and 36 samples from different passage numbers were amplified with both SG0032 (B) and SG0036 (C) breakpoint primers. Passage schematics for SG0032 (E) and SG0036 (F) indicate at which stage the sample cross over occurred; at P4 for SG0032 and P2 for SG0036.

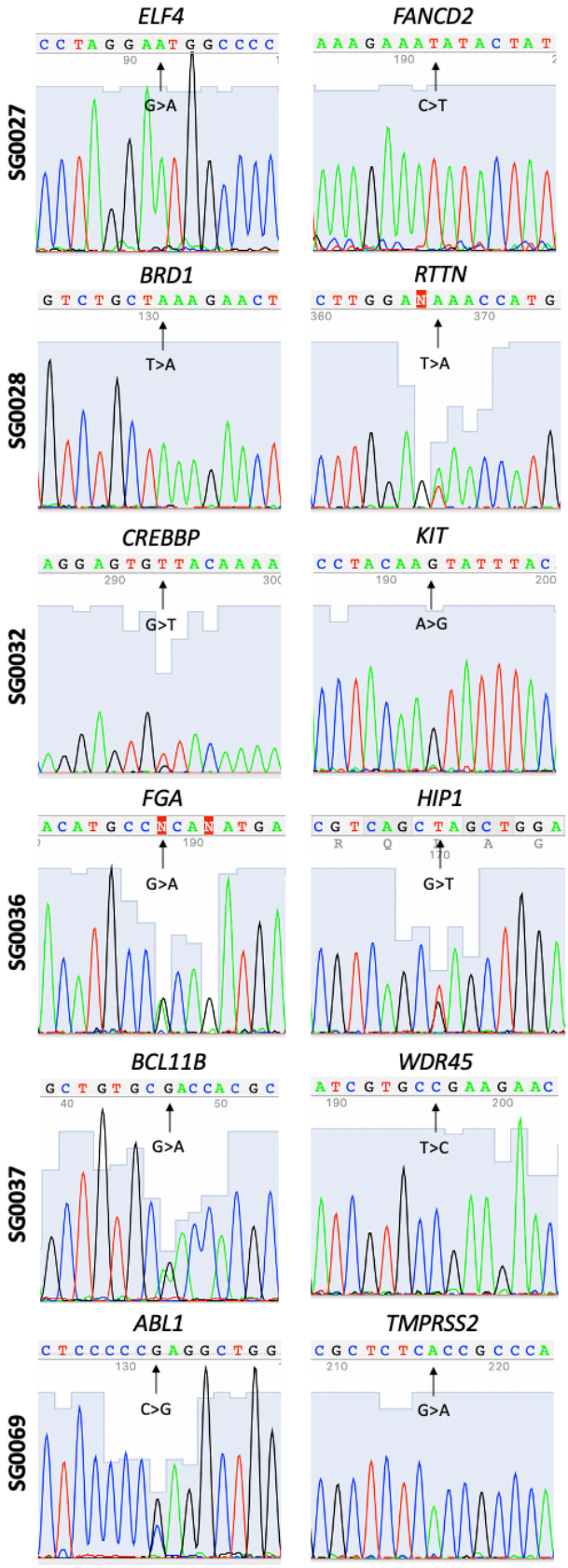

Figure 3-10 PDX line confirmation by mutation analysis

DNA was extracted from snap frozen tumours at P2 for each PDX line and PCR products were Sanger sequenced. The mutations were visualised using 4Peaks software (Nucleobytes B.V.) by comparing

to control sequences, from the PDX lines that were derived from different patient samples that lacked the mutation. Single peaks at the site of mutation indicate a homozygous mutation, whereas double peaks indicate a heterozygous mutation showing both alleles.

3.3.3. Orthotopic engraftment

In addition to the subcutaneous PDX models, I investigated how implanting the tumour samples orthotopically into the base of the submandibular gland would affect growth and integration into the surrounding tissues. I implanted SG0032 PDX tumour fragments into two CD1 nude mice. The PDX line SG0032 was chosen as it was the fastest growing line. Mice were monitored closely to ensure tumour growth did not reach a size limiting mouse mobility. When the tumours and attaching submandibular glands were harvested, the lungs and liver were also dissected and fixed for histological analysis.

Of the two mice implanted with SG0032 tumour fragments, only one mouse grew a tumour and it was harvested at a size of 432 mm^3, 6 months after implantation. FFPE tumour and submandibular gland sections were stained with MYB via IHC to identify tumour tissue (Figure 3-11). The tumour was MYB positive and there was no evidence invasion into the surrounding tissue or upper part of the submandibular gland which was negative for MYB, being localised to the implantation site.

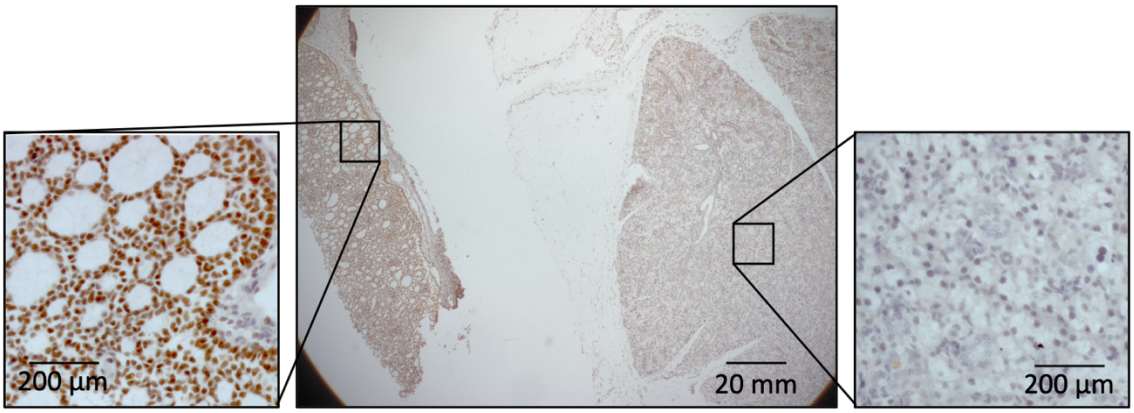

Figure 3-11 SG0032 orthotopic submandibular gland PDX engraftment

MYB IHC staining of FFPE SG0032 implanted submandibular gland. The main image is taken at a 1.6x magnification, scale bar = 20 mm. The enlarged images of highlighted areas are taken at 40x magnification, scale bars = 200 µm.

3.4. Discussion

ACC translational research has been greatly hindered by two main problems; the lack of validated pre-clinical models, and limited patient sample availability due to being an orphan disease. PDX models are a useful tool to address both of these issues, and here I have proven the successful generation and establishment of six ACC PDX lines that histologically and molecularly recapitulate the patient tumour. Furthermore, eight ACC metastatic patient samples were analysed via WES and RNAseq, to identify common targetable mutations or up-regulated pathways that can be therapeutically disrupted.

The genomic profiles of the Royal Marsden patient samples are similar to that of published ACC samples. WES identified an average somatic mutation rate of 0.7 mutations per megabase of exonic region (/Mb), which is higher than a reported rate of 0.31 mutations/Mb identified from 60 ACC samples (A. S. Ho et al., 2013). This higher rate could be due to the samples being more advanced as they are from metastatic sites unlike the samples analysed by Ho et al. However, despite this increase in mutation rate, there were still very few common targetable mutations (Table 3-2). Five samples (62.5%) had heterozygous or homozygous deletion at 12q12-14, that corresponds to the genes *CDK4*, *ARID2* and *SMARCD1*. cBioPortal, collating sequencing information from six studies analysing both primary and metastatic samples, also reported copy number aberrations in this region although at a lower frequency of 12.5%. Chromatin remodelling genes were mutated in 48% of 109 samples analysed in published sequencing studies (A. S. Ho et al., 2013; Rettig et al., 2016; Stephens et al., 2013). Interestingly all samples had mutations in the chromatin remodelling pathway, including SG0032 that had a non-synonymous mutation in *CREBBP* which was reported to be the third most frequent mutated gene on cBioPortal (Table 3-4). This could suggest that HDAC inhibitors are worth investigating. The percentage of samples with mutations in the DNA damage pathway closely correlated with the published values. Tyrosine kinase aberrations were present in 50% of the patient samples, that closely mirrored the published reports. In particular SG0069 possessed an *FGFR2* amplification and FGF signalling mutations have been implicated in 4-12% of ACC cases. Furthermore, *KIT* amplification was detected in SG0032, which has previously only been reported in 3.8%

of cases in a single study (Hou et al., 2020). Strikingly, Notch pathway mutations were not reported in the Royal Marsden patient samples although were present in 18.3% of the published 109 patient samples (A. S. Ho et al., 2013; Rettig et al., 2016; Stephens et al., 2013). However, this difference is likely due to the small sample size of this study (n=8). By grouping the patient samples in terms of the four ACC subgroups used for recurrent and metastatic samples by Ho et al, only SG0031, 32, 35, 36 and 37 would group as *MYB* translocation^{+} other mutation (A. S. Ho et al., 2019). SG0069 could loosely be added to this subgroup having a *MYBL1* translocation. However, SG0027 and 28 would be classified as triple negative, being *MYB*^{WT}, *NOTCH*^{WT} and *TERT*^{WT}.

Table 3-4 Comparison of published and ACC patient sample mutation profiles

	Paper				Thesis
Pathway	**Ho et al. (2013) (n=60)**	**Rettig et al. (2016) (n=25)**	**Stephens et al. (2013) (n=24)**	**Average (± SD) (%)**	**Royal Marsden (n=8)**
MYB	34 (57%)	11 (44%)	19 (79%)	**60% (±17.7%)**	**7 (87.5%)**
Notch	8 (13%)	9 (36%)	3 (12.5%)	**20.5% (±13.4%)**	**0 (0%)**
FGF/IGF/ PI3K	18 (30%)	15 (60%)	4 (17%)	**35.7% (±20.1%)**	**4 (50%)**
Chromatin remodelling	21 (35%)	11 (44%)	16 (67%)	**48.7% (±16.5%)**	**8 (100%)**
DNA damage	16 (26%)		2 (8%)	**17% (±12.7%)**	**2 (25%)**
Axonal guidance		14 (56%)		**56%**	**3 (37.5%)**

Pathway analysis of the transcriptomic profiles gives an insight into ACC niche requirements and dependencies and potential therapeutic targets. The Wnt signalling pathway was significantly upregulated when normalised to normal SG, and this is consistent with published findings (Frerich et al., 2018; Rettig et al., 2016). Wnt signalling has been tightly associated with cancer and is a key pathway regulating development,

stemness and proliferation (Zhan et al., 2017). When normalised to acinic cell carcinoma, a large number of upregulated DEGs are involved in neural signalling. This could be because perineural invasion is a biological property of ACC, with higher clinical rates than acinic cell carcinoma (Moran Amit et al., 2016). In particular, neurotrophic factors and their receptors such as TrkC and the ligand NT3 are highly expressed in ACC, indicating an autocrine signalling loop that may promote survival and invasion. Another identified pathway that could be therapeutically targeted is transcriptional regulation. Interestingly, when normalised to the published normal SG data, genes associated with the pathways viral carcinogenesis and HPV infection were significantly upregulated, although a causal link between ACC development and HPV infection has not been proven (Haeggblom et al., 2018).

The highest and lowest DEGs compared to normal SG closely agree with those from published transcriptomic studies. Engrailed homeobox 1 (*EN1*) was the highest expressed transcript reported by Bell et al with a Log2 fold increase of 11.46 and was the highest in the eight ACC samples when compared to their published normal SG with a Log2 fold increase of 11.28. Brayer et al also identified that *EN1* was highly expressed compared to independent normal SG (Brayer et al., 2016). EN1 is a transcription factor related to embryonic, tissue and central nervous system development. It is a well reported MYB/MYBL1 target gene and expression of EN1 in ACC correlates significantly with poor survival (P = 0.014) (Bell et al., 2012; Drier et al., 2016; Frerich et al., 2018). Although higher expression levels have been reported in solid growth ACC, that correlation was not observed in these patient samples. EN1 is also a prognostic marker in triple negative breast cancer, and pre-clinical functional studies using EN1-targeted interference peptides have demonstrated its potential as a therapeutic target (Beltran et al., 2014; Peluffo et al., 2019). EN1 has not yet been therapeutically targeted in ACC, however it has been identified as a potential biomarker to assess therapeutic efficacy (Bell et al., 2012). *PRAME* was the second most upregulated DEG in the patient samples and also within the top five upregulated DEGs reported by Bell et al and Brayer et al (Bell et al., 2016; Brayer et al., 2016). *PRAME* is a melanoma-associated antigen upregulated in a number of cancers such as triple negative breast cancer, and is currently being investigated as an immunotherapeutic target (Babiak et al., 2014). Bell et al also found

that the most downregulated DEG was statherin (*STATH*), the same as in the Royal Marsden samples (Bell et al., 2016). Statherin is a salivary protein and decreased statherin in saliva has previously been explored as a diagnostic marker for SG malignancies although no significant difference from normal SG was reported (Contucci et al., 2005).

A challenge in PDX-line establishment is ensuring a high tumour success rate, and the method of engraftment can impact this. The ACC PDX line success rate of 54.5% was relatively good compared to published ranges of 17-72% (Katsiampoura et al., 2017; Na et al., 2020). This rate may have been impacted by a C. bovis infection which was present in the mouse colonies during the time of some failed passages. The slow PDX growth is expected given the clinical behaviour of the tumour type. PDX models were initially established via implantation of tumour fragments subcutaneously. This method is similar to that used by The University of Virginia to establish 17 ACC PDX lines, with a success rate of 74%, although two lines were subsequently lost due to Matrigel contamination by Lactate Dehydrogenase Elevating Virus (LDEV) (Moskaluk et al., 2011). Only 12 lines are available through XenoSTART. These samples were implanted as minced tumour opposed to a solid fragment, and Matrigel was originally used however after the contamination was detected its use was discontinued. Implanting minced tumours may reduce variability in growth caused by selection of specific tumour areas. When PDX lines were re-established, I used single cell injections opposed to tumour fragments to promote more uniform growth between mice. Injection of single cells suspended in Matrigel is a common method for PDX establishment and was used by Cornett et al for the establishment of ACC subcutaneous PDX models, where the original tissue was donated by the University of Virginia (Cornett et al., 2019). Furthermore, on re-establishment of PDX lines the strain of mouse was changed from CD1 nude to NSG mice. CD1 were initially used as they were cost efficient, however NSGs historically have a better PDX take-rate (Mattar et al., 2017).

Another challenge is to confirm that the PDX tumours recapitulate the original patient tumour and that histological and molecular characteristics are maintained throughout serial passaging. H&E staining of the PDX tumours identified that the growth patterns

closely resembled those described in the patient tumour pathology reports, and staining for cell type markers agreed with reported features of the growth patterns (Figure 3-5, Figure 3-6). Reportedly MYB is highly expressed in the myoepithelial and basal cells, and negative in ductal cells in ACC (West et al., 2011). Bell et al analysed 156 patient ACC samples and reported that 55% and 65% of cribriform and tubular tumours respectively were positive for MYB, and only 12% of solid tumours were positive, having a higher proportion of luminal cells and fewer myoepithelial-like cells (Bell et al., 2011). In all samples the majority of cells were positive, however in SG0027 there were areas of cells with lower expression which correlated with the CK8 positive luminal cells.

In addition to histological confirmation of the PDX samples, I also confirmed the lines at the molecular level using the WES and RNAseq data. The *MYB/MYBL1-NFIB* translocations were used to confirm that the PDXs were derived from the correct patient samples (Figure 3-8). Sequencing somatic and germline mutations was useful to confirm SG0027 and 28 lines as these two patient tumours did not possess a translocation. Of the five ACC samples having *MYB-NFIB* translocations none of the samples had translocations with the most frequently reported breakpoint of *MYB* exon 14 - *NFIB* exon 9 (Mitani et al., 2010; Persson et al., 2009). As all PDX samples with *MYB/MYBL1-NFIB* translocations had different breakpoints, primers were designed to be specific for each sample to detect fusion transcripts via RT-PCR (Figure 3-2). This proved valuable when SG0032 and SG0036 PDX lines were crossed over during passaging, and the point of crossover could be identified (Figure 3-9). This method was particularly useful for confirmation of the SG0069 line that lacked a formal histological report from the Royal Marsden. The SG0069 primers produced two PCR products but only in SG0069 PDX samples and were absent in the other PDX lines. This indicates that the band is not due to primer-dimers or non-specific amplification. It is possible the double band could be due to alternative splicing of *MYBL1*, although this would need to be confirmed via sequencing. Brayer et al detected evidence of alternative RNA splicing in *MYB* transcripts in other ACC tumour samples also via RT-PCR, resulting in a shortened exon 8 known as exon 8s (Brayer et al., 2016).

It would have been ideal to compare the PDX tumours directly to the original patient tumour sections, however these were not available. It is important to note that the pathology reports for the patient tumours were dated prior to biopsy collection. This means that the reports may be based on different areas of the tumour received for PDX implantation. The ideal validation of the PDX lines would involve direct comparison to the original patient tumour biopsy received via pathological confirmation and WES to detect any genetic drift or selection throughout serial passaging. However, ACC is known to have a low mutation frequency and selected mutations, MYB status and histology were confirmed at each PDX passage.

The ACC PDX lines established by the University of Virginia were confirmed in a similar way (Moskaluk et al., 2011). Firstly, they also compared the patient samples and PDXs via histological analyses. Moskaluk et al conducted unsupervised clustering of patient samples and PDX lines, identifying that the PDX samples mostly clustered with the corresponding patient sample. Lines possessing the *MYB-NFIB* translocation were checked via fluorescence in situ hybridization, however this does not determine the exact breakpoints as I detected in the patient samples, purely confirms that fusions are present. They reported that 10 out of the 12 actively passaging lines had *MYB-NFIB* translocations, whilst the remaining two samples had MYB rearrangement to an alternative gene partner, *TGBFR3*. Overall, the six PDX lines established from the Royal Marsden patient samples are unique from the PDX models maintained at XenoSTART. Firstly, XenoSTART lack a model possessing the *MYBL1-NFIB* translocation (SG0069), therefore this line could be used to investigate biological differences between MYB driven and MYBL1 driven ACC tumours. Secondly, all PDX lines at XenoSTART have *MYB* activation via a translocation whereas the two lines, SG0027 and 28, have high MYB expression via an alternative mechanism. These two samples enable investigation into other mechanisms of *MYB* activation in ACC and what the biological impact of lacking the flanking *NFIB* super-enhancers has on the transcriptional program and also potential therapeutic sensitivities. However, whole exome and whole genome sequencing conducted for 10 of the ACC PDXs from XenoSTART identified that two lines had activating *NOTCH1* mutations, whereas none of the PDXs established and characterised

in this chapter possess these mutations (Adenoid Cystic Carcinoma Research Foundation, www.accrf.org/tools-for-researchers/bioinformatics).

As I have confirmed that the six established PDX ACC lines molecularly and histologically represent the patient samples they are derived from, all future experiments will focus on these lines. It is important to note that as the patient samples are from metastatic sites it is likely that some patients had previous exposure to chemotherapy or radiotherapy, however due to incomplete clinical annotation this information is not known. Knowledge of previous treatment exposure could have further informed or provided insight into certain responses identified in the subsequent *in vitro* and *in vivo* drug investigation chapters as, for example, previous treatment exposure could have resulted in mechanisms of drug resistance within the tumour.

In addition to subcutaneous models, I investigated the effect of implanting tumour fragments orthotopically into the base of the submandibular gland. Cornett et al established and serially passaged orthotopic ACC PDX models also introduced to the submandibular gland with ACC tissue supplied by the University of Texas (Cornett et al., 2019). Whilst I implanted small fragments of subcutaneous tumour, Cornett et al injected 0.7 x 10^6 single subcutaneous ACC tumour cells into the gland. The SG0032 tumour grew isolated from the rest of the submandibular gland, however Cornett et al saw evidence of neoplastic cells invading adjacent SG tissue, skeletal muscle and approximating nerves (Cornett et al., 2019). This may be due to the method of implanting single cells opposed to tumour fragments, or could be due to the original tumour being more high-grade and invasive in nature than SG0032. Cornett et al did not know the clinical course of the patient ACC the PDX was derived from, however the tumour contained areas of solid growth and all sites of metastasis they found were solid growth pattern, indicating high grade ACC. Overall, only one of the two SG0032 implantations successfully grew and growth rate did not increase compared to subcutaneous implantations, although Cornett et al do report faster tumour formation. Furthermore, the surgical method was more technically challenging than subcutaneous implantation due to the positioning of the mouse for the best access, the thinness of the skin in that area and also the proximity of the carotid artery. Another challenge that

would impact *in vivo* experiments was that accurately measuring the tumour growth was difficult due to the placement. Perhaps a way to overcome this issue would be to inject fluorescently labelled dissociated single cells and use an *in vivo* imaging system. Therefore, due to the technical challenges of the orthotopic implantations and that a large number of implantations would be required for an *in vivo* experiment, I will conduct *in vivo* assays using subcutaneously implanted tumours.

4. PDX-derived preclinical *in vitro* drug sensitivities

4.1. Introduction

Therapeutic options for ACC, particularly advanced disease, are very limited with low efficacy. Recent efforts have been focussed on genomic profiling of patient tumours to identify targeted therapies as opposed to non-specific cytotoxic agents. However, as discussed, ACC drug sensitivity research has been hindered by the lack of validated ACC preclinical models (Phuchareon et al., 2009; Zhao et al., 2011). To identify potential therapeutic options for ACC, short-term 2D cultures were derived from the ACC PDX tumours characterised in the previous chapter. These 2D primary cell cultures were applied to hypothesis-driven drug sensitivity assays. Drugs investigated were either identified from published preclinical papers, current clinical trials, or inhibited potential targets identified from the WES and RNAseq analysis from the primary patient tumours.

4.2. 2D culture and drug assay optimisation

Upon PDX harvest, tumours were dissociated to single cells. For all PDX lines, single cells were derived from various passage numbers ranging from P1-P6, and each drug candidate was tested in biological triplicate using cells derived from different PDX passages. Growth medium was adapted from Liu et al who cultured primary tumour epithelial cells in the presence of the Rho kinase inhibitor, Y-27632 (X. Liu et al., 2017). Y-27632 improves survival of human pluripotent stem cells following dissociation, inhibiting anoikis, and prevents the terminal differentiation of epithelial stem cells (Terunuma et al., 2010). All lines grew well as adherent cultures under normal culture conditions. The only exception to this was SG0069 that was non-adherent and so was cultured in suspension. The doubling rate of the PDX-derived 2D cultures was used to determine drug sensitivity assay length, to ensure that the cells would have been through at least two divisions. Doubling rate was calculated using CTG as a surrogate for cell count. A baseline CTG reading was taken one day after cell plating, and again after

5 or 10 days in culture. At 5 days, the division rates for four out of the six lines were under 2-fold (Table 4-1). At 10 days, the division rate was increased to over 3-fold, therefore drug assays were planned to last 10-days with media changes on day 5. However, again the exception to this was SG0069 that, under normal culture conditions, did not actively proliferate within 5 days having a doubling rate of 0.71.

In order to optimise SG0069 growth, the addition of 2% Matrigel was investigated to improve cell adhesion and the addition of the FGFR1 and 2 ligands, FGF2 (20 ng/mL, Peprotech) and FGF10 (20 ng/mL, Peprotech), was investigated to improve cell proliferation. This is because WES analysis identified that SG0069 possessed an *FGFR2* amplification and the RNAseq normalised to SG0043 showed that *FGFR1* is highly expressed in all ACC samples. Evos images from these different growth conditions clearly shows that adherent growth was greatly improved for SG0069 with the addition of both 2% Matrigel, FGF2 and FGF10, moderately increasing the 5-day doubling rate to 1.22 (Figure 4-1). Alternatively, 2% Matrigel addition did not increase growth for SG0036 resulting in a 5-day doubling rate of 1.13 compared to 1.76 under normal conditions.

Table 4-1 Doubling rates of 2D PDX-derived cultures

PDX line	Doubling rate	
	5 day	**10 day**
SG0027	1.64	3.72
SG0028	1.83	3.87
SG0032	2.77	4.68
SG0036	1.76	4.11
SG0037	2.81	3.98
SG0069	0.71	1.54
SG0069*	1.22	3.34

*2% Matrigel + FGF2 and 10

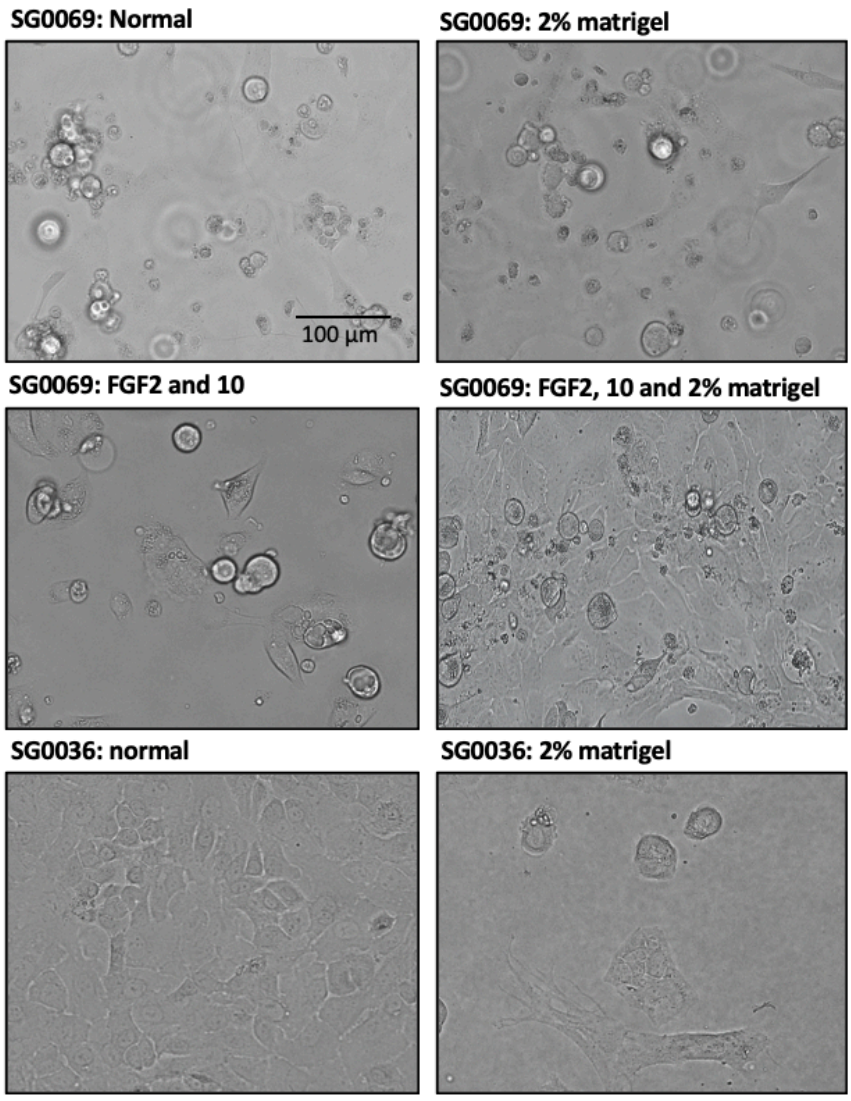

Figure 4-1 Culture optimisation of 2D PDX-derived cultures

Evos images at 10 X magnification of SG0069 or SG0036 after 5-days cultured in normal medium, with 2% Matrigel addition or FGF2 and 10 addition. The optimum condition for SG0069 adherent growth was the addition of both 2% Matrigel, FGF2 and FGF10. Addition of 2% Matrigel to SG0036 medium reduced adherence. Scale bar = 100 µm.

Another factor that was considered prior to drug sensitivity screening was the seeding density of the primary 2D cultures. As they are slower to proliferate than the cell line controls, the seeding density was increased as primary cells are particularly sensitive to stress induced by level of confluency. Therefore, a drug sensitivity assay was conducted for the BRD inhibitor JQ1, with SG0032 seeded at 2000, 4000 and 6000 cells per well of a 96 well plate (Figure 4-2A). Seeding density did not impact response to the drug candidate, however the highest doubling rate was 4.47-fold when seeded at the lowest

density of 2000 cells per well (Figure 4-2B). Therefore, the optimal conditions selected for the 2D drug sensitivity assays were 10-days of treatment seeded at 2000 cells/well in a 96 well plate format, which also conserved limited sample increasing the number of drug assays from the same passage.

A

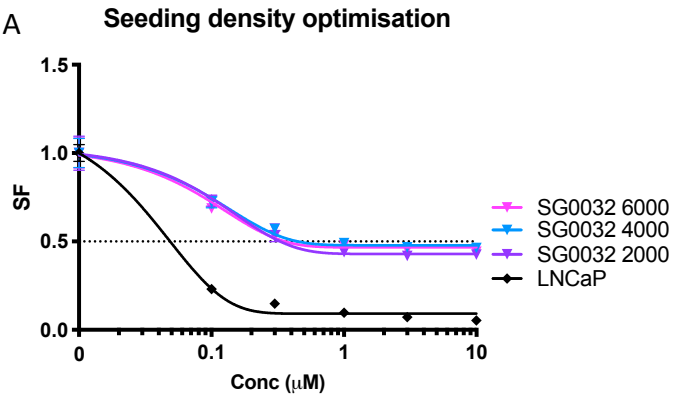

B

Seeding density	Doubling rate
2000	4.47
4000	3.61
6000	3.08

Figure 4-2 Drug sensitivity assay seeding density optimisation

A) 10-day JQ1 sensitivity assay for SG0032 seeded at three plating densities; 2000, 4000 or 6000 cells per well. Cell viability was determined via CTG, and plotted as the mean survival fraction (SF). B) Doubling rate for each seeding density was calculated by normalising the DMSO control to the baseline CTG reading. Data shown is representative of two independent biological repeats and each data point is the mean SF for eight parallel technical replicates, +/- SD.

4.3. Models mirror responses reported in the clinic

It has been widely reported that ACC is non-responsive to 90% of chemotherapeutics in the clinical setting (Laurie et al., 2011). To confirm this, I treated four ACC PDX-derived samples in 2D with increasing doses of the taxane chemotherapy drug, paclitaxel (Figure 4-3A). It is evident that none of the ACC samples were sensitive to paclitaxel as the SF at the highest dose of 1 µM was above 0.5 for all samples.

In addition, HDAC inhibitors have been widely investigated for ACC and they have been tested in phase I and II clinical trials, although with mixed results (Dong et al., 2012; Goncalves et al., 2017). SG0032 was treated with the HDAC inhibitor, vorinostat in 2D (Figure 4-3B). Although SG0032 had a similar IC_{50} value to the control cell line, HCT-116 (colon cancer), 43% of cells remained viable at the highest dose. Therefore, SG0032 was

not sensitive to HDAC inhibition and it would not be an effective treatment to pursue *in vivo*.

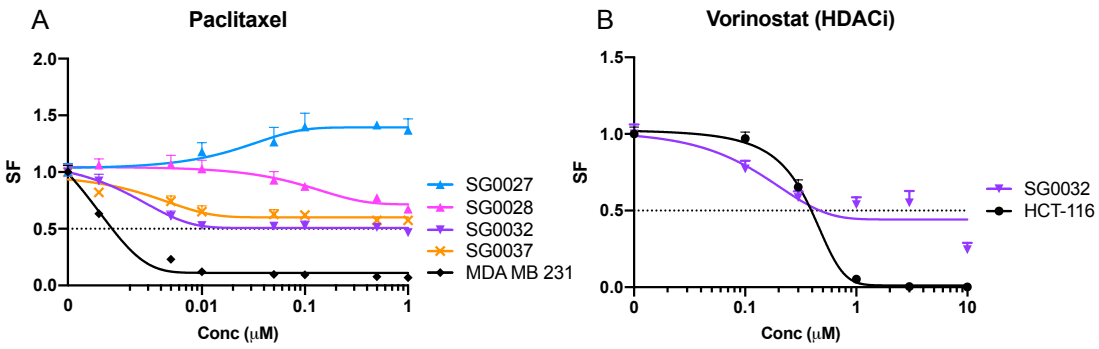

Figure 4-3 2D PDX-derived cultures mirror responses reported in the clinic

A) 10-day paclitaxel sensitivity curves for four ACC PDX-derived primary samples in 2D. B) 10-day drug sensitivity curve for SG0032 treated with the HDAC inhibitor, vorinostat, in 2D. Data shown is representative of three independent biological repeats and each data point is the mean SF for eight parallel technical replicates, +/- SD.

4.4. Potential therapeutic targets

The WES and RNAseq data from the patient samples identified a number of potential therapeutic targets. These targets were either genes amplified according to the WES, or receptors, ligands or active pathways with increased expression based on the RNAseq analysis. As discussed in chapter 3.2.3, in addition to normalising the ACC RNAseq data to the published normal SG data, each patient sample was also normalised to a non-ACC SG patient sample, SG0043. This sample is Acinic cell carcinoma for which high MYB expression is not a hallmark. By choosing potential targets based on both RNAseq normalisations, most potential targets investigated were ACC-specific, being significantly differentially expressed compared to both the non-ACC sample and normal SG.

4.4.1. Bromodomain 4 (BRD4)

MYB is currently the only recognised driver mutation in ACC and is highly expressed in all PDX lines, except SG0069 possessing an alternative *MYBL1-NFIB* translocation. Drier

et al indirectly targeted MYB using the BET bromodomain inhibitor JQ1, as they identified that BRD4 is co-bound to MYB binding sites (Drier et al., 2016). They reported that ACC samples with high MYB levels are more sensitive to BRD4 inhibition, therefore I assessed JQ1 sensitivity in the PDX-derived 2D assays. The IC_{50} values did not correlate with the *MYB* expression levels normalised to SG0043 (Table 3-3). SG0027 and 28 had the highest levels of MYB (via an alternative mechanism to the MYB-NFIB translocation) but whilst SG0027 was the most sensitive sample (IC_{50} 0.27 µM), SG0028 was the least (IC_{50} 1.56 µM) (Figure 4-4A). Both SG0032 and 37 had high MYB via the *MYB-NFIB* translocation and were fairly sensitive with IC_{50} values of 0.67 µM and 0.84 µM. Despite this, in all samples at least 30% of cells remained viable at the highest concentration of drug.

JQ1 is not trialled in the clinic due to its short half-life, however there are a number of other BRD inhibitors currently in trials such as I-BET151. I-BET151 associates with the same intracellular protein complexes as JQ1, having identical molecular activity (Tyler et al., 2017). This clinically relevant BRD inhibitor gave comparable sensitivities to JQ1 in the PDX-derived 2D samples (Figure 4-4B).

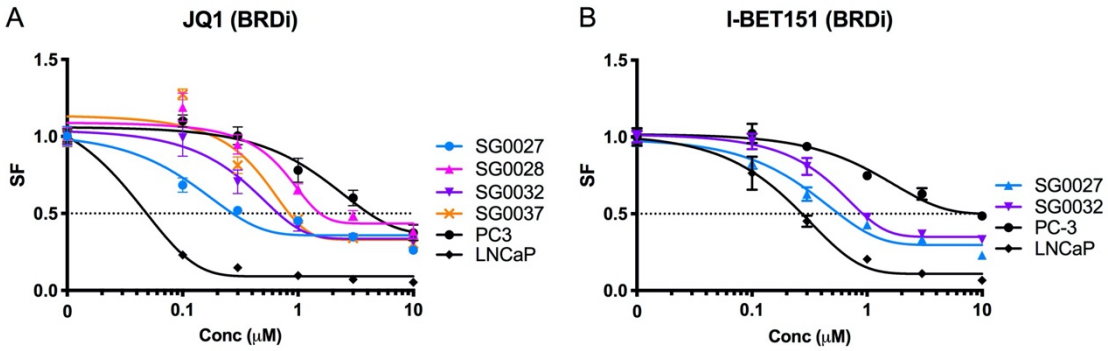

Figure 4-4 Bromodomain inhibitor sensitivity

A) 10-day JQ1 sensitivity curves for four ACC PDX-derived primary samples in 2D. B) 10-day I-BET151 drug curves for two ACC samples. Data shown is representative of three independent biological repeats and each data point is the mean SF for eight parallel technical replicates +/- SD.

4.4.2. FGFR2

WES data identified an *FGFR2* amplification in SG0069 which was confirmed by Alex Pearson (ICR) via digital droplet PCR, reporting a copy number variation of 44.1 compared to the control HOGA1. Therefore, SG0069 was treated in 2D with the FGFR inhibitor, AZD4547 (Figure 4-5A). SG0069 was more sensitive than SG0032 which lacked an *FGFR2* amplification (IC_{50} 1.06 µM and >10 µM respectively). AZD4547 is now classified as a controlled drug, so an alternative FGFR inhibitor was tested, BGJ398, which has similar sensitivities to each FGFR isoform as AZD4547. Despite this, SG0069 was less sensitive to BGJ398 whereas the positive control (a gastric cancer cell line with an *FGFR2* amplification) was far more sensitive (IC_{50} 3.4 µM and 0.03 µM respectively) (Figure 4-5B). Clearly SG0069 was more sensitive to FGFR inhibition than an ACC sample without an *FGFR2* amplification, however it was not as sensitive as expected when compared to the positive cell line.

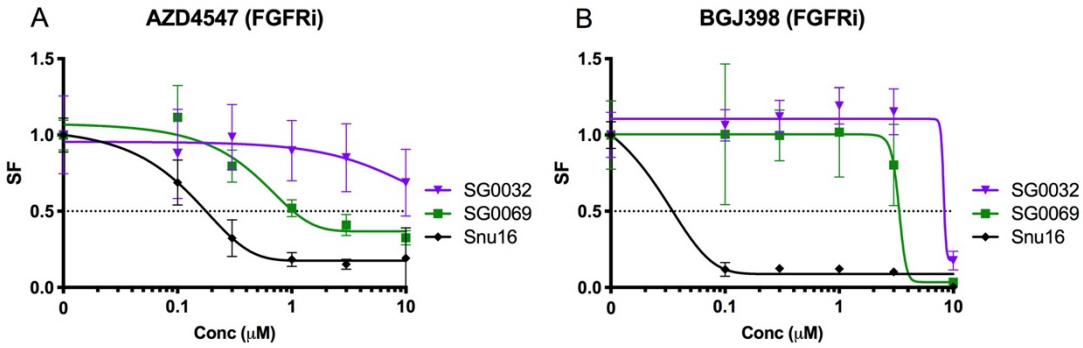

Figure 4-5 FGFR inhibitor sensitivity

10-day 2D drug sensitivity assay for the FGFR inhibitors, AZD4547 (A) and BGJ398 (B), for ACC PDX-derived samples SG0032, and 69. Data shown is representative of three independent biological repeats and each data point is the mean SF for eight parallel technical replicates +/- SD.

4.4.3. Insulin growth factor receptor (IGFR)

I hypothesised that the ACC samples would be sensitive to IGFR inhibition as the RNAseq analysis identified that *IGF2* is highly expressed in ACC when compared to both the normal SG and SG0043. The samples were treated with the IGFR inhibitor OSI-906 in 2D. In accordance with the relative expressed levels compared to SG0043 (Table 3-3),

SG0027 had the highest level of *IGF2* expression and was the most sensitive to IGFR inhibition, whereas SG0069 had the lowest expression level and was least sensitive (Figure 4-6). However, despite being the most sensitive, at 10 µM the SF of SG0027 was 0.4, indicating a surviving population. Therefore, despite having high expression of the ligand IGF2, ACC samples were not particularly sensitive to IGFR inhibition.

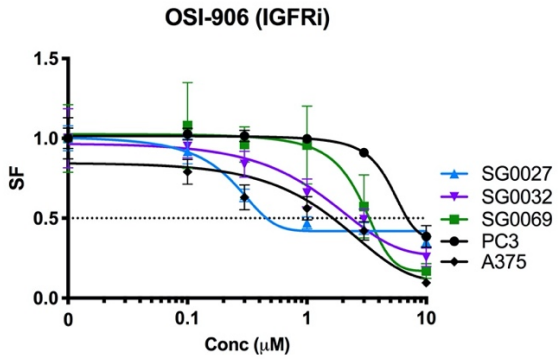

Figure 4-6 IGFR inhibitor sensitivity

10-day primary ACC PDX-derived drug curves treated with the IGFR inhibitor, OSI-906. Data shown is representative of three independent biological repeats and each data point is the mean SF for eight parallel technical replicates +/- SD.

4.4.4. ATR

ATR is a serine/threonine protein kinase involved in activating the DNA damage cell cycle checkpoint. It has been identified as a MYB target gene and is highly expressed in clinical ACC samples (Andersson et al., 2020). Although in the Royal Marsden ACC patient samples there was no significant difference in expression when compared to both normal SG and SG0043, the response to the ATR inhibitor AZD6738 was measured. Compared to the positive control cell line, TOV21G (ovarian cancer), SG0032 and 36 were not sensitive, with IC_{50} values of 1.69 µM and greater than 10 µM respectively (Figure 4-7). Therefore, the lack in sensitivity of the PDX-derived ACC samples agrees with the fact there was no differential expression in ATR compared to normal SG.

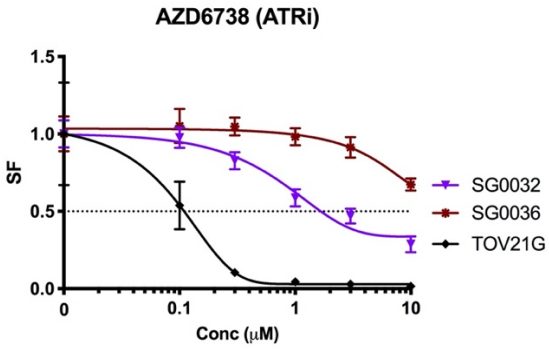

Figure 4-7 ATR inhibitor sensitivity

10-day primary ACC PDX-derived drug curves treated with the ATR inhibitor, AZD6738. Data shown is representative of three independent biological repeats and each data point is the mean SF for eight parallel technical replicates +/- SD.

4.4.5. BCL-2

BCL-2 is a known MYB target and is reportedly highly expressed in ACC patient samples (Persson et al., 2009). Compared to the published normal SG, BCL-2 expression was upregulated in the ACC patient samples compared to normal SG, however expression was not significantly higher when compared to SG0043. In the 2D cultures, following 10-day treatment with the BCL-2 inhibitor Navitoclax, SG0027 was the most sensitive sample with an IC_{50} of 1.88 µM compared to SG0032 with an IC_{50} of 6.4 µM (Figure 4-8). The ACC samples demonstrated mixed sensitivity to BCL-2 inhibition. In the clinic, BCL-2 inhibitors are currently being explored as senolytic agents, chemo- and radio-sensitisers (Lafontaine et al., 2021; Y. Zhu et al., 2016). They are used to selectively target senescent cells by inhibiting the BCL-2 anti-apoptotic pathway. Therefore, a more clinically relevant application to test BCL-2 inhibitor sensitivity within ACC would be as part of a combination, rather than as a single agent.

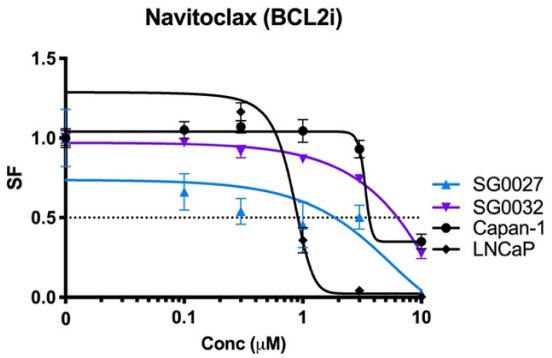

Figure 4-8 BCL2 inhibitor sensitivity

10-day drug sensitivity curve for SG0027 and 32 treated with the BCL2 inhibitor, navitoclax, in 2D. Data shown is representative of three independent biological repeats and each data point is the mean SF for eight parallel technical replicates +/- SD.

4.4.6. Cell cycle dependent kinases (CDKs)

KEGG pathway analysis of the primary patient tumours identified a number of upregulated differentially expressed genes linked to the cell cycle such as *CDK6*, *CCNA2* (cyclin A2), *CCNB1* (cyclin B1), and *CCNB2* (cyclin B2) (see appendix 2, chapter 9.2). Furthermore, a previous unbiased drug screen was conducted in collaboration with the Lord research group at the ICR (work conducted by Carina Mill). Using two ACC PDX-derived samples, a panel of 80 drugs currently in clinical use were screened in 2D besides a range of cell lines from different cancer types. This screen showed that very few compounds were sensitive in the ACC samples, however it identified that SG0032 compared to SG0027 was more sensitive to the pan-CDK inhibitor, flavopiridol (data not shown). I confirmed this difference in sensitivity in a biased flavopiridol assay using the optimised 10-day 2D assays (Figure 4-9A). SG0032 was more sensitive than SG0027 and 28 with an IC_{50} value of 0.05 µM compared to 0.12 µM and 0.16 µM respectively. Flavopiridol is a pan-CDK inhibitor, known to inhibit CDK1, 2, 4, 6 and 9. It has exhibited a degree of clinical efficacy in CLL, however this was limited by toxicity, likely due to the lack of CDK specificity (Byrd et al., 2007). Therefore, due to the known toxicity profile of flavopiridol in the clinic, I researched a number of different clinically relevant inhibitors to identify which CDK activity ACC is particularly sensitive to.

Firstly, the CDK4/6 inhibitor palbociclib was investigated as not only was *CDK6* highly expressed when normalised to the normal SG samples and SG0043, but WES analysis identified that SG0032, 35, 36, 37 and 69 had lost one copy of *CDK4* and loss of CDK4 can be compensated by CDK6. However, the samples were not particularly sensitive to CDK4/6 inhibition (Figure 4-9B). The most sensitive sample was SG0037, having lost one copy of CDK4, with an IC_{50} of 3.3 µM.

The samples were more sensitive to dinaciclib, a CDK1, 2, 5, 9 inhibitor (Figure 4-9C). SG0032 was more sensitive compared to SG0027 (IC_{50} values 5 nM and 9 nM respectively), which was also observed with flavopiridol. However, the sensitivity of ACC has already been tested in a basket phase I clinical trial and although stable disease was reported, 98% of subjects experienced treatment emergent adverse effects, therefore alternative inhibitors were researched (Nemunaitis et al., 2013).

CCT068127, a CDK2, 5, 9 inhibitor, was kindly provided by Stephen Whittaker (ICR). Again, the same pattern of sensitivity was observed with SG0032 being more sensitive than SG0027, with an IC_{50} of 0.6 µM compared to 1.15 µM (Figure 4-9D). However, CCT068127 is not suitable for use *in vivo* and is not commercially available. CYC065 (Cyclacel) is a second generation CDK inhibitor optimised from seliciclib and CCT068127 (Wilson et al., 2011), and is suitable for use *in vivo* and the clinic therefore I repeated the sensitivity assays with this compound (Rao et al., 2017). These showed that SG0037 was particularly sensitive to CYC065 (IC_{50} 0.15 µM), whereas SG0027 was the least sensitive (IC_{50} 0.34 µM), which agreed with results from CCT068127 (Figure 4-9E). The ACC samples were more sensitive to CYC065 than CCT068127, however the samples most and least sensitive to both drugs remain the same.

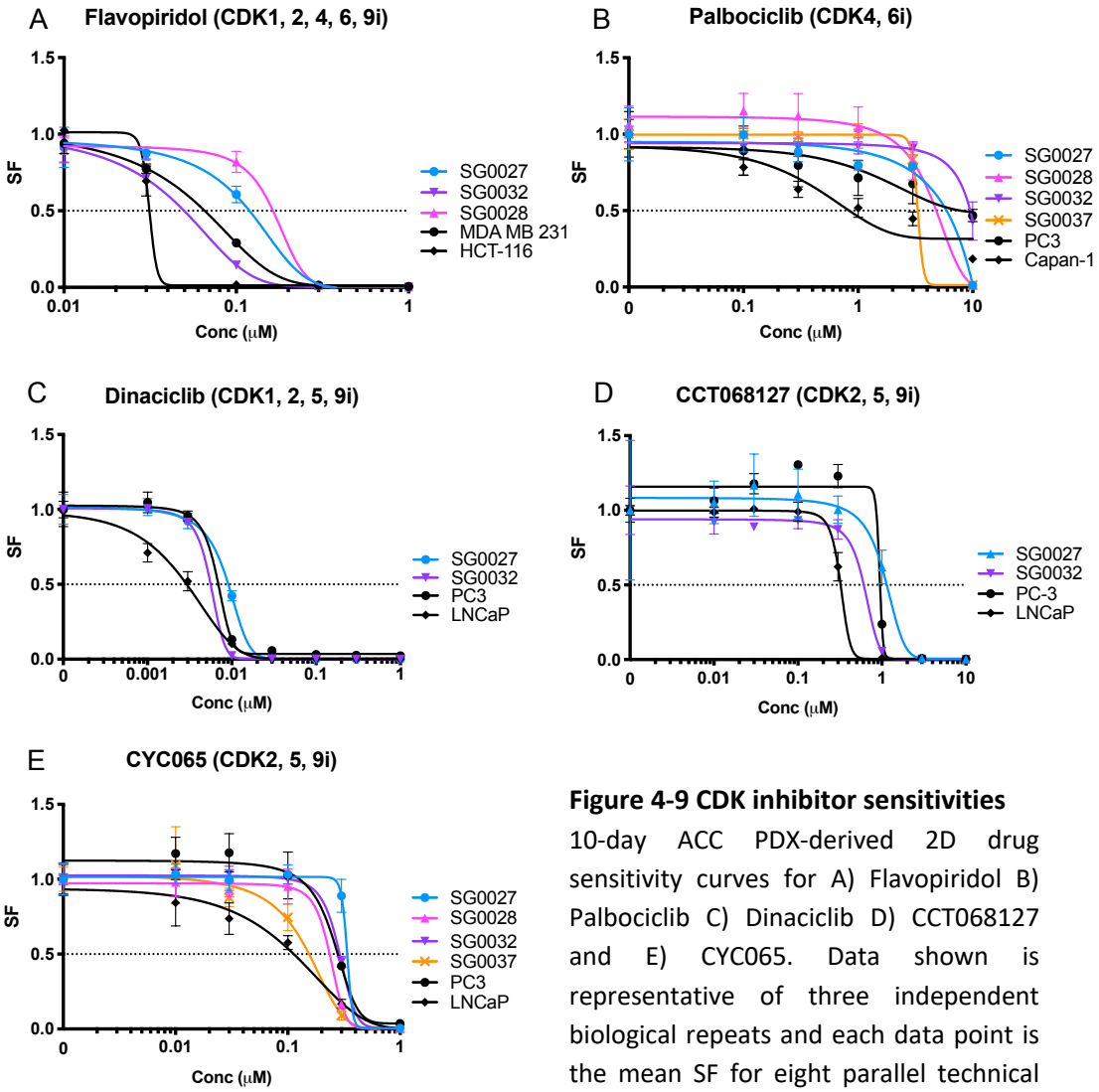

Figure 4-9 CDK inhibitor sensitivities
10-day ACC PDX-derived 2D drug sensitivity curves for A) Flavopiridol B) Palbociclib C) Dinaciclib D) CCT068127 and E) CYC065. Data shown is representative of three independent biological repeats and each data point is the mean SF for eight parallel technical replicates +/- SD.

4.5. Potential therapeutic combinations

As shown, a number of single agents targeting a wide range of potential targets were tested, however very few proved particularly sensitive in the 2D PDX-derived ACC preclinical models. Therefore, I researched combination treatments to see if inhibiting two separate targets would be more effective. I decided to investigate combinations with a CDK2, 5, 9 inhibitor as all samples treated with either CCT068127 or CYC065 were fairly sensitive. Higher doses induced almost 100% cell death which was not observed with the other tested inhibitors.

4.5.1. CDK2, 5, 9 inhibitor combinations

CCT068127 was reported to have a synergistic effect when combined with a BCL-2 inhibitor in AML and CRC (Frame et al., 2015; Whittaker et al., 2018). In addition, CDK2 and 9 inhibitors separately have been identified as synergistic in combination with BRD inhibitors in rhabdoid tumours, AML and medulloblastoma (Bolin et al., 2018; Gerlach et al., 2018; Moreno et al., 2017). Therefore, SG0032 was treated with CCT068127 plus the constant addition of the IC_{20} concentration of either navitoclax or JQ1 (Figure 4-10). The addition of navitoclax had no change on the IC_{50}, however the combination of JQ1 shifted the dose response curve to the left, reducing the IC_{50} from 0.91 to 0.18 µM. This shows that the treatment of the CDK2, 5, 9 inhibitor with a BRD inhibitor was the most promising combination.

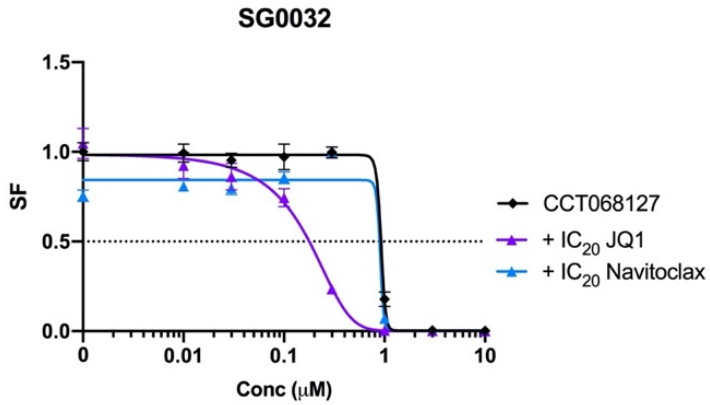

Figure 4-10 Potential CDK inhibitor combinations

2D SG0032 10-day CCT068127 sensitivity assay with constant addition of JQ1 or Navitoclax at the IC_{20} concentrations, 0.25 µM and 2.05 µM respectively. Each luminescence reading was normalised to the untreated CCT068127 control reading. Data shown is representative of two independent biological repeats and each data point is the mean SF for six parallel technical replicates +/- SD.

4.5.2. Combination confirmation in different samples

I then confirmed that the increase in sensitivity of CCT068127 with the addition of JQ1 was also observed when using the clinically relevant drug CYC065, in both SG0027 and 32. Either a constant addition of 0.1 or 0.3 µM JQ1 was added to the serial doses of CYC065 (Figure 4-11). Although each sample had a differing sensitivity to the drugs as

single agents, the addition of JQ1 decreased the surviving fraction of cells, as the dose response curves shifted to the left with increasing JQ1 doses. This shows that CYC065 in combination with JQ1 reduced cell viability, as observed with CCT068127.

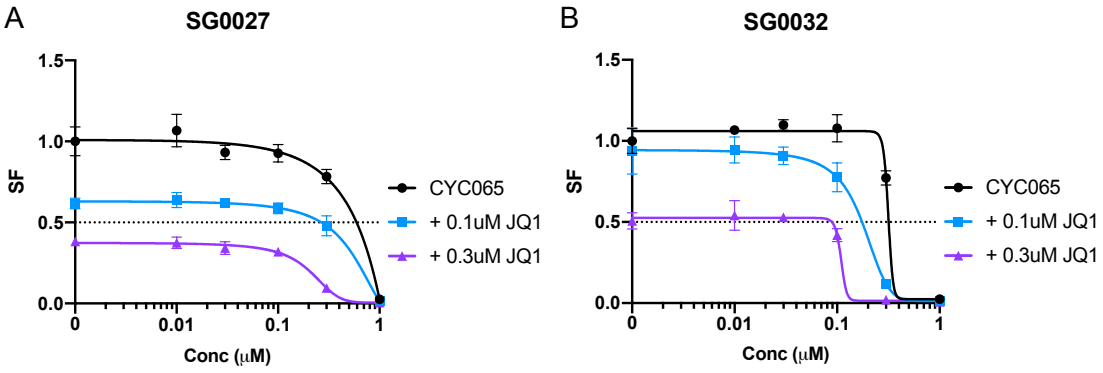

Figure 4-11 CDK and bromodomain inhibitors in combination

10-day 2D CYC065 sensitivity curves with the constant addition of either 0.1 µM and 0.3 µM JQ1 in ACC samples SG0027 (A) and SG0032 (D). Each luminescence reading was normalised to the untreated CYC065 control reading. Data shown is representative of two independent biological repeats and each data point is the mean SF for six parallel technical replicates +/- SD.

4.5.3. Synergistic drug combination

An ideal drug combination is synergistic. This is when the effect of both drugs dosed together is greater than the additive effect of each single drug, meaning that lower doses of each drug in combination can be used. To determine whether the combination of a CDK2, 5, 9 inhibitor and BRD inhibitor was synergistic, the Chou-Talalay constant ratio method was applied. For each ACC line, multiples of the IC_{50} concentration for each single agent were dosed in a constant ratio. The combination index (CI) was then calculated from the fraction affected (Fa) values for single agent response curves compared to the Fa values when dosed in combination. A CI of greater than 1 indicates antagonism, equal to 1 indicates an additive effect, and less than 1 indicates synergy.

Firstly, the level of synergy for CCT068127 and JQ1 in combination was determined in SG0032 (Figure 4-12A). The data points from two repeats are plotted on the CI graph. The graph shows that the combination was highly synergistic when dosed at half the IC_{50} concentrations, where the Fa was 0.78. As discussed, JQ1 is not suitable for clinical use,

therefore to confirm that this combination has clinical relevance the BRD inhibitor IBET-151 was used. I compared the CI graph for CCT068127 in combination with JQ1 with the graph for CCT068127 in combination with I-BET151 (Figure 4-12B). From two repeats, it is evident that the curves were very tightly matched, and that both BRD inhibitors were highly synergistic in combination with CCT068127.

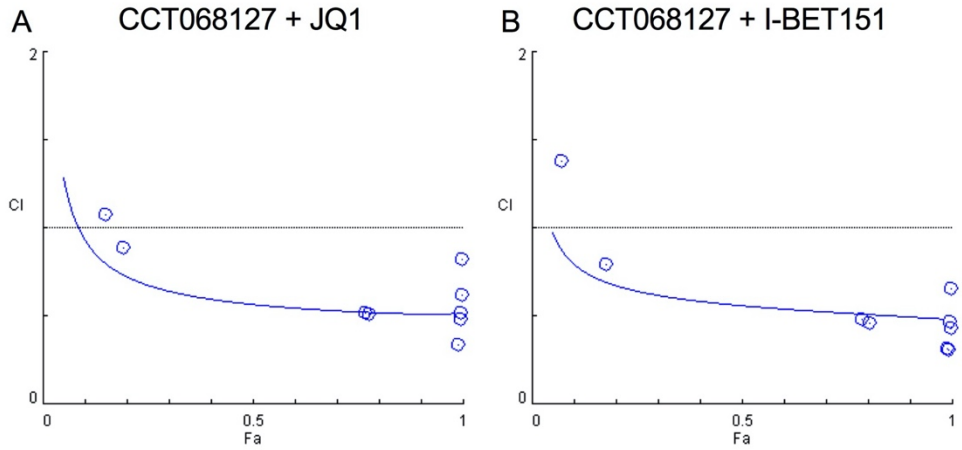

Figure 4-12 Combination synergy: JQ1 vs I-BET151

The combination index (CI) plotted against fraction affected (Fa) for CCT068127 in combination with JQ1 (A) and I-BET151 (B) for sample SG0032. Data points for two independent biological repeats are plotted, with a curve of best fit. Each point representants the mean of six parallel technical repeats.

The combination of CCT068127 and JQ1 was highly synergistic in both SG0032 and 27 (Figure 4-13A and C). However, when CYC065 was used alternatively to CCT068127, although the level of synergy remained similar for SG0027, it was less synergistic in SG0032 (Figure 4-13B and D). In SG0032 following triplicate repeats, the combination of CYC065 and JQ1 was only synergistic when 0.5 x IC_{50} concentrations were dosed together, however, CCT068127 and JQ1 were synergistic at the lowest doses, 0.25 x IC_{50} concentrations.

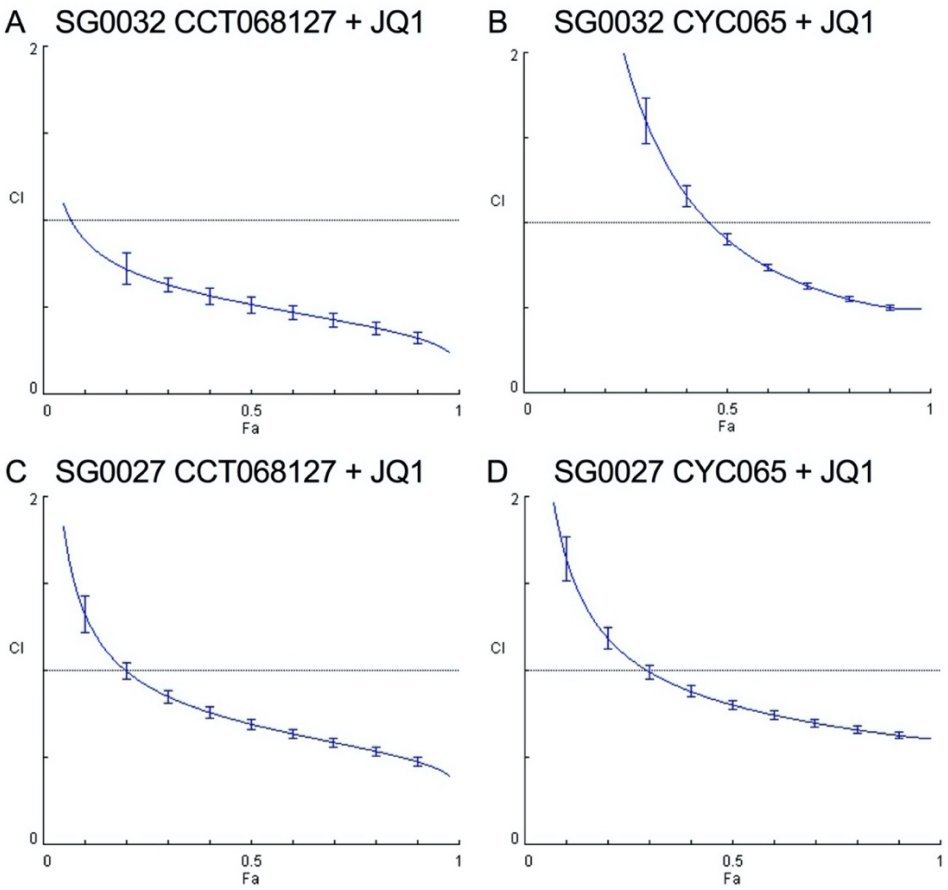

Figure 4-13 Combination synergy: CCT068127 vs CYC065

Combination index (CI) plotted against fraction affected (Fa) for SG0032 (A and B) and SG0027 (C and D). For each sample the CDK inhibitors CCT068127 (A and C) and CYC065 (B and D) have been investigated in combination with JQ1. Using the CompuSyn software (Version 1), the graphs are plotted as the line of best fit +/- 95% confident limit bars for the average of three independent biological repeats.

The level of synergy for CYC065 and JQ1 in combination was determined for four ACC samples; SG0027, 28, 32 and 37 (Figure 4-14A-D). The combination of CYC065 and JQ1 was synergistic in all samples although at differing levels. SG0028 is highly synergistic above the IC_{50} concentration doses, however it is the sample in which the combination has the lowest level of synergy (Figure 4-14B). SG0027 and 32 are synergistic above 0.5 x IC_{50} concentrations (Figure 4-14A and C). The combination is the most synergistic in SG0037, being highly synergistic at the lowest doses tested, 0.25 x IC_{50} concentrations (Figure 4-14D). Overall, despite having differing degrees of synergy, the combination of CYC065 and JQ1 was synergistic in all four tested ACC PDX-derived samples.

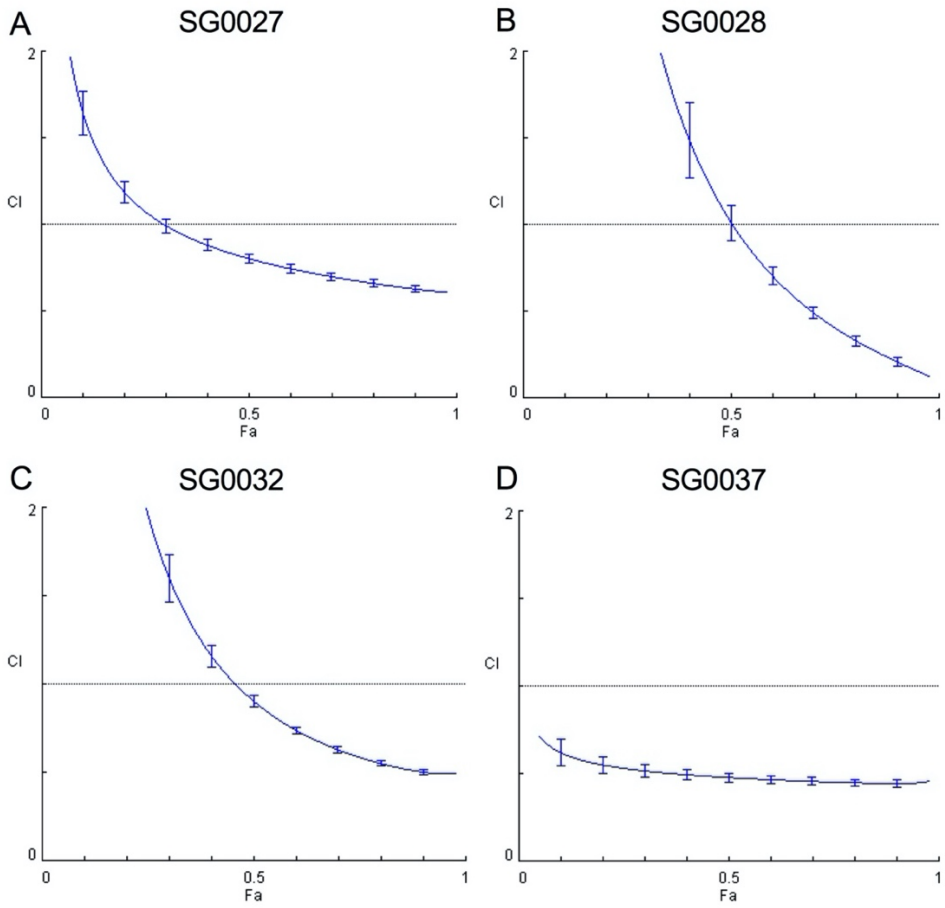

Figure 4-14 Combination synergy: CYC065 and JQ1

The CI Fa plots for four PDX-derived ACC samples in 2D; SG0027 (A), SG0028 (B), SG0032 (C) and SG0037 (D). Using the CompuSyn software (Version 1), the graphs are plotted as the line of best fit +/- 95% confident limit bars for the average of three biological repeats.

4.5.4. Schedule dependent response

Prior to progression to *in vivo* studies, it is best to identify the optimum dosing schedule for a combination. Therefore, SG0027, 28 and 32 were dosed with both drugs either in combination concurrently for 10 days, or as single agents sequentially for half the therapy duration (5 days). For both SG0027 and 28, dosing in combination significantly lowered cell survival compared to sequential dosing at the same concentrations for all dose pairings (Figure 4-15A and B). Whilst there was significantly higher death when dosing concurrently in SG0032, this assay also suggested that the sample is more sensitive to the dose of CYC065 than JQ1 when in combination (Figure 4-15C). Cell death was higher when 0.3 µM CYC065 and 0.1 µM JQ1 were administered, compared to 0.1 µM CYC065 and 0.3 µM JQ1. Furthermore, the surviving fractions for all dosing

schedules were similar when either 0.1 µM or 0.3 µM JQ1 is combined with 0.3 µM CYC065 in SG0032. This data indicates that the *in vivo* assays should be dosed concurrently.

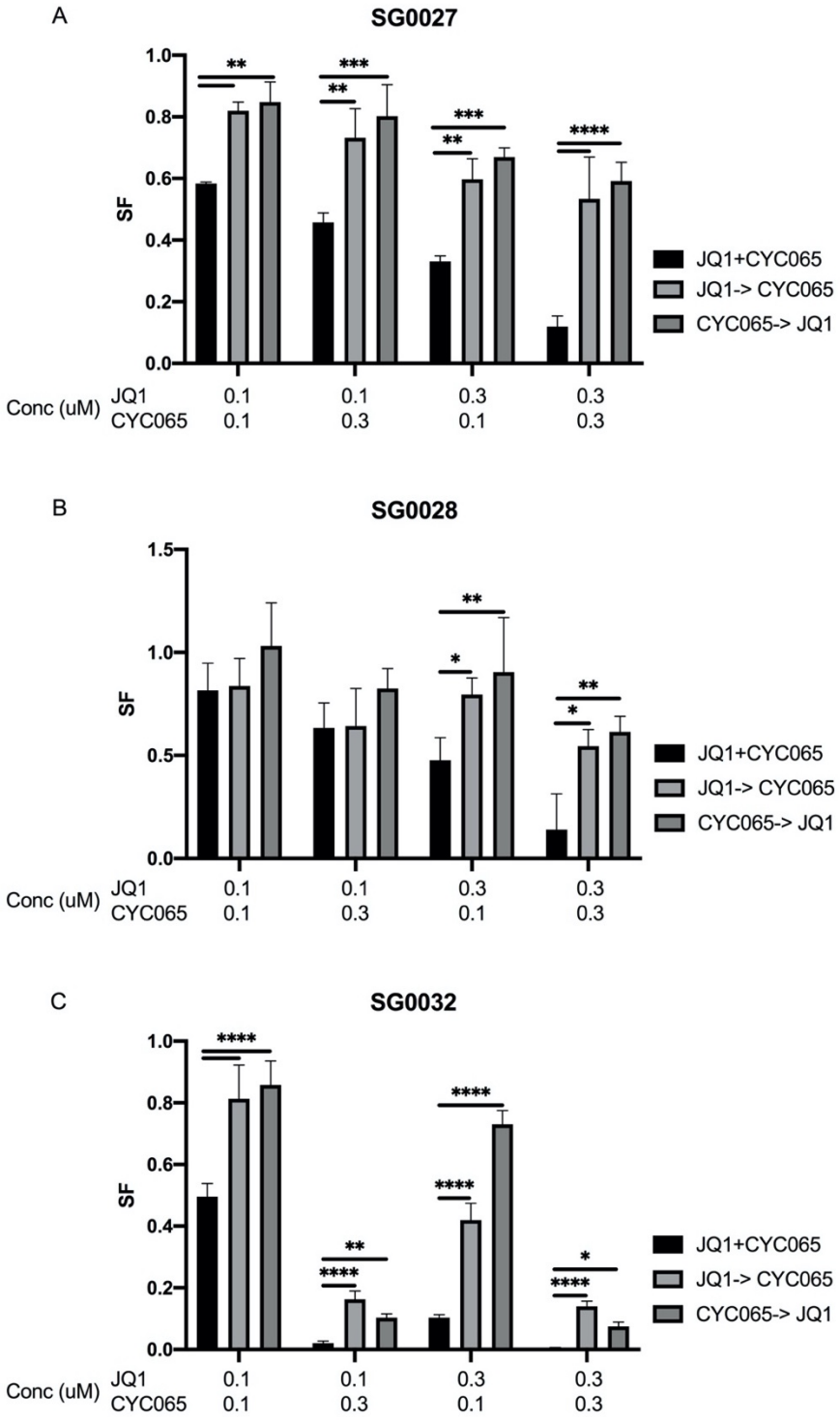

Figure 4-15 Combination schedule dependent response

The survival fractions (SF) for 3 ACC samples; SG0027 (A), 28 (B), and 32 (C), following 10-day combination dosing at 0.1 µM or 0.3 µM of JQ1 and CYC065, either concurrently or sequentially (where the first drug was removed at day 5 of treatment and replaced with the alternative treatment for the remaining 5 days). The luminescence readings at each concentration were normalised to the untreated control to give the survival fraction (SF). Data shown is representative of three independent biological repeats and each data point is the mean SF for eight parallel technical replicates +/- SD. Significance was calculated at each dose combination by a two-way ANOVA for testing for a difference between the SF values following the different dosing schedules, followed by the Tukey multiple comparison test. $P > 0.5$ ns, $P \leq 0.05$ *, $P \leq 0.01$ **, $P \leq 0.001$ ***, $P \leq 0.0001$ ****.

4.6. Discussion

There are currently no clinically approved targeted therapies for ACC, and preclinical therapeutic research has been hindered by the lack of validated ACC models. To address this, I performed biased drug screens to target genes and active pathways identified from published preclinical papers or from the WES and RNAseq analysis from the primary patient tumours using PDX-derived short-term 2D cell viability assays.

A limitation of measuring cell viability via CTG as a measure of drug sensitivity is that it does not take into account the difference in cell division rates between the different lines (Bruna et al., 2016). Hafner et al suggest measuring growth rate metrics to more accurately predict drug sensitivities independent of differing growth rate, which could be effective for PDX-derived cultures as primary cells are known to grow slowly, unevenly and therefore make growth rate difficult to control (Hafner et al., 2016). However, the ACC 2D cultures are slow growing, and having 10-day assays ensures that all lines have doubled at least three-fold, and always taking a baseline reading the day of drugging for each sample confirms that the cells are actively dividing throughout the assay. Cell seeding density was investigated as it has been reported that increased density can promote drug resistance, but also as primary cells are very sensitive to the degree of confluency impacting proliferation and differentiation (Garrido et al., 1995). When treated with the BRD4 inhibitor, JQ1, the IC_{50} values remained the same for all three seeding densities despite them having different growth rates. This implies that the growth rate does not have a large effect on drug response, perhaps as long as all lines

proliferate a minimum of three-fold. Although, to definitively determine that seeding density does not impact drug sensitivity, other drugs should also have been assayed with diverse mechanisms of action.

As there is a linear relationship between ATP metabolism and cell number, a limitation of this type of cell viability assay is that it cannot distinguish between a cytotoxic or a cytostatic agent. Cytotoxic agents induce cell death, whereas cytostatic agents inhibit cell proliferation and after prolonged exposure result in cell death. In both cases ATP metabolism is reduced. To determine the mechanism of cell death, further assays would be required to determine cell proliferation (such as propidium iodide staining to predict cell cycle phase) or cell death marker assays (such as trypan blue or annexin V).

Throughout these targeted drug screens, I established criteria to decide whether samples were sensitive and whether to pursue the investigation of a compound beyond *in vitro* cell viability assays. As there are currently no validated commercially available ACC cell lines, cell lines derived from different cancers with published IC_{50} values were used as positive and negative controls to determine the level of sample sensitivity to various compounds, as well as published ACC sensitivities. These control cell lines were grown in different media to the ACC primary cells. Although I did not control for the differences in medium components, it is important to note that some differences could promote increased proliferation. However, the purpose of these cell lines was to gait drug sensitivities rather than be a direct comparison therefore medium differences did not need to be controlled for. In addition, as the cell lines proliferate at a higher rate than the primary ACC cells, drug assays were 5 days long opposed to 10.

It has been reported in a translational gastric cancer clinical trial that tumours with high-level *FGFR2* amplification had high response rates to FGFR inhibition (A. Pearson et al., 2016). However, although SG0069 possesses an *FGFR2* amplification, it was not deemed sensitive enough to FGFR inhibition to pursue as it was far less sensitive than the positive control cell line. A potential reason to explain this lack of sensitivity could be due to a genetic aberration providing a level of resistance. Pearson et al identified that *FGFR2* amplified cell lines have a distinct oncogene addiction phenotype that brings the PI3K pathway under the control of FGFR2. However, SG0069 has heterozygous loss of *PTEN*,

and Pearson identified that *PTEN* knockdown reduces *FGFR2*-amplified cell line sensitivity to FGFR inhibition. It would be interesting to investigate whether SG0069 is more dependent on MAPK signalling, as has been reported for breast carcinomas with *PTEN* loss (Ebbesen et al., 2016).

BRD inhibitors have been used in other cancers to selectively inhibit oncogenes by binding to super-enhancers with high BRD4 occupancy. MYC has been targeted using BRD inhibitors in multiple myeloma and, furthermore, MYB has previously been inhibited via BRD4 inhibitors in AML (Lovén et al., 2013; Roe et al., 2015). My results found that sensitivity to BRD4 inhibition did not correlate with the level of *MYB* expression. However, Drier et al reported that JQ1 sensitivity in ACC inversely correlated with tumour grade, with grade III tumours being unresponsive *in vivo,* hypothetically due to having a higher proportion of solid growth and therefore luminal cells with a higher dependency on Notch signalling. Again, my results did not see this correlation as SG0027 has areas of solid growth yet was the most sensitive sample to JQ1 inhibition (Figure 4-4A). Although, as all biopsies were from metastatic sites, all samples are high grade.

The ACC samples were not sensitive to IGFR inhibition, with a proportion of viable cells remaining when dosed at the highest concentration. Perhaps IGFR inhibitors would be more effective when used within a combination treatment as suggested by Andersson et al (Andersson et al., 2017). They identified a triple TK inhibitor combination targeting IGFR, EGFR and MET that inhibited proliferation *in vitro*, although they did raise worries over excess toxicity due to the multi-targeted approach.

CDK inhibitors are a large area of research as CDK's can be divided into two subfamilies with different functions; regulators of cell cycle (CDKs 1-6, 11 and 14-18) or transcription (CDKs 7-13, 19 and 20) (Malumbres, 2014). CYC065 is a CDK2, 5 and 9 inhibitor that has recently progressed to clinical trials for advanced solid cancers (NCT02552953) and in combination with a BCL2 inhibitor for CLL (NCT03739554). CDK5 genetic loss has minimal impact on cell viability therefore the predominant pharmacological mechanism of CYC065 is most likely mediated by CDK2 and 9 inhibition (Frame et al., 2020). I investigated the combination of the CDK inhibitor with a BRD inhibitor as this has

recently been shown to be effective in a number of oncogene-driven cancers. BRD inhibitors have proven synergistic with CDK9 inhibitors in AML, MLL and rhabdoid tumours (Gerlach et al., 2018; McCalmont et al., 2020; Moreno et al., 2017). In addition, BRD inhibition in combination with CDK2 inhibition has proven effective in orthotopically transplanted MYC-driven medulloblastoma PDX models (Bolin et al., 2018). Furthermore, a pre-clinical combination drug screen for Burkitts lymphoma identified that the strongest synergy observed out of 96 drug combinations was for a CDK2/7/9 inhibitor and a BRD4 inhibitor (Tomska et al., 2018).

To reduce the risk of systemic toxicity, synergistic combinations are preferred in the hope to reduce doses whilst still obtaining a therapeutic effect. There are two most common methods to measure synergy. The first is the Bliss independence model, an effect-based strategy, where the effect resulting from the combination of both drugs is compared directly to the individual agents (Bliss, 1939). The model assumes that the two drugs act independently of each other having different sites of action. However, this can be difficult to assume in the case of novel combinations where the mechanism of action may be complex or unknown. The second common method is a dose-effect-based strategy known as Loewe Additivity (Loewe, 1928). This takes into account the individual dose-effect curves to determine the expected (additive) effect and has the ability to determine the relationship at all dose ranges of each drug. This method is also independent of drug mechanism. The median effect approach designed by Chou and Talalay is built upon the model of Loewe Additivity (Ting Chao Chou & Talalay, 1984). This method takes into account the dose ratio and by using constant drug ratios, it reduces the data points required whilst receiving the maximal information. This is beneficial for large scale combination drug screens and was used for the Burkitt lymphoma investigation (Tomska et al., 2018). Furthermore, as the Chou-Talalay method can be adopted for *in vivo* studies, the constant-ratio method is cost-effective reducing the number of animals and drug required (Ting Chao Chou, 2006).

I chose to use the Chou-Talalay constant ratio model as this method has been used in a number of recent publications investigating novel drug combinations, and also because I cannot claim that CYC065 and JQ1 act completely independently of each other as the

Bliss model assumes (Moreno et al., 2017; Rao et al., 2017; Tomska et al., 2018; Whittaker et al., 2018). Each ACC line had differing IC_{50} values for the single agents, therefore the doses used for each line were different as multiples of the IC_{50} concentrations were used to follow the constant-ratio plan. Due to this, it is difficult to compare the level of synergy between samples at specific doses, rather the curves can be used to determine if the combination is synergistic for the specific sample. For example, SG0037 was the most synergistic at the lowest ratio of 0.25 x IC_{50} doses. This raises the issue of sample-sample variability as although the combination was synergistic in all lines, the degree of synergy differs (Figure 4-14). There is an argument that, for this reason of heterogeneous patient populations, combinations don't necessarily need to show synergy. By re-analysing human clinical data where single agent and combination therapies are compared, and by mining a database of PDX combination studies, Palmer et al argue that many FDA-approved combinations show patient benefit via independent drug action opposed to drug synergy due to tumour heterogeneity, meaning patients respond to each drug at different degrees (Palmer & Sorger, 2017). They note that clinical trials based on molecular reasoning have been successful, such as co-inhibition of BRAF and MEK for the treatment of BRAF-mutant melanoma (Long et al., 2014), and perhaps that more precise patient stratification could reveal subpopulations of patients in which synergy is observed that is currently masked by high patient-to-patient variability.

It has been reported that drug schedule plays a role in the efficacy of a drug combination, and some *in vitro* studies have found that sequentially staggering the single agents can increase the combination synergy and potentially reduce toxicity (T C Chou et al., 1996; Zoli et al., 1999). Vogus et al investigated schedule dependent synergy for the combination of gemcitabine and doxorubicin for the treatment of triple negative breast cancer (Vogus et al., 2018). This combination has proven beneficial in previous breast cancer clinical studies however, neutropenia was reported to limit the administered doses, hence the investigation of sequential dosing to prevent toxicity. They reported that giving gemcitabine prior to doxorubicin was significantly more synergistic than in the reverse order or concurrently. This order biologically makes sense as gemcitabine arrests cells in G1/S whereas doxorubicin induces arrest in the G2/M

phases. Based on this, I investigated schedule dependent synergy of CYC065 in combination with JQ1 to inform the best dosing schedule to take forward to *in vivo* studies. Logically, if a difference was to be expected in the order of drug treatment, I would predict that JQ1 followed by CYC065 would be the most effective. This is because BRD4 recruits the P-TEFb complex to the promoter, CDK9 is the kinase domain of P-TEFb so BRD4 would inhibit its activity, which would be maintained when CYC065 is administered and JQ1 treatment ceased. However, concurrent treatment was more effective than sequential in either order for all three lines investigated (Figure 4-15). This may be partly because BRD4 mediates a compensatory mechanism to overcome CDK9 inhibition preventing RNA polymerase II pausing (H. Lu et al., 2015; Sonawane et al., 2016). Therefore, BRD4 and CDK9 inhibitors may need to be administered together, and that will be the plan for *in vivo* assays to confirm the sensitivity observed in these 2D PDX-derived assays and to identify potential biomarkers of therapeutic efficacy.

5. *In vitro* PDX-derived preclinical models

5.1. Introduction

ACC research has been hindered by the lack of validated pre-clinical models. Genetic profiling of six commercially available ACC cell lines identified that all were either contaminated with HeLa cervical cancer or T24 bladder lines or were not of human origin, and to-date there are no available SG ACC cell lines from ATCC (Phuchareon et al., 2009). In other cancers, PDX tumour tissue has been widely used to establish 2D and 3D cultures. Both PDX-derived 2D and 3D models have been applied to drug sensitivity assays and also tumour niche studies, identifying microenvironmental factors that are required for tumour survival, growth and metastasis. 3D organoids are thought to be more relevant than 2D models as they can maintain heterogeneity and have a higher degree of structural complexity, closely resembling tumour architecture. Furthermore, there are currently a number of successful PDX/PDO biobanks established such as for breast cancer and CRC, that represent the majority of tumour subtypes and genetic diversity (Bruna et al., 2016; Byrne et al., 2017; S. H. Lee et al., 2018; Sachs et al., 2018). These biobanks are particularly useful for rare cancers for which alternative pre-clinical models are not available. Therefore, in this chapter I aim to optimise the short-term 2D models used in the previous chapter, and also the methodology to establish long-term ACC PDX-derived 3D organoid models.

5.2. 2D PDX-derived models

5.2.1. Recapitulation of the PDX molecular characteristics

To assess how relevant the 2D PDX-derived models were, I investigated whether the 2D cultures molecularly recapitulate the PDX lines. I compared the level of MYB protein expression from three separate SG0032 PDX passages and 2D cultures via western blot (Figure 5-1). It was striking how significantly MYB expression was reduced in the 2D

models. Therefore, to identify other differences at the transcriptional level between the PDX tumours and derived-2D models, an RNAseq was conducted using three paired SG0032 PDX and derived 2D cultures. Pathway enrichment analysis identified significantly upregulated and downregulated pathways from gene set enrichment analysis (GSEA) (Figure 5-2) (full GSEA data supplied in appendix 4, chapter 9.4). E2F targets and the G2M checkpoint pathways were significantly upregulated in the PDX tumours compared to the matching 2D cultures. Whereas pathways downregulated in the PDX samples compared to the 2D cultures included EMT, TNFA, p53 and TGFß signalling. As expected, *MYB* was significantly downregulated in the 2D samples by -4.02 Log2 fold (a 16.22-fold decrease), as well as the well-known MYB downstream target *EN1* by -2.39 Log2 fold. In addition to the enriched pathways identified, by manually mining the DEGs some other key differences were highlighted. Firstly, *WNT3A* was 3.5 Log2 fold higher in the PDX samples than the derived 2D cultures. Secondly, *BMP7* was 4.8 Log2 fold higher in the PDX samples. It was also noticed that a number of genes involved in retinoic acid (RA) signalling were differentially expressed; *ALDH1A3*, *ALDH3B1*, and *RDH10* were significantly lower in the PDX samples compared to the 2D cultures by -8.7, -2.1 and -3.1 Log2 fold respectively. Therefore, it is clear that there are a number of differences between the PDX and 2D-derived cultures, suggesting that culture conditions could be manipulated to make the 2D models more relevant.

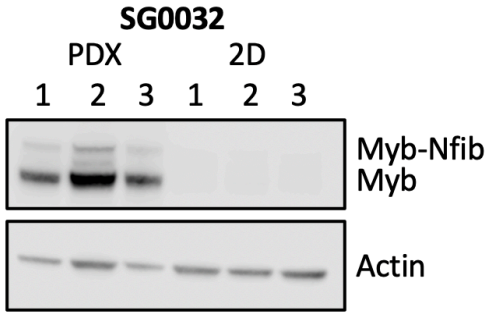

Figure 5-1 MYB expression in SG0032 PDX tumours compared to PDX-derived 2D cultures

MYB expression analysis via Western blot in three SG0032 PDX-derived 2D cultures compared to independent SG0032 PDX tumours. Actin was used as the loading control.

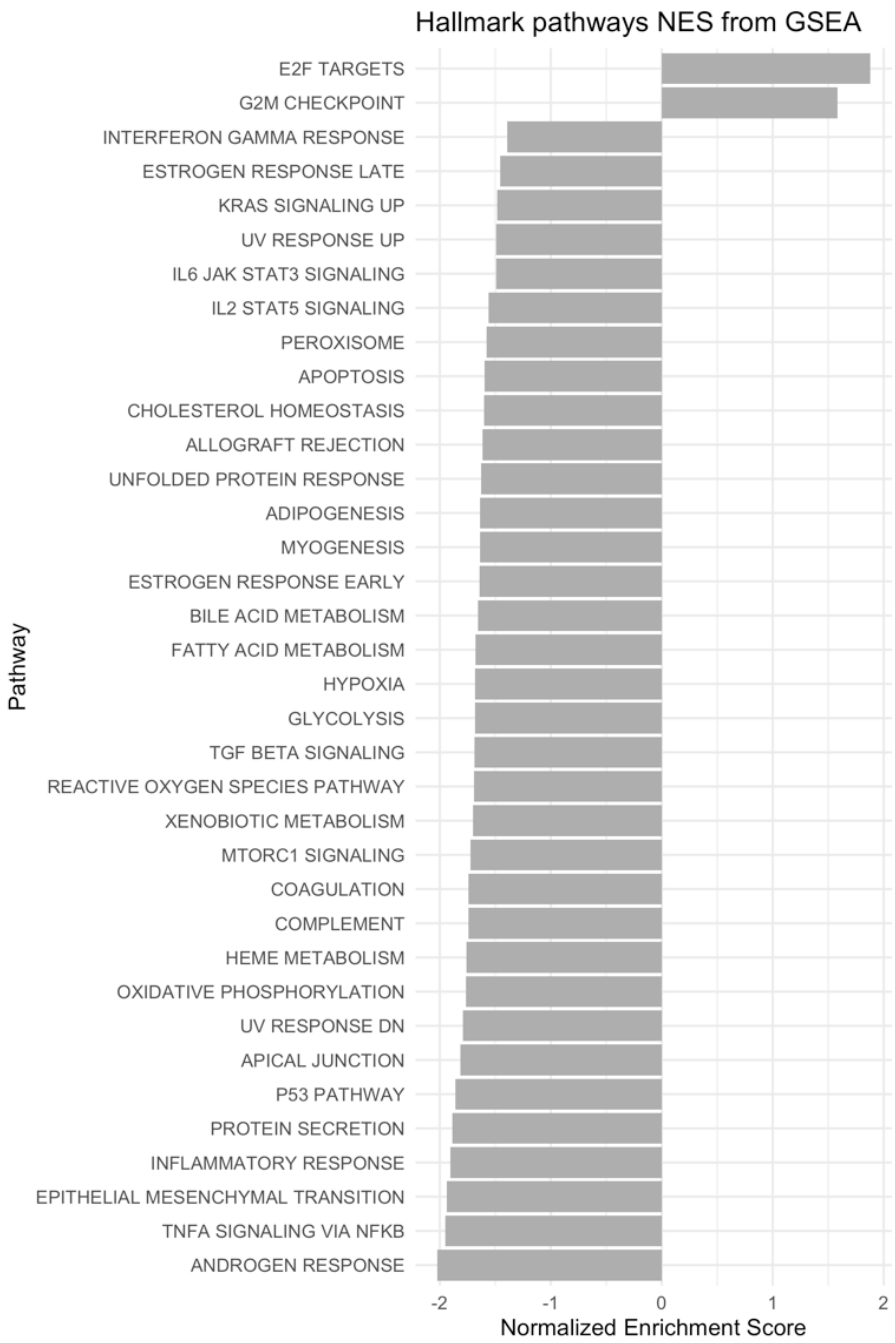

Figure 5-2 Pathway enrichment analysis from SG0032 PDX vs PDX-derived 2D culture RNAseq

Gene set enrichment analysis (GSEA) was performed on the significantly up- and downregulated DEGs in the SG0032 PDX tumours normalised to the SG0032 PDX-derived 2D cultures. Significantly upregulated and downregulated hallmark pathways according to significant DEGs, Padj < 0.05. Hallmark gene sets from the Molecular Signatures Database were used.

5.2.1. 2D culture optimisation

In order to make the 2D PDX-derived cultures more relevant to the PDX tumours, specific inhibitors or ligands were selected according to the enriched pathways and DEGs from the RNAseq, to add to the growth medium. The chosen targets were the Wnt, BMP7, RA, and TGFß signalling pathways. Therefore, I investigated the effect of addition of the following compounds; WNT3A (50 ng/mL, Peprotech), BMP7 (25 ng/mL , ThermoFisher Scientific), the TGFß inhibitor A83-01 (0.5 µM, Bio-techne), and the RA signalling inhibitors 4-diethylamino-benzaldehyde (DEAB) (50 µM, Sigma) and BMS493 (5 µM, gifted by Dr Eric So, ICR). SG0032 PDX-derived cells were plated in 2D in different medium conditions and RNA extracted when cells were over 80% confluent. Analysis of *MYB* expression via q-rtPCR identified that total *MYB* and *MYB-NFIB* transcript expression was significantly increased by 4.5-fold and 4.06-fold respectively following the addition of A83 ($P < 0.0001$) (Figure 5-3A). *EN1* expression was also significantly increased by A83 by 3.7-fold ($P < 0.0001$) and by both the RA signalling inhibitors, DEAB by 3.5-fold ($P = 0.0003$) and BMS493 by 4.7-fold ($P < 0.0001$). However, BMS493 reduced *MYB* expression by one third. Cellular phenotype was also altered with each medium condition; both A83 and WNT3A induced more cystic structures with cell clumps forming with A83 in particular, whereas cystic structures were absent with the addition of BMP7, however both DEAB and BMS493 promoted less adherent 2D growth and more 3D structures (Figure 5-3B). Similar effects were observed in SG0037, with A83 inducing a 4.9-fold increase in *MYB* expression and BMS493 inducing a 4.6-fold increase in *EN1* expression (Figure 5-3C). However, BMS493 also increased *MYB* expression which was opposite to the effect seen in SG0032. Unfortunately, only one biological experiment for the latter line was completed therefore statistical analysis could not be conducted. These studies point to a role for TGFß signalling in regulating MYB expression in 2D models.

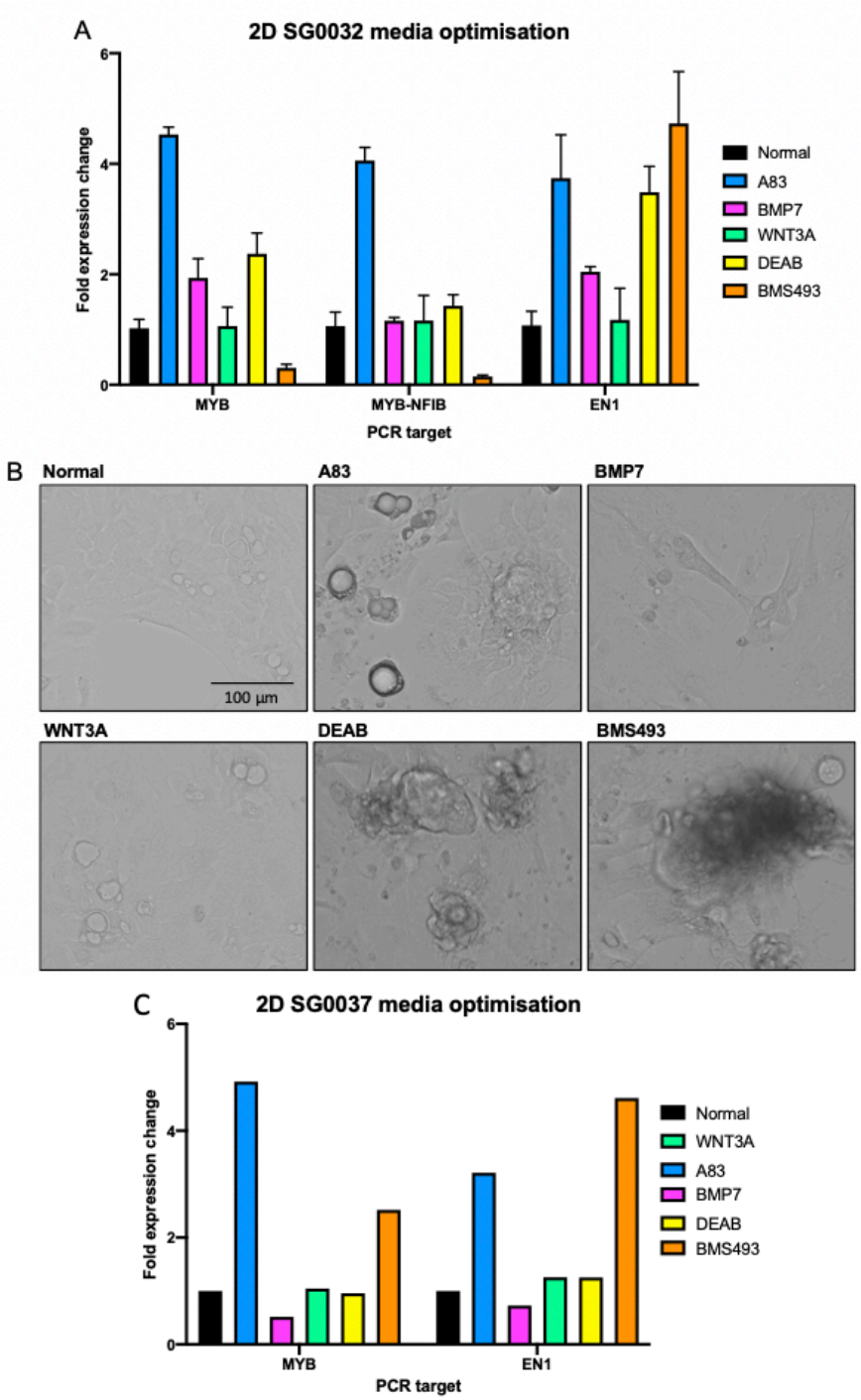

Figure 5-3 2D culture medium optimisation

A) SG0032 PDX-derived cells were cultured in 2D with normal medium with the addition of either A83-01, WNT3A, BMP7, DEAB or BMS493. RNA was extracted and *MYB*, *MYB-NFIB* and *EN1* expression quantified via q-rtPCR. Data was analysed using the comparative CT method ($\Delta\Delta$CT), with samples normalised to the relative housekeeping gene GAPDH values, and then to the normal samples (n=3, mean +/- SE). Significant expression differences are discussed in the text, calculated by a two-way ANOVA identifying differences between fold expression change for all media conditions, followed by Dunnett's multiple comparisons test. B) EVOS images of SG0032 2D growth

under each medium condition at 10x magnification. Scale bar = 100 µm. C) SG0037 PDX-derived cells were cultured under the same medium conditions as SG0032, and expression of *MYB* and *EN1* quantified via q-rtPCR. No statistical analysis was conducted due to results being from one experiment.

The TGFßR1 ALK5 kinase inhibitor, A83-01, has been reported to also inhibit FGFR2 by more than 50% at 1 µM, therefore I investigated reducing the concentration by 5 fold to avoid this non-specific inhibition (Vogt et al., 2011). In addition, an alternative inhibitor SB505124 (1 µM, Stratech) was also investigated to confirm that the observed increased *MYB* expression was through TGFß signalling inhibition. Both TGFß inhibitors significantly increased total *MYB* and translocated *MYB* to the same degree at the transcriptional level ($P < 0.0001$) (Figure 5-4A). Therefore, as both TGFß inhibitors have comparable effects promoting *MYB* expression, it can be concluded that TGFß signalling inhibits *MYB* expression. Although, *EN1* expression was not increased to the same level. Interestingly, images of the 2D cultures show different cellular phenotypes between A83 and SB505124 (Figure 5-4B). Whilst cultures with A83 addition have more cystic structures, the addition of SB505124 induced less adherent growth and more 3D structures. In the RNAseq data TGFß1, TGFßR1 and TGFßR2 are all significantly increased in the 2D PDX-derived cultures, therefore I wanted to investigate whether this increase in TGFß signalling was induced by an existing medium component. There are reports that both EGF and insulin can promote TGFß signalling, with both stimulating TGFß receptor expression, however, removal of EGF or insulin from the medium had no impact on *MYB* expression (Figure 5-4A) (Budi et al., 2015; Shu et al., 2019).

To investigate whether TGFß inhibition affected cell growth, a 10-day assay was conducted in SG0032 PDX-derived 2D cells to assess cell doubling rate. The assay confirmed that 0.5 µM of A83 significantly reduced the doubling rate of SG0032 (Figure 5-4C). However, there was very little difference between the doubling rates from normal, 0.1 µM A83 and 1 µM SB505124 conditions. The lack of difference in doubling rate between normal, 0.1 µM A83 and 1 µM SB505124 conditions did not correlate with the expression levels of the proliferation marker, Ki67 (Figure 5-4A). The TGFß inhibitors induced significantly higher Ki67 expression compared to the normal medium conditions (A83: $P = 0.045$) (SB505124: $P < 0.0001$). To determine whether this discrepancy is due

to increased cell death in the TGFß inhibitor conditions meaning the cell number remains constant across all conditions, caspase-3 should be measured. Despite this, the selected optimum medium condition for SG0032, increasing MYB expression whilst not limiting proliferation, was 0.1 µM A83.

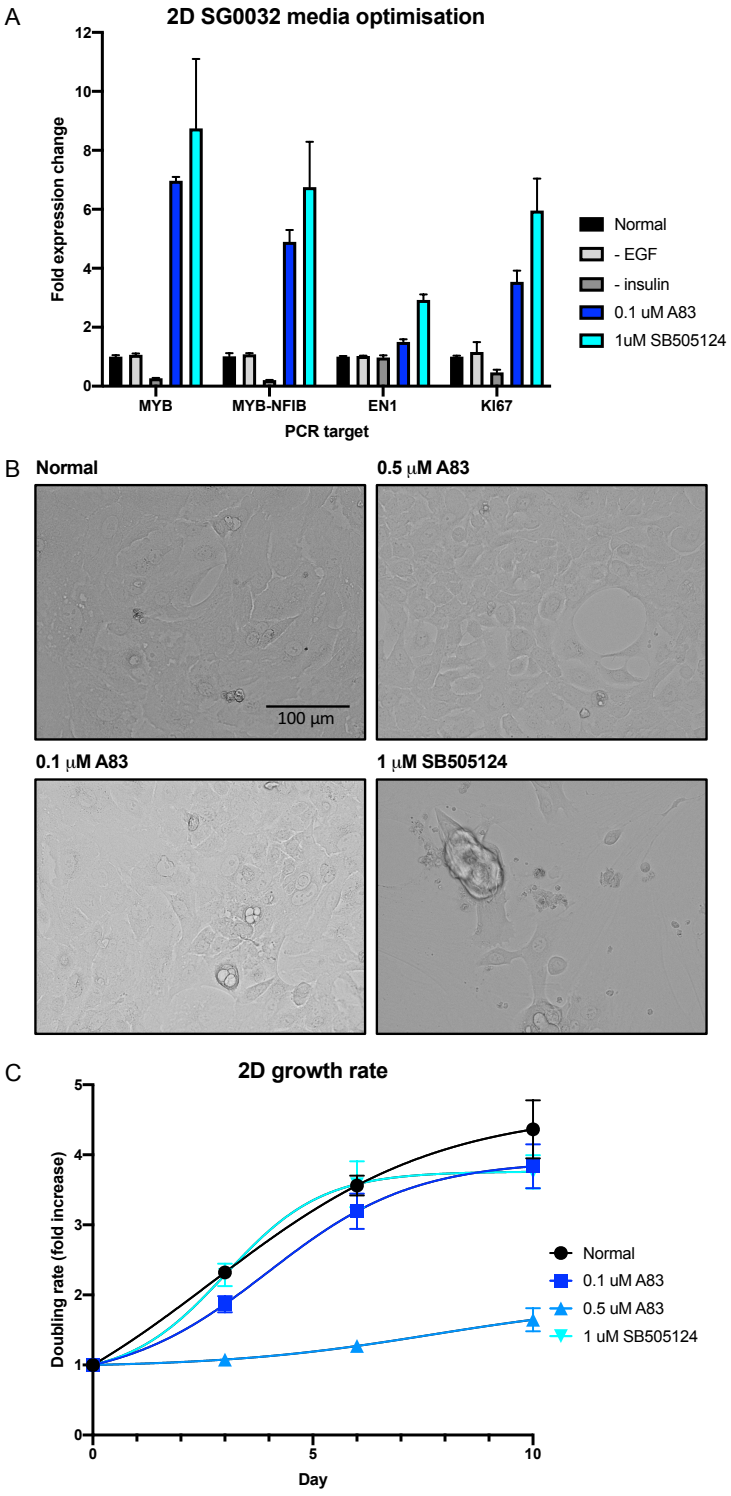

Figure 5-4 The impact of TGFß inhibition on SG0032 2D culture

SG0032 PDX-derived cells were cultured in 2D with normal medium with the addition of either 0.1 µM A83-01, 0.5 µM A83-01 or 1 µM SB505124. A) RNA was extracted and *MYB*, *MYB-NFIB*, *EN1* and *Ki67* expression quantified via q-rtPCR. Data was analysed using the comparative CT method (ΔΔCT), with samples normalised to the relative housekeeping gene GAPDH values, and then to the normal samples (n=3, mean +/- SE). Significant expression differences are discussed in the text, calculated by a two-way ANOVA identifying differences between fold expression change for all media conditions, followed by Dunnett's multiple comparisons test. B) EVOS images of 2D growth under each medium condition at 10x magnification. Scale bar = 100 µm. C) Cell viability was measured via CTG at day 0, day 3, day 6 and day 10 of assay set up. Luminescence readings were normalised to day 0 and expressed as fold increase.

5.2.2. Confirmation of drug sensitivity assays

The drug experiments in the previous chapter were conducted prior to the RNAseq results comparing PDX tumour expression to the same sample in 2D. Therefore, I repeated the drug combination experiments in the optimised culture medium to confirm whether the drug responses were similar. Addition of the TGFß inhibitor, 0.1 µM A83-01, to SG0032 resulted in increased sensitivity to CYC065 alone with IC_{50} values of 0.18 µM and 0.32 µM respectively (Figure 5-5A and B). With the constant addition of 0.1 µM JQ1, SG0032 with A83 was slightly more sensitive than SG0032 cultured in previous condition with IC_{50} values of 0.1 µM and 0.18 µM respectively. One caveat to this is that in the optimised medium condition the addition of 0.3 µM JQ1 at 0.3 µM CYC065 did not result in an SF of 0, suggesting that the cells could potentially be less sensitive to the combination at higher doses. To determine whether the combination remains synergistic under the optimised medium condition, the sensitivity index (SI) was calculated (adapted from Ye et al., 2012; C. Zhang et al., 2019). The SI quantifies the difference between the expected and the observed effect of a drug combination, calculated by:

$$SI = \left[\frac{\text{1-DrugA}_{conc}}{\text{1-Control}} \times \frac{\text{1-DrugB}_{conc}}{\text{1-Control}} \right] - \frac{\text{1-DrugAB}_{conc}}{\text{1-Control}}$$

The SI scale ranges from -1 to 1, with positive values indicating super additivity/synergy and negative values indicating antagonism. The SI values were calculated for the combination of 0.1 µM CYC065 and 0.1 µM JQ1 for SG0032 in both the previous medium

and optimised medium, giving values of 0.228 and 0.001 respectively. This indicates that the drug synergy observed in SG0032 previously is potentially lost in the optimum medium for increased *MYB* expression at the tested doses.

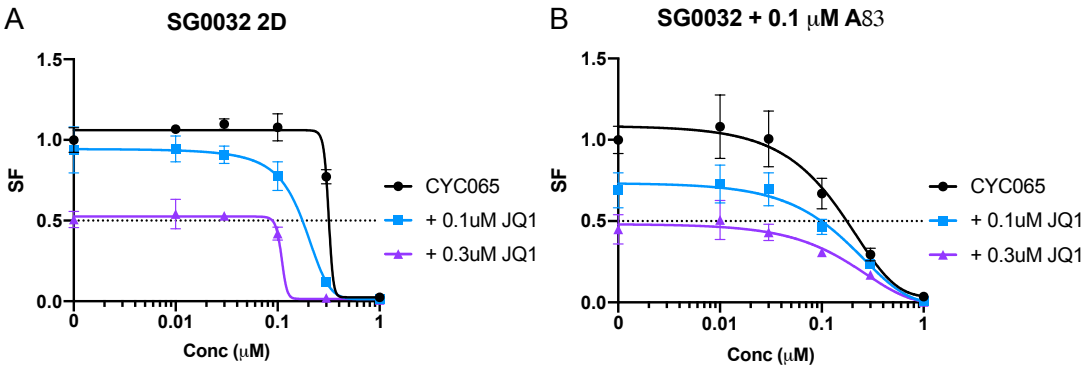

Figure 5-5 Combination confirmation in optimised 2D growth conditions

10-day 2D SG0032 CYC065 sensitivity curves with the constant addition of either 0.1 µM and 0.3 µM JQ1. A) Drug assays conducted using previous media conditions. B) Drug assays conducted in the optimised media, with the addition of 0.1 µM A83-01. Each luminescence reading was normalised to the untreated CYC065 control reading. Data shown is representative of two independent biological repeats and each data point is the mean SF for six parallel technical replicates +/- SD. Corresponding SI values calculated for combination at doses of 0.1 uM CYC065 and 0.1 uM JQ1: A) SI = 0.228 (additive/low synergy) B) SI = 0.001 (no synergy).

5.3. 3D models

3D models are thought be more accurate representations of the patient tumour than 2D models, therefore I aimed to establish long-term 3D PDX-derived models to identify ACC niche requirements and confirm drug sensitivities identified in chapter 4.

5.3.1. Normal murine SG organoids

The culture conditions for normal murine SG organoids have been established and published (Maimets et al., 2016; Nanduri et al., 2014). I cultured murine SG organoids as a model to compare ACC growth requirements. The organoids are highly structured and branched, dependent on Wnt and R-spondin addition. They are highly differentiated having AQP5 positive acinar cells (Figure 5-6A and B).

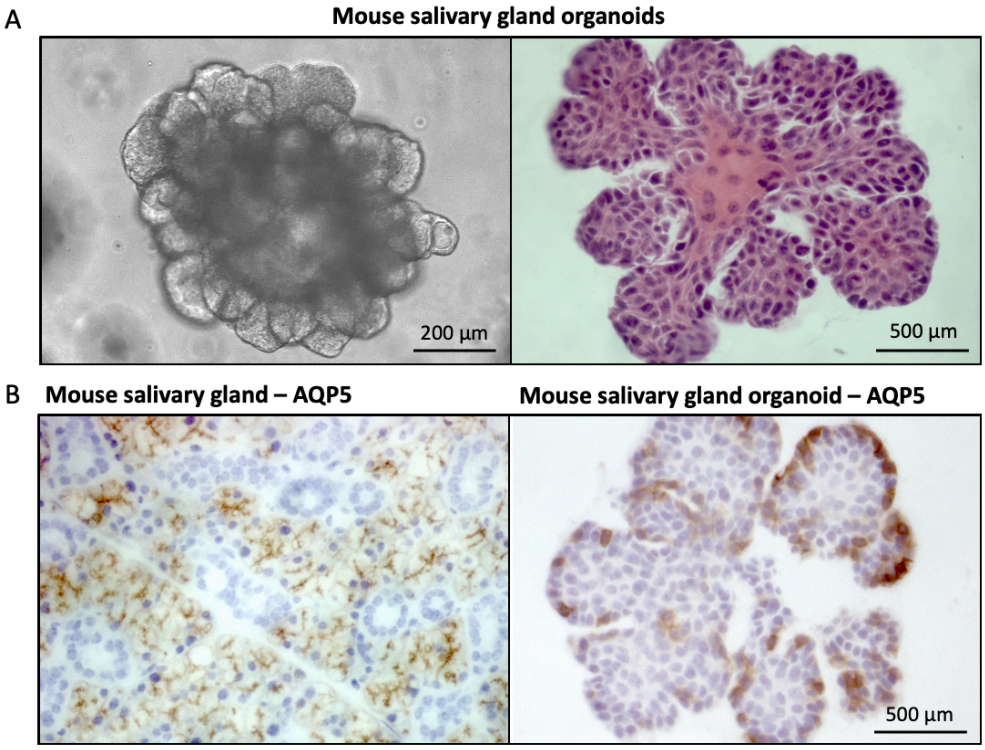

Figure 5-6 Histological analysis of murine normal SG organoids

Adult mouse salivary gland-derived organoids were fixed in 10% formalin, resuspended in histogel, and embedded in paraffin. 4 µm thick sections of normal mouse salivary gland, or organoids were stained with A) H&E or B) aquaporin-5 (AQP5). Slides were images at 20x magnification. Scale bar sizes are indicated in the image.

5.3.2. PDX-derived ACC organoids

Medium for ACC organoids was first taken from that outlined for the normal murine SG organoids. However, it is evident by the decrease in the number and size of organoids that the medium tailored to murine normal SG growth is not optimal for the growth of ACC (Figure 5-7). This suggests that normal SG and ACC have different niche requirements, and rely on different growth factors for proliferation and expansion, and like the 2D PDX-derived cultures, the culture conditions may be inhibiting MYB expression.

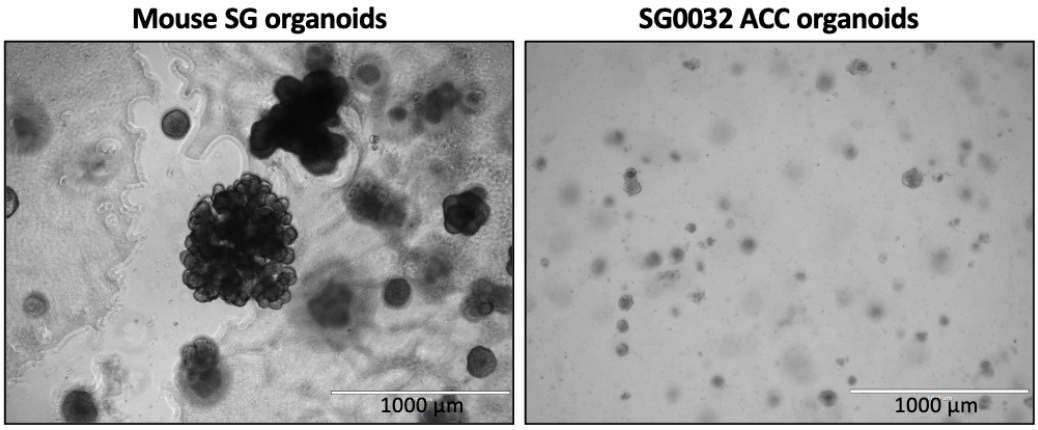

Figure 5-7 Murine salivary gland organoids compared to ACC PDX-derived organoids

EVOS images of mouse SG organoids and SG0032 PDX-derived ACC organoids cultured in published murine SG medium (Maimets et al., 2016; Nanduri et al., 2014). Images taken at 4x magnification. Scale bar = 1000 µm.

Based on the optimum conditions for MYB expression identified in the 2D cultures, I investigated the addition of A83, as well as BMP7 and BMS493 in SG0032 PDX-derived 3D cultures. The addition of A83 significantly increased *MYB* ($P = 0.002$) and translocated *MYB-NFIB* ($P = 0.0004$) expression compared to culture without A83, mirroring the effect observed in the 2D cultures (Figure 5-8A). The addition of BMP7 or BMS493 has no significant effect on expression levels when added to normal medium or with A83 addition. The number of organoids that grew from single cells was slightly higher with the addition of A83 than without, and organoids were generally larger with A83 addition (Figure 5-8B). Despite the organoids with A83 expressing higher *MYB* and being larger, the cultures were unable to be passaged. Therefore, I investigated a range of growth factors and growth conditions, to identify the optimum niche requirements for ACC growth and successful passage to enable 3D organoid line generation. From this point A83 was added to all ACC organoid media, and from here on is referred to as “normal” medium.

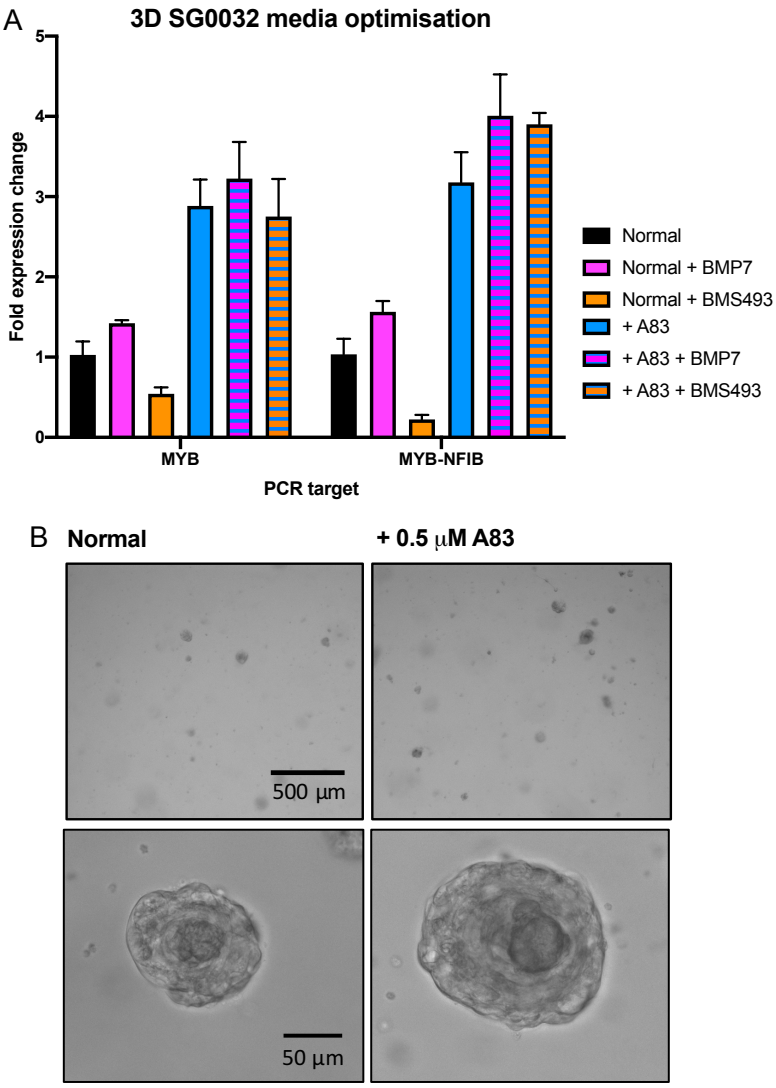

Figure 5-8 SG0032 3D culture medium optimisation

A) SG0032 PDX-derived cells were cultured in 3D with normal medium or with A83-01, with the addition of either BMP7 or BMS493. RNA was extracted and *MYB* and *MYB-NFIB* expression quantified via q-rtPCR. Data was analysed using the comparative CT method ($\Delta\Delta$CT), with samples normalised to the relative housekeeping gene GAPDH values, and then to the untreated samples. Three technical repeats were conducted for each media condition, and data is presented as the mean +/- SE. Significant expression differences are discussed in the text, calculated by a two-way ANOVA identifying differences between fold expression change for all media conditions for each gene, followed by Tukey's multiple comparisons test. B) EVOS images of SG0032 3D growth under each medium condition at 4 and 20x magnification.

Wnt signalling

Canonical Wnt signalling factors were significantly upregulated in the ACC samples compared to normal SG (Figure 3-1), therefore the effect of the Wnt signalling agonist R-spondin (100 ng/mL, Miltenyi Biotec) was investigated. By comparing mouse embryonic SG organoids and PDX-derived organoids it is clear that normal and cancerous tissues have differing pathway dependencies. Embryonic cells are highly pluripotent, having high levels of Wnt (N. Patel et al., 2011). Enhanced Wnt signalling via the Wnt agonist R-spondin resulted in large luminal structures but inhibited branching compared to normal organoid medium that formed budding structures (Figure 5-9). On passaging of the organoids to single cells, removing R-spondin resulted in highly differentiated, branched structures, closely resembling the histological structure of a murine salivary gland. H&E staining showed a complex structure with lumen formation. When SG0032 PDX-derived organoids were treated with R-spondin, organoid count was significantly higher ($P = 0.0096$) although there was no significant increase in organoid area (Figure 5-10). However, further optimisation was needed as organoid passaging was unsuccessful with R-spondin addition.

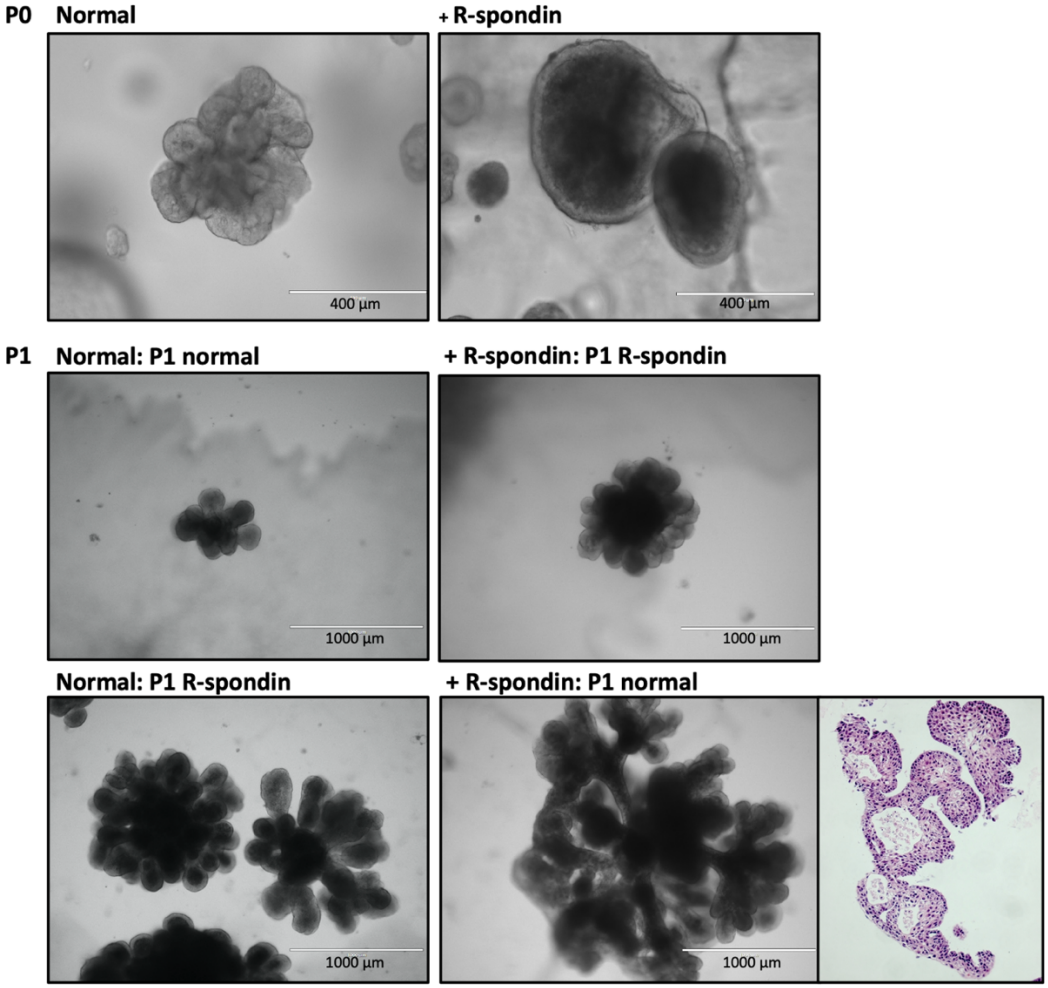

Figure 5-9 Wnt signalling dependency in embryonic mouse salivary gland organoids

Embryonic mouse salivary gland was dissociated to single cells and cultured as organoids. P0: Enhanced Wnt signalling via R-spondin lead to large lumen-like structures with inhibited branching. Scale bar = 400 µm. P1: Normal medium organoids passaged to the same condition formed small budding structures (500 µm), R-spondin grown organoids passaged to R-spondin medium were larger (900 µm) but without branching. Removing R-spondin after passaging resulted in the most complex structure, over 1000 µm. H&E staining showed a highly differentiated large branched structure with lumen formation

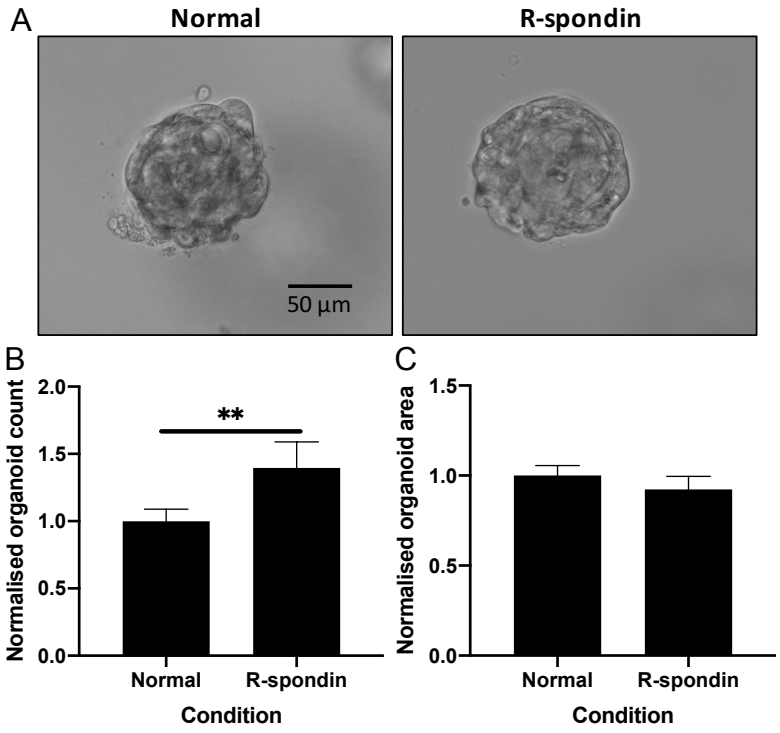

Figure 5-10 SG0032 ACC organoids are not dependent on Wnt signalling

A) The addition of R-spondin to SG0032 organoid medium had no effect on size or structure. No branching was observed and structures were limited (70 µm). B) Organoid count above 50 µm and (C) organoid area normalised to normal ACC medium conditions (n=3, mean +/- SE). After 7 days, significantly more organoids grew with R-spondin (unpaired t test, **, P = 0.0096). Organoid data was analysed using MetaXpress® High-Content Image Acquisition and Analysis Software.

Neural factors

Neural signalling factors were investigated as they were highly expressed in the ACC samples when compared to the non-ACC tumour, SG0043, suggesting a propensity for a neural niche. Three neural pathways were investigated; neurotrophin signalling, neuregulin signalling and muscarinic signalling. The neurotrophin family is highly expressed in ACC according to published reports, and NTRK2 and 3 were highly expressed in ACC compared to normal SG and acinic cell carcinoma (Figure 3-1) (Ivanov, Panaccione, Brown, et al., 2013). NTK signalling is implicated in cell survival and is highly active in neural crest progenitor cells (Youn et al., 2003). Therefore, the NTRK3 natural ligand, NT3 (100 ng/mL, Peprotech) was added to organoid medium for both SG0028 and SG0032 PDX-derived organoids, however this resulted in reduced growth for SG0032 (Figure 5-11A).

Neuregulin (NRG) in a member of the EGFR family, acting on the ErbB receptor. NRG is associated with neuronal survival and neural fate determination and has been found to increase the proliferation of neuronal progenitors from embryonic neural stem cells (Y. Liu et al., 2005). However, addition of NRG-1 (100 ng/mL, Peprotech) reduced organoid growth particularly in SG0032-PDX derived cultures (Figure 5-11A).

Muscarinic (M1) receptors are involved in the parasympathetic nervous system. During salivary organogenesis, parasympathetic innervation maintains epithelial progenitor cells, which is mimicked in explant culture via M1 signalling (Knox et al., 2010). Via parasympathetic ganglion removal and M1 receptor inhibition, it was found that these factors are required for epithelial morphogenesis. The neurotransmitter acetyl choline binds to and activates M1 receptors, therefore the acetyl choline analogue carbamoyl choline (CCh) was used *in vitro* to identify that M1 signalling maintains basal progenitor cells and promotes proliferation. Due to these findings, the addition of CCh was investigated in the ACC-derived organoids. The addition of CCh (10 nM, Sigma) resulted in larger organoid structures in both SG0028 and 32, with significantly more organoids over 50 µm in diameter in SG0032 compared to normal medium ($P = 0.014$) (Figure 5-11A and B). This indicates that ACC is responsive to parasympathetic signalling, however passaging was still unsuccessful.

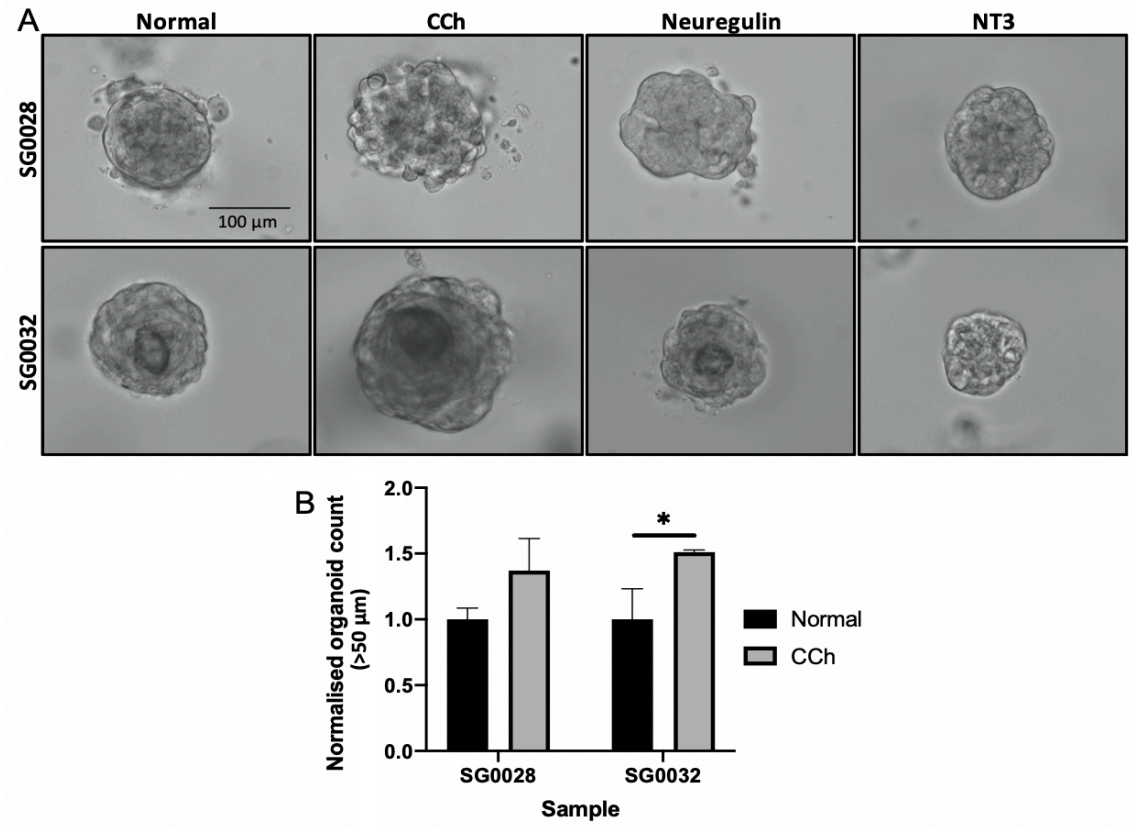

Figure 5-11 The impact of neural factors on ACC organoid growth

SG0028 and 32 PDX-derived organoids were grown in the presence of neuronal signalling factors; carbamoyl choline (CCh), neuregulin, or neurotrophin 3 (NT3). A) Images of representative organoids from each condition for SG0028 and 32 taken at 20x magnification. In both lines, CCh resulted in the largest organoids. Scale bar = 100 µm. B) Number of organoids above 50 µm in diameter for SG0028 and 32 with the addition of CCh, normalised to the normal medium condition (parallel biological triplicates, mean +/- SE). Organoid data was analysed using MetaXpress® High-Content Image Acquisition and Analysis Software. Statistical analysis via a two-way ANOVA identifying differences between organoid count for each medium condition for each PDX sample, followed by Sidak's multiple comparison test (*, P = 0.014).

Hypoxia

Head and neck tumours are reported to have an average tumour oxygen (O_2) percentage of 2% (Mckeown, 2014). Furthermore, it has been reported that hypoxia-inducible factor 1 alpha (HIF-1α) and other hypoxia-related proteins increase invasiveness in ACC (De Mendonça et al., 2020; Lim et al., 2017). Therefore, I compared the culture of normal mouse SG organoids, SG0027-derived and SG0032-derived ACC organoids under hypoxic (2% O_2) and normoxic conditions (20% O_2) (Figure 5-12). There was a stark difference between growth in normoxic and hypoxic conditions. Normal SG organoids under hypoxic conditions were far smaller in size (approximately 150 µm in diameter compared to 400 µm in normoxic) and the branching morphology was inhibited. In contrast both SG0027 and 32 ACC PDX-derived organoids appeared to thrive in hypoxic conditions, growing to at least double the size of when grown in normoxic conditions. Hypoxia was the only condition that enabled passaging of ACC organoids; SG0027 were passaged up to P6 whereas SG0032 were passaged up to P2. However, culturing under hypoxic conditions was limited as there is one hypoxic chamber at 2% O_2 in the institute, so prolonged culture of organoids was dependent on chamber availability. Interestingly, mouse SG organoids did not survive passage under hypoxia whereas they passage indefinitely under normoxic conditions.

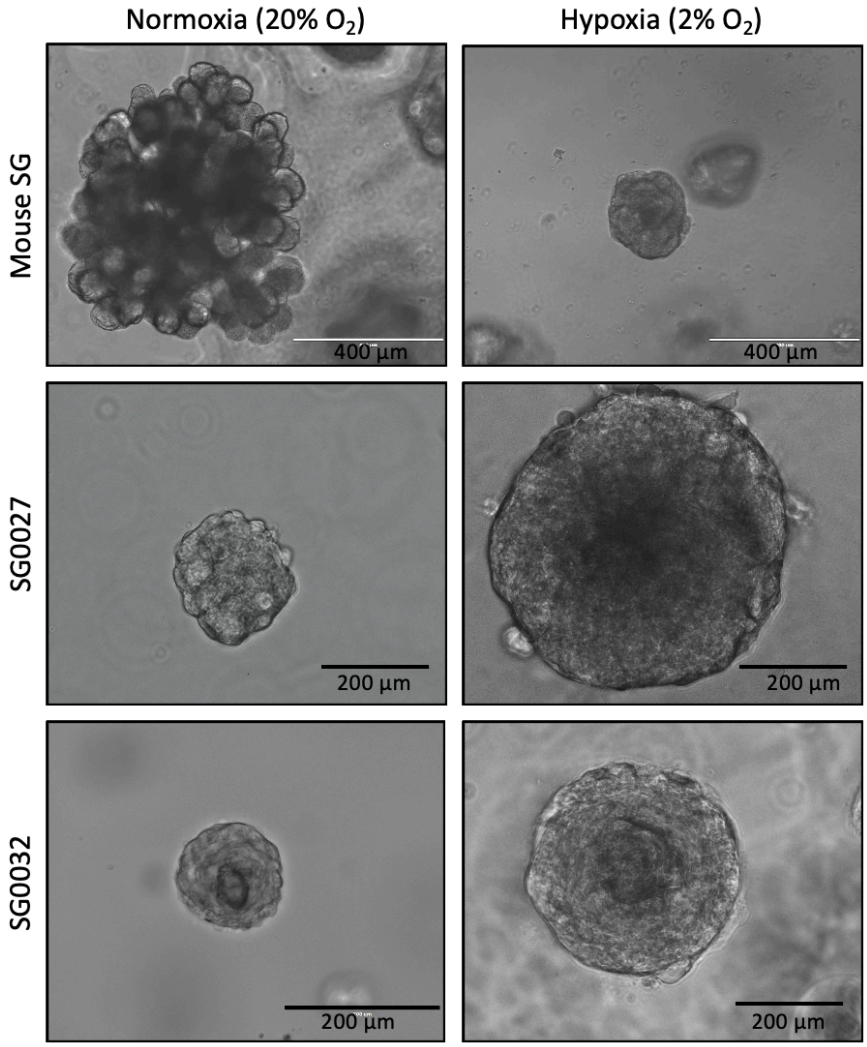

Figure 5-12 ACC organoids prefer a hypoxic environment

Normal mouse SG organoids and SG0027 and 32 PDX-derived ACC organoids were grown in normal culture conditions (normoxic, 20% O_2) and hypoxic conditions (2% O_2). Mouse SG organoids were imaged at 4x magnification, whereas ACC organoids were imaged at 20x magnification. Scale bar for mouse SG organoids = 400 µm, and ACC organoid scale bars = 200 µm.

ACC PDX-derived organoid comparison to PDX lines

Overall, successful organoid cultures were derived from SG0027, 32 and 69. SG0027 and 32 were established under hypoxic conditions, whereas SG0069 was cultured in normoxic conditions. To determine whether the organoids histologically recapitulate the PDX tumour, the organoids were stained via H&E (Figure 5-13). It is clear that the growth patterns are very similar between the PDX tumour and derived-organoids. SG0027 has some areas of more solid growth, SG0032 has a clear cribriform pattern, whereas SG0069 appears to have a solid "bunch of grapes" appearance. To identify the cell types present in the organoids, sections were stained via IHC for luminal marker CK8, and the basal and myoepithelial marker TP63 (Figure 5-14). CK8 and TP63 staining in the organoids closely correlated with the PDX tumour staining. MYB protein expression was also compared between the organoids and PDX. All cells were positive for MYB in the SG0027 organoids, although staining was slightly weaker than in the PDX tumour. SG0069 organoids were negative for MYB expression which correlated with the tumour. SG0032 had a few cells that were very weakly positive for MYB, however all cells within the PDX tumour were strongly positive indicating that MYB expression in SG0032 is differentially expressed.

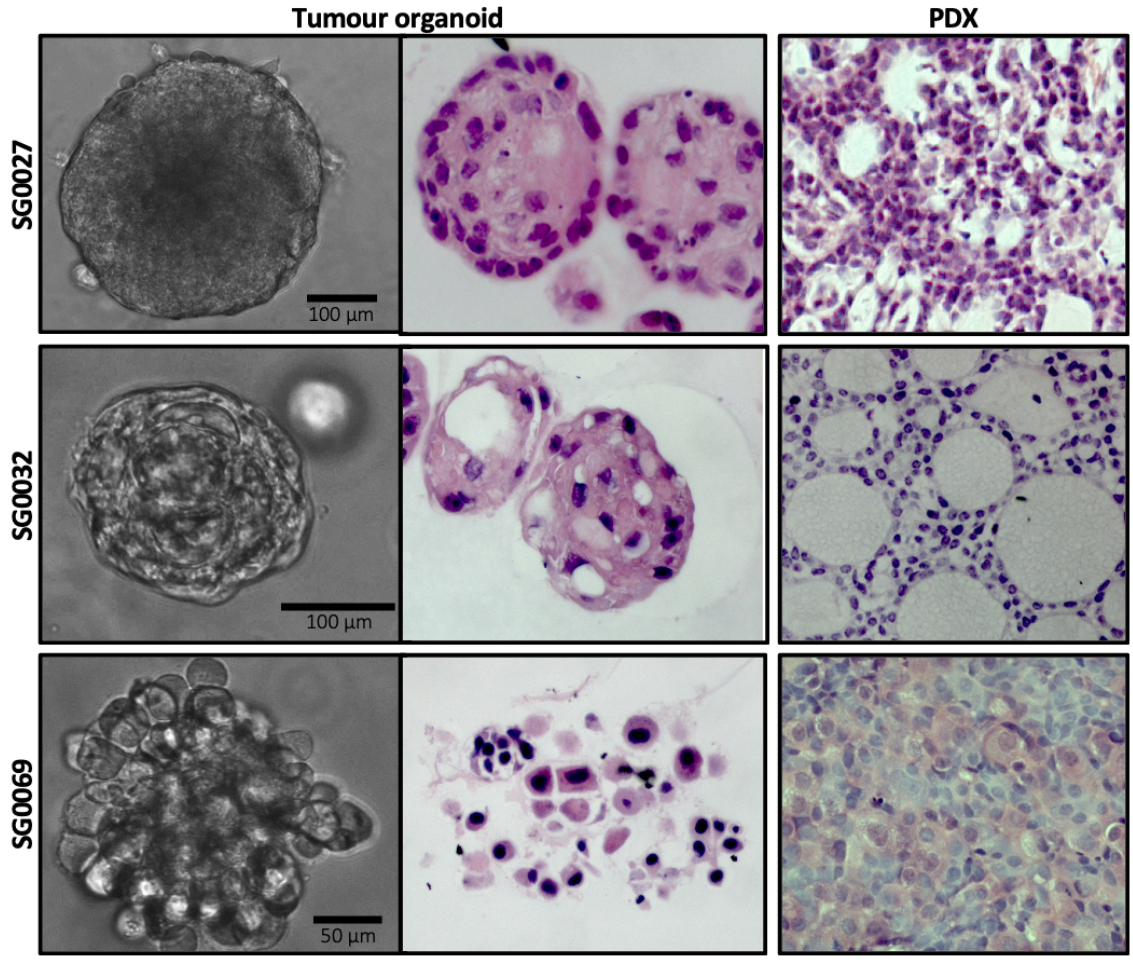

Figure 5-13 ACC PDX-derived organoids recapitulate the PDX growth pattern

ACC PDX-derived organoids were fixed in 10% formalin, resuspended in histogel, and embedded in paraffin. 4 µm thick sections of organoids, or PDX tumour were stained via H&E. SG0027 organoids were passage 4 grown in hypoxia, SG0032 organoids were passage 1 grown in hypoxia, and SG0069 were passage 0 grown under normal culture conditions. Images were taken at 20x magnification.

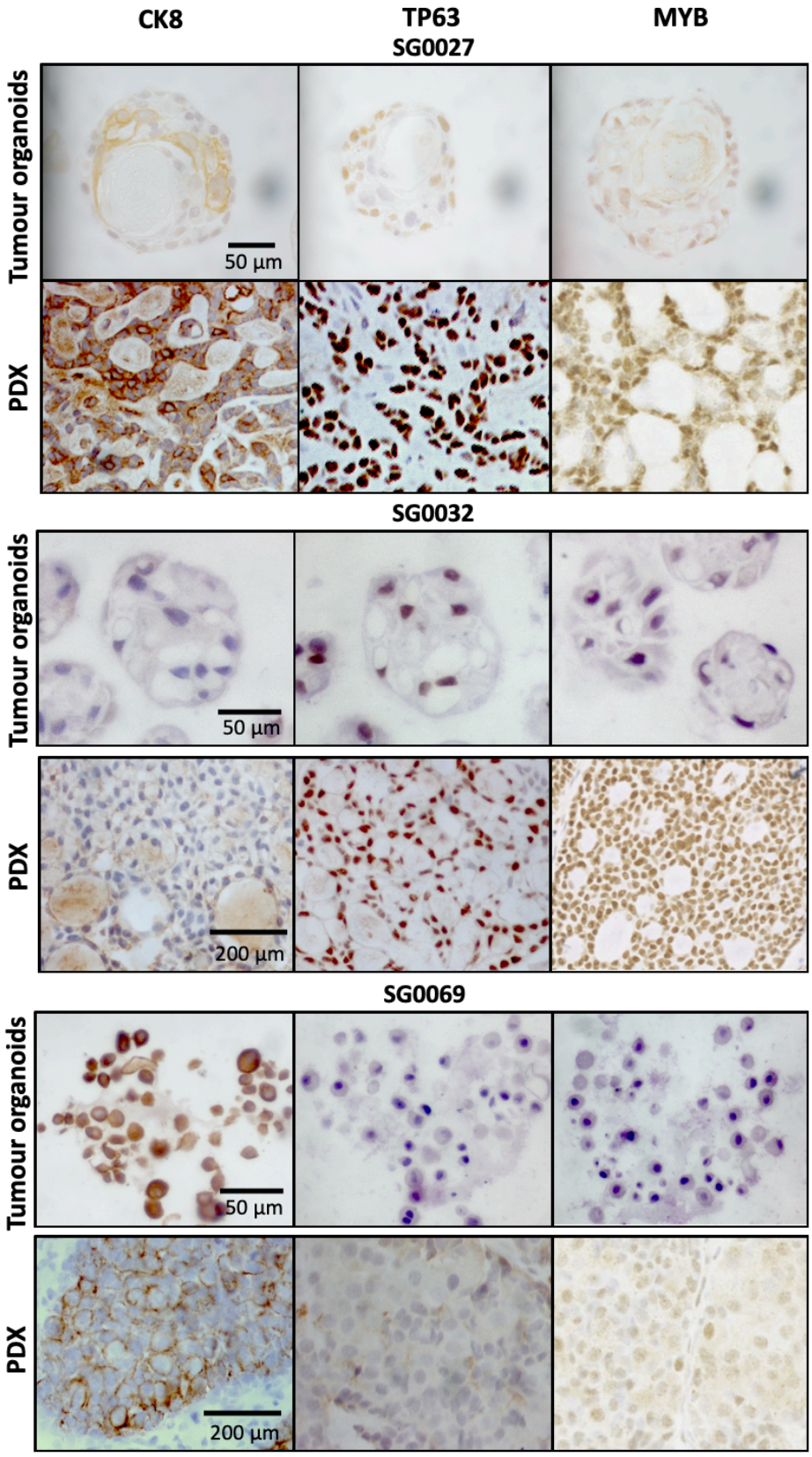

Figure 5-14 ACC PDX-derived organoids recapitulate the PDX cell types

ACC PDX-derived organoids and PDX tumour sections were stained with the luminal cell marker cytokeratin 8 (CK8), the basal cell marker TP63, and MYB. Antibody signal was amplified via DAB and

counterstained using Harris haematoxylin. SG0027 organoids were passage 4 grown in hypoxia, SG0032 organoids were passage 1 grown in hypoxia, and SG0069 were passage 0 grown under normal culture conditions. Slides were imaged at 40x magnification.

5.3.3. ACC organoid drug sensitivity assays

To confirm that the 3D ACC organoids show sensitivity to the combination of CYC065 and JQ1, organoids were treated with serial doses of CYC065 with the constant addition of either 0.1 or 0.3 µM JQ1 (Figure 5-15). SG0027 and 32 in the optimal 3D condition of A83 addition were compared to the sub-optimal 2D curves. Although each sample had a differing sensitivity to the drugs as single agents, the addition of JQ1 decreased the surviving fraction of cells, as the dose response curves shifted to the left with increasing JQ1 doses. The 2D assays and 3D assays are very tightly correlated for both samples, with the SG0027 CYC065 IC_{50} value with 0.1 µM JQ1 addition in 2D being 0.27 µM and in 3D 0.26 µM. This shows that the 3D ACC organoids can be applied to drug sensitivity assays, and that increased MYB does not dramatically alter the sensitivity to CYC065 and JQ1. To confirm that the combination remains synergistic as observed in the 2D models, SI values were calculated. The SI value for SG0027 was calculated in both 2D and 3D at 0.3 µM CYC065 and 0.1 µM JQ1, giving values of 0.08 and 0.455 respectively. This indicates that the combination is more synergistic at these doses in SG0027 in 3D than in 2D. This was also found when SI values were calculated for SG0032 at 0.1 µM CYC065 and 0.3 µM JQ1 in 2D and 3D assays, giving values of 0.176 and 0.253 respectively.

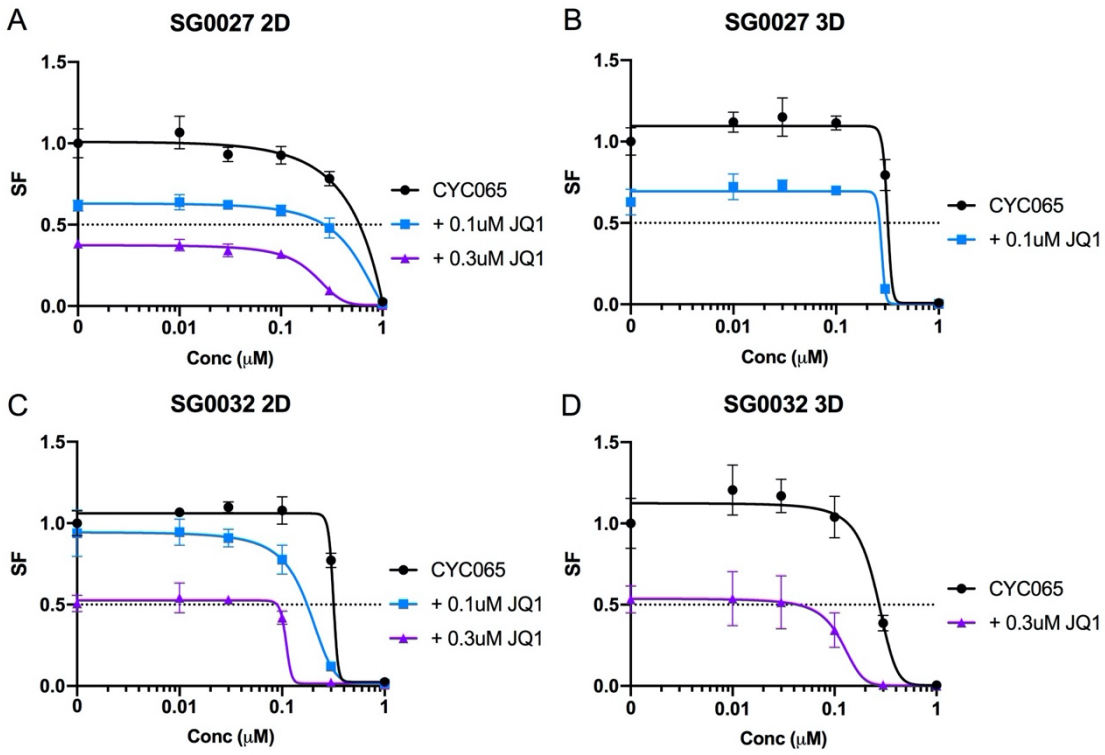

Figure 5-15 2D and 3D CDK and bromodomain inhibitors in combination

10-day 2D and 7-day 3D CYC065 sensitivity curves with the constant addition of either 0.1 µM and 0.3 µM JQ1 in ACC samples SG0027 (A and B) or SG0032 (C and D). Each luminescence reading was normalised to the untreated CYC065 control reading. Data shown is representative of two independent biological repeats and each data point is the mean SF for six parallel technical replicates +/- SD. SI values calculated: SG0027 for combination at doses of 0.3 uM CYC065 and 0.1 uM JQ1, (A) 2D SI = 0.08 (not synergistic) (B) 3D SI = 0.455 (synergistic). SG0032 for combination at doses of 0.1 uM CYC065 and 0.3 uM JQ1, (C) 2D: 0.176 (low additivity) (D) 3D: 0.253 (additivity/low synergy).

5.3.4. Normal SG organoids to predict toxicity

To predict toxicity in tissues other than the tumour, 3D drug assays were conducted using the normal mouse SG organoids. As these organoids divide at a faster rate than the ACC organoids, assays lasted 5 days opposed to 7 days. The mouse SG organoids were less sensitive to both JQ1 and CYC065 than the ACC samples and the negative control cell lines (Figure 5-16A and B). At 10 µM JQ1 treatment, the organoids were smaller but with a clear structure, whereas at 1 µM CYC065 the structures were less defined with many degraded, as shown by the representative images, correlating with SF values at those doses. Furthermore, when treated in combination with the constant additions of 0.1 or 0.3 µM JQ1 to CYC065, the IC_{50} values remained the same and the curves did not shift to the left as seen when the ACC samples were treated at the same doses (Figure 5-16C). Therefore, the normal mouse salivary gland organoids were less sensitive to both single agent JQ1 and CYC065, as well as in combination, compared to the ACC pre-clinical *in vitro* models.

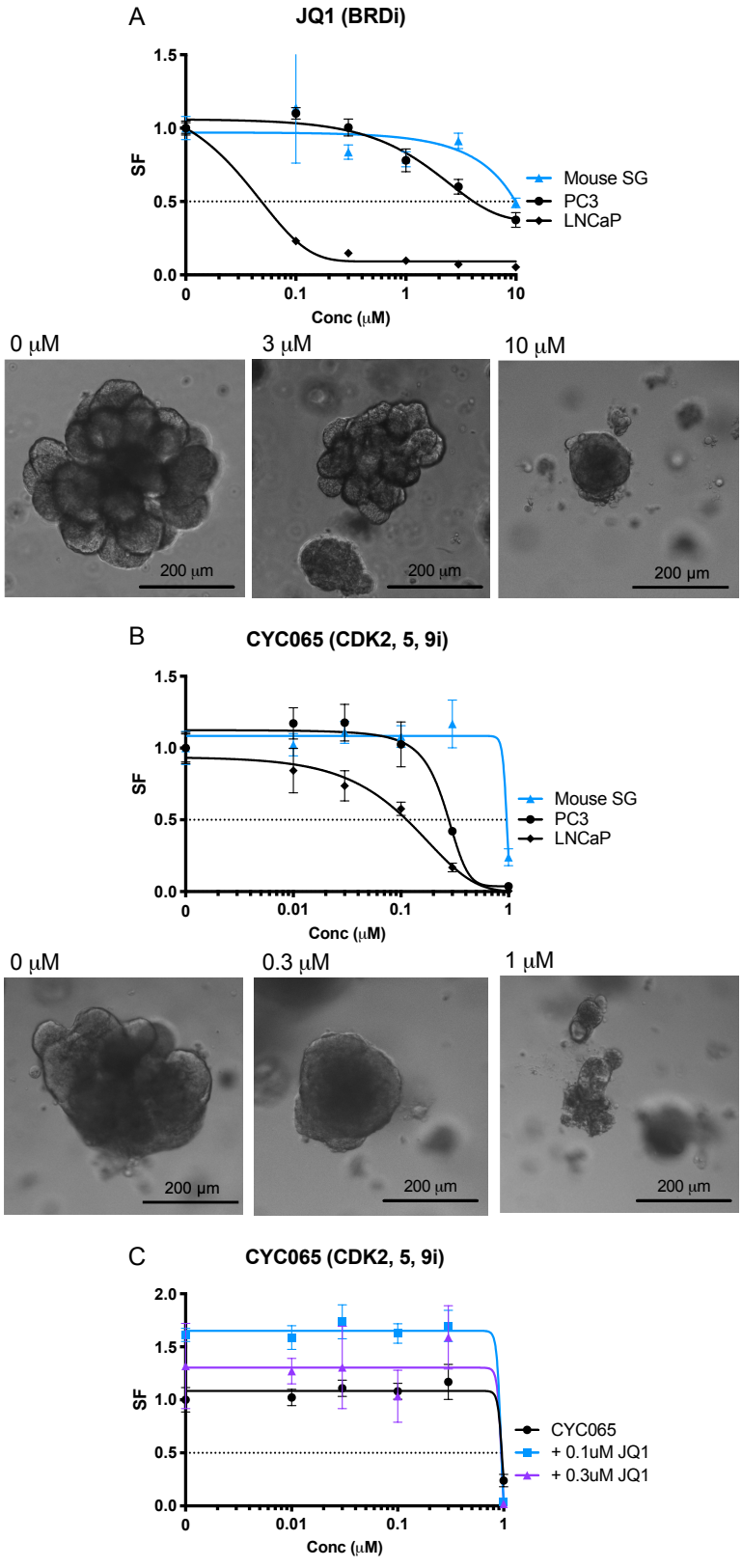

Figure 5-16 Normal mouse salivary gland toxicity assays

7-day 3D mouse SG drug toxicity assays treated with JQ1 (A) and CYC065 (B). Representative images of organoids are shown for increasing concentrations of drug. C) CYC065 response curve with the

constant addition of either 0.1 µM and 0.3 µM JQ1. Each luminescence reading was normalised to the untreated CYC065 control reading. All curves are representative curves conducted in triplicate, +/- SD. Images taken at 20x magnification. Scale bars = 200 µm.

5.4. Discussion

Due to the lack of validated pre-clinical ACC models, most recent progress in ACC research has been made using PDX-derived primary ACC cells, however these models are challenging due to limited passage ability and issues in recapitulation of the PDX lines (Andersson et al., 2017; Nör et al., 2017). Since the start of my studentship, one ACC cell line has been successfully established by Warner et al from a patient tumour over a period of eight years without the use of *in vitro* immortalisation techniques (Warner et al., 2019). The only culture differences to those used for the 2D PDX-derived cultures described in this chapter was the use of fibronectin-coated plates and the addition of 1% bovine brain extract (BBE). Warner et al describe the addition of BBE as "critical" for establishment of their ACC cell line, however neural factors were investigated for PDX-derived 3D organoids and whilst growth was larger, cells did not grow following passaging. The growth rate of the cell line increased with passage which was suggested to be due to the senescence of stromal cells increasing the proportion of tumour cells in the cultures, however as the 2D cultures in this chapter were PDX-derived opposed to directly from patient samples the stroma was of mouse origin and was depleted at the beginning of culture. Warner et al detected low MYB and BCL-2 expression at low passages, and this agreed with the 2D PDX-derived cultures. They also detected low p63 levels in low passages although I found that p63 was not significantly differentially expressed in the 2D PDX-derived cultures compared to the PDX. However, following passage 20, MYB expression was significantly increased, along with the known MYB downstream target BCL-2, although the MYB expression levels still appear slightly less than in the original patient tumour (Warner et al., 2019). Overall, Warner et al have established the first promising ACC patient-derived cell line, that expresses high MYB and MYB targets and can be applied to drug screens, however eight years is a long time to achieve one cell line, and it is yet to be made commercially available. My data

suggests that adding a TGFß inhibitor could avoid the time taken to reach passage 20 for increased MYB expression as observed by Warner et al, although I did not investigate long-term 2D culture, only 3D.

TGFß signalling appears to negatively regulate MYB in ACC, as TGFß inhibitors significantly increased *MYB* expression in both the 2D and 3D PDX-derived models. This effect is the opposite to that observed in ER+ breast cancer, where TGFß enhanced *MYB* expression and increased the half-life of MYB protein (Cesi et al., 2011). Knockdown of TGFß receptors would definitively determine whether TGFß is inhibiting MYB expression, however there are seven Type I and five Type II receptors that TGFß family members bind to making this impractical (Shi & Massagué, 2003). TGFß inhibitors are commonly used for the long-term culture of human adult stem cell-derived organoid cultures and not in mouse. The biological reason for this species-specific requirement is unknown but is used in colon, breast, and liver organoid cultures to name a few (Fujii et al., 2016; Huch et al., 2015; Karthaus et al., 2014; Sachs et al., 2018; Seino et al., 2018). A very recent paper described an ACC organoid culture method where organoids were re-implanted as an orthotopic PDX model (Takada et al., 2021). These organoids are arguably a spheroid-organoid hybrid as the single cells plated were allowed to aggregate before Matrigel was added. Takada et al grew the organoids in a medium very similar to published media for prostate and colorectal cancer organoids, with the addition of dexamethasone taken from published mouse SG organoids (Drost et al., 2016; Fujii et al., 2016; Maimets et al., 2016; Nanduri et al., 2014). This medium also contained A83, however, Takada et al did not investigate whether MYB expression was maintained during organoid culture, only confirming it in the successful organoid-derived PDX tumours. I found that although TGFß inhibition increased MYB expression, it was still approximately 3-4-fold lower than the PDX tumour. My data suggests that MYB is inducible under culture conditions, therefore Takada et al should investigate whether this is the case in their organoid cultures and if so, investigate why MYB expression is restored on implantation to the submandibular gland. This would give insight into what niche factors in the environment enhance MYB expression and could improve pre-clinical *in vitro* ACC models.

An issue with ACC organoid line establishment is successful passaging for long-term culture. Mouse SG cultures grow indefinitely as the ductal compartment harbours stem cells and the published medium promotes Wnt signalling that stimulates self-renewal of these stem cells, facilitating long-term expansion (Maimets et al., 2016). Despite Wnt signalling being a significantly upregulated pathway in ACC compared to normal SG, enhanced Wnt signalling did not increase growth or enable passaging in ACC. The only condition to enable passaging was hypoxia, which disputed the pathway enrichment analysis identifying hypoxia as significantly downregulated in the PDX tumour compared to the 2D cultures. Hypoxia has been linked to stem-cell renewal, with glioblastoma organoids containing a hypoxic core comprised of CSCs (Hubert et al., 2016). However, the establishment of a hypoxic gradient is dependent on organoid size, and as under normal conditions SG0027 and 32 organoids were around 50 µm they may not have been large enough hence cultures thrived when grown in a hypoxic chamber. Fujii et al established 40 CRC organoids and found that 5 were dependent on a hypoxic environment, therefore the different ACC samples may respond differently to hypoxic culture (Fujii et al., 2016). It would be interesting to compare MYB expression in hypoxic and normoxic cultured organoids, and to identify other differences at the transcriptional level also in the PDX tumours. It would also be interesting to assess the effect of R-spondin and CCh in the medium under hypoxic conditions as these both induced a significantly higher number of organoids in normoxic culture. Nonetheless, successful establishment of an ACC organoid line would enable further investigative opportunities such as co-culture with neurons to model PNSI, and also application to drug sensitivity assays.

It is interesting that whilst the optimum 2D medium condition with the addition of A83 appeared to reduce the level of drug synergy observed in SG0032 compared to the previous medium condition, 3D assays with the addition of A83 demonstrated increased synergy. This raises the debate of which *in vitro* model is most representative of the tumour and the best predictive pre-clinical model. However, as the SI value calculation is only an indication of synergy at one dose pairing, further dose combinations should be investigated to definitively determine the level of synergy in both models, and the optimal dose ratio.

Normal “healthy” tissue organoids have been used to predict the toxicity of potential therapeutic compounds. Organoid models have been established to predict hepatotoxicity, cardiotoxicity and nephrotoxicity (Eder et al., 2016; Meng, 2010; Takasato et al., 2015). In addition, normal and cancer organoids have been used to identify potential therapies with selectivity towards cancer cells, such as comparing CRC and normal colon organoids sensitivities (Fiore et al., 2018). Normal SG organoids were far less sensitive than the ACC organoids to the combination of CYC065 and JQ1, suggesting that the potential therapy is ACC selective. This would be confirmed by *in vivo* assays.

6. Drug combination mechanistic investigation

6.1. Introduction

In Chapter 4, a potential drug combination was identified in the ACC PDX-derived *in vitro* models between the CDK2, 9 inhibitor CYC065, and the BRD4 inhibitor, JQ1. The combination was synergistic in SG0027, 28, 32 and 37, and lines remained sensitive when cultured in optimised medium for *MYB* expression. In this chapter, the combination mechanism of action is investigated in both 2D culture and short-term and long-term *in vivo* PDX assays to identify potential anti-MYB activity.

6.2. 2D mechanistic investigation

To determine whether the combination of CYC065 and JQ1 targets *MYB* expression, SG0032 cells in 2D were treated for 8 hours and RNA collected. Targeted q-rtPCR identified that at 8 hours treatment, *MYB* expression in the combination was significantly reduced compared to the untreated control ($P = 0.0004$), although was less significant than the single agents ($P < 0.0001$) (Figure 6-1). *MYB-NFIB* expression was significantly decreased in all treatment conditions compared to the vehicle ($P < 0.0001$). Although these experiments were conducted without A83 in the medium, a difference in *MYB* expression was still observed suggesting that although *MYB* was significantly lower than in the PDX, it was still expressed at a measurable level. Furthermore, the expression levels of selected previously reported MYB downstream targets and genes highly expressed in the ACC patient samples were investigated. There was a significant difference in all downstream target expression between the combination treatment and the untreated control, except for PRAME which was only significantly decreased with the single agent treatments. Whilst there was no significant difference in *BCL2*, *CDK6*, *NOTCH1* or *PRAME* expression, between the single agents and the combination, *EN1* was significantly differentially expressed compared to both single agents; CYC065 ($P = 0.0179$) and JQ1 ($P < 0.0001$).

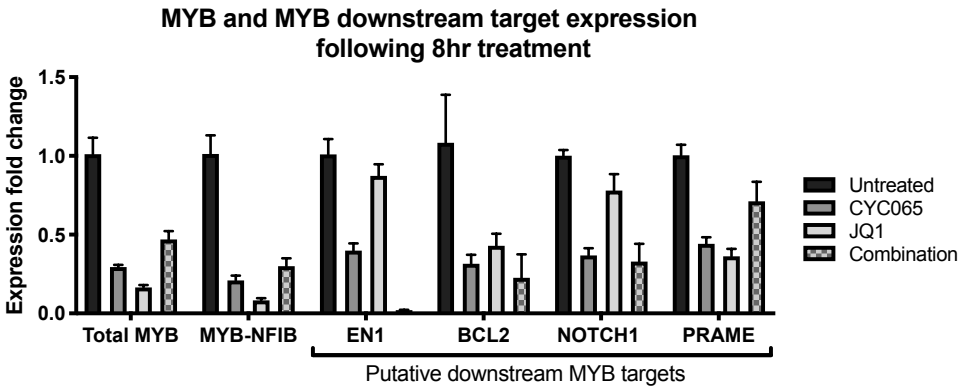

Figure 6-1 *MYB* and putative downstream MYB targets following 8 hr combination treatment

RNA was isolated from 2D cultured SG0032 PDX-derived cells, treated with the IC_{50} concentrations of CYC065, JQ1 or both in combination for 8 hours. Expression of MYB and putative downstream genes was assessed via quantitative rt-PCR using SYBR green. Data was analysed using the comparative CT method ($\Delta\Delta$CT), with samples normalised to the relative housekeeping gene GAPDH values, and then to the untreated samples (n=3, mean +/- SE). Significant expression differences are discussed in the text, calculated by a 2way ANOVA followed by Tukey's multiple comparison test.

In order to identify which genes and pathways are being targeted by the combination therapy, RNAseq was conducted on 2D SG0032 samples in biological triplicate, derived from different PDX passages. Analysis from three different treatment timepoints identified that 12 hours was the optimal treatment time as *MYB*, *MYB-NFIB* and *EN1* were all significantly downregulated (Figure 6-2).

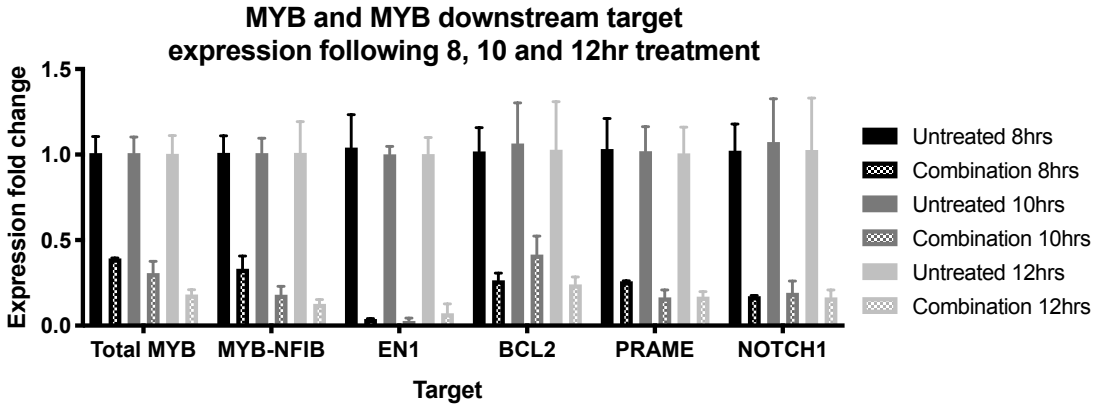

Figure 6-2 Time optimisation for drug combination analysis via 2D RNAseq

RNA was isolated from 2D cultured SG0032 PDX-derived cells following 8-, 10- and 12-hours treatment with the IC_{50} concentrations of both CYC065 and JQ1, or vehicle. Expression of MYB and putative downstream genes was assessed via q rt-PCR using SYBR green. Data was analysed using

the comparative CT method (ΔΔCT), with samples normalised to the relative housekeeping gene GAPDH values, and then to the untreated samples (n=3, mean +/- SE).

RNAseq analysis identified a large number of DEGs between the single agents and the combination. Interestingly, the Venn diagram of downregulated DEGs highlights that the highest number of genes (2309) are downregulated in both CYC065 and the combination implying that CYC065 plays the biggest role in transcriptional repression within the combination treatment (Figure 6-3 A and B). However, the combination independently downregulated 2007 genes that are not affected by JQ1 or CYC065 treatment alone. *MYB* was significantly decreased in the RNAseq data by -1.6 Log2 fold, and the known MYB target *EN1* was also significantly decreased by -4.8 Log2 fold. GSEA pathway analysis of the combination treatment compared to vehicle group shows that MYC targets are significantly downregulated (Figure 6-3C) (full GSEA pathway analysis is provided in appendix 5, chapter 9.5). This suggests that the combination therapy could be working via the suppression of MYB downstream targets.

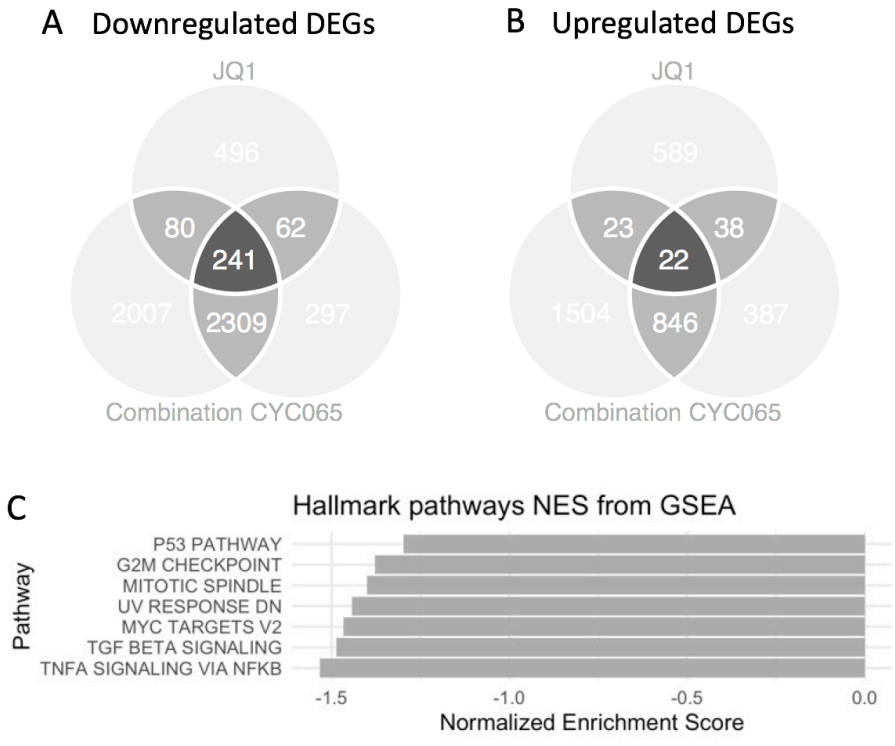

Figure 6-3 RNAseq analysis of vehicle and treated PDX-derived 2D samples

Venn diagrams of significantly downregulated (A) and upregulated (B) differentially expressed genes identified from RNAseq of vehicle, single agent JQ1, CYC065 and combination treatment in 2D

cultured SG0032 PDX-derived cells with medium without 0.1 µM A83 (Log2 fold change < -1 or > 1, P < 0.01). C) Gene set enrichment analysis (GSEA) was performed on the significantly up- and downregulated DEGs in the combination treatment normalised to the vehicle treatment. Significantly upregulated and downregulated hallmark pathways according to significant DEGs, Padj < 0.05. Hallmark gene sets from the Molecular Signatures Database were used.

6.3. *In vivo* confirmation

6.3.1. Short-term *in vivo* investigation

To confirm drug activity and to investigate the combination mechanism in a more clinically relevant model, SG0032 tumour implanted CD1 nude mice were treated for 5 days with 55 mg/kg CYC065 and 50 mg/kg JQ1 and then harvested. Firstly, known drug targets were quantified via western blot to confirm that the drugs were hitting the biological targets (Figure 6-4A). CDK2 is reported to phosphorylate the tumour suppressor retinoblastoma protein (RB) at Thr821, however CDK2 inhibitors have also been shown to inhibit RB phosphorylation at Ser780 (Frame et al., 2020; Hattori et al., 2014; Whittaker et al., 2018; Zarkowska & Mittnacht, 1997). At both potential RB phosphorylation sites, only the combination treatment significantly decreased phosphorylation at S780 (P = 0.0052) and Thr821 (P = 0.0229) (Figure 6-4B and C). This difference in RB phosphorylation at S780 and Thr821 was found to be synergistic by applying the SI calculation, giving values of 0.478 and 0.28 respectively. CDK9 inhibitors inhibit the phosphorylation of RNA polymerase II (RNPII) at Ser2 (reviewed in Jeronimo, Collin & Robert, 2016). There is also evidence that BRD4 inhibitors also inhibit RNPII phosphorylation at this site too (Devaiah et al., 2012). Whilst both CYC065 and JQ1 reduced phosphorylation at RNPII S2, the reduction in expression was only significant following combination treatment (P = 0.044) (Figure 6-4D). In addition, the effect of both drugs in combination on RNPII S2 phosphorylation inhibition was not synergistic as calculated via SI, giving a value of 0.037. Both total RNPII and RB remained fairly constant therefore the reduction in phosphorylation was specific rather than due to a decrease in expression of the total proteins.

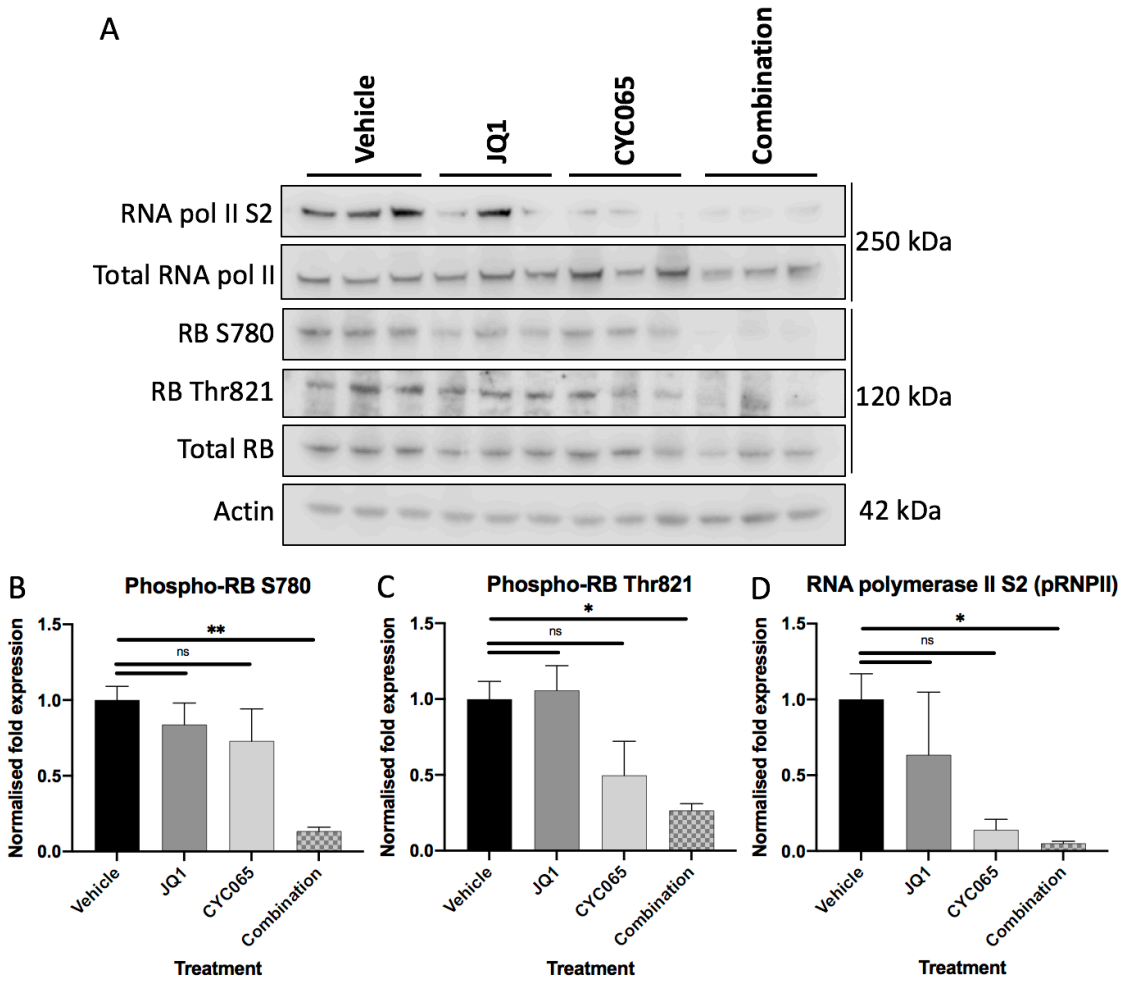

Figure 6-4 Confirmation of drug activity in 5-day treated SG0032 PDX tumours

A) Protein was extracted from snap frozen SG0032 tumours from 5-day treated vehicle, JQ1 (50 mg/kg), CYC065 (55 mg/kg) or combination treated mice. RNA polymerase II S2, total RNA polymerase II, RB S780, RB Thr 821, and total RB were detected by Western blot. The housekeeping gene Actin was used as a loading control. Expression of phospho-RB S780 (B), Phospho-RB Thr821 (C) and RNA polymerase S2 (D) were normalised to the housekeeping gene. Data represents three biological repeats and is expressed as the mean +/- SE. Statistical analysis was conducted using a One-way ANOVA followed by Dunnett's multiple comparisons test (* = $P < 0.05$, ** = $P < 0.01$). Drug synergy on target inhibition was predicted using the SI calculation: B) RB S780 SI = 0.478 (synergistic), C) RB Thr821 SI = 0.28 (additive/low synergy), D) RNPII S2 SI = 0.037 (not synergistic).

Actively proliferating cells were significantly reduced in the combination treatment group compared to vehicle and single agent treated tumours, identified by Ki-67 IHC staining ($P < 0.0001$) (Figure 6-5A). Although, following the 5-day treatment there was no significant difference in the number of caspase-3 positive cells indicating that 5-days may not be long enough to induce cell death (Figure 6-5B). There was no significant difference in MYB expression, although there is apparent variability between the biological triplicates (Figure 6-5C). There is also no significant difference in the expression of the MYB target EN1 (Figure 6-5D). However, the staining of positive EN1 cells was noticeably weaker only in the combination treated tumours compared to the single agent and vehicle treated groups (Figure 6-5E). There appeared to be a difference in nucleolar body expression as the number of cells with strong nucleoli staining was significantly decreased only the combination treated tumours ($P < 0.0001$).

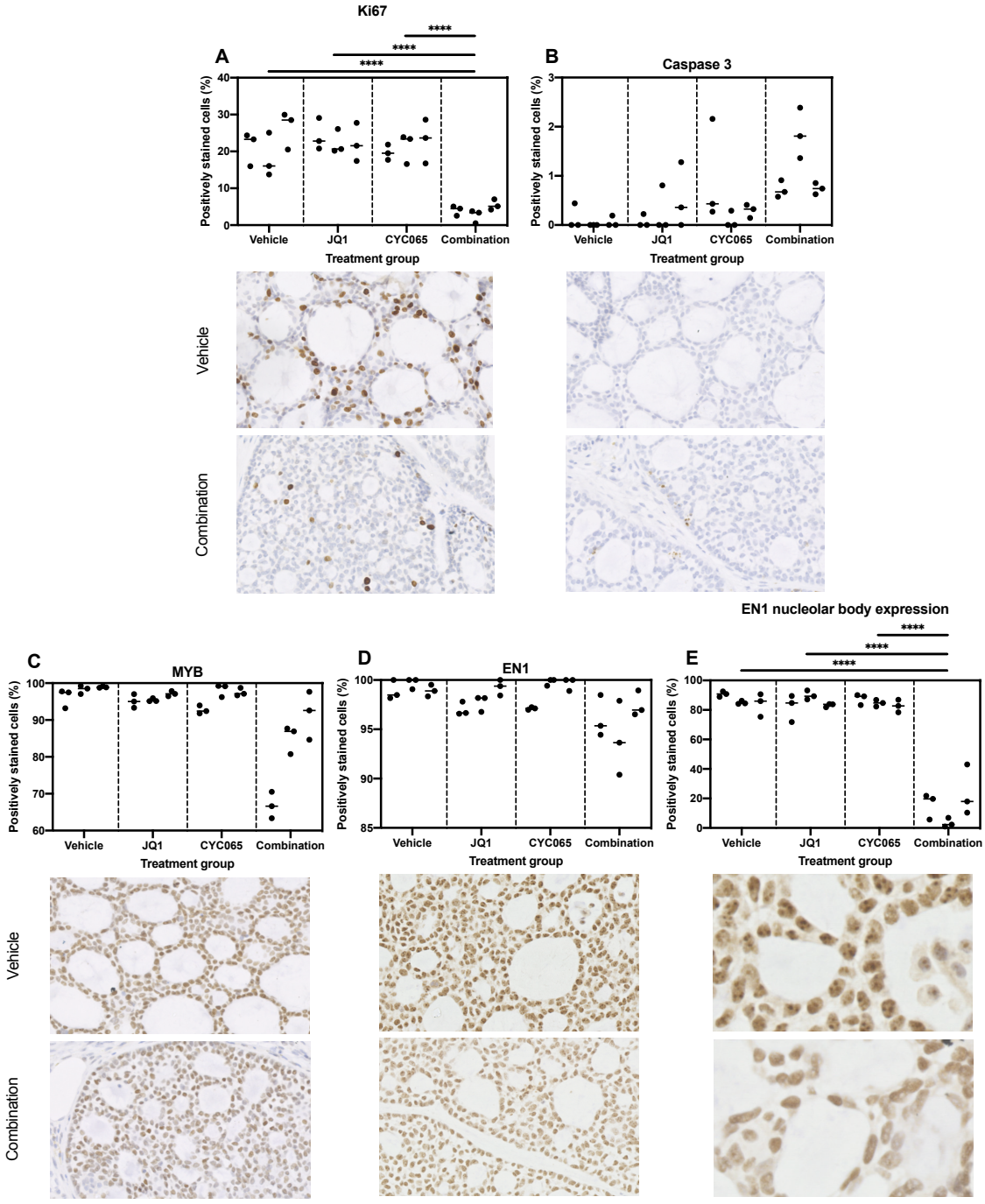

Figure 6-5 Immunohistochemical analysis of 5-day short term treated SG0032 PDX tumours

Following 5-day treatment with either vehicle, JQ1 (50 mg/kg), CYC065 (55 mg/kg) or a combination of both drugs, tumours were harvested and fixed in 10% formalin and paraffin embedded. Three tumours from each experimental arm were stained via immunohistochemistry (IHC). The number of positively stained cells were counted and expressed as a percentage of total cells from triplicate images for each sample. For panels A-D, representative images at 40x magnification are shown for the vehicle and combination arms. For panel E, representative images are shown at 80x magnification. There are no significant differences in expression of MYB or caspase-3 (A and B). C) The combination group has significantly fewer Ki67 positive cells than the vehicle or single agent

groups (****, p = <0.0001). There is no significant difference in engrailed-1 (EN1) protein expression (D), however, there is a significant difference in cells containing EN1 positively stained nucleolar bodies (E). Statistical analysis conducted using nested 1way ANOVA and Tukey's multiple comparisons test.

To identify potential biomarkers of therapeutic activity at the molecular level, the expression of MYB and potential downstream target genes was assessed by q-rtPCR (Figure 6-6). Targets were selected from the 2D combination RNAseq and published MYB targets identified by MYB ChIP-seq (Drier et al., 2016; Mandelbaum et al., 2018). The expression of these targets was checked in the RNAseq data comparing the 2D culture transcriptome to correlating PDX tumours, to ensure that the targets chosen were expressed at a high level in the untreated PDX tumour. *MYB* and translocated *MYB* expression were not significantly different in any treatment condition (analysed via 2way ANOVA followed by Tukey's multiple comparisons test). Interestingly, selected targets were not all affected to the same degrees. *EN1* expression was largely decreased in the combination treated tumours, as was expected from the IHC staining and the 2D RNAseq. *MYC* expression was decreased in the JQ1 single agent group but not in the CYC065 single agent group. However, this decrease was even more pronounced in the combination group, and correlated with the 2D combination treated RNAseq data that identified a significant decrease in *MYC* target expression by 6 Log2 fold. *CDK6*, *NOTCH1 and SOX10* expression was investigated as they are also reported to be MYB targets, however there was large variability in expression between the combination treated tumours. Interestingly, SOX9 is not a widely reported MYB target but was investigated as it was significantly decreased by 6.5 Log2 fold in the 2D combination data. Therefore, the short-term expression data agrees with the 2D data as SOX9 was largely decreased in the combination treated tumours.

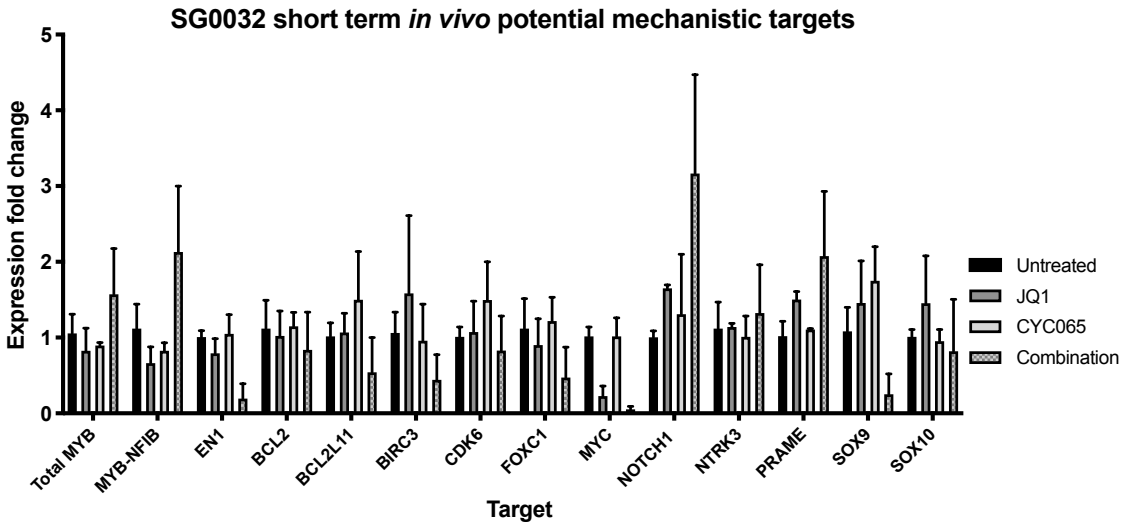

Figure 6-6 Potential mechanistic targets from the short-term treated SG0032 tumours

RNA was isolated from snap frozen SG0032 PDX tumours treated for 5-days *in vivo* with either vehicle, JQ1 (50 mg/kg), CYC065 (55 mg/kg) or a combination of both drugs. Expression of MYB and potential mechanistic targets was assessed via q rt-PCR using SYBR green. Data was analysed using the comparative CT method ($\Delta\Delta$CT), with samples normalised to the relative housekeeping gene GAPDH values, and then to the untreated samples (n=3, mean +/- SE). Data was statically analysed via a 2way ANOVA followed by Tukey's multiple comparison test however due to sample variability no genes were significantly decreased from treatment groups compared to the untreated control.

Two potential mechanisms of cell death were investigated by protein analysis (Figure *6-7*). Increased expression of phospho-Histone H2A.X (Ser139) (p-yH2AX) is a marker of DNA damage, and both CDK2 and BRD4 inhibitors have been reported to induce this (Miller et al., 2019; H. Y. Wang & Kim, 2016). There was a slight increase in p-yH2AX expression in two combination treated tumours compared to the vehicle treated tumours, however this was variable. The other pathway investigated was ribosomal and nuclear stress. Ribosomal stress activates p53-dependent cell cycle arrest, which in turn increases p21 levels (Gilkes et al., 2006). This was investigated due to the specific lack of EN1 nucleolar body staining, however p21 expression was not increased in combination treated tumours.

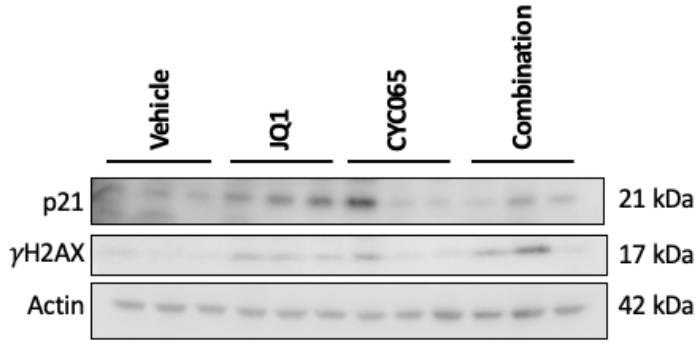

Figure 6-7 Potential mechanisms of cell death induced by the combination treatment

Protein was extracted from snap frozen SG0032 tumours from 5-day treated vehicle, JQ1 (50 mg/kg), CYC065 (55 mg/kg) or combination treated mice. $P21^{WAF1/CIP1}$ and phospho-Histone H2A.X (Ser139) were detected by Western blot. The housekeeping gene Actin was used as a loading control.

6.3.2. Long-term *in vivo* investigation

As proliferation was significantly reduced, as determined via Ki67 expression following 5-day combination treatment, a long-term *in vivo* assay was conducted to determine whether the combination reduces SG0032 tumour growth compared to the single agents. Beforehand, two-week toxicity assays were completed to select well-tolerated doses of each single agent suitable for long term dosing. Two weeks of treatment at 55 mg/kg CYC065 and 50 mg/kg JQ1 was toxic to the mice inducing sudden death, in addition 50 mg/kg CYC065 and 40 mg/kg JQ1 induced excessive weight loss (greater than 10% of body weight). To be cautious, 25 mg/kg CYC065 and 20 mg/kg JQ1 was chosen as CYC065 showed anti-tumour activity when used at a dose lower than 30 mg/kg in AML PDX models (MacKay et al., 2015).

CD1 mice were implanted with SG0032 tumour fragments. When tumours reached between 150-200 mm^3 they were allocated to experimental groups, with 5 mice in each experimental arm. Mice were treated for 35 days in total and all mice survived the treatment regimen. The combined drug treatment of 25 mg/kg CYC065 and 20 mg/kg JQ1 was well tolerated, with percentage body weight loss not exceeding 4.8%. Unfortunately, there was large variability in tumour fold increase at the endpoint of the experiment within the vehicle group, ranging from a percentage increase of 150 to 600%. By looking at the five individual growth curves for each tumour within the

treatment groups opposed to the mean, it is clear that tumour measurements were not consistent (Figure 6-8B-D). Nevertheless, the combination and JQ1 single agent treatment both reduced growth by similar levels, however, CYC065 did not impede tumour growth compared to the vehicle group (Figure 6-8A). The average vehicle tumour volume was 370%, compared to 170% and 195% following JQ1 and combination treatment respectively. This indicates that the combination treatment offered no advantage over single agent JQ1 treatment in inhibiting SG0032 tumour growth and that JQ1 is just as effective alone.

To confirm that the drugs at these lower doses were still hitting their biological targets, the level of RNP II S2 phosphorylation was quantified by Western blot, in three randomly chosen tumours from each treatment group (Figure 6-8E). Expression in both JQ1 single agent and CYC065 single agent groups was significantly reduced, although variable between the three biological repeats (P = 0.0114 and 0.0129 respectively) (Figure 6-8F). However, expression within the combination group was consistent across all three tumours, being completely inhibited (P = 0.0029). Total RNPII expression was not overly consistent, although it did not correlate with reduced RNP II S2 phosphorylation therefore it can be assumed that reduction in phosphorylation was specific. This indicates that the agents at the lower doses are having a biological effect on the tumours.

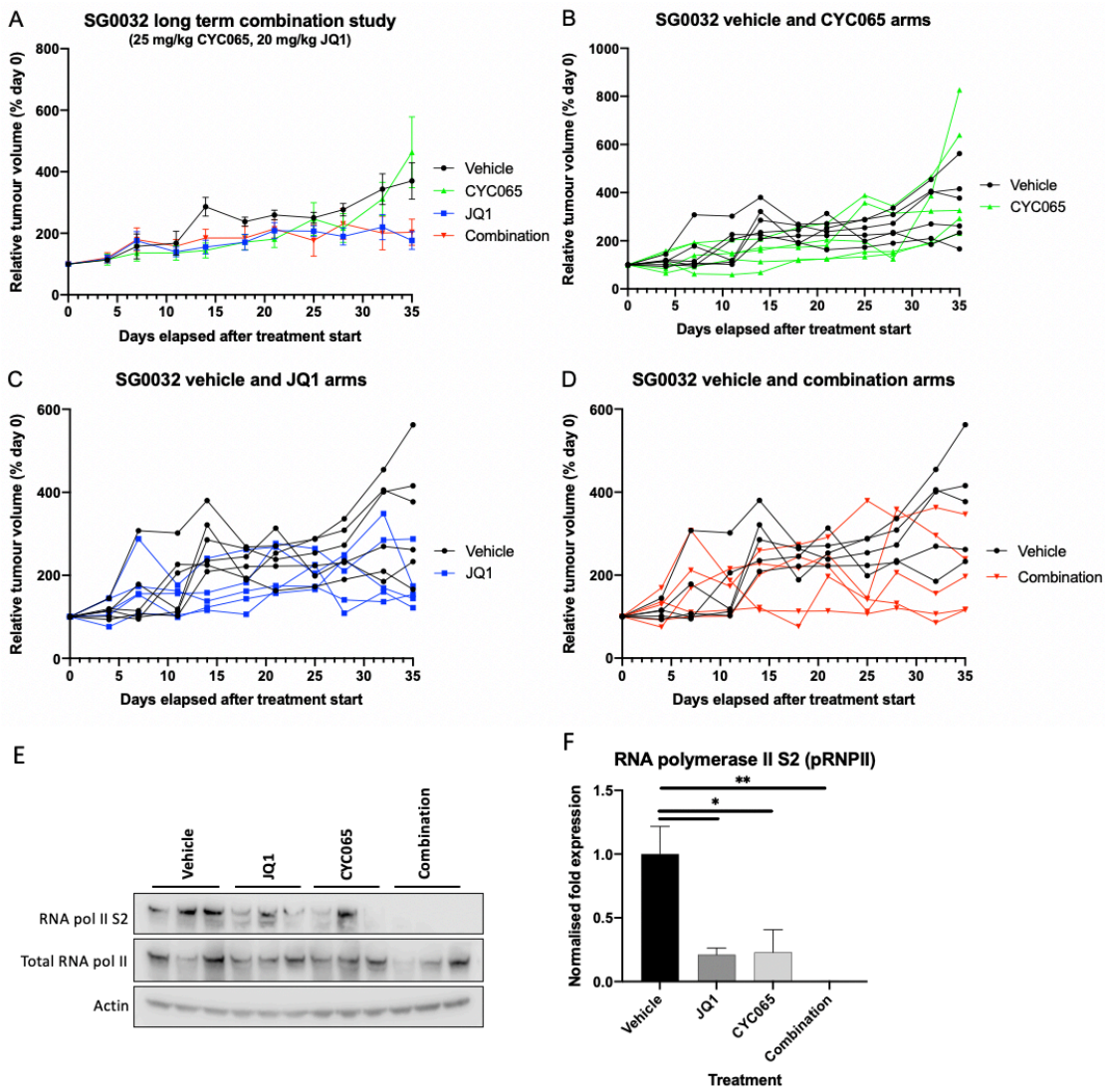

Figure 6-8 *In vivo* efficacy of long-term combination treatment in SG0032 PDX tumours

A) Average tumour volume over 35-days treatment with either vehicle, JQ1 (20 mg/kg), CYC065 (25 mg/kg) or a combination of both drugs (+/- SEM, N = 5). The individual growth curves of each tumour receiving CYC065 (B), JQ1 (C) or the combination treatment (D) compared to the vehicle tumours. E) Expression analysis of RNA polymerase II S2 and total RNA polymerase for three randomly chosen tumours from each treatment group. The housekeeping gene actin is used as a loading control. F) Normalised expression of RNA polymerase II S2 compared to actin, plotted as the mean +/- SE. Statistical analysis was conducted using a One-way ANOVA followed by Dunnett's multiple comparisons test (* = $P < 0.05$, ** = $P < 0.01$).

To confirm similar mechanistic effects were observed in the long-term treatment compared to the short-term treatment, tumours were stained for EN1 (Figure 6-9). Unlike following short-term treatment, positive nucleolar body staining was still present in the long-term combination treated tumours to the same degree as the vehicle and single agent treated tumours.

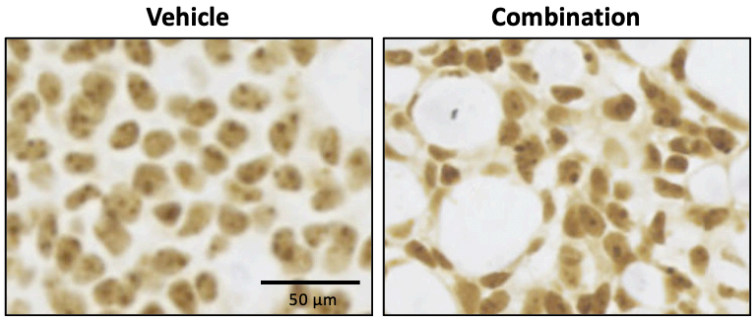

Figure 6-9 Engrailed-1 expression following long-term combination treatment

Following 35-day treatment with either vehicle or a combination of JQ1 (20 mg/kg), CYC065 (25 mg/kg) tumours were harvested and fixed in 10% formalin and paraffin embedded. 4 µm thick sections were stained for EN1 via IHC. Images are taken at 40x magnification. Scale bar = 50 µm.

6.4. Discussion

In pre-clinical drug investigations, it is important to identify that the drugs are hitting their biological targets and to determine the mechanism of drug action as this can inform biomarker selection for therapeutic efficacy. The combination of a CDK2/9 inhibitor with a BRD inhibitor has recently been shown to be effective in a number of oncogene-driven cancers. BRD inhibitors have proven synergistic with CDK9 inhibitors in AML, MLL and rhabdoid tumours (Gerlach et al., 2018; McCalmont et al., 2020; Moreno et al., 2017). In addition, BRD inhibition in combination with CDK2 inhibition has proven effective in orthotopically transplanted MYC-driven medulloblastoma PDX models (Bolin et al., 2018). All these studies identify that the combination inhibits oncogene expression by targeting super-enhancers. As ACC is thought to be MYB driven, and super-enhancers with MYB binding sites are known to promote the ACC transcriptional programme, I hypothesised that the BRD and CDK2, 9 inhibitor

combination would be effective by disrupting super-enhancer activity thereby regulating MYB and MYB downstream target expression.

It is clear that the combination of both CYC065 and JQ1 has a different impact on the transcriptome to the agents individually. From the investigated MYB downstream targets, not all targets were downregulated and the only differential expression observed was in the combination treated tumours. An exception to this was *MYC* expression that was also decreased with JQ1 single agent treatment. However, as proliferation was not decreased in the JQ1 single agent treated tumours, only in the combination treated tumours, this suggests that there are other differences occurring in the combination group impeding growth, other than suppressed *MYC* expression. CYC065 alone did not affect *MYC* expression, potentially due to a BRD4-mediated compensatory mechanism previously reported in response to CDK9 inhibition (H. Lu et al., 2015). My data confirms that the combination of both drugs is required to alter the transcriptional programme. This data could also suggest varied MYB activity at different downstream promoters, explaining why known MYB targets were affected differently. *SOX9* was also only decreased in the combination treated group in both the 2D and PDX models. SOX9 is a transcription factor involved in embryogenesis and lineage commitment including neural crest development, but is not a widely reported MYB target (Matheu et al., 2012). Two published studies using CYC065 to treat neuroblastoma and AML detected a significant reduction in the pro-survival gene *MCL1*, however this was expressed at low levels in the PDX tumour so was not investigated as a biomarker (Frame et al., 2020; Poon et al., 2020).

As MYB autoregulates its own expression by binding to super-enhancers, I was expecting MYB expression itself to be downregulated following combination treatment, however interestingly, it was not. I had hypothesised that by inhibiting MYB expression, the expression of MYB-specific downstream targets would be downregulated as the binding of MYB at enhancers or promoters would have been reduced, altering the transcriptional programme. A possible explanation to higher than expected *MYB* levels is that the transcripts most sensitive to CDK9 inhibition are those with short half-lives, these transcripts tend to be apoptosis regulators, such as *BCL2*, and key cell-cycle

regulators, such as *MYC* (Lam et al., 2001). According to this study, *MYB* mRNA has a half-life of over 8 hours, whereas *BCL2* and *MYC* have half-lives of 2.28 and 1.59 hours respectively. The effect of the *NFIB* translocation on *MYB* transcript stability is unknown, so potentially *MYB-NFIB* transcripts could have longer half-lives. To determine if this is the mechanism, ChIP-seq could be used to compare between vehicle and combination treated samples the active super-enhancers MYB binds to and at which downstream targets. In medulloblastoma, mapping of the enhancer landscape in each sub-group identified unique sets of super-enhancers that correlated with tumour heterogeneity, therefore this should also be investigated in the other lines such as SG0027 that lacks the NFIB translocation to observe whether the downstream targets differ based on enhancer activity (Lin et al., 2016). This is likely given that the patient tumour cluster plot showed that samples with the same mechanism of MYB activation group closest based on their expression profiles at the transcriptional level (Figure 3-3). Alternatively, as SOX9 was downregulated and it is not a widely identified MYB target, the reason for only a select few MYB targets being downregulated by the combination treatment and not MYB itself could be due to targeting general super-enhancers. EN1, MYC and SOX9 are transcription factors and positively regulate their own expression by binding to large super-enhancers themselves, so potentially these associated super-enhancers may be more sensitive than the translocated NFIB super-enhancer to the *MYB* gene by having higher BRD4 occupancy (D. Chen et al., 2018; Ohba et al., 2015; Peluffo et al., 2019).

Potential mechanisms of cell death were investigated to understand the mechanism of drug action, however further work is required. The protein p53 can induce apoptosis or cell senescence in response to DNA damage, dysregulated cell growth, and ribosomal stress. The nucleolus is the site of ribosome biogenesis, and as EN1 expression was significantly absent from the nucleoli in the combination treated samples, the expression of the p53 downstream target p21 was investigated to detect potential ribosomal stress, however no difference was observed. Nucleolar stress could be assessed by nucleolin staining. An alternative avenue to investigate is inhibition of ribosomal RNA (rRNA) processing. Ribosome biogenesis is required for proliferation, however inhibition of RNPII inhibits rRNA processing (Burger et al., 2013). This in turn inhibits ribosome assembly and induces cell death. To determine if this is a mechanism

of action for the therapies, as single agents or in combination, the levels of unprocessed 47S, intermediate 37S and mature 18S and 28S rRNAs should be measured. The pan-CDK inhibitor flavopiridol has been reported to induce cell death in a p53-independent manor due to its CDK9 inhibition potency (Shapiro et al., 1999). This could be a similar mechanism to that observed in the combination treated samples. It would be interesting to investigate whether the combination increases cell cycle arrest compared to the single agents, both of which report G0/G1 arrest (Delmore et al., 2011; Frame et al., 2015).

There were issues with toxicity in the *in vivo* experiments. A difficulty with combination *in vivo* assays is balancing efficacy with toxicity. The normal SG organoid toxicity model suggested that ACC was more sensitive to the combination than normal tissue. However, it is difficult to extrapolate *in vitro* drug concentrations to *in vivo* doses due to a number of factors such as ADME (drug absorption, distribution, metabolism and excretion), mouse species and length of assay. The most common way to conduct a combination drug investigation *in vivo* is to administer the same dose of drug used for the single agent arm in the combination group (Gerlach et al., 2018; McCalmont et al., 2020; Moreno et al., 2017). However, an advantage of a synergistic combination is that less drug can be used whilst achieving greater efficacy, reducing the potential of drug-induced toxicity. Whilst the doses used in the 5-day combination assay, were tolerated for 5-days, they were toxic when dosed for 2 weeks therefore doses had to be re-evaluated for a long-term study. The doses of the short-term 5-day *in vivo* assays were selected from published studies, and recommendation from the drug supplier (Drier et al., 2016; Frame et al., 2020). The lower long-term assay doses were decided upon using the rationale that if the combination was truly synergistic, a greater effect would be seen in the combination group than the single agents at the same low doses.

It is important to recognise that the long-term *in vivo* assay was not conducted under optimum conditions. Firstly, the tumour measurements were inconsistent, with large discrepancies from one measurement to the next. This could be because the SG0032 tumour is soft, and has a tendency to breakup forming two or three smaller tumours in close proximity. This could make consistent measurements of width and length more

challenging. This experiment is being completed again and to overcome this issue, tumours were implanted as single cell injections in the hope that tumours grow more uniform and are more malleable during mouse handing. Secondly, there is a large variation in growth rate within the vehicle group. Finally, it is important to mention that on day 25 of drugging the experimental mice tested positive for C. bovis. This infection can impact PDX growth (Vedder et al., 2019), therefore it is unknown whether the variation in relative tumour volume within the vehicle group or treatment groups is due to infection. However, as mice from all experimental cages tested positive for C. bovis, it can be presumed that all mice were "equally" infected.

The dose of CYC065 will be increased during the experimental repeat for a number of reasons. Firstly, the growth curves imply that JQ1 was equally as effective as the combination treatment in slowing tumour growth, whereas CYC065 did not slow tumour growth at all. Therefore, to confirm whether this was due to the lower doses of drugs not hitting their biological targets within the tumours, the level of phosphorylated RNPII S2 was quantified. There was large variability in the pRNPII levels in the CYC065 treatment group indicating that the dose can be increased to ensure biological efficacy. Secondly, the biomarker identified from the 2D assays and short-term *in vivo* assays, EN1, showed no change in localisation following long-term treatment at the reduced doses in stained tumour sections. The clear observation of negative nucleolar body staining in the short-term combination group was not detected following the long-term treatment. Thirdly, as the drug was well tolerated even when mice were compromised and positive for C. bovis, there is potential room for dose escalation.

A very important area to further this investigation is to conduct these experiments in other ACC PDX lines, as all mechanistic data described is using sample SG0032 so all conclusions are SG0032 centric. Furthermore, 2D *in vitro* assays indicate that the combination is more synergistic in SG0027 than SG0032. It would be interesting to investigate the expression of downstream MYB targets following combination treatment in SG0027 and 28 as these samples have MYB activation via an alternative mechanism to the *MYB-NFIB* translocation. This would therefore give insight into how the NFIB-flanking super-enhancers impact the MYB transcriptional program and

whether this alters drug sensitivities. It would also be interesting to investigate how MYBL1-NFIB driven ACC responds at the transcriptional level to the combination by using sample SG0069, to identify differences in the MYB- and MYBL1-driven tumour response.

7. Discussion

ACC is an orphan disease with low survival rates owing to a number of issues; an unpredictable disease course, radio- and chemotherapy resistance and a lack of targeted therapies. Research to address these issues and properties has been hindered as there are currently very few validated ACC pre-clinical models and, to-date, no commercially available cells lines. Therefore, this studentship aimed to;

a) Identify potential therapeutic targets from the genomic and transcriptomic analyses of ACC patient tumours
b) Optimise and establish relevant PDX-derived preclinical models in both 2D and 3D conditions
c) Use these models to identify novel therapeutic options for ACC, to confirm these *in vivo* and identify potential therapeutic biomarkers to demonstrate therapeutic efficacy.

To achieve this, eight metastatic ACC patient tumours were analysed via WES and RNAseq to identify common mutations or differentially expressed genes that could be therapeutically targeted. RNAseq data was analysed by normalising to both normal SG data and an Acinic cell carcinoma patient sample to highlight ACC-specific active pathways. PDX establishment was successful for 6 out of 11 patient sample implantations, and all histologically and molecularly recapitulated the patent samples

7.1. Relevant ACC pre-clinical model establishment

The six successfully established ACC PDX lines represent three different ACC molecular groups; MYB-NFIB driven, MYBL1-NFIB driven, and MYB driven by an alternative mechanism. They are therefore a valuable collection of ACC pre-clinical models that would enable investigation into the biological differences between MYB-driven and MYBL1-driven ACC tumours, investigation into other mechanisms of *MYB* activation in ACC and what the biological impact of lacking the flanking *NFIB* super-enhancers has on the transcriptional program and also potential therapeutic sensitivities. The

representation of the three ACC sub-groups makes this project unique, as MYB without a translocation- and MYBL1-driven PDX models have not been established by XenoSTART (Moskaluk et al., 2011).

Establishing ACC *in vitro* models is a challenging task due to the limited passage number of primary cells and significantly lower MYB expression in culture. There has been two successful patient sample-derived ACC models reported; a 2D cell line by Warner et al, and a 3D organoid model by Takada et al (Takada et al., 2021; Warner et al., 2019). However, in the 2D line MYB was not expressed at high levels until passage 20, and the expression of MYB in the 3D model was not assessed whilst in culture. My data agreed that under normal culture conditions MYB expression was significantly decreased compared to the PDX tumours they were derived from. Through RNAseq analysis comparing SG0032 PDX expression to the derived-2D cultures, the TGFß signalling pathway was significantly upregulated in the 2D cultures. Addition of TGFß inhibitors in both 2D and 3D PDX-derived models significantly increased *MYB* expression, suggesting that MYB is negatively regulated by TGFß signalling. This has not been reported in ACC before, and is contradictory to observations in ER+ breast cancer, where TGFß enhances MYB expression (Cesi et al., 2011). TGFß is known to have oncogenic functions such as inducing a tumour suppressive microenvironment and promoting invasion, metastasis, angiogenesis and proliferation (Padua & Massagué, 2009; Papageorgis, 2015; Tauriello et al., 2018). TGFß1 has been reported to promote migration and invasion in ACC, although this was determined using the cell line SACC-83 that was transfected with overexpressing MYB lentiviral vectors opposed to patient-derived lines with existing MYB activation. As TGFß signalling downregulates MYB, ACC cells may require MYB downregulation to promote EMT and migrate. This is further suggested by the GSEA comparing PDX tumours to derived-2D cultures where the EMT pathway was significantly upregulated in the 2D cultures. Therefore, it would be interesting to observe differences in migration in the PDX-derived cells with and without the TGFß inhibitor quantifying MYB expression, to determine whether this could be a potential therapeutic option following surgical resection to inhibit distant metastasis and local recurrence.

Interestingly, the growth rate of the 2D cultures was not increased when treated with TGFß inhibitors. This implies that ACC cells are able to proliferate in the absence or low levels of MYB expression, therefore questioning the presumption that ACC is dependent on MYB for tumour progression. Data further supporting this is that despite increased MYB expression in the 3D organoids by the addition of a TGFß inhibitor, the cultures still failed to passage.

Hypoxia was required to enable long-term passaging of ACC organoids, tested in two PDX-derived lines. Head and neck tumours are reported to have an average tumour oxygen percentage of 2%, and one study identified that hypoxia-related proteins are highly expressed in ACC tumour samples compared to normal SG tissue, therefore culture of *in vitro* PDX-derived models in hypoxic conditions may reflect the hypoxic micro-environment of the patient tumours (De Mendonça et al., 2020; Mckeown, 2014). An area of future work would be to investigate the effect of hypoxic culture on *MYB* and MYB downstream target expression to identify changes at the transcriptional level. It would be interesting to compare differences to the normal SG organoids for which hypoxia inhibited growth.

The establishment of these 2D and 3D cultures provides relevant ACC models to investigate other biological properties of the cancer, in addition to therapeutic sensitivities. One particular property associated with poor prognosis is PNSI, occurring in 52-78% of cases (M. Amit et al., 2015; M. Huang et al., 1997; Ko et al., 2007; Vrielinck et al., 1988). Papers investigating neurotropic factors and neural invasion in other cancers have used co-cultures of primary cell models with mouse-derived dorsal root ganglia explants (Gil et al., 2010; Na'ara et al., 2016; Nan et al., 2019). This has been used to investigate how sympathetic innervation contributes to perineural invasion in ACC, although this was using the cell line SACC-83 (Ma et al., 2019). Furthermore, local recurrence and distant metastasis are common in ACC disease progression, therefore these models could also be applied to study ACC-ECM interactions via invasion assays, ACC-stromal interactions via co-culture assays, and niche dependencies for survival and proliferation as studied in this thesis. It would be interesting to also compare these effects between the three organoid lines established that each have a different

mechanism of MYB/MYBL1 activation and growth pattern to assess whether these prognostic factors promote increased invasive or metastatic properties as reported in the clinic. Furthermore, these ACC properties can be investigated *in vivo*. For example, whilst orthotopic SG0032 fragment implantation to the submandibular gland did not show evidence of neural or local tissue invasion, Cornett at al did report these findings when *in vitro* cultured ACC single cells were implanted (Cornett et al., 2019). Although this may be due to a number of patient tumour and technical implantation properties, in light of the finding that TGFß signalling is increased under normal culture conditions and that MYB is downregulated in response, this assay could be used to test the theory that downregulated MYB expression is required for and promotes ACC cell EMT and metastasis. Cornett et al did not determine the level of MYB expression whilst the ACC-derived cells were in culture, only in the established tumours from engraftment, so potentially it could have been that the level of MYB expression in the SG0032 tumour fragments was higher than that of the cultured cells limiting invasion. Therefore, it would be interesting to compare the level of invasiveness of implanted ACC single cells cultured with and without the addition of a TGFß inhibitor to determine if low MYB expression upon engraftment promotes invasive behaviour *in vivo*.

7.2. Promising therapeutic combination investigation

Oncogenic transcription factors are difficult to directly target, and the inhibition of these factors is an on-going area of research. Indirectly inhibiting transcription factors by targeting regulators of transcription has proven effective for a range of oncogene-driven cancers. Regulators of transcription include the transcriptional co-activator BRD4, and the transcriptional CDK, CDK9. BRD4 recruits P-TEFb to acetylated chromatin, whereas CDK9 is the kinase domain of P-TEFb that phosphorylates RNA polymerase II inducing transcription initiation and elongation (Jeronimo et al., 2016; Yang et al., 2005). BRD4 and CDK9 inhibitors have been used in combination to inhibit oncogenic transcription factors such as MYC, by targeting super-enhancers with high BRD4 occupancy (Gerlach et al., 2018; McCalmont et al., 2020; Moreno et al., 2017). Therefore, as MYB is known to interact with super-enhancers in ACC, particularly in the case of the *MYB-NFIB*

translocation by binding the NFIB flanking super-enhancers, the combination of JQ1 and CYC065 was hypothesised to inhibit *MYB* and MYB downstream target transcription. However, this does not appear to be the mechanism of action as MYB expression was not decreased in the short-term combination treated tumours. It is likely that the combination treatment is not specific to MYB, and targets general super-enhancers with high BRD4 occupancy. However, ChIP-seq would determine this by comparing between vehicle and combination treated samples, identifying the active super-enhancers MYB binds to and at which downstream targets. Furthermore, as all mechanistic analysis was conducted in one ACC line, SG0032 that possesses the MYB-NFIB translocation, it would be interesting to repeat these studies with the MYBL1-NFIB line and a line with MYB activation via another mechanism, to determine whether the downregulated targets are the same, and if the super-enhancer landscape is different in these alternative sub-groups.

Nevertheless, whether the combination mechanism of action is through inhibition of MYB or not, proliferation was significantly decreased in the short-term combination treated tumours compared to both single agent and vehicle treated tumours. Unfortunately, the long-term study was not optimal due to irregular tumour measurements, variability in growth within the vehicle control group and C. bovis infected mice. To overcome these issues, the experiment has been set up again, with mice implanted with single cell injections opposed to tumour chunks to promote uniform growth. There was also an issue of toxicity, therefore the long-term study was completed using 2-fold lower drug doses than the short term. In the repeat, higher doses will be used as although the low doses were very well tolerated, the localisation of the biomarker EN1 was not altered as it was in the short-term tumours. Although the normal SG organoids showed less sensitivity to the potential drug combination than the ACC organoids, clearly there is a small therapeutic window and concentrations above which are severely toxic to normal tissues. All tissue types have normal super-enhancers that confer tissue specificity by the binding of tissue-specific transcription factors (Lovén et al., 2013). This drug combination may be disrupting normal biological processes and global transcription, resulting in toxicity. If toxicity remains an issue and a balance with efficacy cannot be found within the therapeutic window, there are alternative drugs to

investigate. A novel type of therapy utilised to inhibit oncogenic transcription factors are proteolysis-targeting chimeras (PROTACs) that target a specific protein for ubiquitylation and subsequent proteasomal degradation (Nalawansha & Crews, 2020). Crews et al identified that the pan-BET PROTAC, ARV-771, induced c-MYC degradation with an IC_{50} of < 1 nM and induced apoptosis through PARP cleavage in castration-resistant prostate cancer (Raina et al., 2016). As a single molecule of this drug has the ability to mediate destruction of multiple target proteins by repeated cycles of binding and degradation, it is likely that less frequent dosing is required for efficacy which would be more tolerable than the combination dosing regimen I have investigated where the drugs are administered by two different routes (Bondeson et al., 2015).

Despite the limitations of the long-term study, the combination treatment and JQ1 single treatment impeded ACC tumour growth to similar degrees. JQ1 has previously been investigated in ACC PDX models by Drier et al, who reported that whilst low grade tumours were sensitive, high grade tumours were not (Drier et al., 2016). The apparent *in vivo* sensitivity of SG0032 may be due to the tumour being low grade ACC, having a classic cribriform growth pattern without areas of solid growth. Therefore, this study should be conducted using the line SG0027 which has solid histology. This may show that the combination of JQ1 with CYC065 is required for high grade tumours with areas of solid growth whereas JQ1 alone is efficacious for low grade tumours. If this proves true *in vivo*, the Perzin/Szanto grading system, classifying tumours with over 30% solid growth as high grade, could be a method of patient stratification for treatment groups in the clinic (Perzin et al., 1978; Szanto et al., 1984). This could potentially have been predicted by the increased level of drug synergy observed in SG0027 assays compared to SG0032. However, despite not observing tumour regression with either JQ1 single agent or in combination with CYC065, stabilised tumour growth is a promising result. As there are currently no available targeted treatments for ACC patients, research should continue into this combination *in vivo*, with the potential to progress to clinical trial.

I have investigated the targeting of MYB in depth as its activation is the most frequent genetic aberration in ACC, however this has proven complicated as the proposed combination appears to have a very small therapeutic window and be less tumour

specific than hoped. If toxicity cannot be overcome, perhaps it would be more fruitful to consider combinations that target more than one pathway, for example a combination of a BRD inhibitor with a γ-secretase inhibitor interfering with Notch signalling as activating NOTCH1 mutations and a higher dependency on Notch signalling in general is a feature of high-grade ACC with the worst prognosis.

7.3. Concluding remarks

This study has provided novel information regarding 2D and 3D PDX-derived *in vitro* model methodologies. These models mostly histologically and molecularly recapitulate the PDX tumours, and have proven to be accurate models to predict drug sensitivities. Notably, I identified that TGFß signalling negatively regulates MYB expression, and that hypoxia enables long-term passaging of ACC PDX-derived organoid cultures, which is inhibitory in normal SG organoids. Further research into these pathways could further identify methods for potential clinical intervention. In addition, a synergistic drug combination was identified between the BRD4 inhibitor JQ1 and the CDK2, 9 inhibitor CYC065. This combination was synergistic in four PDX-derived 2D lines and sensitivity was maintained the 3D models. Moreover, the combination significantly reduced proliferation following short-term *in vivo* treatment, and EN1, MYC and SOX9 have been identified as potential biomarkers of therapeutic efficacy. Validation in a long-term assay is on-going, and efficacy should also be explored *in vivo* in additional ACC PDX lines with differing mechanisms of MYB activation and histological grade. Overall, this study has resulted in the establishment of a number of ACC pre-clinical *in vitro* and *in vivo* models that have the capacity to further research into unmet areas of ACC, improving patient care and survival.

8. References

Agulnik, M., Cohen, E. W. E., Cohen, R. B., Chen, E. X., Vokes, E. E., Hotte, S. J., Winquist, E., Laurie, S., Hayes, D. N., Dancey, J. E., Brown, S., Pond, G. R., Lorimer, I., Daneshmand, M., Ho, J., Tsao, M.-S., & Siu, L. L. (2007). Phase II study of lapatinib in recurrent or metastatic epidermal growth factor receptor and/or erbB2 expressing adenoid cystic carcinoma and non adenoid cystic carcinoma malignant tumors of the salivary glands. *Journal of Clinical Oncology : Official Journal of the American Society of Clinical Oncology*, *25*(25), 3978–3984. https://doi.org/10.1200/JCO.2007.11.8612

Amit, M., Binenbaum, Y., Trejo-Leider, L., Sharma, K., Ramer, N., Ramer, I., Agbetoba, A., Miles, B., Yang, X., Lei, D., Bjorndal, K., Godballe, C., Mucke, T., Wolff, K. D., Eckardt, A. M., Copelli, C., Sesenna, E., Palmer, F., Ganly, I., … Gil, Z. (2015). International collaborative validation of intraneural invasion as a prognostic marker in adenoid cystic carcinoma of the head and neck. *Head and Neck*, *37*(7), 1038–1045. https://doi.org/10.1002/HED

Amit, Moran, Eran, A., Billan, S., Fridman, E., Na'ara, S., Charas, T., & Gil, Z. (2016). Perineural Spread in Noncutaneous Head and Neck Cancer: New Insights into an Old Problem. *Journal of Neurological Surgery, Part B: Skull Base*, *77*(2), 86–95. https://doi.org/10.1055/s-0036-1571834

Andersson, M. K., Afshari, M. K., Andrén, Y., Wick, M. J., & Stenman, G. (2017). Targeting the Oncogenic Transcriptional Regulator MYB in Adenoid Cystic Carcinoma by Inhibition of IGF1R/AKT Signaling. *Journal of the National Cancer Institute*, *109*(9), djx017. https://doi.org/10.1093/jnci/djx017

Andersson, M. K., Mangiapane, G., Nevado, P. T., Tsakaneli, A., Carlsson, T., Corda, G., Nieddu, V., Abrahamian, C., Chayka, O., Rai, L., Wick, M., Kedaigle, A., Stenman, G., & Sala, A. (2020). ATR is a MYB regulated gene and potential therapeutic target in adenoid cystic carcinoma. *Oncogenesis*, *9*(1). https://doi.org/10.1038/s41389-020-0194-3

Aster, J. C., Pear, W. S., & Blacklow, S. C. (2017). The Varied Roles of Notch in Cancer. *Annual Review of Pathology: Mechanisms of Disease*, *12*(1), 245–275.

https://doi.org/10.1146/annurev-pathol-052016-100127

Babiak, A., Steinhauser, M., Götz, M., Herbst, C., Döhner, H., & Greiner, J. (2014). Frequent T cell responses against immunogenic targets in lung cancer patients for targeted immunotherapy. *Oncol Rep*, *31*(1), 384–390. https://doi.org/10.3892/or.2013.2804

Bell, D., Bell, A. H., Bondaruk, J., Hanna, E. Y., & Weber, R. S. (2016). In-depth characterization of the salivary adenoid cystic carcinoma transcriptome with emphasis on dominant cell type. *Cancer*, *122*(10), 1513–1522. https://doi.org/10.1002/cncr.29959

Bell, D., Bell, A., Roberts, D., Weber, R. S., & El-Naggar, A. K. (2012). Developmental transcription factor EN1—a novel biomarker in human salivary gland adenoid cystic carcinoma. *Cancer*, *118*(5), 1288–1292. https://doi.org/10.1002/cncr.26412

Bell, D., Ferrarotto, R., Fox, M. D., Roberts, D., Hanna, E. Y., Weber, R. S., & El-naggar, A. K. (2015). Analysis and significance of c-MET expression in adenoid cystic carcinoma of the salivary gland. *Cancer Biology and Therapy*, *16*(6), 834–838.

Bell, D., Roberts, D., Karpowicz, M., Hanna, E. Y., Weber, R. S., & El-Naggar, A. K. (2011). Clinical significance of Myb protein and downstream target genes in salivary adenoid cystic carcinoma. *Cancer Biology and Therapy*, *12*(7), 569–573. https://doi.org/10.4161/cbt.12.7.17008

Beltran, A. S., Graves, L. M., & Blancafort, P. (2014). Novel role of Engrailed 1 as a prosurvival transcription factor in basal-like breast cancer and engineering of interference peptides block its oncogenic function. *Oncogene*, *33*, 4767–4777. https://doi.org/10.1038/onc.2013.422

Bertotti, A., Migliardi, G., Galimi, F., Sassi, F., Torti, D., Isella, C., Corà, D., di Nicolantonio, F., Buscarino, M., Petti, C., Ribero, D., Russolillo, N., Muratore, A., Massucco, P., Pisacane, A., Molinaro, L., Valtorta, E., Sartore-Bianchi, A., Risio, M., … Trusolino, L. (2011). A molecularly annotated platform of patient- derived xenografts ("xenopatients") identifies HER2 as an effective therapeutic target in cetuximab-resistant colorectal cancer. *Cancer Discovery*, *1*(6), 508–523. https://doi.org/10.1158/2159-8290.CD-11-0109

Betancur, P., Bronner-Fraser, M., & Sauka-Spengler, T. (2010). Genomic code for Sox10 activation reveals a key regulatory enhancer for cranial neural crest. *Proceedings*

of the National Academy of Sciences, *107*(8), 3570–3575. https://doi.org/10.1073/pnas.0906596107

Bjørndal, K., Krogdahl, A., Therkildsen, M. H., Charabi, B., Kristensen, C. A., Andersen, E., Schytte, S., Primdahl, H., Johansen, J., Pedersen, H. B., Andersen, L. J., & Godballe, C. (2015). Salivary adenoid cystic carcinoma in Denmark 1990-2005: Outcome and independent prognostic factors including the benefit of radiotherapy. Results of the Danish Head and Neck Cancer Group (DAHANCA). *Oral Oncology*, *51*(12), 1138–1142. https://doi.org/10.1016/j.oraloncology.2015.10.002

Bjørndal, K., Krogdahl, A., Therkildsen, M. H., Overgaard, J., Johansen, J., Kristensen, C. A., Homøe, P., Sørensen, C. H., Andersen, E., Bundgaard, T., Primdahl, H., Lambertsen, K., Andersen, L. J., & Godballe, C. (2011). Salivary gland carcinoma in Denmark 1990-2005: A national study of incidence, site and histology. Results of the Danish Head and Neck Cancer Group (DAHANCA). *Oral Oncology*, *47*(7), 677–682. https://doi.org/10.1016/j.oraloncology.2011.04.020

Bleijs, M., Wetering, M. Van De, Clevers, H., & Drost, J. (2019). *Xenograft and organoid model systems in cancer research*. 1–11. https://doi.org/10.15252/embj.2019101654

Bliss, C. . (1939). The toxicity of poisons applied jointly. *Annals of Applied Biology*, *26*(3), 585–615. https://doi.org/10.1111/j.1744-7348.1939.tb06990.x

Boeckx, C., Baay, M., Wouters, A., Specenier, P., Vermorken, J. B., Peeters, M., & Lardon, F. (2013). Anti-Epidermal Growth Factor Receptor Therapy in Head and Neck Squamous Cell Carcinoma: Focus on Potential Molecular Mechanisms ofDrugResistance. *The Oncologist*, *0031*(0), 1051–1062.

Bolin, S., Borgenvik, A., Persson, C. U., Sundström, A., Qi, J., Bradner, J. E., Weiss, W. A., Cho, Y. J., Weishaupt, H., & Swartling, F. J. (2018). Combined BET bromodomain and CDK2 inhibition in MYC-driven medulloblastoma. *Oncogene*, *37*, 2850–2862. https://doi.org/10.1038/s41388-018-0135-1

Bondeson, D. P., Mares, A., Smith, I. E. D., Ko, E., Campos, S., Miah, A. H., Mulholland, K. E., Routly, N., Buckley, D. L., Gustafson, J. L., Zinn, N., Grandi, P., Shimamura, S., Bergamini, G., Faelth-Savitski, M., Bantscheff, M., Cox, C., Gordon, D. A., Willard, R. R., … Crews, C. M. (2015). Catalytic in vivo protein knockdown by small-

molecule PROTACs. *Nature Chemical Biology*, *11*(8), 611–617. https://doi.org/10.1038/nchembio.1858

Boneparte, J. P., Hart, R., Trites, J., & Taylor, M. S. (2008). Incidence of adenoid cystic carcinoma in nova scotia: 30-year population-based epidemiologic study. *Journal of Otolaryngology - Head & Neck Surgery*, *37*(5), 642–648.

Brayer, K. J., Frerich, C. A., Kang, H., & Ness, S. A. (2016). Recurrent Fusions in MYB and MYBL1 Define a Common, Transcription Factor-Driven Oncogenic Pathway in Salivary Gland Adenoid Cystic Carcinoma. *Cancer Discovery*, *6*(2), 176–187. https://doi.org/10.1016/j.physbeh.2017.03.040

Brill, L. B., Kanner, W. A., Fehr, A., Andrén, Y., Moskaluk, C. A., Löning, T., Stenman, G., & Frierson, H. F. J. (2011). Analysis of MYB expression and MYB-NFIB gene fusions in adenoid cystic carcinoma and other salivary neoplasms. *Modern Pathology : An Official Journal of the United States and Canadian Academy of Pathology, Inc*, *24*(9), 1169–1176. https://doi.org/10.1038/modpathol.2011.86

Brodeur, J., Monti, A., Kollipara, S., Connolly, K., Boudrow, A., Tissire, H., Meetze, K., & Rideout, W. (2009). Knock-in of human HGF into the mouse genome maintains endogenous HGF regulation and supports the growth of HGF-dependent human cancer cell lines. *American Association for Cancer Research*, *69*(9), Abs. 305.

Bruna, A., Rueda, O. M., Greenwood, W., Batra, A. S., Callari, M., Batra, R. N., Pogrebniak, K., Sandoval, J., Cassidy, J. W., Tufegdzic-Vidakovic, A., Sammut, S. J., Jones, L., Provenzano, E., Baird, R., Eirew, P., Hadfield, J., Eldridge, M., McLaren-Douglas, A., Barthorpe, A., … Caldas, C. (2016). A Biobank of Breast Cancer Explants with Preserved Intra-tumor Heterogeneity to Screen Anticancer Compounds. *Cell*, *167*(1), 260–274. https://doi.org/10.1016/j.cell.2016.08.041

Budi, E. H., Muthusamy, B. P., & Derynck, R. (2015). The insulin response integrates increased TGF-β signaling through Akt-induced enhancement of cell surface delivery of TGF-β receptors. *Science Signalling*, *8*(396), ra96. https://doi.org/10.1126/scisignal.aaa9432.The

Burger, K., Mühl, B., Rohrmoser, M., Coordes, B., Heidemann, M., Kellner, M., Gruber-Eber, A., Heissmeyer, V., Strässer, K., & Eick, D. (2013). Cyclin-dependent kinase 9 links RNA polymerase II transcription to processing of ribosomal RNA. *Journal of Biological Chemistry*, *288*(29), 21173–21183.

https://doi.org/10.1074/jbc.M113.483719

Byrd, J. C., Lin, T. S., Dalton, J. T., Wu, D., Phelps, M. A., Fischer, B., Moran, M., Blum, K. A., Rovin, B., Brooker-McEldowney, M., Broering, S., Schaaf, L. J., Johnson, A. J., Lucas, D. M., Heerema, N. A., Lozanski, G., Young, D. C., Suarez, J.-R., Colevas, A. D., & Grever, M. R. (2007). Flavopiridol administered using a pharmacologically derived schedule is associated with marked clinical efficacy in refractory, genetically high-risk chronic lymphocytic leukemia. *Blood*, *109*(2), 399–404. https://doi.org/10.1182/blood-2006-05-020735

Byrne, A. T., Alférez, D. G., Amant, F., Annibali, D., Arribas, J., Biankin, A. V., Bruna, A., Budinská, E., Caldas, C., Chang, D. K., Clarke, R. B., Clevers, H., Coukos, G., Dangles-Marie, V., Gail Eckhardt, S., Gonzalez-Suarez, E., Hermans, E., Hidalgo, M., Jarzabek, M. A., … Trusolino, L. (2017). Interrogating open issues in cancer precision medicine with patient-derived xenografts. *Nature Reviews Cancer*, *17*(4), 254–268. https://doi.org/10.1038/nrc.2016.140

Carpenter, G. H. (2013). The secretion, components, and properties of saliva. *Annual Review of Food Science and Technology*, *4*(1), 267–276. https://doi.org/10.1146/annurev-food-030212-182700

Castellanos, D. A., Tsoulfas, P., Frydel, B. R., Gajavelli, S., Bes, J. C., & Sagen, J. (2002). TrkC overexpression enhances survival and migration of neural stem cell transplants in the rat spinal cord. *Cell Transplantation*, *11*(3), 297–307. https://doi.org/10.3727/096020198389942

Cesi, V., Casciati, A., Sesti, F., Tanno, B., Calabretta, B., & Raschellà, G. (2011). TGFβ-induced c-Myb affects the expression of EMT-associated genes and promotes invasion of ER+ breast cancer cells. *Cell Cycle*, *10*(23), 4149–4161. https://doi.org/10.4161/cc.10.23.18346

Chapuy, B., Cheng, H., Watahiki, A., Ducar, M. D., Tan, Y., Chen, L., Roemer, M. G. M., Ouyang, J., Christie, A. L., Zhang, L., Gusenleitner, D., Abo, R. P., Farinha, P., von Bonin, F., Thorner, A. R., Sun, H. H., Gascoyne, R. D., Pinkus, G. S., van Hummelen, P., … Shipp, M. A. (2016). Diffuse large B-cell lymphoma patient-derived xenograft models capture the molecular and biological heterogeneity of the disease. *Blood*, *127*(18), 2203–2213. https://doi.org/10.1182/blood-2015-09-672352

Chen, D., Zhao, Z., Huang, Z., Chen, D. C., Zhu, X. X., Wang, Y. Z., Yan, Y. W., Tang, S.,

Madhavan, S., Ni, W., Huang, Z. P., Li, W., Ji, W., Shen, H., Lin, S., & Jiang, Y. Z. (2018). Super enhancer inhibitors suppress MYC driven transcriptional amplification and tumor progression in osteosarcoma. *Bone Research*, *6*(1), 1–7. https://doi.org/10.1038/s41413-018-0009-8

Chen, E. Y., Tan, C. M., Kou, Y., Duan, Q., Wang, Z., Meirelles, G. V., Clark, N. R., & Ma'ayan, A. (2013). Enrichr: Interactive and collaborative HTML5 gene list enrichment analysis tool. *BMC Bioinformatics*, *14*. https://doi.org/10.1186/1471-2105-14-128

Chou, T C, Otter, G. M., & Sirotnak, F. M. (1996). Schedule-dependent synergism of taxol or taxotere with edatrexate against human breast cancer cells in vitro. *Cancer Chemotherapy and Pharmacology*, *37*(3), 222–228. https://doi.org/10.1007/BF00688320

Chou, Ting Chao. (2006). Theoretical basis, experimental design, and computerized simulation of synergism and antagonism in drug combination studies. *Pharmacological Reviews*, *58*(3), 621–681. https://doi.org/10.1124/pr.58.3.10

Chou, Ting Chao, & Martin, N. (2005). *CompuSyn for Drug Combinations: PC Software and User's Guide*. ComboSyn Inc, Paramus.

Chou, Ting Chao, & Talalay, P. (1984). Quantitative analysis of dose-effect relationships: the combined effects of multiple drugs or enzyme inhibitors. *Advances in Enzyme Regulation*, *22*(C), 27–55. https://doi.org/10.1016/0065-2571(84)90007-4

Christensen, J. G., Burrows, J., & Salgia, R. (2005). c-Met as a target for human cancer and characterization of inhibitors for therapeutic intervention. *Cancer Letters*, *225*(1), 1–26. https://doi.org/10.1016/j.canlet.2004.09.044

Chua, C. W., Shibata, M., Lei, M., Toivanen, R., Barlow, L. J., Bergren, S. K., Badani, K. K., McKiernan, J. M., Benson, M. C., Hibshoosh, H., & Shen, M. M. (2014). Single luminal epithelial progenitors can generate prostate organoids in culture. *Nature Cell Biology*, *16*(10), 951–961. https://doi.org/10.1038/ncb3047

Cohen, R. B., Delord, J. P., Doi, T., Piha-Paul, S. A., Liu, S. V., Gilbert, J., Algazi, A. P., Damian, S., Hong, R. L., Le Tourneau, C., Day, D., Varga, A., Elez, E., Wallmark, J., Saraf, S., Thanigaimani, P., Cheng, J., & Keam, B. (2018). Pembrolizumab for the treatment of advanced salivary gland carcinoma. *American Journal of Clinical*

Oncology: Cancer Clinical Trials, *41*(11), 1083–1088. https://doi.org/10.1097/COC.0000000000000429

Contucci, A. M., Inzitari, R., Agostino, S., Vitali, A., Fiorita, A., Cabras, T., Scarano, E., & Messana, I. (2005). Statherin levels in saliva of patients with precancerous and cancerous lesions of the oral cavity: a preliminary report. *Oral Diseases*, *11*(2), 95–99. https://doi.org/10.1111/j.1601-0825.2004.01057.x

Cornett, A., Athwal, H. K., Hill, E., Murphy, G., Yeoh, K., Moskaluk, C. A., Witt, R. L., D'Silva, N. J., Agarwal, S., & Lombaert, I. M. A. (2019). Serial patient-derived orthotopic xenografting of adenoid cystic carcinomas recapitulates stable expression of phenotypic alterations and innervation. *EBioMedicine*, *41*, 175–184. https://doi.org/10.1016/j.ebiom.2019.02.011

Cross, R. S., Malaterre, J., Davenport, A. J., Carpinteri, S., Anderson, R. L., Darcy, P. K., & Ramsay, R. G. (2015). Therapeutic DNA vaccination against colorectal cancer by targeting the MYB oncoprotein. *Clinical and Translational Immunology*, *4*(1), e30-10. https://doi.org/10.1038/cti.2014.29

Cutz, J. C., Guan, J., Bayani, J., Yoshimoto, M., Xue, H., Sutcliffe, M., English, J., Flint, J., LeRiche, J., Yee, J., Squire, J. A., Gout, P. W., Lam, S., & Wang, Y. Z. (2006). Establishment in severe combined immunodeficiency mice of subrenal capsule xenografts and transplantable tumor lines from a variety of primary human lung cancers: Potential models for studying tumor progression-related changes. *Clinical Cancer Research*, *12*(13), 4043–4054. https://doi.org/10.1158/1078-0432.CCR-06-0252

Dai, L., Lu, C., Yu, X., Dai, L. J., & Zhou, J. X. (2015). Construction of orthotopic xenograft mouse models for human pancreatic cancer. *Experimental and Therapeutic Medicine*, *10*(3), 1033–1038. https://doi.org/10.3892/etm.2015.2642

Daneshbod, Y., Daneshbod, K., & Khademi, B. (2009). Diagnostic Difficulties in the Interpretation of Fine Needle Aspirate Samples in Salivary Lesions. *Acta Cytologica*, *53*(1), 53–70.

De Matos, F. R., De Araújo Lima, E. D. N., Queiroz, L. M. G., & Da Silveira, É. J. D. (2012). Analysis of inflammatory infiltrate, perineural invasion, and risk score can indicate concurrent metastasis in squamous cell carcinoma of the tongue. *Journal of Oral and Maxillofacial Surgery*, *70*(7), 1703–1710.

https://doi.org/10.1016/j.joms.2011.08.023

De Mendonça, R. P., Chemelo, G. P., Mitre, G. P., Branco, D. C., Da Costa, N. M. M., Tuji, F. M., Da Silva Kataoka, M. S., Mesquita, R. A., De Melo Alves Júnior, S., & De Jesus Viana Pinheiro, J. (2020). Role of hypoxia-related proteins in adenoid cystic carcinoma invasion. *Diagnostic Pathology*, *15*(1), 4–11. https://doi.org/10.1186/s13000-020-00967-3

de Paula, F., Teshima, T. H. N., Hsieh, R., Souza, M. M., Nico, M. M. S., & Lourenco, S. V. (2017). Overview of Human Salivary Glands: Highlights of Morphology and Developing Processes. *Anatomical Record*, *300*(7), 1180–1188. https://doi.org/10.1002/ar.23569

Degos, L., & Wang, Z. Y. (2001). All trans retinoic acid in acute promyelocytic leukemia. *Oncogene*, *20*(49 REV. IIS. 6), 7140–7145. https://doi.org/10.1038/sj.onc.1204763

Del Signore, A. G., & Megwalu, U. C. (2017). The rising incidence of major salivary gland cancer in the United States. *Ear Nose Throat Journal*, *86*(3), E13–E16.

Delmore, J. E., Issa, G. C., Lemieux, M. E., Rahl, P. B., Shi, J., Jacobs, H. M., Kastritis, E., Gilpatrick, T., Paranal, R. M., Qi, J., Chesi, M., Schinzel, A., Mckeown, M. R., Heffernan, T. P., Vakoc, R., Bergsagel, P. L., Ghobrial, I. M., Richardson, P. G., Richard, A., … Mitsiades, C. S. (2011). BET bromodomain inhibition as a therpeutic strategy to target c-Myc. *Cell*, *146*(6), 904–917. https://doi.org/10.1016/j.cell.2011.08.017.BET

Devaiah, B. N., Lewis, B. A., Cherman, N., Hewitt, M. C., Albrecht, B. K., Robey, P. G., Ozato, K., Sims, R. J., & Singer, D. S. (2012). BRD4 is an atypical kinase that phosphorylates Serine2 of the RNA Polymerase II carboxy-terminal domain. *Proceedings of the National Academy of Sciences of the United States of America*, *109*(18), 6927–6932. https://doi.org/10.1073/pnas.1120422109

Dick de Haan, L., De Mulder, P. H. M., Vermorken, J. B., Schornagel, J. H., Vermey, A., & Verweij, J. (1992). Cisplatin-based chemotherapy in advanced adenoid cystic carcinoma of the head and neck. *Head & Neck*, *14*(4), 273–277. https://doi.org/10.1002/hed.2880140403

Dijkstra, K. K., Cattaneo, C. M., Weeber, F., Chalabi, M., De, J. Van, Kelderman, S., Rooij, N. Van, Leerdam, M. E. Van, & Depla, A. (2018). Generation of tumor-reactive T cells by co-culture of peripheral blood lymphocytes and tumor organoids. *Cell*,

174(6), 1586–1598. https://doi.org/10.1016/j.cell.2018.07.009.Generation

Dong, M., Ning, Z. Q., Xing, P. Y., Xu, J. L., Cao, H. X., Dou, G. F., Meng, Z. Y., Shi, Y. K., Lu, X. P., & Feng, F. Y. (2012). Phase I study of chidamide (CS055/HBI-8000), a new histone deacetylase inhibitor, in patients with advanced solid tumors and lymphomas. *Cancer Chemotherapy and Pharmacology*, *69*, 1413–1422.

Drier, Y., Cotton, M. J., Williamson, K. E., Gillespie, S. M., Ryan, R. J. H., Kluk, M. J., Carey, C. D., Rodig, S. J., Sholl, L. M., Afrogheh, A. H., Faquin, W. C., Queimado, L., Qi, J., Wick, M. J., El-Naggar, A. K., Bradner, J. E., Moskaluk, C. A., Aster, J. C., Knoechel, B., & Bernstein, B. E. (2016). An oncogenic MYB feedback loop drives alternate cell fates in adenoid cystic carcinoma. *Nature Genetics*, *48*(3), 265–272. https://doi.org/10.1038/ng.3502

Drost, J., Karthaus, W. R., Gao, D., Driehuis, E., Sawyers, C. L., Chen, Y., & Clevers, H. (2016). Organoid culture systems for prostate epithelial and cancer tissue. *Nature Protocols*, *11*(2), 347–358. https://doi.org/10.1038/nprot.2016.006

Drost, J., Van Jaarsveld, R. H., Ponsioen, B., Zimberlin, C., Van Boxtel, R., Buijs, A., Sachs, N., Overmeer, R. M., Offerhaus, G. J., Begthel, H., Korving, J., Van De Wetering, M., Schwank, G., Logtenberg, M., Cuppen, E., Snippert, H. J., Medema, J. P., Kops, G. J. P. L., & Clevers, H. (2015). Sequential cancer mutations in cultured human intestinal stem cells. *Nature*, *521*(7550), 43–47. https://doi.org/10.1038/nature14415

Ebbesen, S. H., Scaltriti, M., Bialucha, C. U., Morse, N., Kastenhuber, E. R., Wen, H. Y., Dow, L. E., Baselga, J., & Lowe, S. W. (2016). PTEN Loss promotes MAPK pathway dependency in HER2/neu breast carcinomas. *Proceedings of the National Academy of Sciences of the United States of America*, *113*(11), 3030–3035. https://doi.org/10.1073/pnas.1523693113

Eder, A., Vollert, I., Hansen, A., & Eschenhagen, T. (2016). Human engineered heart tissue as a model system for drug testing. *Advanced Drug Delivery Reviews*, *96*, 214–224. https://doi.org/10.1016/j.addr.2015.05.010

Ellington, C. L., Goodman, M., Kono, S. A., Grist, W., Wadsworth, T., Chen, A. Y., Owonikoko, T., Ramalingam, S., Shin, D. M., Khuri, F. R., Beitler, J. J., & Saba, N. F. (2012). Adenoid cystic carcinoma of the head and neck: Incidence and survival trends based on 1973-2007 Surveillance, Epidemiology, and End Results data.

Cancer, *118*(18), 4444–4451. https://doi.org/10.1002/cncr.27408

Even, C., Lassen, U., Merchan, J., Le Tourneau, C., Soria, J. C., Ferte, C., Ricci, F., Diener, J. T., Yuen, E., Smith, C., Oakley, G. J., Benhadji, K. A., & Massard, C. (2020). Safety and clinical activity of the Notch inhibitor, crenigacestat (LY3039478), in an open-label phase I trial expansion cohort of advanced or metastatic adenoid cystic carcinoma. *Investigational New Drugs*, *38*(2), 402–409. https://doi.org/10.1007/s10637-019-00739-x

Eveson, J. W., & Cawson, R. A. (1985). Tumours of the minor (oropharyngeal) salivary glands: a demographic study of 336 cases. *Journal of Oral Pathology*, *14*(6), 500–509.

Fan, H., Demirci, U., & Chen, P. (2019). Emerging organoid models: Leaping forward in cancer research. *Journal of Hematology and Oncology*, *12*(1), 1–10. https://doi.org/10.1186/s13045-019-0832-4

Ferrarotto, R., Heymach, J. V., & Glisson, B. S. (2016). MYB-fusions and other potential actionable targets in adenoid cystic carcinoma. In *Current Opinion in Oncology* (Vol. 28, Issue 3). https://doi.org/10.1097/CCO.0000000000000280

Ferrarotto, R., Mitani, Y., Diao, L., Guijarro, I., Wang, J., Zweidler-McKay, P., Bell, D., William, W. N., Glisson, B. S., Wick, M. J., Kapoun, A. M., Patnaik, A., Eckhardt, G., Munster, P., Faoro, L., Dupont, J., Lee, J. J., Futreal, A., El-Naggar, A. K., & Heymach, J. V. (2017). Activating NOTCH1 mutations define a distinct subgroup of patients with adenoid cystic carcinoma who have poor prognosis, propensity to bone and liver metastasis, and potential responsiveness to Notch1 inhibitors. *Journal of Clinical Oncology*, *35*(3), 352–360. https://doi.org/10.1200/JCO.2016.67.5264

Ferrarotto, R., Wirth, L. J., Muzaffar, J., Rodriguez, C. P., Xia, B., Perez, C. A., Bowles, D. W., Winquist, E., Hotte, S. J., Metcalf, R., Even, C., Gordon, G. B., Gordon, G., & Ho, A. (2020). ACCURACY a phase II trial of AL101, a selective gamma secretase inhibitor, in subjects with recurrent/metastatic (R/M) adenoid cystic carcinoma (ACC) harboring Notch activating mutations (Notchmut). *Annals of Oncology*, *31*(4_suppl), S599–S628. https://doi.org/10.1200/JCO.2019.37.15_suppl.TPS6098

Fiore, D., Ramesh, P., Proto, M. C., Piscopo, C., Franceschelli, S., Anzelmo, S., Medema, J. P., Bifulco, M., & Gazzerro, P. (2018). Rimonabant kills colon cancer stem cells

without inducing toxicity in normal colon organoids. *Frontiers in Pharmacology*, *8*(Jan), 1–15. https://doi.org/10.3389/fphar.2017.00949

Frame, S., Saladino, C., Davis, S., Blake, D., & Zheleva, D. (2015). CYC065, potential therapeutic agent for AML and MLL leukaemia. *Clinical Lymphoma, Myeloma & Leukemia*, *15*(Supplement), S183.

Frame, S., Saladino, C., Mackay, C., Atrash, B., Sheldrake, P., Mcdonald, E., Id, P. A. C., Workman, P., Blake, D., & Id, D. Z. (2020). Fadraciclib (CYC065), a novel CDK inhibitor , targets key pro-survival and oncogenic pathways in cancer. *PLoS ONE*, 1–31. https://doi.org/10.1371/journal.pone.0234103

Frerich, C. A., Brayer, K. J., Painter, B. M., Kang, H., Mitani, Y., El-Naggar, A. K., & Ness, S. A. (2018). Transcriptomes define distinct subgroups of salivary gland adenoid cystic carcinoma with different driver mutations and outcomes. *Oncotarget*, *9*(7), 7341–7358.

Fujii, M., Shimokawa, M., Date, S., Takano, A., Matano, M., Nanki, K., Ohta, Y., Toshimitsu, K., Nakazato, Y., Kawasaki, K., Uraoka, T., Watanabe, T., Kanai, T., & Sato, T. (2016). A Colorectal Tumor Organoid Library Demonstrates Progressive Loss of Niche Factor Requirements during Tumorigenesis. *Cell Stem Cell*, *18*(6), 827–838. https://doi.org/10.1016/j.stem.2016.04.003

Gao, D., Vela, I., Sboner, A., Iaquinta, P. J., Karthaus, W. R., Gopalan, A., Dowling, C., Wanjala, J. N., Undvall, E. A., Arora, V. K., Wongvipat, J., Kossai, M., Ramazanoglu, S., Barboza, L. P., Di, W., Cao, Z., Zhang, Q. F., Sirota, I., Ran, L., … Chen, Y. (2014). Organoid cultures derived from patients with advanced prostate cancer. *Cell*, *159*(1), 176–187. https://doi.org/10.1016/j.cell.2014.08.016

Gao, H., Korn, J. M., Ferretti, S., Monahan, J. E., Wang, Y., Singh, M., Zhang, C., Schnell, C., Yang, G., Zhang, Y., Balbin, O. A., Barbe, S., Cai, H., Casey, F., Chatterjee, S., Chiang, D. Y., Chuai, S., Cogan, S. M., Collins, S. D., … Sellers, W. R. (2015). High-throughput screening using patient-derived tumor xenografts to predict clinical trial drug response. *Nature Medicine*, *21*(11), 1318–1325. https://doi.org/10.1038/nm.3954

Garrido, C., Chauffert, B., Pinard, D., Tibaut, F., Genne, P., Assem, M., & Dimanche-Boitrel, M. T. (1995). Circumvention of confluence-dependent resistance in a human multi-drug-resistant colon-cancer cell line. *International Journal of*

Cancer, *61*(6), 873–879. https://doi.org/10.1002/ijc.2910610621

George, E., Kim, H., Krepler, C., Wenz, B., Makvandi, M., Tanyi, J. L., Brown, E., Zhang, R., Brafford, P., Jean, S., Mach, R. H., Lu, Y., Mills, G. B., Herlyn, M., Morgan, M., Zhang, X., Soslow, R., Drapkin, R., Johnson, N., … Simpkins, F. (2017). A patient-derived-xenograft platform to study BRCA-deficient ovarian cancers. *JCI Insight*, *2*(1), 1–18. https://doi.org/10.1172/jci.insight.89760

George, O. L., & Ness, S. A. (2014). Situational awareness: Regulation of the myb transcription factor in differentiation, The cell cycle and oncogenesis. *Cancers*, *6*(4), 2049–2071. https://doi.org/10.3390/cancers6042049

Gerlach, D., Tontsch-Grunt, U., Baum, A., Popow, J., Scharn, D., Hofmann, M. H., Engelhardt, H., Kaya, O., Beck, J., Schweifer, N., Gerstberger, T., Zuber, J., Savarese, F., & Kraut, N. (2018). The novel BET bromodomain inhibitor BI 894999 represses super-enhancer-associated transcription and synergizes with CDK9 inhibition in AML. *Oncogene*, *37*(20), 2687–2701. https://doi.org/10.1038/s41388-018-0150-2

Gil, Z., Cavel, O., Kelly, K., Brader, P., Rein, A., Gao, S. P., Carlson, D. L., Shah, J. P., Fong, Y., & Wong, R. J. (2010). Paracrine regulation of pancreatic cancer cell invasion by peripheral nerves. *Journal of the National Cancer Institute*, *102*(2), 107–118. https://doi.org/10.1093/jnci/djp456

Gilbert, J., Li, Y., Pinto, H. A., Jennings, T., Kies, M. S., Silverman, P., & Forastiere, A. A. (2006). Phase II trial of taxol in salivary gland malignancies (E1394): A trial of the Eastern Cooperative Oncology Group. *Head and Neck*, *28*(3), 197–204. https://doi.org/10.1002/hed.20327

Gilkes, D. M., Chen, L., & Chen, J. (2006). MDMX regulation of p53 response to ribosomal stress. *EMBO Journal*, *25*(23), 5614–5625. https://doi.org/10.1038/sj.emboj.7601424

Girdler, R., Odell, E., & Putnam, G. (2016). *Public Health England: Epidemiology and management of major salivary gland cancers*.

Goncalves, P. H., Heilbrun, L. K., Barrett, M. T., Kummar, S., Hansen, A. R., Siu, L. L., Piekarz, R. L., Sukari, A. W., Chao, J., Pilat, M. J., Smith, D. W., Casetta, L., Boerner, S. A., Chen, A., Lenkiewicz, E., Malasi, S., & LoRusso, P. M. (2017). A phase 2 study of vorinostat in locally advanced, recurrent, or metastatic adenoid cystic

carcinoma. *Oncotarget*, *8*(20), 32918–32929. https://doi.org/10.18632/oncotarget.16464

Guenot, D., Guérin, E., Aguillon-Romain, S., Pencreach, E., Schneider, A., Neuville, A., Chenard, M. P., Duluc, I., Du Manoir, S., Brigand, C., Oudet, P., Kedinger, M., & Gaub, M. P. (2006). Pimary tumour genetic alterations and intra-tumoral heterogeneity are maintained in xenografts of human colon cancers showing chromosome instability. *Journal of Pathology*, *208*(5), 643–652. https://doi.org/10.1002/path.1936

Haeggblom, L., Ursu, R. G., Mirzaie, L., Attoff, T., Gahm, C., Nordenvall, L. H., & Näsman, A. (2018). No evidence for human papillomavirus having a causal role in salivary gland tumors. *Diagnostic Pathology*, *13*(1), 1–5. https://doi.org/10.1186/s13000-018-0721-0

Hafner, M., Niepel, M., Chung, M., & Sorger, P. K. (2016). Growth rate inhibition metrics correct for confounders in measuring sensitivity to cancer drugs. *Nature Methods*, *13*(6), 521–527. https://doi.org/10.1038/nmeth.3853

Haller, F., Bieg, M., Will, R., Körner, C., Weichenhan, D., Bott, A., Ishaque, N., Lutsik, P., Moskalev, E. A., Mueller, S. K., Bähr, M., Woerner, A., Kaiser, B., Scherl, C., Haderlein, M., Kleinheinz, K., Fietkau, R., Iro, H., Eils, R., … Agaimy, A. (2019). Enhancer hijacking activates oncogenic transcription factor NR4A3 in acinic cell carcinomas of the salivary glands. *Nature Communications*, *10*(1), 368. https://doi.org/10.1038/s41467-018-08069-x

Hattori, T., Uchida, C., Takahashi, H., Yamamoto, N., Naito, M., & Taya, Y. (2014). Distinct and site-specific phosphorylation of the retinoblastoma protein at serine 612 in differentiated cells. *PLoS ONE*, *9*(1), e86709. https://doi.org/10.1371/journal.pone.0086709

Ho, A. L., Dunn, L., Sherman, E. J., Fury, M. G., Baxi, S. S., Chandramohan, R., Dogan, S., Morris, L. G. T., Cullen, G. D., Haque, S., Sima, C. S., Ni, A., Antonescu, C. R., Katabi, N., & Pfister, D. G. (2016). A phase II study of axitinib (AG-013736) in patients with incurable adenoid cystic carcinoma. *Annals of Oncology*, *27*(10), 1902–1908. https://doi.org/10.1093/annonc/mdw287

Ho, A. S., Kannan, K., Roy, D. M., Morris, L. G. T., Ganly, I., Katabi, N., Ramaswami, D., Walsh, L. A., Eng, S., Huse, J. T., Zhang, J., Dolgalev, I., Huberman, K., Heguy, A.,

Viale, A., Drobnjak, M., Leversha, M. A., Rice, C. E., Singh, B., … Chan, T. A. (2013). The Mutational Landscape of Adenoid Cystic Carcinoma. *Nature Genetics*, *45*(7), 791–798. https://doi.org/10.1038/ng.2643

Ho, A. S., Ochoa, A., Jayakumaran, G., Zehir, A., Valero Mayor, C., Tepe, J., Makarov, V., Dalin, M. G., He, J., Bailey, M., Montesion, M., Ross, J. S., Miller, V. A., Chan, L., Ganly, I., Dogan, S., Katabi, N., Tsipouras, P., Ha, P., … Morris, L. G. T. (2019). Genetic hallmarks of recurrent/metastatic adenoid cystic carcinoma. *Journal of Clinical Investigation*, *129*(10), 4276–4289. https://doi.org/10.1172/JCI128227

Hoffman, R. M. (2015). Patient-derived orthotopic xenografts: Better mimic of metastasis than subcutaneous xenografts. *Nature Reviews Cancer*, *15*(8), 451–452. https://doi.org/10.1038/nrc3972

Hoffmann, K., Berger, H., Kulbe, H., Thillainadarasan, S., Mollenkopf, H., Zemojtel, T., Taube, E., Darb-esfahani, S., Mangler, M., Sehouli, J., Chekerov, R., Braicu, E. I., Meyer, T. F., & Kessler, M. (2020). Stable expansion of high-grade serous ovarian cancer organoids requires a low-Wnt environment. *The EMBO Journal*, *e104013*, 1–23. https://doi.org/10.15252/embj.2019104013

Hou, H., Jia, D., Yan, W., Zhang, X., Wang, C., Li, Y., Chen, H., Huang, W., Li, Z., & Zhang, X. (2020). KIT/PDGFRA/KDR amplification defines a novel molecular subtype of adenoid cystic carcinoma patients who may benefit from treatment with tyrosine kinase inhibitors. *Translational Cancer Research*, *9*(8), 4703–4714. https://doi.org/10.21037/tcr-20-637

Huang, E. J., & Reichardt, L. F. (2001). Neurotrophins: Roles in neuronal development and function. *Annual Review of Neuroscience*, *24*, 677–736. https://doi.org/10.1146/annurev.neuro.24.1.677

Huang, M., Ma, D., Sun, K., Yu, G., Guo, C., & Gao, F. (1997). Factors influencing survival rate in adenoid cystic carcinoma of the salivary glands. *International Journal of Oral and Maxillofacial Surgery*, *26*(6), 435–439. https://doi.org/10.1016/S0901-5027(97)80008-2

Hubert, C. G., Rivera, M., Spangler, L. C., Wu, Q., Mack, S. C., Prager, B. C., Couce, M., McLendon, R. E., Sloan, A. E., & Rich, J. N. (2016). A three-dimensional organoid culture system derived from human glioblastomas recapitulates the hypoxic gradients and cancer stem cell heterogeneity of tumors found in vivo. *Cancer*

Research, *76*(8), 2465–2477. https://doi.org/10.1158/0008-5472.CAN-15-2402.A

Huch, M., Gehart, H., Van Boxtel, R., Hamer, K., Blokzijl, F., Verstegen, M. M. A., Ellis, E., Van Wenum, M., Fuchs, S. A., De Ligt, J., Van De Wetering, M., Sasaki, N., Boers, S. J., Kemperman, H., De Jonge, J., Ijzermans, J. N. M., Nieuwenhuis, E. E. S., Hoekstra, R., Strom, S., … Clevers, H. (2015). Long-term culture of genome-stable bipotent stem cells from adult human liver. *Cell*, *160*(1–2), 299–312. https://doi.org/10.1016/j.cell.2014.11.050

Hugo, H., Cures, A., Suraweera, N., Drabsch, Y., Purcell, D., Mantamadiotis, T., Phillips, W., Dobrovic, A., Zupi, G., Gonda, T. J., Iacopetta, B., & Ramsay, R. G. (2006). Mutations in the MYB intron I regulatory sequence increase transcription in colon cancers. *Genes, Chromosomes & Cancer*, *45*(12), 1143–1154. https://doi.org/10.1002/gcc.20378

Iseli, T. A., Karnell, L. H., Graham, S. M., Funk, G. F., Buatti, J. M., Gupta, A. K., Robinson, R. A., & Hoffman, H. T. (2009). Role of radiotherapy in adenoid cystic carcinoma of the head and neck. *Journal of Laryngology and Otology*, *123*(10), 1137–1144. https://doi.org/10.1017/S0022215109990338

Ivanov, S. V., Panaccione, A., Brown, B., Guo, Y., Moskaluk, C. A., Wick, M. J., Brown, J. L., Ivanova, A. V., Issaeva, N., El-Naggar, A. K., & Yarbrough, W. G. (2013). TrkC signaling is activated in adenoid cystic carcinoma and requires NT-3 to stimulate invasive behavior. *Oncogene*, *32*(32), 3698–3710. https://doi.org/10.1038/onc.2012.377

Ivanov, S. V., Panaccione, A., Nonaka, D., Prasad, M. L., Boyd, K. L., Brown, B., Guo, Y., Sewell, A., & Yarbrough, W. G. (2013). Diagnostic SOX10 gene signatures in salivary adenoid cystic and breast basal-like carcinomas. *British Journal of Cancer*, *109*(2), 444–451. https://doi.org/10.1038/bjc.2013.326

Jakob, J. A., Kies, M. S., Glisson, B. S., Kupferman, M. E., Liu, D. D., Lee, J. J., El-Naggar, A. K., Gonzalez-Angulo, A. M., & Blumenschein, G. R. (2015). A Phase II study of Gefitinib in Patients with Advanced Salivary Gland Cancers. *Head & Neck*, *37*(5), 644–649. https://doi.org/10.1016/j.physbeh.2017.03.040

Jeng, Y. M., Lin, C. Y., & Hsu, H. C. (2000). Expression of the c-kit protein is associated with certain subtypes of salivary gland carcinoma. *Cancer Letters*, *154*(1), 107–111. https://doi.org/10.1016/S0304-3835(00)00387-6

Jeronimo, C., Collin, P., & Robert, F. (2016). The RNA Polymerase II CTD: The Increasing Complexity of a Low-Complexity Protein Domain. *Journal of Molecular Biology*, *428*(12), 2607–2622. https://doi.org/10.1016/j.jmb.2016.02.006

Karthaus, W. R., Iaquinta, P. J., Drost, J., Gracanin, A., Boxtel, R. Van, Wongvipat, J., Dowling, C. M., Gao, D., Begthel, H., Sachs, N., Vries, R. G. J., Cuppen, E., Chen, Y., Sawyers, C. L., & Clevers, H. C. (2014). Identification of multipotent luminal progenitor cells in human prostate organoid cultures. *Cell*, *159*(1), 163–175. https://doi.org/10.1016/j.cell.2014.08.017.Identification

Katsiampoura, A., Raghav, K., Jiang, Z. Q., Menter, D. G., Varkaris, A., Morelli, M. P., Manuel, S., Wu, J., Sorokin, A. V., Rizi, B. S., Bristow, C., Tian, F., Airhart, S., Cheng, M., Broom, B. M., Morris, J., Overman, M. J., Powis, G., & Kopetz, S. (2017). Modeling of patient-derived xenografts in colorectal cancer. *Molecular Cancer Therapeutics*, *16*(7), 1435–1442. https://doi.org/10.1158/1535-7163.MCT-16-0721

Kaufman, C. K., Mosimann, C., Fan, Z. P., Yang, S., Thomas, A., Ablain, J., Tan, J. L., Fogley, R. D., van Rooijen, E., Hagedorn, E., Ciarlo, C., White, R., Matos, D., Puller, A. C., Santoriello, C., Liao, E., Young, R. A., & Zon, L. I. (2016). A zebrafish melanoma model reveals emergence of neural crest identity during melanoma initiation Charles. *Science*, *351*(6272), aad2197. https://doi.org/10.1126/science.aad2197.A

Keam, B., Kang, E. J., Ahn, M.-J., Ock, C.-Y., Lee, K. W., Kwon, J. H., Yang, Y., Choi, Y. H., Kim, M. K., Ji, J. H., Yun, T., Nam, B.-H., & Kim, S.-B. (2020). Randomized phase II study of axitinib versus observation in patients with recurred or metastatic adenoid cystic carcinoma. *Journal of Clinical Oncology*, *38*(15_suppl), 6503. https://doi.org/10.1200/JCO.2020.38.15_suppl.6503

Kessler, M., Hoffmann, K., Brinkmann, V., Thieck, O., Jackisch, S., Toelle, B., Berger, H., Mollenkopf, H. J., Mangler, M., Sehouli, J., Fotopoulou, C., & Meyer, T. F. (2015). The Notch and Wnt pathways regulate stemness and differentiation in human fallopian tube organoids. *Nature Communications*, *6*(May), 8989. https://doi.org/10.1038/ncomms9989

Khafif, A., Anavi, Y., Haviv, J., Fienmesser, R., Calderon, S., & Marshak, G. (2005). Adenoid cystic carcinoma of the salivary glands: A 20-year review with long-term

follow-up. *Ear, Nose and Throat Journal*, *84*(10), 662–667. https://doi.org/10.1177/014556130508401016

Kim, J., Geyer, F. C., Martelotto, L. G., Ng, C. K. Y., Lim, R. S., Selenica, P., Li, A., Pareja, F., Fusco, N., Edelweiss, M., Kumar, R., Gularte-Merida, R., Forbes, A. N., Khurana, E., Mariani, O., Badve, S., Vincent-Salomon, A., Norton, L., Reis-Filho, J. S., & Weigelt, B. (2018). MYBL1 rearrangements and MYB amplification in breast adenoid cystic carcinomas lacking the MYB–NFIB fusion gene. *Journal of Pathology*, *244*(2), 143–150. https://doi.org/10.1002/path.5006

Knosp, W. M., Knox, S. M., & Hoffman, M. P. (2012). Salivary gland organogenesis. *Wiley Interdisciplinary Reviews: Developmental Biology*, *1*(1), 69–82. https://doi.org/10.1002/wdev.4

Knox, S. M., Lombaert, I. M. A., Reed, X., Vitale-Cross, L., Gutkind, J. S., & Hoffman, M. P. (2010). Parasympathetic innervation maintains epithelial progenitor cells during salivary organogenesis. *Science*, *329*(5999), 1645–1647. https://doi.org/10.1126/science.1192046.Parasympathetic

Ko, Y. H., Lee, M. A., Hong, Y. S., Lee, K. S., Jung, C. K., Kim, Y. S., Sun, D. Il, Kim, B. S., Kim, M. S., & Kang, J. H. (2007). Prognostic ractors affecting the clinical outcome of adenoid cystic carcinoma of the head and neck. *Japanese Journal of Clinical Oncology*, *37*(11), 805–811. https://doi.org/10.1093/jjco/hym119

Kooreman, N. G., de Almeida, P. E., Stack, J. P., Nelakanti, R. V., Diecke, S., Shao, N. Y., Swijnenburg, R. J., Sanchez-Freire, V., Matsa, E., Liu, C., Connolly, A. J., Hamming, J. F., Quax, P. H. A., Brehm, M. A., Greiner, D. L., Shultz, L. D., & Wu, J. C. (2017). Alloimmune Responses of Humanized Mice to Human Pluripotent Stem Cell Therapeutics. *Cell Reports*, *20*(8), 1978–1990. https://doi.org/10.1016/j.celrep.2017.08.003

Kopper, O., de Witte, C. J., Lõhmussaar, K., Valle-Inclan, J. E., Hami, N., Kester, L., Balgobind, A. V., Korving, J., Proost, N., Begthel, H., van Wijk, L. M., Revilla, S. A., Theeuwsen, R., van de Ven, M., van Roosmalen, M. J., Ponsioen, B., Ho, V. W. H., Neel, B. G., Bosse, T., … Clevers, H. (2019). An organoid platform for ovarian cancer captures intra- and interpatient heterogeneity. *Nature Medicine*, *25*(5), 838–849. https://doi.org/10.1038/s41591-019-0422-6

Kuleshov, M. V., Jones, M. R., Rouillard, A. D., Fernandez, N. F., Duan, Q., Wang, Z.,

Koplev, S., Jenkins, S. L., Jagodnik, K. M., Lachmann, A., McDermott, M. G., Monteiro, C. D., Gundersen, G. W., & Ma'ayan, A. (2016). Enrichr: a comprehensive gene set enrichment analysis web server 2016 update. *Nucleic Acids Research*, *44*(W1), W90–W97. https://doi.org/10.1093/nar/gkw377

Lafontaine, J., Cardin, G. B., Malaquin, N., Boisvert, J. S., Rodier, F., & Wong, P. (2021). Senolytic targeting of bcl-2 anti-apoptotic family increases cell death in irradiated sarcoma cells. *Cancers*, *13*(3), 1–20. https://doi.org/10.3390/cancers13030386

Lam, L. T., Pickeral, O. K., Peng, A. C., Rosenwald, A., Hurt, E. M., Giltnane, J. M., Averett, L. M., Zhao, H., Davis, R. E., Sathyamoorthy, M., Wahl, L. M., Harris, E. D., Mikovits, J. A., Monks, A. P., Hollingshead, M. G., Sausville, E. A., & Staudt, L. M. (2001). Genomic-scale measurement of mRNA turnover and the mechanisms of action of the anti-cancer drug flavopiridol. *Genome Biology*, *2*(10), 1–11. https://doi.org/10.1186/gb-2001-2-10-research0041

Laurie, S. A., Ho, A. L., Fury, M. G., Sherman, E., & Pfister, D. G. (2011). Systemic therapy in the management of metastatic or locally recurrent adenoid cystic carcinoma of the salivary glands: a systematic review. *The Lancet Oncology*, *12*(8), 815–824. https://doi.org/10.1016/S1470-2045(10)70245-X

Lee, S. H., Hu, W., Matulay, J. T., Al-Ahmadie, H., Solit, D. B., & Shen, M. M. (2018). Tumor Evolution and Drug Response in Patient-Derived Organoid Models of Bladder Cancer Correspondence In Brief A biobank of patient-derived bladder tumor organoids faithfully recapitulates features of human cancer and enables analysis of clonal evolution and drug responses. *Cell*, *173*, 515–528. https://doi.org/10.1016/j.cell.2018.03.017

Lee, S. K., Kwon, M. S., Lee, Y. S., Choi, S. H., Kim, S. Y., Cho, K. J., & Nam, S. Y. (2012). Prognostic value of expression of molecular markers in adenoid cystic cancer of the salivary glands compared with lymph node metastasis: A retrospective study. *World Journal of Surgical Oncology*, *10*(1), 1. https://doi.org/10.1186/1477-7819-10-266

Li, H., Yang, Z., Wang, W., Wang, J., Zhang, J., Liu, J., Yang, T., & Yang, Y. (2019). NT-3 / TrkC Axis Contributes to the Perineural Invasion and the Poor Prognosis in Human Salivary Adenoid Cystic Carcinoma. *Journal of Cancer*, *10*(24), 6065–6073. https://doi.org/10.7150/jca.33635

Li, N., Xu, L., Zhao, H., El-Naggar, A. K., & Sturgis, E. M. (2012). A Comparison of the Demographics, Clinical Features, and Survival of Patients with Adenoid Cystic Carcinoma of Major and Minor Salivary Glands Versus Less Common Sites within the SEER Registry. *Cancer*, *118*(16), 3945–3953. https://doi.org/10.1038/jid.2014.371

Licitra, L., Marchini, S., Spinazzè, S., Rossi, A., Rocca, A., Grandi, C., & Molinari, R. (1991). Cisplatin in advanced salivary gland carcinoma. A phase II study of 25 patients. *Cancer*, *68*(9), 1874–1877. https://doi.org/10.1002/1097-0142(19911101)68:9<1874::AID-CNCR2820680904>3.0.CO;2-S

Lim, Y. S., Cha, W., Park, M. W., Jeong, W. J., & Ahn, S. H. (2017). HIF1α in tumorigenesis of adenoid cystic carcinoma. *Anticancer Research*, *37*(2), 599–606. https://doi.org/10.21873/anticanres.11353

Lin, C. Y., Erkek, S., Tong, Y., Yin, L., Federation, A. J., Zapatka, M., Haldipur, P., Kawauchi, D., Risch, T., Warnatz, H. J., Worst, B. C., Ju, B., Orr, B. A., Zeid, R., Polaski, D. R., Segura-Wang, M., Waszak, S. M., Jones, D. T. W., Kool, M., … Northcott, P. A. (2016). Active medulloblastoma enhancers reveal subgroup-specific cellular origins. *Nature*, *530*(7588), 57–62. https://doi.org/10.1038/nature16546

Linxweiler, M., Kuo, F., Katabi, N., Lee, M., Nadeem, Z., Dalin, M. G., Makarov, V., Chowell, D., Dogan, S., Ganly, I., Ari Hakimi, A., Wong, R. J., Riaz, N., Ho, A. L., Chan, T. A., & Morris, L. G. T. (2020). The immune microenvironment and neoantigen landscape of aggressive salivary gland carcinomas differ by subtype. *Clinical Cancer Research*, *26*(12), 2859–2870. https://doi.org/10.1158/1078-0432.CCR-19-3758

Liu, X., Krawczyk, E., Suprynowicz, F. A., Palechor-Ceron, N., Yuan, H., Dakic, A., Simic, V., Zheng, Y. L., Sripadhan, P., Chen, C., Lu, J., Hou, T. W., Choudhury, S., Kallakury, B., Tang, D., Darling, T., Thangapazham, R., Timofeeva, O., Dritschilo, A., … Schlegel, R. (2017). Conditional reprogramming and long-term expansion of normal and tumor cells from human biospecimens. *Nature Protocols*, *12*(2), 493–451. https://doi.org/10.1038/nprot.2016.174

Liu, Y., Ford, B. D., Mann, M. A., & Fischbach, G. D. (2005). Neuregulin-1 increases the proliferation of neuronal progenitors from embryonic neural stem cells.

Developmental Biology, *283*(2), 437–445. https://doi.org/10.1016/j.ydbio.2005.04.038

Lloyd, S., Yu, J. B., Wilson, L. D., & Decker, R. H. (2011). Determinants and patterns of survival in adenoid cystic carcinoma of the head and neck, including an analysis of adjuvant radiation therapy. *American Journal of Clinical Oncology: Cancer Clinical Trials*, *34*(1), 76–81. https://doi.org/10.1097/COC.0b013e3181d26d45

Locati, L. D., Galbiati, D., Calareso, G., Alfieri, S., Singer, S., Cavalieri, S., Bergamini, C., Bossi, P., Orlandi, E., Resteghini, C., Platini, F., Granata, R., Quattrone, P., Mancinelli, M., Mariani, L., Lo Vullo, S., & Licitra, L. F. (2020). Patients with adenoid cystic carcinomas of the salivary glands treated with lenvatinib: Activity and quality of life. *Cancer*, *126*(9), 1888–1894. https://doi.org/10.1002/cncr.32754

Loewe, S. (1928). Die quantitativen Probleme der Pharmakologie. *Ergebnisse Der Physiologie*, *27*(1), 47–187. https://doi.org/10.1007/BF02322290

Long, G. V, Stroyakovskiy, D., Gogas, H., Levchenko, E., de Braud, F., Larkin, J., Garbe, C., Jouary, T., Hauschild, A., Grob, J. J., Chiarion Sileni, V., Lebbe, C., Mandalà, M., Millward, M., Arance, A., Bondarenko, I., Haanen, J. B. A. G., Hansson, J., Utikal, J., … Flaherty, K. (2014). Combined BRAF and MEK Inhibition versus BRAF Inhibition Alone in Melanoma. *New England Journal of Medicine*, *371*(20), 1877–1888. https://doi.org/10.1056/NEJMoa1406037

Lovén, J., Hoke, H. A., Lin, C. Y., Lau, A., Orlando, D. A., Vakoc, C. R., Bradner, J. E., Lee, T. I., & Young, R. A. (2013). Selective inhibition of tumor oncogenes by disruption of super-enhancers. *Cell*, *153*(2), 320–334. https://doi.org/10.1016/j.cell.2013.03.036

Lu, B. J., Zhu, J., Gao, L., Xie, L., Xu, J. Y., & Lai, M. D. (2005). Diagnostic accuracy and pitfalls in fine needle aspiration cytology of salivary glands: a study of 113 cases. *Chinese Journal of Pathology*, *34*(11), 706–710.

Lu, H., Xue, Y., Yu, G. K., Arias, C., Lin, J., Fong, S., Faure, M., Weisburd, B., Ji, X., Mercier, A., Sutton, J., Luo, K., Gao, Z., & Zhou, Q. (2015). Compensatory induction of MYC expression by sustained CDK9 inhibition via a BRD4-dependent mechanism. *ELife*, *4*(JUNE2015), 1–26. https://doi.org/10.7554/eLife.06535

Ma, C., Gao, T., Ju, J., Zhang, Y., Li, Y., Zhao, Z., Chai, J., & Yang, X. (2019). Sympathetic

innervation contributes to perineural invasion of salivary adenoid cystic carcinoma via the β 2-adrenergic receptor. *OncoTargets and Therapy*, *12*, 1475–1495.

MacKay, C., Frame, S., Saladino, C., Pohler, E., Zheleva, D., & Blake, D. G. (2015). Abstract B182: Molecular basis for clinical development of the novel CDK2/9 inhibitor CYC065 in oncology. *AACR-NCI-EORTC International Conference*, *November*, B182–B182. https://doi.org/10.1158/1535-7163.targ-15-b182

Maimets, M., Rocchi, C., Bron, R., Pringle, S., Kuipers, J., Giepmans, B. N. G., Vries, R. G. J., Clevers, H., De Haan, G., Van Os, R., & Coppes, R. P. (2016). Long-Term in Vitro Expansion of Salivary Gland Stem Cells Driven by Wnt Signals. *Stem Cell Reports*, *6*(1), 150–162. https://doi.org/10.1016/j.stemcr.2015.11.009

Malumbres, M. (2014). Cyclin-dependent kinases. *Genome Biology*, *15*, 122–132.

Mandelbaum, J., Shestopalov, I. A., Henderson, R. E., Chau, N. G., Knoechel, B., Wick, M. J., & Zon, L. I. (2018). Zebrafish blastomere screen identifies retinoic acid suppression of MYB in adenoid cystic carcinoma. *The Journal of Experimental Medicine*, *215*(10), 2673–2685. https://doi.org/10.1084/jem.20180939

Marieb, E. N., & Hoehn, K. (2010). *Human Anatomy & Physiology* (8th ed.). Pearson Education.

Massard, C., Azaro, A., Soria, J. C., Lassen, U., Le Tourneau, C., Sarker, D., Smith, C., Ohnmacht, U., Oakley, G., Patel, B. K. R., Yuen, E. S. M., Benhadji, K. A., & Rodon, J. (2018). First-in-human study of LY3039478, an oral Notch signaling inhibitor in advanced or metastatic cancer. *Annals of Oncology*, *29*(9), 1911–1917. https://doi.org/10.1093/annonc/mdy244

Matano, M., Date, S., Shimokawa, M., Takano, A., Fujii, M., Ohta, Y., Watanabe, T., Kanai, T., & Sato, T. (2015). Modeling colorectal cancer using CRISPR-Cas9-mediated engineering of human intestinal organoids. *Nature Medicine*, *21*(3), 256–262. https://doi.org/10.1038/nm.3802

Matheu, A., Collado, M., Wise, C., Manterola, L., Cekaite, L., Tye, A. J., Canamero, M., Bujanda, L., Schedl, A., Cheah, K. S. E., Skotheim, R. I., Lothe, R. A., De Munain, A. L., Briscoe, J., Serrano, M., & Lovell-Badge, R. (2012). Oncogenicity of the developmental transcription factor Sox9. *Cancer Research*, *72*(5), 1301–1315. https://doi.org/10.1158/0008-5472.CAN-11-3660

Matsuba, H. M., Spector, G. J., Thawley, S. E., Simpson, J. R., Mauney, M., & Pikul, F. J. (1986). Adenoid cystic salivary gland carcinoma: A histopathologic review of treatment failure pattrens. *Cancer*, *57*(3), 519–524. https://doi.org/10.1002/hed.2890080312

Mattar, M., Abdel-Wahab, O., Poirier, J. T., Scaltriti, M., & de Stanchina, E. (2017). Chapter 3 - Methodologies for Developing and Maintaining Patient-Derived Xenograft Mouse Models. In R. Uthamanthil & P. B. T.-P. D. T. X. M. Tinkey (Eds.), *Patient Derived Tumor Xenograft Models: Promise, Potential and Practice* (pp. 119–134). Academic Press. https://doi.org/https://doi.org/10.1016/B978-0-12-804010-2.00009-6

McCalmont, H., Li, K. L., Jones, L., Toubia, J., Bray, S. C., Casolari, D. A., Mayoh, C., Samaraweera, S. E., Lewis, I. D., Prinjha, R. K., Smithers, N., Wang, S., Lock, R. B., & D'Andrea, R. J. (2020). Efficacy of combined CDK9/BET inhibition in preclinical models of MLL-rearranged acute leukemia. *Blood Advances*, *4*(2), 296–300. https://doi.org/10.1182/bloodadvances.2019000586

Mckeown, S. R. (2014). Defining normoxia , physoxia and hypoxia in tumours — implications for treatment response. *British Journal of Radiology*, *October 2013*, 1–12. https://doi.org/10.1259/bjr.20130676

Meng, Q. (2010). Three-dimensional culture of hepatocytes for prediction of drug-induced hepatotoxicity. *Expert Opinion on Drug Metabolism & Toxicology*, *6*(6), 733–746. https://doi.org/10.1517/17425251003674356

Mestas, J., & Hughes, C. C. W. (2004). Of Mice and Not Men: Differences between Mouse and Human Immunology. *The Journal of Immunology*, *172*(5), 2731–2738. https://doi.org/10.4049/jimmunol.172.5.2731

Miller, A. L., Fehling, S. C., Garcia, P. L., Gamblin, T. L., Council, L. N., van Waardenburg, R. C. A. M., Yang, E. S., Bradner, J. E., & Yoon, K. J. (2019). The BET inhibitor JQ1 attenuates double-strand break repair and sensitizes models of pancreatic ductal adenocarcinoma to PARP inhibitors. *EBioMedicine*, *44*, 419–430. https://doi.org/10.1016/j.ebiom.2019.05.035

Mitani, Y., Li, J., Rao, P. H., Zhao, Y. J., Bell, D., Lippman, S. M., Weber, R. S., Caulin, C., & El-Naggar, A. K. (2010). Comprehensive analysis of the MYB-NFIB gene fusion in salivary adenoid cystic carcinoma: Incidence, variability, and clinicopathologic

significance. *Clinical Cancer Research*, *16*(19), 4722–4731. https://doi.org/10.1158/1078-0432.CCR-10-0463

Mitani, Y., Liu, B., Rao, P. H., Borra, V. J., Zafereo, M., Weber, R. S., Kies, M., Lozano, G., Andrew Futreal, P., Caulin, C., & El-Naggar, A. K. (2016). Novel MYBL1 Gene Rearrangements with Recurrent MYBL1-NFIB Fusions in Salivary Adenoid Cystic Carcinomas Lacking t(6;9) Translocations. *Clinical Cancer Research*, *22*(3), 725–733. https://doi.org/10.1158/1078-0432.CCR-15-2867-T

Mitsunaga, S., Hasebe, T., Kinoshita, T., Konishi, M., Takahashi, S., Gotohda, N., Nakagohri, T., & Ochiai, A. (2007). Detail histologic analysis of nerve plexus invasion in invasive ductal carcinoma of the pancreas and its prognostic impact. *American Journal of Surgical Pathology*, *31*(11), 1636–1644. https://doi.org/10.1097/PAS.0b013e318065bfe6

Moreno, N., Holsten, T., Mertins, J., Zhogbi, A., Johann, P., Kool, M., Meisterernst, M., & Kerl, K. (2017). Combined BRD4 and CDK9 inhibition as a new therapeutic approach in malignant rhabdoid tumors. *Oncotarget*, *8*(49), 84986–84995. www.impactjournals.com/oncotarget

Moskaluk, C. A., Baras, A. S., Mancuso, S. A., Fan, H., Davidson, R. J., Dirks, D. C., Golden, W. L., & Frierson, H. F. (2011). Development and characterization of xenograft model systems for adenoid cystic carcinoma. *Laboratory Investigation*, *91*(10), 1480–1490. https://doi.org/10.1038/labinvest.2011.105

Na'ara, S., Gil, Z., & Amit, M. (2016). In Vitro modeling of cancerous neural invasion: The dorsal root ganglion model. *Journal of Visualized Experiments*, *2016*(110), 1–6. https://doi.org/10.3791/52990

Na, Y. S., Ryu, M. H., Park, Y. S., Lee, C. W., Lee, J. K., Park, Y., Park, J. M., Ma, J., & Kang, Y. K. (2020). Establishment of patient-derived xenografts from patients with gastrointestinal stromal tumors: analysis of clinicopathological characteristics related to engraftment success. *Scientific Reports*, *10*(1), 1–8. https://doi.org/10.1038/s41598-020-64552-w

Nagel, H., Hotze, H. J., Laskawi, R., Chilla, R., & Droese, M. (1999). Cytologic diagnosis of adenoid cystic carcinoma of salivary glands. *Diagnostic Cytopathology*, *20*(6), 358–366.

Nalawansha, D. A., & Crews, C. M. (2020). PROTACs: An Emerging Therapeutic

Modality in Precision Medicine. *Cell Chemical Biology*, *27*(8), 998–1014. https://doi.org/10.1016/j.chembiol.2020.07.020

Nan, L., Qin, T., Xiao, Y., Qian, W., Li, J., Wang, Z., Ma, J., Ma, Q., & Wu, Z. (2019). Pancreatic Stellate Cells Facilitate Perineural Invasion of Pancreatic Cancer via HGF / c-Met Pathway. *Cell Transplantation*, *28*(9), 1289–1298. https://doi.org/10.1177/0963689719851772

Nanduri, L. S. Y., Baanstra, M., Faber, H., Rocchi, C., & Zwart, E. (2014). Purification and Ex Vivo Expansion of Fully Functional Salivary Gland Stem Cells. *Stem Cell Reports*, *3*(6), 957–964.

Nemunaitis, J. J., Small, K. A., Kirschmeier, P., Zhang, D., Zhu, Y., Jou, Y. M., Statkevich, P., Yao, S. L., & Bannerji, R. (2013). A first-in-human, phase 1, dose-escalation study of dinaciclib, a novel cyclin-dependent kinase inhibitor, administered weekly in subjects with advanced malignancies. *Journal of Translational Medicine*, *11*(1), 1. https://doi.org/10.1186/1479-5876-11-259

Nör, F., Warner, K. A., Zhang, Z., Acasigua, G. A., Alexander, T., Kerk, S. A., Helman, J., Sant'Ana Filho, M., Wang, S., & Nör, J. E. (2017). Therapeutic Inhibition of the MDM2 – p53 Interaction Prevents Recurrence of Adenoid Cystic Carcinomas. *Clinical Cancer Research*, *23*(4), 1036–1048. https://doi.org/10.1158/1078-0432.CCR-16-1235

O'Rourke, J. P., & Ness, S. A. (2008). Alternative RNA Splicing Produces Multiple Forms of c-Myb with Unique Transcriptional Activities. *Molecular and Cellular Biology*, *28*(6), 2091–2101. https://doi.org/10.1128/mcb.01870-07

Ohba, S., He, X., Hojo, H., & McMahon, A. . (2015). Distinct transcriptional programs underlie Sox9 regulation of the mammalian chondrocyte. *Cell Reports*, *12*(2), 229–243. https://doi.org/10.1016/j.celrep.2015.06.013.Distinct

Öhlund, D., Handly-Santana, A., Biffi, G., Elyada, E., Almeida, A. S., Ponz-Sarvise, M., Corbo, V., Oni, T. E., Hearn, S. A., Lee, E. J., Chio, I. I. C., Hwang, C. Il, Tiriac, H., Baker, L. A., Engle, D. D., Feig, C., Kultti, A., Egeblad, M., Fearon, D. T., … Tuveson, D. A. (2017). Distinct populations of inflammatory fibroblasts and myofibroblasts in pancreatic cancer. *The Journal of Experimental Medicine*, *214*(3), 579–596. https://doi.org/10.1084/jem.20162024

Padua, D., & Massagué, J. (2009). Roles of TGFβ in metastasis. *Cell Research*, *19*(1), 89–

102. https://doi.org/10.1038/cr.2008.316

Palmer, A. C., & Sorger, P. K. (2017). Combination cancer therapy can confer benefit via patient-to-patient variability without drug additivity or synergy. *Cell*, *171*(7), 1678–1691. https://doi.org/10.1016/j.cell.2017.11.009.Combination

Panaccoine, A., Chang, M. T., Carbone, B. E., Guo, Y., Moskaluk, C. A., Virk, R. K., Chiriboga, L., Prasad, M. L., Judson, B., Mehra, S., Yarbrough, W. G., & Ivanov, S. V. (2016). NOTCH1 and SOX10 are Essential for Proliferation and Radiation Resistance of Cancer Stem-like Cells in Adenoid Cystic Carcinoma. *Clinical Cancer Research*, *22*(8), 2083–2095. https://doi.org/10.1016/j.physbeh.2017.03.040

Papageorgis, P. (2015). TGF*β* Signaling in Tumor Initiation, Epithelial-to-Mesenchymal Transition, and Metastasis. *Journal of Oncology*, *2015*, 587193. https://doi.org/10.1155/2015/587193

Patel, N., Sharpe, P. T., & Miletich, I. (2011). Coordination of epithelial branching and salivary gland lumen formation by Wnt and FGF signals. *Developmental Biology*, *358*(1), 156–167. https://doi.org/https://doi.org/10.1016/j.ydbio.2011.07.023

Patel, V. N., & Hoffman, M. P. (2014). Salivary Gland Development: A template for regeneration. *Seminars in Cell and Developmental Biology*, *0*, 52–60. https://doi.org/10.1016/j.semcdb.2013.12.001.Salivary

Patel, V. N., Rebustini, I. T., & Hoffman, M. P. (2006). Salivary gland branching morphogenesis. *Differentiation*, *74*(7), 349–364. https://doi.org/10.1111/j.1432-0436.2006.00088.x

Pauli, C., Hopkins, B. D., Prandi, D., Shaw, R., Fedrizzi, T., Sboner, A., Sailer, V., Augello, M., Puca, L., Rosati, R., McNary, T., Churakova, Y., Cheung, C., Triscott, J., Pisapia, D., Rao, R., Mosquera, J. M., Robinson, B., Faltas, B. M., … Rubin, M. A. (2017). Personalized In Vitro and In Vivo Cancer Models to Guide Precision Medicine. *Cancer Discovery*, *7*(5), 462–477. https://doi.org/10.1097/CCM.0b013e31823da96d.Hydrogen

Pearson, A., Smyth, E., Babina, I. S., Herrera-Abreu, M. T., Tarazona, N., Peckitt, C., Kilgour, E., Smith, N. R., Geh, C., Rooney, C., Cutts, R., Campbell, J., Ning, J., Fenwick, K., Swain, A., Brown, G., Chua, S., Thomas, A., Johnston, S. R. D., … Turner, N. C. (2016). High-level clonal FGFR amplification and response to FGFR inhibition in a translational clinical trial. *Cancer Discovery*, *6*(8), 838–851.

https://doi.org/10.1158/2159-8290.CD-15-1246

Pearson, A. T., Finkel, K. A., Warner, K. A., Nör, F., Tice, D., Martins, M. D., Jackson, T. L., & Nör, J. E. (2016). Patient-derived xenograft (PDX) tumors increase growth rate with time. *Oncotarget*, *7*(7), 7993–8005. https://doi.org/10.18632/oncotarget.6919

Pederson, A. W., Salama, J. K., Haraf, D. J., Witt, M. E., Stenson, K. M., Portugal, L., Seiwert, T., Villaflor, V. M., Cohen, E. E. W., Vokes, E. E., & Blair, E. A. (2011). Adjuvant chemoradiotherapy for locoregionally advanced and high-risk salivary gland malignancies. *Head and Neck Oncology*, *3*(1), 1–6. https://doi.org/10.1186/1758-3284-3-31

Peluffo, G., Subedee, A., Harper, N. W., Kingston, N., Jovanovic, B., Flores, F., Stevens, L. E., Beca, F., Trinh, A., Chilamakuri, C. S. R., Papachristou, E. K., Murphy, K., Su, Y., Marusyk, A., D'Santos, C. S., Rueda, O. M., Beck, A. H., Caldas, C., Carroll, J. S., & Polyak, K. (2019). EN1 is a transcriptional dependency in triple-negative breast cancer associated with brain metastasis. *Cancer Research*, *79*(16), 4173–4183. https://doi.org/10.1158/0008-5472.CAN-18-3264

Persson, M., Andren, Y., Mark, J., Horlings, H. M., Persson, F., & Stenman, G. (2009). Recurrent fusion of MYB and NFIB transcription factor genes in carcinomas of the breast and head and neck. *Proceedings of the National Academy of Sciences*, *106*(44), 18740–18744. https://doi.org/10.1073/pnas.0909114106

Perzin, K. H., Gullane, P., & Clairmont, A. C. (1978). Adenoid cystic carcinomas arising in salivary glands. A correlation of histologic features and clinical course. *Cancer*, *42*(265–282).

Pfeffer, R., Talmi, Y., Catane, R., Symon, Z., Yosepovitch, A., & Levitt, M. (2005). Imatinib for advanced adenoid cystic carcinoma of head and neck. A phase II study. *Cancer Research*, *65*(9 Supplement), 1356 LP – 1356. http://cancerres.aacrjournals.org/content/65/9_Supplement/1356.1.abstract

Pham, T., Pereira, L., Roth, S., Galletta, L., Link, E., Akhurst, T., Solomon, B., Michael, M., Darcy, P., Sampurno, S., Heriot, A., Ramsay, R., & Desai, J. (2019). First-in-human phase I clinical trial of a combined immune modulatory approach using TetMYB vaccine and Anti-PD-1 antibody in patients with advanced solid cancer including colorectal or adenoid cystic carcinoma: The MYPHISMO study protocol

(NCT03287427). *Contemporary Clinical Trials Communications*, *16*(June), 100409. https://doi.org/10.1016/j.conctc.2019.100409

Phillips, B., & Gazet, J. C. (1970). Transplantation of primary explants of human tumour to mice treated with antilymphocyte serum. *British Journal of Cancer*, *24*(1), 92–95.

Phuchareon, J., Ohta, Y., Woo, J. M., Eisele, D. W., & Tetsu, O. (2009). Genetic profiling reveals cross-contamination and misidentification of 6 adenoid cystic carcinoma cell lines: ACC2, ACC3, ACCM, ACCNS, ACCS and CAC2. *PLoS ONE*, *4*(6), 6–13. https://doi.org/10.1371/journal.pone.0006040

Poon, E., Lin, C. Y., Chesler, L., Poon, E., Liang, T., Jamin, Y., Walz, S., Kwok, C., Hakkert, A., Barker, K., Urban, Z., Thway, K., Zeid, R., Hallsworth, A., Box, G., Ebus, M. E., Licciardello, M. P., Sbirkov, Y., Tardif, N., … Chesler, L. (2020). Orally bioavailable CDK9/2 inhibitor shows mechanism-based therapeutic potential in MYCN-driven neuroblastoma. *The Journal of Clinical Investigation*, *130*(11), 5875–5892.

Pyle, A. D., Lock, L. F., & Donovan, P. J. (2006). Neurotrophins mediate human embryonic stem cell survival. *Nature Biotechnology*, *24*(3), 344–350. https://doi.org/10.1038/nbt1189

Rafael, O. C., Paul, D., Chen, S., & Kraus, D. (2016). Adenoid cystic carcinoma of submandibular gland metastatic to great toes: case report and literature review. *Clinical Case Reports*, *4*(8), 820–823. https://doi.org/10.1002/ccr3.635

Raina, K., Lu, J., Qian, Y., Altieri, M., Gordon, D., Rossi, A. M. K., Wang, J., Chen, X., Dong, H., Siu, K., Winkler, J. D., Crew, A. P., Crews, C. M., & Coleman, K. G. (2016). PROTAC-induced BET protein degradation as a therapy for castration-resistant prostate cancer. *Proceedings of the National Academy of Sciences of the United States of America*, *113*(26), 7124–7129. https://doi.org/10.1073/pnas.1521738113

Rao, S. S., Stoehr, J., Dokic, D., Wan, L., Decker, J. T., Konopka, K., Thomas, A. L., Wu, J., Kaklamani, V. G., Shea, L. D., & Jeruss, J. S. (2017). Synergistic effect of eribulin and CDK inhibition for the treatment of triple negative breast cancer. *Oncotarget*, *8*(48), 83925–83939. https://doi.org/10.18632/oncotarget.20202

Rehovot, Israel, & Wilmington, D. (2019). Ayala Pharmaceuticals presents encouraging preliminary safety and efficacy data in patients with recurrent/metastatic adenoid

cystic carcinoma with progressing disease and notch activating mutations from ongoing phase 2 clinical trial at ESMO [news releas. *Ayala Pharmaceuticals, Inc*.

Rettig, E. M., Talbot, C. C., Sausen, M., Jones, S., Bishop, J. A., Wood, L. D., Tokheim, C., Niknafs, N., Karchin, R., Fertig, E. J., Wheelan, S. J., Marchionni, L., Considine, M., Fakhry, C., Papadopoulos, N., Kinzler, K. W., Vogelstein, B., Ha, P. K., & Agrawal, N. (2016). Whole-genome sequencing of salivary gland adenoid cystic carcinoma. *Cancer Prevention Research*, *9*(4). https://doi.org/10.1158/1940-6207.CAPR-15-0316

Roe, J., Mercan, F., Rivera, K., Pappin, D. J., & Vakoc, C. R. (2015). BET bromodomain inhibition suppresses the functional output of hematopoietic transcription factors in acute myeloid leukemia. *Molecular Cell*, *58*(6), 1028–1039. https://doi.org/10.1016/j.gde.2016.03.011

Ross, J. S., Wang, K., Rand, J. V., Sheehan, C. E., Jennings, T. A., Al-Rohil, R. N., Otto, G. A., Curran, J. C., Palmer, G., Downing, S. R., Yelensky, R., Lipson, D., Balasubramamian, S., Garcia, L., Mahoney, K., Ali, S. M., Miller, V. A., & Stephens, P. J. (2014). Comprehensive genomic profiling of relapsed and metastatic adenoid cystic carcinomas by next generation sequencing reveals potential new routes to targeted therapies. *The American Journal of Surgical Pathology*, *38*(2), 235–238.

Ross, P. J., Teoh, E. M., A'Hern, R. P., Rhys-Evans, P. H., Harrington, K. J., Nutting, C. M., & Gore, M. E. (2009). Epirubicin, Cisplatin and Protracted Venous Infusion 5-Fluorouracil Chemotherapy for Advanced Salivary Adenoid Cystic Carcinoma. *Clinical Oncology*, *21*(4), 311–314. https://doi.org/10.1016/J.CLON.2008.12.009

Rothova, M., Thompson, H., Lickert, H., & Tucker, A. S. (2012). Lineage tracing of the endoderm during oral development. *Developmental Dynamics*, *241*(7), 1183–1191. https://doi.org/10.1002/dvdy.23804

Sachs, N., de Ligt, J., Kopper, O., Gogola, E., Bounova, G., Weeber, F., Balgobind, A. V., Wind, K., Gracanin, A., Begthel, H., Korving, J., van Boxtel, R., Duarte, A. A., Lelieveld, D., van Hoeck, A., Ernst, R. F., Blokzijl, F., Nijman, I. J., Hoogstraat, M., … Clevers, H. (2018). A Living Biobank of Breast Cancer Organoids Captures Disease Heterogeneity. *Cell*, *172*(1), 373–386. https://doi.org/10.1016/j.cell.2017.11.010

Sachs, N., Papaspyropoulos, A., Zomer-van Ommen, D. D., Heo, I., Böttinger, L., Klay, D., Weeber, F., Huelsz-Prince, G., Iakobachvili, N., Amatngalim, G. D., Ligt, J.,

Hoeck, A., Proost, N., Viveen, M. C., Lyubimova, A., Teeven, L., Derakhshan, S., Korving, J., Begthel, H., … Clevers, H. (2019). Long-term expanding human airway organoids for disease modeling. *The EMBO Journal*, *38*(4), 1–20. https://doi.org/10.15252/embj.2018100300

Saida, K., Murase, T., Ito, M., Fujii, K., & Takino, H. (2018). PIK3CA , BRAF , and AKT1 , in salivary gland adenoid cystic carcinoma. *Oncotarget*, *9*(24), 17043–17055.

Sato, T., Stange, D. E., Ferrante, M., Vries, R. G. J., Van Es, J. H., Van Den Brink, S., Van Houdt, W. J., Pronk, A., Van Gorp, J., Siersema, P. D., & Clevers, H. (2011). Long-term Expansion of Epithelial Organoids From Human Colon, Adenoma, Adenocarcinoma, and Barrett's Epithelium. *YGAST*, *141*, 1762–1772. https://doi.org/10.1053/j.gastro.2011.07.050

Sato, T., Vries, R. G., Snippert, H. J., Van De Wetering, M., Barker, N., Stange, D. E., Van Es, J. H., Abo, A., Kujala, P., Peters, P. J., & Clevers, H. (2009). Single Lgr5 stem cells build crypt-villus structures in vitro without a mesenchymal niche. *Nature*, *459*(7244), 262–265. https://doi.org/10.1038/nature07935

Schoenfeld, J. D., Sher, D. J., Norris, C. M., Haddad, R. I., Posner, M. R., Balboni, T. A., & Tishler, R. B. (2012). Salivary gland tumors treated with adjuvant intensity-modulated radiotherapy with or without concurrent chemotherapy. *International Journal of Radiation Oncology Biology Physics*, *82*(1), 308–314. https://doi.org/10.1016/j.ijrobp.2010.09.042

Schramm, V. L., Srodes, C., & Myers, E. N. (1981). Cisplatin Therapy for Adenoid Cystic Carcinoma. *Archives of Otolaryngology*, *107*(12), 739–741. https://doi.org/10.1001/archotol.1981.00790480015004

Seino, T., Kawasaki, S., Shimokawa, M., Tamagawa, H., Toshimitsu, K., Fujii, M., Ohta, Y., Matano, M., Nanki, K., Kawasaki, K., Takahashi, S., Sugimoto, S., Iwasaki, E., Takagi, J., Itoi, T., Kitago, M., Kitagawa, Y., Kanai, T., & Sato, T. (2018). Human Pancreatic Tumor Organoids Reveal Loss of Stem Cell Niche Factor Dependence during Disease Progression. *Cell Stem Cell*, *22*(3), 454-467.e6. https://doi.org/10.1016/j.stem.2017.12.009

Sha, W., Zheng, M., & Ke, D. (2019). *Hypoxia promotes vasculogenic mimicry formation by vascular endothelial growth factor A mediating epithelial - mesenchymal transition in salivary adenoid cystic carcinoma*. *February*, 1–11.

https://doi.org/10.1111/cpr.12600

Shan, C., Wei, J., Hou, R., Wu, B., & Yang, Z. (2016). *Schwann cells promote EMT and the Schwann - like differentiation of salivary adenoid cystic carcinoma cells via the BDNF / TrkB axis*. 427–435. https://doi.org/10.3892/or.2015.4366

Shapiro, G. I., Koestner, D. A., Matranga, C. B., & Rollins, B. J. (1999). Flavopiridol induces cell cycle arrest and p53-independent apoptosis in non-small cell lung cancer cell lines. *Clinical Cancer Research*, *5*(10), 2925–2938.

Shi, Y., & Massagué, J. (2003). Mechanisms of TGF-β signaling from cell membrane to the nucleus. *Cell*, *113*(6), 685–700. https://doi.org/10.1016/S0092-8674(03)00432-X

Shu, D. Y., Hutcheon, A. E. K., Zieske, J. D., & Guo, X. (2019). Epidermal Growth Factor Stimulates Transforming Growth Factor-Beta Receptor Type II Expression In Corneal Epithelial Cells. *Scientific Reports*, *9*(1), 1–11. https://doi.org/10.1038/s41598-019-42969-2

Shultz, L. D., Lyons, B. L., Burzenski, L. M., Gott, B., Chen, X., Chaleff, S., Kotb, M., Gillies, S. D., King, M., Mangada, J., Greiner, D. L., & Handgretinger, R. (2005). Human Lymphoid and Myeloid Cell Development in NOD/LtSz- scid IL2R γ null Mice Engrafted with Mobilized Human Hemopoietic Stem Cells . *The Journal of Immunology*, *174*(10), 6477–6489. https://doi.org/10.4049/jimmunol.174.10.6477

Simões-Costa, M., & Bronner, M. E. (2015). Establishing neural crest identity: a gene regulatory recipe. *Development*, *142*(2), 242–257. https://doi.org/10.1242/dev.105445

Smarda, J., Sugarman, J., Glass, C., & Lipsick, J. (1995). Retinoic acid receptor alpha suppresses transformation by v-myb. *Molecular and Cellular Biology*, *15*(5), 2474–2481. https://doi.org/10.1128/mcb.15.5.2474

Sonawane, Y. A., Taylor, M. A., Napoleon, J. V., Rana, S., Contreras, J. I., & Natarajan, A. (2016). Cyclin Dependent Kinase 9 Inhibitors for Cancer Therapy. *Journal of Medicinal Chemistry*, *59*(19), 8667–8684. https://doi.org/10.1021/acs.jmedchem.6b00150

Spiro, R. H., Huvos, A. G., & Strong, E. W. (1974). Adenoid cystic carcinoma of salivary origin: A clinicopathologic study of 242 cases. *The American Journal of Surgery*,

128(4), 512–520.

Spiro, R. H., Koss, L. G., Hajdu, S. I., & Strong, E. W. (1973). Tumours of minor salivary origin: a clinicopathologic study of 492 cases. *Cancer*, *31*(1), 117–129.

Sridharan, V., Gjini, E., Liao, X., Chau, N. G., Haddad, R. I., Severgnini, M., Hammerman, P., El-Naggar, A., Freeman, G. J., Hodi, F. S., Rodig, S. J., Dranoff, G., & Schoenfeld, J. D. (2016). Immune Profiling of Adenoid Cystic Carcinoma: PD-L2 Expression and Associations with Tumor-Infiltrating Lymphocytes. *Cancer Immunology Research*, *4*(8), 679–687. https://doi.org/10.1158/2326-6066.CIR-16-0031

Stephens, P. J., Davies, H. R., Mitani, Y., Van Loo, P., Shlien, A., Tarpey, P. S., Papaemmanuil, E., Cheverton, A., Bignell, G. R., Butler, A. P., Gamble, J., Gamble, S., Hardy, C., Hinton, J., Jia, M., Jayakumar, A., Jones, D., Latimer, C., McLaren, S., … Futreal, P. A. (2013). Whole exome sequencing of adenoid cystic carcinoma. *Journal of Clinical Investigation*, *123*(7), 2965–2968. https://doi.org/10.1172/JCI67201

Szanto, P. A., Luna, M. A., Tortoledo, M. E., & White, R. A. (1984). Histologic grading of adenoid cystic carcinoma of the salivary glands. *Cancer*, *54*(6), 1062–1069.

Takada, K., Aizawa, Y., Sano, D., Okuda, R., & Sekine, K. (2021). Establishment of PDX-derived salivary adenoid cystic carcinoma cell lines using organoid culture method. *International Journal of Cancer*, *148*(1), 193–202. https://doi.org/10.1002/ijc.33315

Takasato, M., Er, P. X., Chiu, H. S., Maier, B., Baillie, G. J., Ferguson, C., Parton, R. G., Wolvetang, E. J., Roost, M. S., Chuva de Sousa Lopes, S. M., & Little, M. H. (2015). Kidney organoids from human iPS cells contain multiple lineages and model human nephrogenesis. *Nature*, *526*(7574), 564–568. https://doi.org/10.1038/nature15695

Tauriello, D. V. F., Palomo-Ponce, S., Stork, D., Berenguer-Llergo, A., Badia-Ramentol, J., Iglesias, M., Sevillano, M., Ibiza, S., Cañellas, A., Hernando-Momblona, X., Byrom, D., Matarin, J. A., Calon, A., Rivas, E. I., Nebreda, A. R., Riera, A., Attolini, C. S.-O., & Batlle, E. (2018). TGFβ drives immune evasion in genetically reconstituted colon cancer metastasis. *Nature*, *554*(7693), 538–543. https://doi.org/10.1038/nature25492

Tchekmedyian, V., Sherman, E. J., Dunn, L., Tran, C., Katabi, N., Ni, A., Haque, S.,

Pfister, D. G., & Ho, A. L. (2018). A phase II study of lenvatinib in patients with progressive, recurrent/metastatic adenoid cystic carcinoma. *Journal of Clinical Oncology*, *36*(15_suppl), 6022. https://doi.org/10.1200/JCO.2018.36.15_suppl.6022

Terunuma, A., Limgala, R. P., Park, C. J., Choudhary, I., & Vogel, J. C. (2010). Efficient procurement of epithelial stem cells from human tissue specimens using a rho-associated protein kinase inhibitor Y-27632. *Tissue Engineering - Part A*, *16*(4), 1363–1368. https://doi.org/10.1089/ten.tea.2009.0339

Therasse, P., Arbuck, S. G., Eisenhauer, E. A., Wanders, J., Kaplan, R. S., Rubinstein, L., Verweij, J., Van Glabbeke, M., Van Oosterom, A. T., Christian, M. C., & Gwyther, S. G. (2000). New guidelines to evaluate the response to treatment in solid tumors. *Journal of the National Cancer Institute*, *92*(3), 205–216. https://doi.org/10.1093/jnci/92.3.205

Thiele, C. J., Cohen, P. S., & Israel, M. A. (1988). Regulation of c-myb expression in human neuroblastoma cells during retinoic acid-induced differentiation. *Molecular and Cellular Biology*, *8*(4), 1677–1683. https://doi.org/10.1128/mcb.8.4.1677

Thompson, L. (2006). World Health Organisation classification of tumours: pathology and genetics of head and neck tumours. *Ear Nose Throat Journal*, *85*(2), 74.

Tomska, K., Kurilov, R., Lee, K. S., Hüllein, J., Lukas, M., Sellner, L., Walther, T., Wagner, L., Oleś, M., Brors, B., Huber, W., & Zenz, T. (2018). *Drug-based perturbation screen uncovers synergistic drug combinations in Burkitt lymphoma*. *May*, 1–12. https://doi.org/10.1038/s41598-018-30509-3

Toolan, H. W. (1953). Growth of human tumors in cortisone-treated laboratory animals: the possibility of obtaining permanently transplantable human tumors. *Cancer Research*, *13*(4), 389–394.

Tsoneva, D., Minev, B., Frentzen, A., Zhang, Q., Wege, A. K., & Szalay, A. A. (2017). Humanized Mice with Subcutaneous Human Solid Tumors for Immune Response Analysis of Vaccinia Virus-Mediated Oncolysis. *Molecular Therapy - Oncolytics*, *5*(June), 41–61. https://doi.org/10.1016/j.omto.2017.03.001

Tyler, D., Vappiani, J., Cañeque, T., Lam, E. Y. ., Ward, A., Gilan, O., Chan, Y. ., Hienzsch, A., Rutkowska, A., Werner, T., Wagner, A. ., Lugo, D., Gregory, R., Ramirez Molina,

C., Garton, N., Wellaway, C. ., Jackson, S., MacPherson, L., Figueiredo, M., … Dawson, M. . (2017). Click chemistry enables preclinical evaluation of targeted epigenetic therapies. *Science*, *356*(6345), 1397–1401. https://doi.org/10.1126/science.aal2066.Click

van der Wal, J. E., Becking, A. G., Snow, G. B., & Van Der Waal, I. (2002). Distant metastases of adenoid cystic carcinoma of the salivary glands and the value of diagnostic examinations during follow-up. *Head and Neck*, *24*(8), 779–783. https://doi.org/10.1002/hed.10126

van Herpen, C. M. L., Locati, L. D., Buter, J., Thomas, J., Bogaerts, J., Lacombe, D., de Mulder, P., Awada, A., Licitra, L., Bernier, J., & Vermorken, J. B. (2008). Phase II study on gemcitabine in recurrent and/or metastatic adenoid cystic carcinoma of the head and neck (EORTC 24982). *European Journal of Cancer*, *44*(17), 2542–2545. https://doi.org/10.1016/j.ejca.2008.08.014

van Weert, S., van der Waal, I., Witte, B. I., René Leemans, C., & Bloemena, E. (2015). Histopathological grading of adenoid cystic carcinoma of the head and neck: Analysis of currently used grading systems and proposal for a simplified grading scheme. *Oral Oncology*, *51*(1), 71–76. https://doi.org/10.1016/j.oraloncology.2014.10.007

Varga, G. (2015). Physiology of the salivary glands. *Surgery (United Kingdom)*, *33*(12), 581–586. https://doi.org/10.1016/j.mpsur.2015.09.003

Vedder, A. R., Miedel, E. L., Ragland, N. H., Balasis, M. E., Letson, C. T., Engelman, R. W., & Padron, E. (2019). Effects of Corynebacterium bovis on Engraftment of Patient-derived Chronic-Myelomonocytic Leukemia Cells in NSGS Mice. *Comparative Medicine*, *69*(4), 276–282. https://doi.org/10.30802/AALAS-CM-18-000138

Vila, L., Liu, H., Al-Quran, S. Z., Coco, D. P., Dong, H. J., & Liu, C. (2009). Identification of c-kit gene mutations in primary adenoid cystic carcinoma of the salivary gland. *Modern Pathology*, *22*(10), 1296–1302. https://doi.org/10.1038/modpathol.2009.95

Vinagre, J., Almeida, A., Pópulo, H., Batista, R., Lyra, J., Pinto, V., Coelho, R., Celestino, R., Prazeres, H., Lima, L., Melo, M., Rocha, A. G. Da, Preto, A., Castro, P., Castro, L., Pardal, F., Lopes, J. M., Santos, L. L., Reis, R. M., … Soares, P. (2013). Frequency of

TERT promoter mutations in human cancers. *Nature Communications*, *72*(4), 281–284. https://doi.org/10.1038/ncomms3185

Vlachogiannis, G., Hedayat, S., Vatsiou, A., Jamin, Y., Fernández-mateos, J., Khan, K., Lampis, A., Eason, K., Huntingford, I., Burke, R., Rata, M., Koh, D., Tunariu, N., Collins, D., Hulkki-wilson, S., Ragulan, C., Spiteri, I., Moorcraft, S. Y., Chau, I., … Valeri, N. (2018). Patient-derived organoids model treatment response of metastatic gastrointestinal cancers. *Cancer*, *359*(6378), 920–926.

Vogt, J., Traynor, R., & Sapkota, G. P. (2011). The specificities of small molecule inhibitors of the TGFß and BMP pathways. *Cellular Signalling*, *23*(11), 1831–1842. https://doi.org/10.1016/j.cellsig.2011.06.019

Vogus, D. R., Pusuluri, A., Chen, R., & Mitragotri, S. (2018). Schedule dependent synergy of gemcitabine and doxorubicin : Improvement of in vitro efficacy and lack of in vitro-in vivo correlation. *Bioengineering & Translational Medicine*, *November 2017*, 49–57. https://doi.org/10.1002/btm2.10082

Vrielinck, L. J. G., Ostyn, F., van Damme, B., van den Bogaert, W., & Fossion, E. (1988). The significance of perineural spread in adenoid cystic carcinoma of the major and minor salivary glands. *International Journal of Oral and Maxillofacial Surgery*, *17*(3), 190–193. https://doi.org/10.1016/S0901-5027(88)80030-4

Wallrapp, C., Müller-Pillasch, F., Solinas-Toldo, S., Lichter, P., Friess, H., Büchler, M., Fink, T., Adler, G., & Gress, T. M. (1997). Characterization of a High Copy Number Amplification at 6q24 in Pancreatic Cancer Identifies c-myb as a Candidate Oncogene. *Cancer Research*, *57*(15), 3135 LP – 3139. http://cancerres.aacrjournals.org/content/57/15/3135.abstract

Wang, H. Y., & Kim, N. H. (2016). CDK2 is required for the DNA damage response during porcine early embryonic development. *Biology of Reproduction*, *95*(2), 1–13. https://doi.org/10.1095/biolreprod.116.140244

Wang, L., Wang, Y., Bian, H., Pu, Y., & Guo, C. (2013). Molecular characteristics of homologous salivary adenoid cystic carcinoma cell lines with different lung metastasis ability. *Oncology Reports*, *30*(1), 207–212. https://doi.org/10.3892/or.2013.2460

Warner, K. A., Oklejas, A. E., Pearson, A. T., Zhang, Z., Wu, W., Divi, V., Rodriguez-ramirez, C., Castilho, R. M., Peter, J., Sciences, R., Arbor, A., Arbor, A., Arbor, A.,

Arbor, A., Medicine, O., & Arbor, A. (2019). UM-HACC-2A: MYB-NFIB fusion-positive human adenoid cystic carcinoma cell line. *Oral Oncology*, *734*, 21–28. https://doi.org/10.1016/j.oraloncology.2018.10.012.UM-HACC-2A

West, R. B., Kong, C., Clarke, N., Gilks, T., Lipsick, J., Kwok, S., Montgomery, K. D., Varma, S., & Le, Q. (2011). MYB expression and translocation in adenoid cystic carcinomas and other salivary gland tumors with clinicopathologic correlation. *American Journal of Surgical Pathology*, *35*(1), 92–99. https://doi.org/10.1097/PAS.0b013e3182002777.MYB

Whittaker, S. R., Barlow, C., Martin, M. P., Mancusi, C., Wagner, S., Self, A., Barrie, E., Te Poele, R., Sharp, S., Brown, N., Wilson, S., Jackson, W., Fischer, P. M., Clarke, P. A., Walton, M. I., McDonald, E., Blagg, J., Noble, M., Garrett, M. D., & Workman, P. (2018). Molecular profiling and combinatorial activity of CCT068127: a potent CDK2 and CDK9 inhibitor. *Molecular Oncology*, *12*(3), 287–304. https://doi.org/10.1002/1878-0261.12148

Wilson, S. C., Atrash, B., Barlow, C., Eccles, S., Fischer, P. M., Hayes, A., Kelland, L., Jackson, W., Jarman, M., Mirza, A., Moreno, J., Nutley, B. P., Raynaud, F. I., Sheldrake, P., Walton, M., Westwood, R., Whittaker, S., Workman, P., & McDonald, E. (2011). Design, synthesis and biological evaluation of 6-pyridylmethylaminopurines as CDK inhibitors. *Bioorganic and Medicinal Chemistry*, *19*(22), 6949–6965. https://doi.org/10.1016/j.bmc.2011.08.051

Xu, L. H., Zhao, F., Yang, W. W., Chen, C. W., Du, Z. H., Fu, M., Ge, X. Y., & Li, S. L. (2019). MYB promotes the growth and metastasis of salivary adenoid cystic carcinoma. *International Journal of Oncology*, *54*(5), 1579–1590. https://doi.org/10.3892/ijo.2019.4754

Yang, Z., Yik, J. H. N., Chen, R., He, N., Jang, M. K., Ozato, K., & Zhou, Q. (2005). Recruitment of P-TEFb for stimulation of transcriptional elongation by the bromodomain protein Brd4. *Molecular Cell*, *19*(4), 535–545. https://doi.org/10.1016/j.molcel.2005.06.029

Yarbrough, W. G., Panaccione, A., Chang, M. T., & Ivanov, S. V. (2016). Clinical and Molecular Insights Into Adenoid Cystic Carcinoma : Neural Crest-Like Stemness as a Target. *Laryngoscope Investigative Otolaryngology*, *1*(4), 60–77. https://doi.org/10.1002/lio2.22

Ye, F., Bauer, J. A., Pietenpol, J. A., & Shyr, Y. (2012). Analysis of high-throughput RNAi screening data in identifying genes mediating sensitivity to chemotherapeutic drugs: statistical approaches and perspectives. *BMC Genomics*, *13 Suppl 8*(Suppl 8). https://doi.org/10.1186/1471-2164-13-s8-s3

Youn, Y. H., Feng, J., Tessarollo, L., Ito, K., & Sieber-Blum, M. (2003). Neural crest stem cell and cardiac endothelium defects in the TrkC null mouse. *Molecular and Cellular Neuroscience*, *24*(1), 160–170. https://doi.org/https://doi.org/10.1016/S1044-7431(03)00125-8

Zarkowska, T., & Mittnacht, S. (1997). Differential phosphorylation of the retinoblastoma protein by G1/S cyclin-dependent kinases. *Journal of Biological Chemistry*, *272*(19), 12738–12746. https://doi.org/10.1074/jbc.272.19.12738

Zemanová, K., & Šmarda, J. (1998). Oncoprotein v-Myb and retinoic acid receptor α are mutual antagonists. *Blood Cells, Molecules and Diseases*, *24*(2), 239–250. https://doi.org/10.1006/bcmd.1998.0189

Zhan, T., Rindtorff, N., & Boutros, M. (2017). Wnt signaling in cancer. *Oncogene*, *36*(11), 1461–1473. https://doi.org/10.1038/onc.2016.304

Zhang, C., Stockwell, S. R., Elbanna, M., Ketteler, R., Freeman, J., Eccles, S., Haven, A. De, Florence, B., Angela, R., Paul, H., Workman, P., & Mittnacht, S. (2019). Signalling involving MET and FAK supports cell division independent of the activity of the cell cycle-regulating CDK4 / 6 kinases. *Oncogene*, 5905–5920. https://doi.org/10.1038/s41388-019-0850-2

Zhang, J., Peng, B., & Chen, X. (2005). Expressions of nuclear factor κB, inducible nitric oxide synthese, and vascular endothelial growth factor in adenoid cystic carcinoma of salivary glands: Correlations with the angiogenesis and clinical outcome. *Clinical Cancer Research*, *11*(20), 7334–7343. https://doi.org/10.1158/1078-0432.CCR-05-0241

Zhao, M., Sano, D., Pickering, C. R., Jasser, S. A., Henderson, Y. C., Clayman, G. L., Sturgis, E. M., Ow, T. J., Lotan, R., Carey, T. E., Sacks, P. G., Grandis, J. R., Sidransky, D., Heldin, N. E., & Jeffrey, N. (2011). Assembly And Initial Characterization Of A Panel Of 85 Genomically Validated Cell Lines From Diverse Head And Neck Tumor Sites. *Clinical Cancer Research*, *17*(23), 7248–7264. https://doi.org/10.1158/1078-0432.CCR-11-0690.Assembly

Zheng, B., Ren, T., Huang, Y., Sun, K., Wang, S., Bao, X., Liu, K., & Guo, W. (2018). PD-1 axis expression in musculoskeletal tumors and antitumor effect of nivolumab in osteosarcoma model of humanized mouse. *Journal of Hematology and Oncology*, *11*(1), 1–13. https://doi.org/10.1186/s13045-018-0560-1

Zhu, G., Zhang, L., Li, R., Dou, S., Yang, W., & Zhang, C. (2018). Phase II trial of apatinib in patients with recurrent and/or metastatic adenoid cystic carcinoma of the head and neck: Updated analysis. *Journal of Clinical Oncology*, *36*(15_suppl), 6026. https://doi.org/10.1200/JCO.2018.36.15_suppl.6026

Zhu, S., Schuerch, C., & Hunt, J. (2015). Review and updates of immunohistochemistry in selected salivary gland and head and neck tumors. *Archives of Pathology and Laboratory Medicine*, *139*(1), 55–66. https://doi.org/10.5858/arpa.2014-0167-RA

Zhu, Y., Tchkonia, T., Fuhrmann-Stroissnigg, H., Dai, H. M., Ling, Y. Y., Stout, M. B., Pirtskhalava, T., Giorgadze, N., Johnson, K. O., Giles, C. B., Wren, J. D., Niedernhofer, L. J., Robbins, P. D., & Kirkland, J. L. (2016). Identification of a novel senolytic agent, navitoclax, targeting the Bcl-2 family of anti-apoptotic factors. *Aging Cell*, *15*(3), 428–435. https://doi.org/10.1111/acel.12445

Zoli, W., Ricotti, L., Barzanti, F., Dal Susino, M., Frassineti, G. L., Milandri, C., Casadei Giunchi, D., & Amadori, D. (1999). Schedule-dependent interaction of doxorubicin, paclitaxel and gemcitabine in human breast cancer cell lines. *International Journal of Cancer*, *80*(3), 413–416. https://doi.org/10.1002/(SICI)1097-0215(19990129)80:3<413::AID-IJC13>3.0.CO;2-I

9. Appendix

9.1. ACC patient sample WES data

SG0027

Somatic mutations

Gene Name	Effect	Severity	Genomic Location	Amino acid	cDNA location	^VAF Tumour
ABCA6	NSC	Moderate	17:67074843-67138029	p.R660C	c.1978G>A	0.51
ADM2	NSC	Moderate	22:50919985-50924869	p.G103A	c.308G>C	0.52
ANKRD35	NSC	Moderate	1:145549230-145568526	p.D925H	c.2773G>C	0.5
ARHGAP5	NSC	Moderate	14:32545320-32628934	p.Q213R	c.638A>G	0.5
BMPR2	NSC	Moderate	2:203241659-203432474	p.I540F	c.1618A>T	0.5
COL2A1	SC	Low	12:48366748-48398269	p.G750G	c.2250G>A	0.56
ERICH1	NSC	Moderate	8:564746-688106	p.P22T	c.64G>T	0.55
FLNB	NSC	Moderate	3:57994127-58157982	p.A550V	c.1649C>T	0.95
GLTSCR1	SC	Low	19:48111453-48206533	p.P824P	c.2472A>C	0.1
GPR113	NSC	Moderate	2:26531041-26569685	p.A673T	c.2017C>T	0.54
HOMER3	NSC	Moderate	19:19040010-19052070	p.K57R	c.170T>C	0.64
KRTAP5-1	SC	Low	11:1605572-1606513	p.G192G	c.576T>G	0.1
MAGI1	FRAME_SHIFT	High	3:65342053-66024509	p.X92X	c.275*>-C	0.9
NOX1	NSC	Moderate	X:100098313-100129334	p.R151H	c.452C>T	0.73
SLC16A10	SC	Low	6:111408781-111552397	p.T25T	c.75G>T	0.54
STAG2	FRAME_SHIFT	High	X:123094062-123556514	p.X228X	c.684*>-C	0.98
SYT6	NSC	Moderate	1:114631913-114696541	p.E221D	c.663C>A	0.5
TTC39B	STOP_GAINED	High	9:15163620-15307358	p.E295*	c.883C>A	0.51
VEGFB	FRAME_SHIFT	High	11:64002010-64006259	p.X168X	c.502*>-C	0.52
WDR41	NSC	Moderate	5:76721795-76916436	p.L140M	c.418G>T	0.54
WDR41	NSC	Moderate	5:76721795-76916436	p.E139D	c.417T>A	0.55
ZBED6	NSC	Moderate	1:203765437-203769686	p.V607M	c.1819G>A	0.5

Copy number variations involving genes found in the CGC list

Genomic Locus	**Copy number variation**	**Gene Names**
3p13-3p14.2	lost one copy	MITF, FOXP1, FHIT
3p21.1-3p25.3	lost one copy	BAP1, PBRM1, CACNA1D, SETD2, CTNNB1, MYD88, MLH1, XPC, RAF1, PPARG, VHL, SRGAP3, FANCD2
4p15.2	gain	SLC34A2

5q35.1-5q35.3	gain	TLX3, NPM1, RANBP17, NSD1
6p21.1-6p21.32	amplification	TFEB, CCND3, PIM1, HMGA1, FANCE, DAXX
6p21.1-6p22.3	gain	HIST1H4I, TRIM27, HIST1H3B, DEK
6q23.3-6q25.3	lost one copy	TNFAIP3, ECT2L, EZR
7q22.1	gain	TRRAP
8q24.3	gain	RECQL4
11p15.5	gain	HRAS
11q13.1	gain	MALAT1
11q14.2	lost one copy	PICALM
11q22.2	amplification	BIRC3
11q22.3-11q23.3	gain	ATM, DDX10, SDHD, POU2AF1, PCSK7, PAFAH1B2, MLL, DDX6, CBL, ARHGEF12
11q24.3	lost one copy	KCNJ5, FLI1
12p13.2	gain	ETV6
12q14.1	gain	CDK4
12q24.31	gain	CLIP1
14q22.1-14q22.3	amplification	NIN, KTN1
14q23.3	lost one copy	MAX, GPHN
14q31.1	lost one copy	TSHR
16p13.3	gain	TSC2, TRAF7, AXIN1
17q25.3	gain	ASPSCR1
19p13.11-19p13.3	gain	JAK3, ELL, BRD4, TPM4, CALR, LYL1, DNM2, SMARCA4, FSTL3, STK11, TCF3, GNA11, MAP2K2, SH3GL1, MLLT1
19q12-19q13.42	gain	CCNE1, CEBPA, LSM14A, CEP89, CD79A, CIC, AKT2, BCL3, CBLC, ERCC2, KLK2, PPP2R1A, TFPT, ZNF331, CNOT3
Xp11.22-Xp11.3	gain	SSX2, KDM5C, GATA1, SSX1, SSX4, WAS, TFE3, KDM6A
Xp11.4	lost one copy	BCOR
Xp22.2	lost one copy	ZRSR2
Xq13.1	gain	FOXO4, MED12, NONO
Xq25	lost one copy	STAG2
Xq26.1-Xq28	lost one copy	ELF4, GPC3, PHF6, RPL10, MTCP1, ATP2B3

Germline mutations with allele frequency change in SG0027 in comparison to the normal (CGC genes)

Gene Name	**Amino acid change**	**cDNA location**	**Genomic location**	***Effect**	**Severity**	**^VAF Tumour**	**^VAF Normal**
ELF4	p.V408M	c.1222C>T	X:129198849-129244691	NSC	MODERATE	1.00	0.50
FANCD2	p.L237L	c.711G>C	3:10068098-10143614	SC	LOW	0.95	0.50
FANCD2	p.L1366L	c.4098T>G	3:10068098-10143614	SC	LOW	0.94	0.48
TSHR	p.N187N	c.561T>C	14:81421333-81612646	SC	LOW	1.00	0.42

SG0028

Somatic mutations

Gene Name	*Effect	Severity	Genomic Location	Amino acid	cDNA location	^VAF Tumour
BRD1	STOP_GAINED	High	22:50166931-50221160	p.L87*	c.260A>T	0.9
OR5A1	NSC	Moderate	11:59210617-59211667	p.N83H	c.247A>C	0.61
RTTN	NSC	Moderate	18:67671029-67873181	p.E448V	c.1343T>A	0.53

Copy number variations involving genes found in the CGC list

Genomic Locus	Copy number variation	Gene Names
1p22.1	gain	RPL5
6q23.3-6q24.1	gain	TNFAIP3, ECT2L
7p11.2	gain	EGFR
7q11.21-7q11.23	gain	SBDS, ELN, HIP1
7p12.2	gain	IKZF1
7p15.1-7p15.2	gain	JAZF1, HOXA9, HOXA11, HOXA13, HNRNPA2B1
7p21.2-7p22.2	gain	ETV1, PMS2, RAC1, CARD11
7q21.2-7q22.1	gain	AKAP9, CDK6, TRRAP, CUX1
7q31.2-7q36.1	gain	MET, POT1, SMO, CREB3L2, KIAA1549, BRAF, EZH2, MLL3
11p11.2-11p15.5	gain	CREB3L1, DDB2, EXT2, WT1, LMO2, FANCF, CARS, NUP98, LMO1, HRAS
11q13.1-11q14.2	gain	MEN1, MALAT1, CCND1, NUMA1, PICALM
11q21-11q24.3	gain	MAML2, BIRC3, ATM, DDX10, SDHD, POU2AF1, PCSK7, PAFAH1B2, MLL, DDX6, CBL, ARHGEF12, KCNJ5, FLI1
12q24.12	gain	SH2B3
16p13.3	gain	TSC2, TRAF7, AXIN1, CREBBP
16q24.3	gain	FANCA

Germline mutations with allele frequency change in SG0028 in comparison to the normal (CGC genes)

Gene Name	Amino acid change	cDNA location	Genomic location	*Effect	Severity	^VAF Tumour	^VAF Normal
ATM	p.P1526P	c.4578C>T	11:108093211-108239829	SC	LOW	0.70	0.29
BCR	p.N796S	c.2387A>G	22:23521891-23660224	NSC	MODERATE	0.93	0.38
CLTCL1	p.A1063A	c.3189T>C	22:19166986-19279239	SC	LOW	0.95	0.47
CLTCL1	p.M1316V	c.3946T>C	22:19166986-19279239	NSC	MODERATE	0.91	0.46
MKL1	p.S648G	c.1942A>G	22:40806285-41032706	NSC	MODERATE	0.86	0.54

SG0031

Somatic mutations

Gene Name	*Effect	Severity	Genomic Location	Amino acid	cDNA location	^VAF Tumour
BCOR	FRAME_SHIFT	High	X:39909068-40036582	p.X603X	c.1807*>-C	0.66
KRTAP27-1	STOP_GAINED	High	21:31709331-31710012	p.C45*	c.135A>T	0.54

Copy number variations involving genes found in the CGC list

Genomic Locus	Copy number variation	Gene Names
1q21.1	gain	PDE4DIP
1p31.1-1p31.3	gain	FUBP1, CDC73, JAK1
2p22.2	gain	STRN
2q31.1	copy neutral LOH	HOXD13
2q31.2-2q32.2	gain	NFE2L2, PMS1
4q12	amplification	FIP1L1, CHIC2, PDGFRA
6q22.33	loss	RSPO3, PTPRK
6q23.3-6q24.1	gain	MYB, TNFAIP3, ECT2L
7p21.2	gain	ETV1, AKAP9, CDK6
12q12-12q15	gain	ARID2, LRIG3, WIF1, HMGA2, MDM2, PTPRB
18q21.33	gain	BCL2

Germline mutations with allele frequency change in SG0031 in comparison to the normal (CGC genes)

Gene Name	Amino acid change	cDNA location	Genomic location	*Effect	Severity	^VAF Tumour	^VAF Normal
PTPRK	p.L674L	c.2022G>T	6:128289924-128841870	SC	LOW	0.91	0.52

SG0032

Somatic mutations

Gene Name	Effect*	Severity	Genomic location	Amino acid	cDNA location	^VAF Tumour
ARHGEF40	NSC	Moderate	14:21538429-21558399	p.P1000S	c.2998C>T	0.52
CREBBP	NSC	Moderate	16:3775055-3930722	p.W1502C	c.4506C>A	0.67

Copy number variations involving genes found in the CGC list

Genomic Locus	Copy number variation	Gene Names
1p35.1	Gain	LCK, RNF198
4q12	Amplification	CEP135, CHIC2, FIP1L1, KDR, KIT, MRPL22P1, PDGFRA
5q12.1	Gain	SETP21

6p21.31-6p21.32	Gain	ITPR3, DAXX
7q22.1	Gain	MUC12, MUC17
11q13.1	Gain	MEN1
12q13.2-12q13.33	Lost one copy	ATF1, CCDC65, COL2A1, DDIT3, HOXC11, HOXC13, IL23A, METTL7A, METTL7B, MLL2, NAB2, NACA, STAT6
12q14.1	Lost one copy	CDK4, METTL1, METTL21B
14q11.2	Gain	ABHD4, BCL2L2, IL25, MRPL52, ZFHX2
14q12	Gain	CBLN3, TINF2
16p11.2-16p12.3	Gain	FUS, IL21R, IL27, ITPRIPL2, METTL9, NFATC2IP, PALB2, SETD1A, TP53TG3, TP53TG3B, ZNF267
16q12.1	Gain	CBLN1, CYLD, ITFG1
16p13-16p13.13	Gain	AXIN1, CCDC64B, CIITA, CREBBP, ERCC4, HERPUD1, ITFG3, METRN, METTL22, MYH11, RNF151, SOCS1, TNFRSF17, TRAF7, TSC2, ZNF174, ZNF200, ZNF205, ZNF213, ZNF263
16q21-16q24.3	Gain	ATMIN, CBFA2T3, CBFB, CDH1, CDH11, CDH13, CDH15, CDH16, CTRB1, FANCA, FHOD1, MAF, PHLPP2, RLTPR, RNF166, SETD6, ZFHX3, ZNF19, ZNF23, ZNF276
17q25.1	Gain	GALK1, H3F3B
21p11.2	Gain	MAFIP

Germline mutations with allele frequency change in SG0032 in comparison to the normal (CGC genes)

Gene Name	Amino acid change	cDNA location	Genomic location	*Effect	Severity	^VAF Tumour	^VAF Normal
GATA2	p.P5P	c.15G>C	3:128198270-128212028	SC	LOW	0.61	0.18
KIT	p.K546K	c.1638A>G	4:55524085-55606881	SC	LOW	0.94	0.47
MLL2/KMT2D	p.P3557P	c.10671T>C	12:49412758-49453557	SC	LOW	0.93	0.42
MLL2/KMT2D	p.P3557P	c.10671T>C	12:49412758-49453557	SC	LOW	0.93	0.42

SG0035

Copy number variations involving genes found in the CGC list

Genomic Locus	Copy number variation	Gene Names
1p34.3-1p36.13	lost one copy	SFPQ, THRAP3, CSF3R, LCK, MDS2, ARID1A, SPEN, SDHB, PAX7
1p36.21-1p36.32	lost one copy	SPEN, CAMTA1, RPL22, CAMTA1, TNFRSF14, PRDM16
12q12-12q14.1	homozygous deletion	ARID2, COL2A1, SMARCD1, ATF1, HOXC13, HOXC11, NACA, NAB2, STAT6, DDIT3, CDK4, LRIG3

Germline mutations with allele frequency change in SG0035 in comparison to the normal (CGC genes)

Gene Name	Amino acid change	cDNA location	Genomic location	*Effect	Severity	^VAF Tumour	^VAF Normal
CUX1	p.P1450P	c.4350G>A	7:101459219-101927250	SC	LOW	0.83	0.30

SG0036

Somatic mutations

Gene Name	*Effect	Severity	Genomic Location	Amino acid	cDNA location	^VAF Tumour
FGA	SC	Low	4:155504278-155511918	p.P255P	c.765C>T	0.57
HIP1	STOP_GAINED	High	7:75162621-75368280	p.E411*	c.1231C>A	0.59
PDCD1	SC	Low	2:242792033-242801060	p.V10V	c.30G>A	0.51

Copy number variations involving genes found in the CGC list

Genomic Locus	Copy number	Gene Names
6q23.3-6q25.3	lost one copy	TNFAIP3, ECT2L, ARID1B, EZR
12q12-12q14.1	lost one copy	ARID2, COL2A1, SMARCD1, ATF1, HOXC13, HOXC11, NACA, NAB2, STAT6, DDIT3, CDK4, LRIG3

Germline mutations with allele frequency change in SG0036 in comparison to the normal (CGC genes)

Gene Name	Amino acid change	cDNA location	Genomic location	*Effect	Severity	^VAF Tumour	^VAF Normal
ECT2L	p.N67N	c.201T>C	6:139117063-139225207	SC	LOW	0.98	0.50
LRIG3	p.L6L	c.16G>A	12:59265931-59314303	SC	LOW	1.00	0.37
LRIG3	p.S27S	c.81T>G	12:59265931-59314303	SC	LOW	1.00	0.44
NACA	p.I769I	c.2307A>G	12:57106212-57125412	SC	LOW	0.98	0.36
NACA	p.L688P	c.2063A>G	12:57106212-57125412	NSC	MODERATE	0.98	0.41
NACA	p.S642T	c.1924A>T	12:57106212-57125412	NSC	MODERATE	0.95	0.35
NACA	p.F405S	c.1214A>G	12:57106212-57125412	NSC	MODERATE	1.00	0.43
NACA	p.V336E	c.1007A>T	12:57106212-57125412	NSC	MODERATE	1.00	0.38
NACA	p.I891I	c.2673A>T	12:57106212-57125412	SC	LOW	1.00	0.59
NACA	p.L893L	c.2677G>A	12:57106212-57125412	SC	LOW	1.00	0.53

SG0037

Somatic mutations

Gene Name	*Effect	Severity	Genomic Location	Amino acid	cDNA location	^VAF Tumour
BCL11B	NSC	Moderate	14:99635624-99737861	p.D461N	c.1381C>T	0.56
PDZD2	NSC	Moderate	5:31639517-32111037	p.M1836I	c.5508G>A	0.56
WDR45	NSC	Moderate	X:48929385-48958108	p.L85P	c.254A>G	0.97

Copy number variations involving genes found in the CGC list

Genomic Locus	Copy number variation	Gene Names
1q21.1-1q21.2	gain	PDE4DIP, BCL9
9q34.2-9q34.3	gain	RALGDS, BRD3, NOTCH1
12q12-12q14.3	lost one copy	ARID2, COL2A1, SMARCD1, ATF1, HOXC13, HOXC11, NACA, NAB2, STAT6, DDIT3, CDK4, LRIG3, WIF1, HMGA2
20q13.33	gain	SS18L1

Germline mutations with allele frequency change in SG0037 in comparison to the normal (CGC genes)

Gene Name	Amino acid change	cDNA location	Genomic location	*Effect	Severity	^VAF Tumour	^VAF Normal
COL2A1	p.T9S	c.25T>A	12:48366748-48398269	NSC	MODERATE	1.00	0.47
ROS1	p.S2229C	c.6686G>C	6:117609463-117747018	NSC	MODERATE	0.50	0.09
TRIM33	p.Q382Q	c.1146T>C	1:114935399-115053781	SC	LOW	0.53	0.21

SG0069

Copy number variations involving genes found in the CGC list

Genomic Locus	Copy number variation	Gene Names
5p13.1-5p13.2	lost on copy	LIFR, IL7R
5q11.2-5q13.1	lost on copy	IL6ST, MAP3K1, PIK3R1
5p15.33	lost on copy	TERT
5q22.2	lost on copy	APC
5q32-5q35.3	lost on copy	PDGFRB, CD74, ITK, EBF1, PWWP2A, RANBP17, TLX3, NPM1, FGFR4, NSD1
9p23-9p24.1	gain	NFIB, JAK2, CD274
10q11.21-10q11.23	lost one copy	RET, NCOA4
10p11.22-10p14	gain	KIF5B, ABI1, MLLT10, GATA3
10q21.2-10q25.3	lost one copy	CCDC6, PRF1, BMPR1A, PTEN, FAS, TLX1, NFKB2, SUFU, NT5C2, VTI1A, TCF7L2, KIAA1598

10q26.13	amplification	FGFR2
12p11.23-12p13.33	gain	PPFIBP1, ETNK1, KRAS, CDKN1B, ETV6, ZNF384, CCND2, ERC1, KDM5A
12q12-12q15	lost one copy	ARID2, COL2A1, SMARCD1, ATF1, HOXC13, HOXC11, NACA, NAB2, STAT6, DDIT3, CDK4, LRIG3, WIF1, HMGA2, MDM2, PTPRB
12q21.33	lost one copy	BTG1
14q11.2-14q13.3	lost one copy	CCNB1IP1, NKX2-1
14q21.1-14q23.3	lost one copy	FOXA1, NIN, KTN1, MAX, GPHN
14q31.1-14q32.33	lost one copy	TSHR, BCL11B, TRIP11, GOLGA5, DICER1, TCL6, TCL1A, AKT1
15q14-15q15.1	lost one copy	C15orf55, BUB1B
15q21.2-15q26.1	lost one copy	MYO5A, TCF12, MAP2K1, PML, NTRK3, IDH2, CRTC3, BLM
16p11.2-16p13.3	lost one copy	FUS, IL21R, PALB2, GRIN2A, TSC2, TRAF7, AXIN1, CREBBP, MYH11, ERCC4, CIITA, SOCS1, TNFRSF17
16q12.1-16q13	lost one copy	CYLD, HERPUD1
16q21-16q24.3	lost one copy	CDH11, CBFB, CDH1, MAF, CBFA2T3, FANCA
17p12-17p13.3	homozygous deletion	MAP2K4, NCOR1, TP53, PER1, GAS7, USP6, YWHAE
21q22.11	gain	OLIG2
21q22.2-21q22.12	lost one copy	ERG, TMPRSS2, U2AF1, RUNX1
22q11.21-22q13.2	gain	CLTCL1, BCR, SMARCB1, MN1, CHEK2, EWSR1, NF2, MYH9, PDGFB, MKL1, EP300
Xq13.1	lost one copy	FOXO4, MED12, NONO
Xq21.1-Xq28	lost one copy	ATRX, STAG2, ELF4, GPC3, PHF6, ATP2B3, RPL10, MTCP1

Germline mutations with allele frequency change in SG0069 in comparison to the normal (CGC genes)

Gene Name	**Amino acid change**	**cDNA location**	**Genomic location**	***Effect**	**Severity**	**^VAF Tumour**	**^VAF Normal**
ABL1	p.P803P	c.2409C>G	9:133589268-133763062	SC	LOW	0.76	0.44
FSTL3	p.L47L	c.139C>T	19:676389-683392	SC	LOW	0.73	0.25
KRAS	p.D60D	c.180A>G	12:25357723-25403870	SC	LOW	0.71	0.40
NIN	p.A872A	c.2616G>T	14:51186481-51297839	SC	LOW	0.71	0.42
RUNX1	p.P463P	c.1389G>C	21:36160098-37357047	SC	LOW	0.74	0.47
TMPRSS2	p.G296G	c.888G>A	21:42836478-42903043	SC	LOW	0.74	0.51

9.2. KEGG pathway analysis of DEGs normalised to normal salivary gland

Pathway	Adjusted p-value	Genes
Upregulated DEGs		
Systemic lupus erythematosus	1.30E-32	HIST2H2AA3, HIST2H2AA4, HIST2H2AB, HIST2H2AC, HIST1H2AE, HIST1H2AG, HIST3H2BB, HIST1H2AB, HIST1H2AL, HIST1H2AI, HIST1H2AH, HIST1H2AK, HIST1H2AJ, H2AFX, ACTN4, HIST2H2BF, HIST2H3A, HIST1H2BF, HIST1H2BE, HIST1H2BH, HIST1H2BG, HIST1H2BB, HIST2H3D, HIST2H3C, HIST1H2BD, HIST1H2BC, HIST1H2BN, HIST1H2BM, HIST1H2BO, HIST1H3J, HIST1H2BJ, HIST1H2BI, HIST1H2BL, HIST1H2BK, HIST2H4A, HIST1H3A, HIST2H4B, HIST1H3F, HIST1H3G, HIST1H3H, HIST1H3I, HIST1H3B, HIST1H3C, HIST1H3D, HIST1H3E, HIST1H4K, HIST1H4L, HIST1H4A, HIST1H4B, HIST3H2A, H2AFY2, HIST1H4H, HIST1H4J, HIST1H4D, HIST1H4F
Alcoholism	6.63E-27	HIST2H2AA3, HIST2H2AA4, HIST2H2AB, HIST2H2AC, HIST1H2AE, HIST1H2AG, HIST3H2BB, HRAS, HIST1H2AB, HIST1H2AL, HIST1H2AI, HIST1H2AH, HIST1H2AK, HIST1H2AJ, H2AFX, HIST2H2BF, HIST2H3A, ADORA2B, HIST1H2BF, HIST1H2BE, HIST1H2BH, HIST1H2BG, HIST1H2BB, HIST2H3D, HIST2H3C, HIST1H2BD, HIST1H2BC, HIST1H2BN, HIST1H2BM, HIST1H2BO, HIST1H3J, HIST1H2BJ, HIST1H2BI, HIST1H2BL, HIST1H2BK, HIST2H4A, HIST1H3A, HIST2H4B, HIST1H3F, HIST1H3G, HIST1H3H, HIST1H3I, HIST1H3B, HIST1H3C, HIST1H3D, HIST1H3E, HIST1H4K, HIST1H4L, GRIN2C, HIST1H4A, HIST1H4B, HIST3H2A, H2AFY2, HIST1H4H, HIST1H4J, HIST1H4D, HIST1H4F
Viral carcinogenesis	5.14E-08	HIST1H2BN, HIST1H2BM, HIST1H2BO, HIST1H2BJ, HIST1H2BI, SRC, HIST1H2BL, HIST1H2BK, PIK3R2, CDC20, HIST2H4A, HIST2H4B, HIST3H2BB, HRAS, HIST1H4K, HIST1H4L, CDKN2A, ACTN4, HIST2H2BF, CCNA2, HIST1H4A, HIST1H4B, CDK6, HIST1H2BF, HIST1H4H, HIST1H2BE, HIST1H2BH, HIST1H4J, HIST1H2BG, HIST1H2BB, TP53, HIST1H4D, HIST1H2BD, HIST1H4F, HIST1H2BC
Cell cycle	5.41E-07	MCM7, BUB1B, TTK, PKMYT1, CDC20, CCNB2, CCNB1, CDC45, PTTG1, ORC1, MYC, E2F1, E2F2, BUB1, CDKN2A, CDC6, CDC25C, CDC25B, SMC1B, CCNA2, CDK6, MCM3, MCM4, TP53, MCM2
Breast cancer	1.45E-05	NOTCH3, NOTCH1, LEF1, PIK3R2, DLL3, WNT6, FGF9, MYC, HEY2, E2F1, E2F2, HRAS, FZD1, JAG2, TCF7L1, FZD2, JAG1, WNT3A, FZD7, WNT7B, FZD9, FGF17, CDK6, TP53, FGFR1
Ribosome	2.65E-05	RPL32, RPL31, RPLP0, RPL10A, RPL6, RPL7, RPS15, RPL7A, RPS17, RPS19, RPL18A, RPS18, RPL36, RPL35, RPL13, RPS2, RPS11, RPL21, RPS7, RPS5, RPL13A, RPL23A, RPS26, RPL26, RPL29

Human papillomavirus infection	1.16E-04	NOTCH3, LAMA5, NOTCH1, ITGB4, PIK3R2, LAMC2, THBS2, WNT6, PARD6A, TERT, HEY2, E2F1, HRAS, HES2, HES4, FZD1, TCF7L1, FZD2, JAG1, LAMB3, WNT3A, FZD7, WNT7B, FZD9, LAMB1, PPP2R3B, TUBG1, VEGFA, CCNA2, COL2A1, CDK6, COL4A2, COL4A1, COL9A1, COL9A3, COL9A2, TP53, LLGL1, ITGA9
ECM-receptor interaction	2.14E-04	LAMA5, LAMB3, ITGB4, LAMC2, LAMB1, HMMR, THBS2, COL2A1, COL4A2, COL4A1, SV2A, COL9A1, COL9A3, COL9A2, AGRN, ITGA9
Pathways in cancer	5.47E-04	HSP90AB1, SLC2A1, LAMC2, FGF9, MYC, HEY2, RAC3, HRAS, DAPK1, DAPK3, KIF7, PGF, SMO, COL4A2, COL4A1, CKS2, BIRC5, TP53, NOTCH3, CEBPA, LAMA5, NOTCH1, GSTP1, LEF1, PDGFA, TGFA, PIK3R2, RASGRP1, DLL3, WNT6, TERT, E2F1, E2F2, PLCG1, FZD1, JAG2, ARNT2, TCF7L1, FZD2, JAG1, LAMB3, CDKN2A, WNT3A, FZD7, WNT7B, FZD9, IGF2, LAMB1, VEGFA, FGF17, CDK6, FGFR1
Bladder cancer	1.33E-03	SRC, CDKN2A, DAPK1, MYC, DAPK3, E2F1, E2F2, HRAS, TP53, VEGFA
Hepatocellular carcinoma	2.41E-03	FZD1, TCF7L1, FZD2, WNT3A, CDKN2A, FZD7, GSTP1, WNT7B, LEF1, FZD9, IGF2, TGFA, PIK3R2, WNT6, CDK6, TERT, MYC, E2F1, E2F2, PLCG1, TP53, HRAS
Axon guidance	2.46E-03	SRC, SEMA6D, SEMA3A, SEMA4C, PIK3R2, EFNA4, BMP7, NTN1, NTN3, EFNB1, EFNA3, EFNB3, PARD6A, SMO, RAC3, PLXNB1, PLCG1, EPHA1, BMPR1B, HRAS, EPHB4, NGEF, EPHB3
Basal cell carcinoma	2.46E-03	FZD1, WNT6, TCF7L1, FZD2, SMO, WNT3A, FZD7, WNT7B, LEF1, FZD9, KIF7, TP53
Hippo signalling pathway	2.63E-03	FZD1, TEAD4, TCF7L1, FZD2, WNT3A, FZD7, WNT7B, LEF1, FZD9, WTIP, BMP7, SMAD7, WNT6, PARD6A, MYC, BIRC5, DCHS1, BMPR1B, LLGL1, TEAD2, TP73
Transcriptional misregulation in cancer	7.75E-03	CEBPA, ARNT2, SLC45A3, HIST1H3J, PDGFA, PLAT, ETV4, HIST2H3A, HIST1H3A, MYC, HIST1H3F, HIST1H3G, HIST1H3H, HIST1H3I, TCF3, HIST2H3D, HIST1H3B, TP53, HIST2H3C, HIST1H3C, HIST1H3D, HIST1H3E
Focal adhesion	7.56E-03	LAMA5, LAMB3, ITGB4, SRC, RASGRF1, PDGFA, PIK3R2, LAMC2, LAMB1, ACTN4, THBS2, PGF, VEGFA, COL2A1, COL4A2, COL4A1, COL9A1, RAC3, FLNA, COL9A3, COL9A2, HRAS, ITGA9
Downregulated DEGs		
Salivary secretion	1.87E-17	PRH2, ADRB1, ATP1A2, LPO, AQP5, ADRB2, STATH, ADCY8, ADRA1A, HTN1, CST5, SLC9A1, CST4, HTN3, CST2, CST1, PRB1, DMBT1, PRB2, MUC7, NOS1, PRKACB, SLC12A2, AMY1A, AMY1B, AMY1C, PRKCA, ATP2B2, ATP1B1, LYZ, MUC5B, PLCB4, TRPV6, FXYD2
Pancreatic secretion	1.38E-05	PNLIPRP1, SLC12A2, RYR2, AMY2A, AMY2B, PLA2G2C, PLA2G2A, ATP2A3, PRKCA, RAB27B, ATP1A2, ATP2B2, ATP1B1, ADCY8, SLC9A1, PLCB4, CA2, KCNQ1, FXYD2, SLC26A3, CFTR

Carbohydrate digestion and absorption	3.72E-04	G6PC, AMY2A, AMY2B, AMY1A, SI, AMY1B, FXYD2, AMY1C, ATP1A2, SLC5A1, ATP1B1, TAS1R3
Regulation of lipolysis in adipocytes	4.26E-05	FABP4, PDE3B, PTGER3, AQP7, ADRB1, PLIN1, ADRB2, ADCY8, PTGS2, PRKACB, MGLL, TSHR
PPAR signalling pathway	5.45E-05	CPT1A, ACSL1, CYP4A11, ADIPOQ, AQP7, FABP3, FABP4, ACADL, ACOX2, PLIN4, HMGCS2, CD36, PLIN1, PLIN5
Thyroid hormone synthesis	5.45E-05	GPX2, PRKCA, ATP1A2, ATP1B1, ADCY8, TSHR, SLC5A5, TPO, PLCB4, TG, IYD, CREB3L1, FXYD2, PRKACB
Retinol metabolism	7.60E-05	UGT2B10, UGT2B11, ADH1A, CYP4A11, UGT2B28, ADH4, CYP2C9, DHRS9, ALDH1A1, RDH16, AOX1, UGT1A8, UGT1A6
cAMP signalling pathway	1.50E-04	RYR2, GRIA2, PTGER3, PDE3B, ADRB1, ATP1A2, ADRB2, ADCY8, SLC9A1, GRIN2A, CREB3L1, PDE4A, PRKACB, GRIA3, GRIA4, ATP2B2, FOS, ATP1B1, GRIN2B, TSHR, FXYD2, PPP1R1B, PDE3A, VIP, CFTR, RAPGEF3
Morphine addiction	1.54E-04	GABRA2, GABRB2, KCNJ6, PDE1B, GABRA4, PDE3B, PRKCA, OPRM1, ADCY8, PDE3A, PDE4A, PDE7B, PDE8B, PRKACB, KCNJ3
Adrenergic signalling in cardiomyocytes	1.76E-04	RYR2, PRKCA, ADRB1, ATP1A2, ATP2B2, ADRB2, ATP1B1, ADCY8, ADRA1A, PIK3CG, SLC9A1, CACNB2, CACNB4, PLCB4, CREB3L1, KCNQ1, FXYD2, AGTR1, PRKACB, RAPGEF3
Circadian entrainment	3.18E-04	GRIA2, RYR2, KCNJ6, PRKCA, FOS, ADCY8, GRIN2B, GRIN2A, PLCB4, RASD1, NOS1, PRKACB, GRIA3, GRIA4, KCNJ3
Amphetamine addiction	3.61E-04	GRIA2, GRIN2A, MAOB, MAOA, CREB3L1, PPP1R1B, PRKCA, FOS, PRKACB, GRIN2B, GRIA3, GRIA4

9.3. KEGG pathway analysis of upregulated DEGs normalised to SG0043, acinic cell carcinoma

Pathway	**Adjusted P-value**	**Genes**
Focal adhesion	2.45E-05	SHC4;ITGB4;SRC;LAMA3;PDGFB;PDGFA;PIK3R3;PIK3CD;LAMC2;PIK3R1;EGFR;MYLK;COMP;PDGFC;ITGB7;ITGB6;LAMB3;CAV2;EGF;LAMB1;COL4A2;COL4A4;COL4A6;COL9A2;MYL9;MET;BIRC2;BIRC3;ITGA9
Pathways in cancer	1.05E-04	WNT2B;CALML5;SLC2A1;PIK3CD;CALML3;LAMC2;FGF2;GLI3;EDNRA;WNT5B;DAPK1;RUNX1;COL4A2;COL4A4;KIT;COL4A6;MET;BIRC2;BIRC3;CEBPA;LEF1;LAMA3;PDGFB;PDGFA;TGFA;PIK3R3;PIK3R1;PTGS2;RASGRP1;DLL1;EGFR;

		WNT6;RXRA;GNG2;FZD1;JAG2;GSTM3;GSTM1;GADD45B;LAMB3;STAT1;CDKN2A;WNT3A;EGF;FZD7;STAT2;IGF2;LAMB1;CDK6;GNB4;FGFR2;FGFR1
PI3K-Akt signaling pathway	1.07E-04	CSF1;ITGB4;LAMA3;PDGFB;PDGFA;TGFA;PIK3R3;PIK3CD;LAMC2;PIK3R1;AREG;FGF2;EGFR;NTF4;COMP;RXRA;GNG2;MYB;PDGFC;ITGB7;ITGB6;NTRK2;LAMB3;EGF;IGF2;PPP2R5D;LAMB1;NGF;CDK6;COL4A2;COL4A4;KIT;COL4A6;GNB4;COL9A2;MET;FGFR2;FGFR1;ITGA9
Human papillomavirus infection	4.40E-04	WNT2B;ITGB4;LAMA3;PIK3R3;PIK3CD;PARD6G;LAMC2;PIK3R1;PTGS2;EGFR;LFNG;COMP;WNT6;ITGB7;ITGB6;ATP6V1C2;FZD1;WNT5B;LAMB3;STAT1;WNT3A;EGF;FZD7;STAT2;MX1;HLA-B;PPP2R5D;LAMB1;CDK6;COL4A2;COL4A4;COL4A6;COL9A2;IRF9;ITGA9
Glioma	4.61E-04	SHC4;CALML5;GADD45B;EGF;CDKN2A;PDGFB;PIK3CD;PIK3R3;TGFA;PDGFA;CALML3;PIK3R1;EGFR;CDK6
Small cell lung cancer	4.63E-04	LAMB3;GADD45B;LAMA3;PIK3CD;PIK3R3;LAMC2;LAMB1;PIK3R1;PTGS2;RXRA;CDK6;COL4A2;COL4A4;COL4A6;BIRC2;BIRC3
Melanoma	4.91E-04	GADD45B;EGF;CDKN2A;PDGFB;PIK3CD;PIK3R3;PDGFA;PIK3R1;FGF2;EGFR;CDK6;PDGFC;MET;FGFR1
Ras signaling pathway	6.71E-04	SHC4;CALML5;CSF1;PDGFB;PDGFA;TGFA;PIK3R3;PIK3CD;CALML3;PIK3R1;FGF2;RASGRP1;EGFR;NTF4;HTR7;GNG2;PDGFC;NTRK2;PLA2G4F;EGF;IGF2;NGF;KIT;GNB4;MET;FGFR2;FGFR1
Hippo signaling pathway	6.93E-04	FZD1;YAP1;WNT2B;WNT5B;WNT3A;FZD7;ITGB2;LEF1;PARD6G;AREG;BMP6;NKD1;WNT6;RASSF2;FRMD6;RASSF6;SNAI2;BMPR1B;BIRC2;TP73;TEAD3
Breast cancer	6.96E-04	SHC4;FZD1;JAG2;WNT2B;WNT5B;GADD45B;WNT3A;EGF;FZD7;LEF1;PIK3R3;PIK3CD;PIK3R1;FGF2;DLL1;EGFR;WNT6;CDK6;KIT;FGFR1
Wnt signaling pathway	6.99E-04	FZD1;RNF43;WNT2B;MMP7;WNT5B;WNT3A;SERPINF1;FZD7;LEF1;DKK1;NKD1;NFATC4;WNT6;SFRP1;TBL1Y;RSPO3;ROR2;RSPO1;NOTUM;LGR6;LGR4
ECM-receptor interaction	7.74E-04	LAMB3;ITGB4;LAMA3;LAMC2;LAMB1;COMP;COL4A2;SV2A;COL4A4;COL4A6;ITGB7;ITGB6;COL9A2;ITGA9
Systemic lupus erythematosus	0.00145327	HIST1H3J;C1S;HIST1H4L;C1R;C4A;HIST3H2A;H2AFJ;HLA-DPB1;HIST1H2BE;HIST1H3G;HIST3H2BB;HIST1H2BH;HLA-DOA;HIST1H2BB;HIST1H3C;HLA-DQA2;HIST1H4D;HIST1H4F
Complement and coagulation cascades	0.00175426	SERPINB2;C1S;C1R;ITGB2;FGG;SERPINF2;CFI;PLAUR;F3;C4A;PLAU;CD59;CFB
Transcriptional misregulation in cancer	0.00175847	CEBPA;MEF2C;CEBPB;HIST1H3J;GADD45B;BCL11B;HPGD;PDGFA;ETV4;RUNX1;MYCN;RXRA;PLAU;TLX1;NFKBIZ;HIST1H3G;ITGB7;PROM1;HIST1H3C;CDK14;MET;BIRC3
C-type lectin receptor signaling pathway	0.00229957	EGR2;CALML5;SRC;STAT1;STAT2;PIK3R3;PIK3CD;CALML3;PIK3R1;LSP1;PTGS2;NFATC4;CLEC7A;CASP1;IRF9
Hepatocellular carcinoma	0.0025978	SHC4;FZD1;GSTM3;GSTM1;WNT2B;WNT5B;GADD45B;WNT3A;CDKN2A;FZD7;LEF1;IGF2;PIK3R3;TGFA;PIK3CD;PIK3R1;EGFR;WNT6;CDK6;MET

Axon guidance	0.002743	EPHA4;SEMA4A;EPHA7;WNT5B;TRPC3;SEMA3C;SRC;SEMA3A;PIK3R3;PIK3CD;PARD6G;SEMA3E;PIK3R1;SEMA3F;NTN1;NFATC4;RGMA;EFNB1;BMPR1B;MYL9;MET
Central carbon metabolism in cancer	0.00370966	NTRK3;KIT;SLC2A1;PIK3CD;PIK3R3;SLC1A5;PIK3R1;MET;EGFR;FGFR2;FGFR1
Gastric cancer	0.00409026	SHC4;FZD1;WNT2B;WNT5B;GADD45B;WNT3A;EGF;FZD7;LEF1;PIK3R3;PIK3CD;PIK3R1;FGF2;EGFR;WNT6;RXRA;MET;FGFR2
Staphylococcus aureus infection	0.00504779	C4A;C1S;C1R;ITGB2;FGG;CFI;HLA-DPB1;DSG1;HLA-DOA;HLA-DQA2;CFB
Hepatitis C	0.0060486	DDX58;EGF;STAT1;STAT2;MX1;PIK3R3;PIK3CD;PIK3R1;IFIT1;EGFR;SOCS3;CDK6;RXRA;OAS2;CLDN8;CLDN23;LDLR;IRF9
Epstein-Barr virus infection	0.00811197	GADD45B;STAT1;DDX58;STAT2;HLA-B;TAP2;PIK3R3;TAP1;PIK3CD;PIK3R1;RUNX3;CDK6;OAS2;HLA-DPB1;BLNK;VIM;CD247;HLA-DOA;B2M;HLA-DQA2;IRF9
Amoebiasis	0.00830559	LAMB3;IL1R1;ITGB2;LAMA3;PIK3CD;PIK3R3;LAMC2;LAMB1;PIK3R1;GNA15;COL4A2;COL4A4;COL4A6
Prostate cancer	0.00844642	EGF;LEF1;PDGFB;PDGFA;PIK3R3;TGFA;PIK3CD;PIK3R1;EGFR;PLAU;PDGFC;FGFR2;FGFR1
Phagosome	0.01120256	COLEC12;SFTPA2;C1R;ITGB2;TAP2;HLA-B;TAP1;COMP;MRC2;TUBB6;CLEC7A;HLA-DPB1;TLR6;SFTPA1;HLA-DOA;HLA-DQA2;ATP6V1C2
Non-small cell lung cancer	0.01223734	RXRA;CDK6;GADD45B;EGF;CDKN2A;PIK3CD;PIK3R3;TGFA;PIK3R1;EGFR
Cell adhesion molecules (CAMs)	0.01671731	NLGN1;CADM1;NRXN1;ITGB2;HLA-B;VTCN1;CD2;CDH3;CLDN8;CLDN23;HLA-DPB1;ITGB7;HLA-DOA;HLA-DQA2;ITGA9;JAM3
Aldosterone-regulated sodium reabsorption	0.01701524	SCNN1G;SCNN1B;SCNN1A;PIK3CD;PIK3R3;SFN;PIK3R1
MAPK signaling pathway	0.0202142	CSF1;PDGFB;PDGFA;TGFA;AREG;FGF2;RASGRP1;EGFR;NTF4;RPS6KA6;RPS6KA2;PDGFC;MAP3K6;NTRK2;MEF2C;PLA2G4F;GADD45B;IL1R1;EGF;CACNA2D3;IGF2;NGF;KIT;MET;FGFR2;FGFR1
Rap1 signaling pathway	0.0204297	CALML5;CSF1;SRC;EGF;ITGB2;PDGFB;PDGFA;PIK3R3;PIK3CD;PARD6G;CALML3;PIK3R1;NGF;FGF2;EGFR;PDGFC;KIT;MET;FGFR2;FGFR1
Estrogen signaling pathway	0.02185582	SHC4;CALML5;SRC;PIK3R3;TGFA;KRT23;PIK3CD;CALML3;PIK3R1;EGFR;KRT19;KRT17;KRT16;KRT15;KRT14
Alcoholism	0.02273564	SHC4;NTRK2;CALML5;HIST1H3J;HIST1H4L;CALML3;GNG2;HIST3H2A;H2AFJ;GNB4;HIST1H2BE;HIST1H3G;HIST3H2BB;HIST1H2BH;HIST1H2BB;HIST1H3C;HIST1H4D;HIST1H4F

Signaling pathways regulating pluripotency of stem cells	0.02302178	FZD1;WNT2B;WNT5B;DLX5;WNT3A;FZD7;PIK3R3;PIK3CD;INHBB;PIK3R1;FGF2;WNT6;BMPR1B;FGFR2;FGFR1
Fluid shear stress and atherosclerosis	0.02369889	GSTM3;MEF2C;GSTM1;CALML5;IL1R1;CAV2;SRC;PDGFB;PDGFA;PIK3R3;PIK3CD;CALML3;PIK3R1;NPPC;BMPR1B
Pancreatic cancer	0.02388423	CDK6;GADD45B;EGF;STAT1;CDKN2A;PIK3CD;PIK3R3;TGFA;PIK3R1;EGFR
Basal cell carcinoma	0.02440763	FZD1;WNT6;WNT2B;WNT5B;GADD45B;WNT3A;FZD7;LEF1;GLI3
Regulation of actin cytoskeleton	0.02595925	GSN;ITGB4;SRC;EGF;ITGB2;PDGFB;PDGFA;PIK3R3;PIK3CD;PIK3R1;FGF2;EGFR;MYLK;PDGFC;ITGB7;ITGB6;MYL9;FGFR2;FGFR1;ITGA9
Proteoglycans in cancer	0.02721242	FZD1;WNT2B;WNT5B;WNT3A;CAV2;SRC;FZD7;IGF2;PLAUR;PIK3R3;PIK3CD;PIK3R1;FGF2;EGFR;WNT6;PLAU;HPSE;MET;FGFR1
Kaposi sarcoma-associated herpesvirus infection	0.02741483	CALML5;SRC;STAT1;STAT2;HLA-B;PDGFB;PIK3R3;PIK3CD;CALML3;PIK3R1;PTGS2;FGF2;NFATC4;CDK6;GNG2;GNB4;CCR5;IRF9
Neurotrophin signaling pathway	0.0331292	SHC4;NTRK2;CALML5;NTRK3;PIK3R3;PIK3CD;CALML3;PIK3R1;NGF;NTF4;RPS6KA6;RPS6KA2;TP73

9.4. GSEA from SG0032 PDX normalised to SG0032-derived 2D cultures

Pathway	**Adjusted p-value**	**Genes**
E2F Targets	0.0005	TOP2A MCM7 HMGB2 LMNB1 TK1 MKI67 BIRC5 STMN1 ASF1B RRM2 PLK1 MYBL2 TCF19 CDK1 PSIP1 KIF22 MCM2 TMPO AURKB USP1 HELLS CDKN2C NASP CDC20 CDKN1B TACC3 MCM3 KIF2C MXD3 RAD51AP1 POLE BUB1B RNASEH2A HMMR MCM5 PAN2 WEE1 CIT BRCA2 DLGAP5 LUC7L3 KIF4A DEPDC1 GINS1 KIF18B HNRNPD SMC4 CDC25B WDR90 CDCA3 SPC24 DEK SHMT1 NCAPD2 EZH2 SPAG5 PNN CENPM ILF3 CCNB2 CCP110 PLK4 CBX5 ATAD2 SRSF2 MAD2L1 EXOSC8 POLD1 MCM6 GINS4 CDK4 CTCF PSMC3IP PDS5B SUV39H1 MMS22L SPC25 PCNA SMC3 RFC3 LIG1 BRCA1 CDCA8 CENPE TP53 NUDT21 ESPL1 DDX39A TIMELESS
G2M Checkpoint	0.0041	TOP2A LMNB1 NUSAP1 CENPF MKI67 BIRC5 STMN1 PLK1 MYBL2 PRC1 GINS2 CDK1 KIF22 MCM2 UBE2C TMPO AURKB BUB1 CDKN2C NASP KIF11 CDC20 CCNA2 CDKN1B TACC3 MCM3 KIF2C KIF20B POLE CHAF1A HMMR MCM5 KIF15 BRCA2 PBK KIF4A HNRNPD SMC4 CDC7 CDC25B NDC80 E2F1 TTK EZH2 CDC45 FOXN3 TRAIP CDC6 ILF3 CCNB2 CENPA SMC2 PLK4 TROAP SFPQ SAP30 NEK2 SRSF2

		MAD2L1 FBXO5 MCM6 CDK4 CTCF PDS5B CASP8AP2 SUV39H1 RPS6KA5 FANCC ATRX RBL1 EXO1 POLQ TPX2 CENPE ESPL1 DDX39A
Interferon Gamma Response	0.0226	MVP BPGM IL4R CDKN1A ICAM1 PFKP SPPL2A HIF1A ZNFX1 ST3GAL5 RIPK2 VAMP8 CD274 CASP3 TAP1 FAS IL6 BANK1 PIM1 IRF5 CASP4 TDRD7 GCH1 PTGS2 LATS2 SLAMF7 PTPN1 GBP6 TOR1B SRI PNP TRIM21 PSMB2 ARL4A CASP1 CXCL11 MYD88 TNFSF10 NAMPT TNFAIP2 SECTM1
Estrogen response late	0.0119	SLC7A5 PRSS23 HSPB8 SFN CD44 KLK10 CA2 GJB3 CAV1 PERP DYNLT3 ST14 LAMC2 MYOF OPN3 TPBG SGK1 CLIC3 CCND1 FABP5 FLNB HOMER2 KRT19 PKP3 DNAJC1 RAB31 TPD52L1 TSTA3 ST6GALNAC2 SLC27A2 CDH1 CCNA1 NRIP1 FKBP5 SCNN1A GALE TSPAN13 SLC16A1 LLGL2 RPS6KA2 ASS1 ELOVL5 TST AMFR SLC1A4 SLC26A2 UNC13B SLC29A1 MAPK13 MOCS2 RBBP8 SERPINA1 BTG3 ADD3 SLC9A3R1
KRAS Signalling up	0.0087	ALDH1A3 BPGM INHBA DCBLD2 EPHB2 EMP1 ANKH GALNT3 CA2 LIF ST6GAL1 PLAUR PLAU NRP1 JUP SLPI F2RL1 PDCD1LG2 AMMECR1 RABGAP1L PLEK2 TSPAN1 TSPAN13 PTGS2 ITGBL1 ITGB2 EPB41L3 YRDC AKAP12 HBEGF ETS1 PTPRR SPON1 MAFB CROT WNT7A CCND2 MALL TOR1AIP2 HDAC9 ACE BTC STRN
UV Response up	0.0087	GLS CDKN2B GPX3 ICAM1 CLTB CA2 CCND3 BAK1 JUNB YKT6 MAOA SPR TFRC SLC25A4 CYB5R1 CYP1A1 LYN CASP3 TAP1 TMBIM6 MMP14 TUBA4A IL6 RPN1 RRAD DNAJB1 FURIN MGAT1 NAT1 SQSTM1 GCH1 TST TGFBRAP1 BTG3 BID ATP6V1F FKBP4 ATP6V1C1 STIP1 GRPEL1 STK25 IL6ST ACAA1 DDX21 ALDOA SIGMAR1
IL6 JAK STAT3 Signalling	0.0226	IL4R CD44 OSMR TNFRSF12A BAK1 LTBR TGFB1 PTPN11 FAS CSF1 IL6 TNFRSF1A TNFRSF21 GRB2 PIM1 ITGA4 IFNGR1 ITGB3 IFNAR1 PTPN1 LEPR IL6ST IL13RA1 CXCL11 MYD88
IL2 STAT5 Signalling	0.0017	IL4R ALCAM EMP1 CDCP1 CD44 SLC1A5 MYO1E CA2 LIF SYNGR2 MYO1C CCND3 NRP1 ADAM19 BCL2L1 ANXA4 CKAP4 CAPG ITGAV PHLDA1 SERPINB6 CASP3 NT5E TGM2 SH3BGRL2 RABGAP1L CSF1 IGF2R KLF6 TNFRSF21 PIM1 FURIN PLEC IFNGR1 FAH AHR TWSG1 IRF6 ECM1 SNX14 SLC39A8 PNP CYFIP1 PTGER2 HIPK2 MAPKAPK2 RNH1 CCND2 PRKCH CTSZ ARL4A
Peroxisome	0.0078	MVP RETSAT DHCR24 ACSL4 ACSL1 YWHAH TSPO SLC25A4 SLC27A2 PRDX1 CDK7 ITGB1BP1 CLN8 VPS4B ELOVL5 IDH1 SLC35B2 CTPS1 PRDX5 SCP2 CRAT IDH2 GSTK1 LONP2 ACAA1 HRAS ABCD3 DHRS3 ACOX1
Apoptosis	0.0014	PEA15 RETSAT EMP1 CDKN1A CD44 ANKH GPX3 GADD45A VDAC2 CAV1 TNFRSF12A TGFB2 IER3 GPX1 SLC20A1 BCL2L1 CCND1 ANXA1 GNA15 TSPO KRT18 LGALS3 MCL1 SC5D F2R CASP3 TAP1 CCNA1 FAS IGFBP6 IL6 LUM SPTAN1 IGF2R DNAJC3 TIMP3 PPP2R5B BAX FEZ1 GSR HSPB1 CASP4 IFNGR1 SQSTM1 GCH1 PTK2 BCAP31 PSEN1 BTG3 BID
Cholesterol Homeostasis	0.0067	ALCAM MAL2 TNFRSF12A PLAUR ETHE1 FABP5 LGALS3 SC5D S100A11 CPEB2 SQLE LSS CXCL16 ACTG1 STARD4 LDLR ANXA5 NSDHL DHCR7 JAG1 GNAI1
Allograft rejection	0.0014	INHBA IL4R CDKN2A THY1 GCNT1 ICAM1 LIF CCND3 TGFB2 GBP2 HIF1A CAPG TGFB1 RIPK2 RPL9 LYN F2R TAP1 FAS CSF1 IL6 TLR1 ELF4 TAP2 NPM1 DEGS1 ABI1

		EIF5A IFNGR1 BCAT1 ITGB2 IL11 TPD52 TLR6 ABCE1 ETS1 IL18 CCND2 GALNT1 HDAC9
Unfolded protein response	0.0017	SLC7A5 NABP1 TUBB2A BAG3 WIPI1 PAIP1 EIF4G1 DNAJB9 YWHAZ SEC31A KDELR3 SHC1 SRPRB DNAJC3 NPM1 LSM1 SERP1 SLC1A4 SPCS3 ATF6 SEC11A KIF5B CALR HERPUD1 EIF2S1 ATP6V0D1 HSPA5 EXOC2 YIF1A DCTN1 ALDH18A1 EIF4E EIF2AK3 DNAJA4
Adipogenesis	0.0005	RETSAT HSPB8 NABP1 MGLL GPX3 GADD45A YWHAG MYLK SLC1A5 GBE1 ME1 ESYT1 STOM ATP1B3 DNAJB9 DHRS7 SNCG REEP5 C3 TKT ACLY GHITM SDHC CD151 AGPAT3 ACO2 IFNGR1 CMPK1 LPCAT3 IDH1 TST FAH PGM1 UBQLN1 RNF11 GRPEL1 DHCR7 MTCH2 SCP2 RIOK3 CRAT SOWAHC TALDO1 ELOVL6 IDH3A ARL4A CPT2 ESRRA DLD ALDOA RMDN3 ACOX1 COL15A1 G3BP2 BCL2L13 UQCR11 CS GPD2 MGST3 DNAJC15 MRPL15 NMT1 DLAT BAZ2A DECR1 DDT UQCR10 SOD1 ACADL
Myogenesis	0.001	COL1A1 FST ABLIM1 HSPB8 CDKN1A GJA5 GPX3 CHRNB1 MYLK NQO1 SPHK1 SYNGR2 MYO1C ACTA1 CNN3 TPM3 ACSL1 TGFB1 CRYAB MAPRE3 IGFBP7 ADAM12 TPD52L1 MRAS PDE4DIP FHL1 SVIL KIFC3 TPM2 SPTAN1 FLII REEP1 ADCY9
Estrogen response early	0.0005	SLC7A5 PRSS23 ABLIM1 HSPB8 SFN CD44 SEC14L2 FHL2 KLK10 KRT8 GJA1 RHOD DYNLT3 ENDOD1 MYOF OPN3 TPBG CLIC3 CCND1 B4GALT1 FLNB KRT18 LAD1 KRT19 RAB31 SNX24 TPD52L1 THSD4 SLC27A2 KLF10 TGM2 ZNF185 NRIP1 SLC37A1 SVIL SLC1A1 FKBP5 SCNN1A REEP1 RRP12 UGCG SLC39A6 SLC16A1 ADCY9 RPS6KA2 ELOVL5 WWC1 AMFR SLC1A4 SLC26A2 RBBP8 CLDN7 TIPARP ADD3 SLC9A3R1 SH3BP5 FKBP4 FARP1 DHCR7 ABAT SYBU NADSYN1 TUBB2B CBFA2T3 IL6ST AREG KCNK15
Bile acid Metabolism	0.0019	RETSAT DHCR24 BCAR3 OPTN ACSL1 GCLM TFCP2L1 RBP1 SLC27A2 NPC1 IDH1 SLC29A1 SLC35B2 PRDX5 SCP2 IDH2 GSTK1 LONP2 CROT ABCD3 BMP6
Fatty acid Metabolism	0.0005	RETSAT DHCR24 ACSL4 MGLL CA2 ACSL1 ME1 YWHAH HSPH1 S100A10 MAOA SERINC1 SMS RAP1GDS1 CYP1A1 TP53INP2 HCCS SDHC ACO2 ELOVL5 LGALS1 IDH1 LDHA PCBD1 CRYZ NSDHL CRAT OSTC BLVRA UGDH ACAA1 PDHB CPT2 DLD SUCLA2 ALDOA DLST ACOX1 GPD2 HADHB PTS METAP1 FH HMGCL DECR1 ACADL HSD17B4 PRDX6 PDHA1 EPHX1 UROS ACOT8
Hypoxia	0.0005	F3 LOX NDST1 ANXA2 CDKN1A P4HA2 ACKR3 GPC1 CAV1 PFKP SRPX FOSL2 IER3 GBE1 IDS PLAUR SERPINE1 TPBG SDC4 CITED2 XPNPEP1 PGK1 UGP2 TGFBI GYS1 KDELR3 HK1 TGM2 TPST2 DUSP1 TES IL6 AK4 KLF6 PIM1 EXT1 TPI1 PGM1 TIPARP LDHA CHST3 AKAP12 ADORA2B TPD52 HDLBP PGM2 DTNA NAGK ETS1 PRDX5 HSPA5 MYH9 CASP6 GPI CHST2 AMPD3 PDGFB ALDOA LXN
Glycolysis	0.0005	PLOD2 PYGL P4HA2 CD44 PGAM1 CHPF DSC2 PKP2 PKM GPC1 PFKP IER3 PPIA TPBG SLC16A3 ME1 CITED2 B4GALT1 COPB2 PGK1 UGP2 TGFA PRPS1 TGFBI GOT2 TSTA3 GYS1 SLC35A3 GFPT1 SDC1 CHPF2 KDELR3 NT5E SDHC AK4 MET GALE PMM2 EXT1 TPI1 GPR87 TXN IDH1 PPP2CB TPST1 LDHA ALG1 ADORA2B EXT2 HDLBP B4GALT4 FKBP4 ARPP19 PGM2 NSDHL HSPA5 ME2 TALDO1 CASP6 CHST2 IL13RA1 GCLC DLD SLC25A13 ALDOA

TGF BETA Signalling	0.0033	THBS1 PMEPA1 BCAR3 SERPINE1 SKIL SLC20A1 JUNB TGFB1 RAB31 KLF10 CDH1 TJP1 ID3 ACVR1 TGFBR1 FURIN FKBP1A SMURF1 SMURF2
ROS Pathway	0.0044	GPX3 NQO1 PDLIM1 PFKP GCLM JUNB HMOX2 MGST1 PRDX1 ABCC1 GSR TXNRD1 TXN MBP OXSR1 STK25 FTL GCLC LAMTOR5 NDUFS2 G6PD SOD1 PRDX4 PRDX6 CDKN2D
Xenobiotic Metabolism	0.0005	RETSAT SLC1A5 NQO1 CA2 ATP2A2 TGFB2 SERPINE1 EPHA2 SLC12A4 JUP ABCC3 MAOA DHRS7 CYP1A1 TMBIM6 ACOX3 COMT FAS CDA SERTAD1 SSR3 TNFRSF1A NPC1 SAR1B ACO2 GSR ELOVL5 GCH1 IDH1 AOX1 FAH BCAT1 CYFIP2 CNDP2 PINK1 TPST1 AKR1C2 PDLIM5 ACP2 CYP26A1 ARPP19 XDH ATOH8 CROT CASP6 ADH5 UGDH GCLC ABHD6 ACOX1 PTGES ASL PTS DHRS1 RBP4 GSS GAD1 NMT1 DDT GART MCCC2 SLC35D1 PAPSS2 BCAR1
MTORC1 Signalling	0.0005	PLOD2 SLC7A5 CDKN1A DHCR24 SLC1A5 ATP2A2 GBE1 PPIA ACTR2 ME1 ACTR3 RAB1A DAPP1 YKT6 PGK1 TFRC PSMD14 SC5D CORO1A ATP6V1D ACLY MLLT11 TUBA4A SYTL2 TES RPN1 PRDX1 EIF2S2 AK4 USO1 SQLE PPA1 M6PR GSR TPI1 TXNRD1 SQSTM1 HSPA4 ELOVL5 PSMD12 IDH1 SERP1 SLC1A4 PGM1 PSMB5 ABCF2 BCAT1 ITGB2 ARPC5L ADD3 LDHA CTSC SLC9A3R1 PNO1 PSME3 TUBG1 PSMC6 STARD4 SEC11A LDLR STIP1 CALR GSK3B DHCR7 PNP HSPA5 ACSL3 PSMC2 ELOVL6 GPI SKAP2 GCLC ETF1 ALDOA HMGCR PSMC4 SDF2L1 NAMPT PITPNB ACACA BHLHE40 EDEM1 UFM1 SLC7A11 NFKBIB HSPD1 PSMA3 RIT1 NMT1 G6PD UBE2D3 LTA4H
Coagulation	0.0005	F3 THBS1 PRSS23 CAPN2 MMP15 FN1 THBD GNG12 SERPINE1 PLAU COMP BMP1 WDR1 ANXA1 ADAM9 LAMP2 ARF4 CTSB C3 DUSP14 MMP14 PREP GDA TIMP3 FURIN RABIF KLK8 ITGB3 SERPINA1
Complement	0.0005	F3 MMP15 CA2 EHD1 FN1 PLAUR SERPINE1 ME1 SPOCK2 XPNPEP1 CALM1 ADAM9 LAMP2 CTSB LGALS3 LIPA GMFB LYN USP14 CASP3 C3 MMP14 CDA MMP12 GNAI2 PREP MSRB1 IL6 GRB2 PIM1 RABIF CASP4 PFN1 USP15 PPP2CB SERPINA1 PSEN1 CTSL CTSC RHOG ANXA5 PDP1 HSPA5 MMP13 PIK3CA SERPINB2 GNAI3 CASP1 PDGFB
Heme Metabolism	0.0005	BPGM CAST P4HA2 HTATIP2 ELL2 CA2 OPTN CCND3 PICALM LRP10 SLC30A1 ENDOD1 GCLM LAMP2 TRAK2 CDR2 ADIPOR1 CTSB TFRC SEC14L1 ATG4A C3 HAGH ATP6V0A1 PPP2R5B TMEM9B NNT NEK7 TRIM58 SNCA USP15 DAAM1 NFE2L1 GDE1 ANK1 RIOK3 SLC10A3 BLVRA MOCOS DMTN SDCBP MOSPD1 GCLC IGSF3 SYNJ1 PDZK1IP1 FECH ARL2BP NCOA4 SIDT2 MGST3 NUDT4 CDC27 CLCN3 YPEL5 SLC7A11
Oxidative Phosphorylation	0.0005	RETSAT VDAC2 ATP1B1 TIMM17A CYCS ATP6V0E1 GOT2 VDAC1 SLC25A4 ATP6V1H ATP6V1D CYB5R3 HCCS MFN2 SDHC OAT BAX ACO2 OGDH NNT ETFA IDH1 ATP6V1E1 SLC25A20 ATP6V0B LDHA ATP6V1F ATP6V1C1 NDUFB2 GRPEL1 ATP6V1G1 COX17 NDUFS1 PDP1 IDH2 NDUFB3 ACAA1 IDH3A TCIRG1 GPI PDHB COX7A2 OPA1 DLD SUCLA2 DLST NDUFA1 UQCR11 CS HADHB UQCRC2 MGST3 NDUFC1 NDUFS2 MRPL15 FH GLUD1 DLAT NDUFA8 DECR1 UQCR10 MRPL35 MRPS12 PDHX PDHA1 UQCRFS1 SUCLG1 MDH1 POR UQCRH NDUFAB1 CASP7

		PHYH SDHB ACAT1 COX5B NDUFA4 PRDX3 MDH2 SLC25A3 POLR2F COX6B1 AIFM1 COX5A VDAC3 ACAA2 TIMM8B CYC1 COX7A2L
UV Response DN	0.0005	F3 COL1A1 ANXA2 TGFBR2 RND3 SLC7A1 EFEMP1 FHL2 MGLL INPP4B GCNT1 PLCB4 CAV1 GJA1 SERPINE1 NRP1 DLG1 CITED2 ANXA4 SYNJ2 TJP1 DUSP1 MET COL1A2 ABCC1 LPAR1 NEK7 ITGB3 CAP2 VAV2 DAB2 SIPA1L1 ADD3 IRS1 PTPRM ADORA2B PDLIM5 ERBB2 DDAH1 MAPK14 SRI LDLR
Apical Junction	0.0005	AMIGO2 LAMB3 ITGA3 RRAS CDH3 ADAMTS5 LAYN MSN THY1 ICAM1 FSCN1 SIRPA CAP1 ACTA1 NFASC LIMA1 CDSN ACTN1 LAMC2 CDH8 JUP YWHAH BMP1 DLG1 B4GALT1 ADAM9 FLNC CLDN4 ACTG2 CRB3 PCDH1 TGFBI LAMA3 NEGR1 VASP CD274 NF2 CTNNA1 CLDN11 CDH1 TJP1 MYL9 ZYX BAIAP2 GNAI2 SHC1 MYL12B PARVA DSC3 RSU1 ARPC2 PFN1 ACTB PTK2 MAPK13 VAV2 CLDN7 MPP5 CNN2 ACTG1 IRS1 ITGB4 MAPK14 TUBG1 ADRA1B
P53 Pathway	0.0005	CDKN2B RETSAT SFN CDKN1A SLC3A2 CDKN2A DGKA GADD45A TM7SF3 DRAM1 LIF SPHK1 VDR ZMAT3 CCND3 PERP IER3 SERPINB5 ST14 PHLDA3 KRT17 PLK2 BAK1 EPHA2 IRAK1 TGFA ZNF365 S100A10 TGFB1 STOM MAPKAPK3 RHBDF2 VAMP8 TPD52L1 WWP1 SEC61A1 SDC1 F2R TAP1 OSGIN1 EPS8L2 FAS BAIAP2 RRAD GM2A BAX
Protein Secretion	0.0005	AP2M1 COPB2 TMED2 YKT6 LAMP2 KRT18 ATP1A1 CLN5 CAV2 SEC31A ATP6V1H SCRN1 CLTC RPS6KA3 COPB1 STX12 IGF2R ARCN1 USO1 M6PR SCAMP3 ADAM10 SEC22B VPS4B TMX1 AP3S1 AP1G1 SNX2 MAPK1 SEC24D AP2B1 OCRL CTSC AP3B1 TPD52 ARFGEF1 STAM RAB5A YIPF6 SCAMP1 GBF1 RAB22A ICA1 VAMP3 CLTA ARF1 VAMP7 TOM1L1 DNM1L RAB2A TSG101 CLCN3 ARFGAP3 SOD1 STX7 RER1 AP2S1 ARFIP1 LMAN1 ZW10 SGMS1 GOSR2 ARFGEF2
Inflammatory Response	0.0005	F3 INHBA DCBLD2 IL4R CDKN1A SLC7A1 ICAM1 EDN1 SLC31A2 LIF SPHK1 PVR ATP2A2 OSMR RNF144B PLAUR SERPINE1 TPBG GNA15 HIF1A PCDH7 SGMS2 ITGA5 FZD5 RIPK2 LYN ITGB8 MMP14 CSF1 IL6 TLR1 MET KLF6 ABI1 LPAR1 GCH1 ITGB3 ROS1 PSEN1 IFNAR1 HBEGF AHR ADORA2B SRI LDLR RHOG
Epithelial Mesenchymal Transition	0.0005	PLOD2 COL1A1 LOX THBS1 FSTL3 PMEPA1 TNC INHBA GLIPR1 CD44 TPM1 GADD45A MYLK THY1 MFAP5 PVR FN1 PTHLH GPC1 TNFRSF12A CDH2 SPOCK1 GJA1 PLAUR SERPINE1 LAMC2 COMP PDLIM4 SDC4 BMP1 CALD1 NNMT CAPG TPM4 TGFB1 ITGA5 TGFBI MXRA5 LAMA3 ADAM12 ITGAV FAP SDC1 NT5E TGM2 MMP14 ANPEP FAS MYL9 IL6 TPM2 IL32 LUM TIMP3 CALU COL1A2 OXTR COPA COLGALT1 ITGB3 LGALS1 COL12A1 CAP2 DAB2 PLOD3 EDIL3 LOXL1 FSTL1 MATN3 NID2 TAGLN WNT5A ECM1 NOTCH2 SFRP4 VEGFC COL5A2 PFN2
TNFA Signalling via NFKB	0.0005	F3 PMEPA1 TNC INHBA LAMB3 CDKN1A CD44 TUBB2A GADD45A ACKR3 DRAM1 ICAM1 EDN1 LIF SPHK1 EHD1 CLCF1 FOSL2 IER3 SIK1 PLAUR SERPINE1 PLAU SGK1 PLK2 SERPINB8 SDC4 CCND1 PHLDA2 B4GALT1 JUNB F2RL1 DNAJB4 RIPK2 MCL1 PHLDA1 SLC2A6 KLF10 TAP1 TRIP10 FJX1 DUSP1 CSF1 IL6 PANX1 KLF6 B4GALT5 SQSTM1 GCH1 PTGS2 NFE2L2 TNIP1 BTG3 TIPARP YRDC HBEGF PDLIM5 CEBPD LDLR
Androgen Response	0.0005	ALDH1A3 PMEPA1 DHCR24 ADAMTS1 ANKH INPP4B ELL2 KRT8 CCND3 ACTN1 SGK1 CCND1 B4GALT1 TMEM50A HOMER2 SLC38A2 KRT19 DNAJB9 UBE2J1

		ITGAV SMS UAP1 RPS6KA3 CDK6 MYL12A FKBP5 RRP12 GSR ELOVL5 PGM3 STK39 SLC26A2 SPCS3 SEC24D AKAP12 PDLIM5 TPD52

9.5. GSEA from SG0032 combination treated PDX tumours normalised to vehicle treated tumours

Pathway	**Adjusted p-value**	**Genes**
P53 Pathway	0.0065	PLK2 HEXIM1 TRAF4 BTG2 ZFP36L1 TSC22D1 IER5 TOB1 DDIT4 VDR RAP2B PPP1R15A BLCAP AEN TXNIP FOXO3 SERTAD3 RNF19B PHLDA3 RAB40C POM121 CDKN2B OSGIN1 CSRNP2 TP63 PLK3 CCNK KLF4 DNTTIP2 PPM1D LIF MDM2 FBXW7 TRIB3 CDKN2AIP BTG1 APAF1 SP1 MXD1 ZNF365 NOL8 MKNK2 IP6K2 PTPRE SESN1 CDK5R1 BMP2 BAIAP2 RRP8 XPC PDGFA SPHK1
G2M Checkpoint	0.0012	AMD1 MYC PAFAH1B1 CTCF TLE3 UCK2 YTHDC1 MAPK14 RASAL2 ABL1 CUL3 SMAD3 CUL1 PML CDKN1B CCNT1 PRPF4B EFNA5 ARID4A E2F3 MTF2 RBM14 INCENP CCNF KATNA1 MARCKS KPNA2 PDS5B XPO1 NUP98 H2AFX E2F4 BCL3 SQLE MEIS1 CKS2 SNRPD1 NUP50 DBF4 ORC5 KIF22 SFPQ AURKA CDC27 DR1 STAG1 HNRNPD CASP8AP2 CDC25A SRSF1 RAD21 POLA2 DKC1 SAP30 TOP1 CDC25B
Mitotic Spindle	0.0012	ARF6 CDC42EP1 PAFAH1B1 BCAR1 ARHGEF2 KIF1B CSNK1D PPP4R2 ARHGEF7 RASAL2 ABL1 AKAP13 ARHGEF3 CDC42EP4 MAP3K11 ARL8A NCK1 MAP1S TLK1 CYTH2 CDC42EP2 GEMIN4 NEDD9 SOS1 RICTOR MARK4 SMC3 INCENP ARHGEF11 LATS1 KATNA1 FGD4 MARCKS CLASP1 ARHGAP29 RASA1 TAOK2 SAC3D1 TIAM1 MID1 BCL2L11 SSH2 PLEKHG2 ARFGEF1 CLIP2 CKAP5 WASF2 MID1IP1 KIF22 AURKA SPTAN1 APC ARHGAP27 ALS2 WASL CDC27 TUBGCP3 RAPGEF6 TUBGCP6 NET1
UV Response DN	0.0012	CITED2 ID1 SNAI2 BHLHE40 MT1E MYC RND3 GCNT1 ZMIZ1 DUSP1 IRS1 RUNX1 YTHDC1 MAPK14 SMAD3 PIK3R3 CDKN1B NR3C1 PRDM2 DYRK1A MIOS CDK13 PHF3 SCAF8 WDR37 DAB2 VAV2 ACVR2A TJP1 SFMBT1 SMAD7 PTEN PEX14 DLC1 MRPS31 INPP4B NIPBL NR1D2 FYN ATXN1 APBB2
MYC Targets V2	0.0072	MYC WDR43 PPRC1 NOP16 NOP2 GNL3 MPHOSPH10 WDR74 NOP56 GRWD1 RRP12 PUS1 BYSL NDUFAF4 TBRG4 RCL1 TFB2M SUPV3L1 UTP20 NIP7 HK2 DUSP2 AIMP2 FARSA NOC4L
TGF BETA Signalling	0.0051	ID1 TGIF1 SMURF1 SLC20A1 ID3 PPP1R15A BCAR3 SKI SMAD3 SKIL ID2 SMAD1 ARID4B TRIM33 TJP1 SMAD7 CDK9 BMP2 SMURF2

TNFA Signalling via NFKB	0.0012	PLK2 MCL1 FOSL2 CEBPB SIK1 SPSB1 BHLHE40 SGK1 BTG2 KLF6 MYC TGIF1 TSC22D1 IER5 PPP1R15A PNRC1 DUSP1 FJX1 ZFP36 RNF19B NFE2L2 CEBPD SMAD3 EFNA1 ID2 KLF4 SNN NFKB2 ETS2 LIF BCL6 FOSL1 PHLDA1 DDX58 EDN1 KLF9 DUSP4 IRS2 MAP2K3 PFKFB3 BTG1 TRIB1 NFIL3 ZBTB10 CCNL1 MXD1 TNFAIP3 MARCKS KDM6B PTPRE NFKBIA PTGER4 RIPK2 BMP2 TIPARP TRIP10 BCL3 SPHK1 CLCF1 RELA TNFAIP8 RELB G0S2 SOCS3 EGR3 FUT4 IER3 CFLAR DNAJB4 NFKBIE DUSP5 BIRC3